2012

Turbine Blade Internal Cooling: Trailing Edge, Coolant-Passage Entry, Bend Effect and Improvement in Thermal Performance

Krishnendu Saha
Louisiana State University and Agricultural and Mechanical College

TURBINE BLADE INTERNAL COOLING: TRAILING EDGE, COOLANT-PASSAGE ENTRY, BEND EFFECT AND IMPROVEMENT IN THERMAL PERFORMANCE

A Dissertation

Submitted to the Graduate Faculty of the
Louisiana State University and
Agricultural and Mechanical College
in partial fulfillment of the
requirements for the degree of
Doctor of Philosophy

in

The Department of Mechanical Engineering

by
Krishnendu Saha
B.S., Jadavpur University, Kolkata, India, 2006
December 2012

ACKNOWLEDGMENTS

I would like to express my gratitude and appreciation towards my adviser Dr. Sumanta Acharya for giving me the opportunity to work in this project under his guidance. I would also like to thank him for his invaluable technical and professional guidance at different stages of my PhD. Without his support and guidance, this work could not have been done.

I would also like to express my gratitude towards Dr. Dimitris Nikitopoulos and Dr. Ingmar Schoegl for serving as advisory committee members and Dr. Shengmin Guo for numerous helpful suggestions. I would like to thank Mr. Don Colvin, Mr. Barry Savoy, Mr. Jim Layton (late), Mr. Paul Rodriguez, Mr. Joe Bell and Mr. George Gascon for helping me fabricate different test sections at different stages of my PhD work.

I would also like to thank my labmates and colleagues: Mr. Del Segura, Mr. Amir Estiaghi, Mr. Shengrong Zhu, Mr. Srinibas Karmakar, and Mr. Prasad Kalghatgi for helping me in various ways during my research. I am most fortunate to have my brother, Mr. Dibyendu Saha, to be with me and support me during the toughest moments of my PhD program. I would like to thank him and my parents for being the constant source of motivation, without whom this work could never have been done.

TABLE OF CONTENTS

NOMENCLATURE

A = Area

AR = Channel Aspect Ratio = Channel width (W)/ Channel height (H)

D_h = Hydraulic diameter of a channel

D_{in} = Hydraulic diameter of the entry sub-channel of the lattice

D_m = Hydraulic diameter of a sub-channel at the middle cross of the lattice

D_p = Groove print diameter

DR = Density ratio = $(\rho_b - \rho_w)/ \rho_b = (T_w - T_b)/ T_w$

d = Penetration depth

e = Rib height

f = Average friction factor

f_0 = Friction factor for fully developed flow in a smooth circular channel

H = Channel height

h = Heat transfer coefficient

k = Thermal conductivity of air

L = Length of a channel

Nu = Nusselt number = hD_h/k

Nu_0 = Nusselt number for a fully developed flow in a smooth circular channel

Pr = Prandtl number

P= Rib pitch

Δp = Pressure drop between two pressure tappings

q_w = Wall heat flux

Re = Reynolds number = $\rho V D_h /\mu$

Re_s = Reynolds number at the inlet of a sub-channel

Ro = Rotation number = $\Omega D_h / V$

s = Channel lengthwise direction

t = Time

T_W= Wall temperature at time t

T_0= Wall temperature at time t=0

T_∞= Mainstream air temperature

TPF= Thermal performance factor

V = Velocity of air

V_b = Average fluid velocity at test section inlet

V_{in}= Velocity of air at inlet

V_m = Velocity in a sub-channel at the middle cross section of the lattice

W = Channel width

x = Streamwise distance

Δx= Distance between two pressure tapings

y = Distance perpendicular to streamwise direction

α = Diffusivity

δ = Dimple/groove depth

ρ = Density of air

μ= Dynamic viscosity of air

τ_d = Dimensionless penetration time

LIST OF TABLES

LIST OF FIGURES

ABSTRACT

Efficient cooling of gas turbine blade is imperative for safe operation of the gas turbine engine at high temperatures. In the present work, two converging lattice structures suitable for trailing edge applications are tested and their performance is compared with a conventional pin-fin configuration. Another constant cross section lattice structure is tested to see the cooling efficiency of lattice channels with different number of sub-channels. Converging lattice structures show higher heat transfer enhancement and comparable or higher thermal performance than traditional pin-fin cooling used in gas turbine trailing edge. The highest pressure drop incurred in a multi-pass channel is at the bend region. A turbine designer always desires to reduce the pressure drop in the bend region without reducing the heat transfer in that region. A total of nine different bend geometries are studied numerically and their performance is compared with a baseline U-bend geometry. Modifications for the bend geometry are made along the channel divider wall and at the endwall of the 180 degree bend. From the numerical study, two geometries (symmetrical bulb and bulb-bow combination) are down selected for experimental study with the goal of improving the Thermal Performance Factor (TPF) in the coolant channel. Different shapes and arrangements of rib turbulators were studied over the last few decades to enhance local turbulence close to the hot gas turbine blade wall and promote secondary flow close to the wall. A combination of angled grooves and angled ribs are used to find the heat transfer and pressure drop across the channel and compare their performance with standard ribbed channel. A 1:4 Aspect Ratio (AR) two-pass cooling channel is tested with three different entrance geometries under stationary conditions. It is seen that the presence of the complex entrance geometries changes the heat transfer enhancement profile at the inlet of the test section significantly when compared to a fully developed entrance. Numerical simulations are

done in rotating condition to see the complex interaction of the entrance geometry driven flow and rotation induced flow.

CHAPTER 1: INTRODUCTION

1.1 Motivation

Gas turbine engines are gaining popularity as an efficient means of power generation in aircraft propulsion and land-based power generation. The schematic of a gas turbine engine is shown in Figure 1.1. The compressor draws air from the atmosphere and raises pressure before it enters the combustion chamber. Fuel is mixed with air in the combustion chamber, which releases energy, and the high temperature air then passes through the turbine that causes the air to expand. The expanded air then hits the turbine blade causing rotation of the turbine blade. For aircraft gas turbine engine, the air is exhausted through a nozzle to provide thrust.

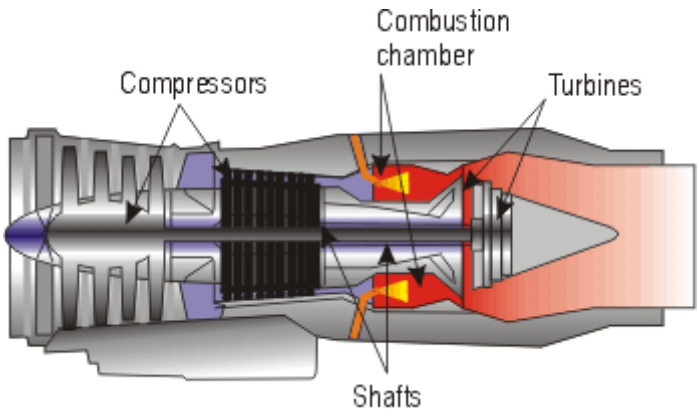

Figure 1.1: Schematic of a gas turbine engine (Advanced Materials for Gas Turbine Engines – High Pressure Turbine)

To increase the efficiency of a gas turbine engine, the temperature of air entering the gas turbine must be as high as possible without causing the blade to fail. Typically turbine engines are operated at 1600 -1800 K, which is far above the permissible temperature limit of the blade material. Thus cooling of the blades is indispensable for the safe operation of the engine. The blades are cooled internally and externally by passing cool air over the surface and through a cooling passage inside the blade. Cooling air is extracted from the compressor which affects the

efficiency of the engine adversely because less mass flow of air is available in the combustion chamber for power generation. In a typical modern turbine engine, up to 20 percent of air is extracted from the compressor portion of the engine and passed through the internal cooling channels of the blade. Therefore, the goal is to maximize cooling while taking a minimum amount of air from the compressor. Thorough understanding of the flow through the coolant channels can assist designers towards a more efficient design of the engines operating at higher efficiency with increased power output.

1.2 Gas turbine blade cooling techniques

Different cooling techniques used in gas turbine blades are shown in Figure 1.2. The leading edge faces the highest heat load coming from the hot air in the combustion chamber. The leading edge of the channel is cooled by impinging cold air on the internal wall of the leading edge.

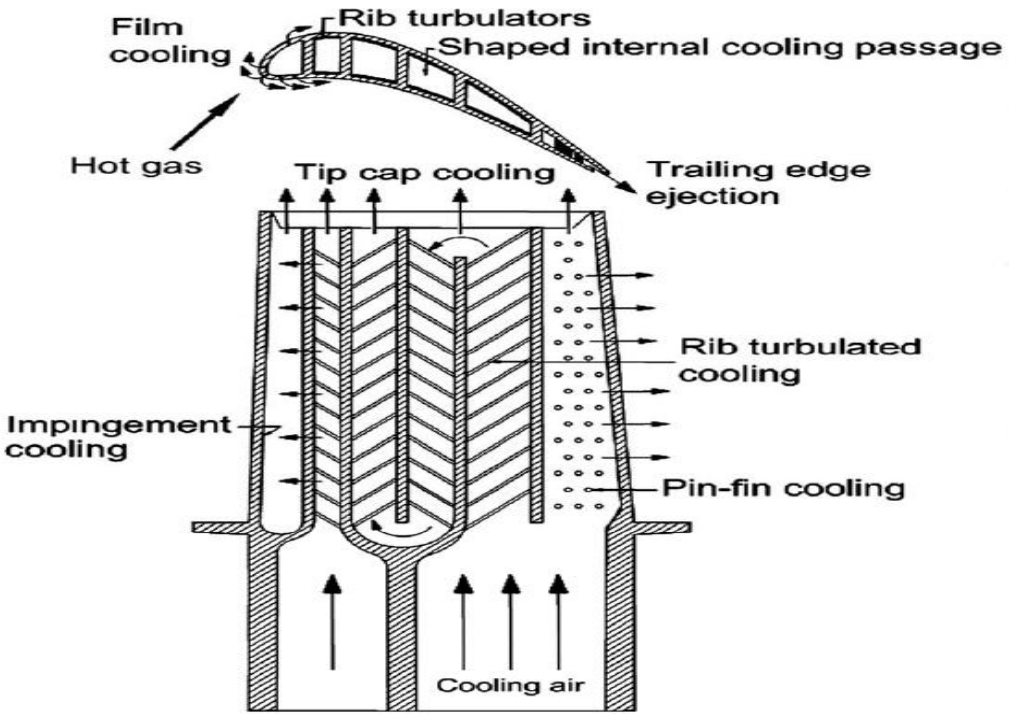

Figure 1.2: Different cooling techniques used in gas turbine blades (Han et al., 2000)

The leading edge is further protected by passing the cooling air from the internal channels through some discrete holes drilled on the leading edge surface. Cold air extracted from these holes, called film cooling holes, forms a protective layer of cold air and prevents direct contact of the hot gas with the blade surface. The mid chord of the blade is cooled from internal air passing through serpentine internal cooling passages. The walls of the internal cooling passages are mounted with turbulence promoters called ribs which trip the hydrodynamic boundary layer and enhance mixing. Trailing edges are more vulnerable to failure compared to the other parts of the blade due to the small cross section in the trailing edge region. Circular cylinders placed in an array, called pin-fins, are generally used in the trailing edge of the gas turbine blade which extends from the suction side to the pressure side of the blade. Blockage of the internal cooling air by the pin-fins produces complex vortex structures and enhanced mixing, resulting in higher heat transfer from the internal wall of the blade.

1.3 Internal cooling

1.3.1 Stationary rib configurations: In a typical gas turbine internal cooling channel, ribs are cast on two opposite walls (leading and trailing wall) of the internal cooling channel to promote turbulence and enhance heat transfer. When air flows over a rib, it separates from the rib at the top and reattaches to the blade surface between the ribs. This separation and reattachment enhances turbulent mixing and as a result enhances heat transfer from the blade surface, as compared to a smooth surface. The schematic of a flow over a ribbed surface is shown in Figure 1.3. Extensive work has been done over the years studying different aspects of ribbed geometries under stationary and rotating conditions. Some key parameters studied include: a) rib angle of attack, b) rib pitch, c) rib height, d) channel AR effect on ribs, e) rib orientation and other

innovative rib designs. The literature available on heat transfer in a ribbed channel under a stationary frame is abundant. They are classified into different key parameters as explained above.

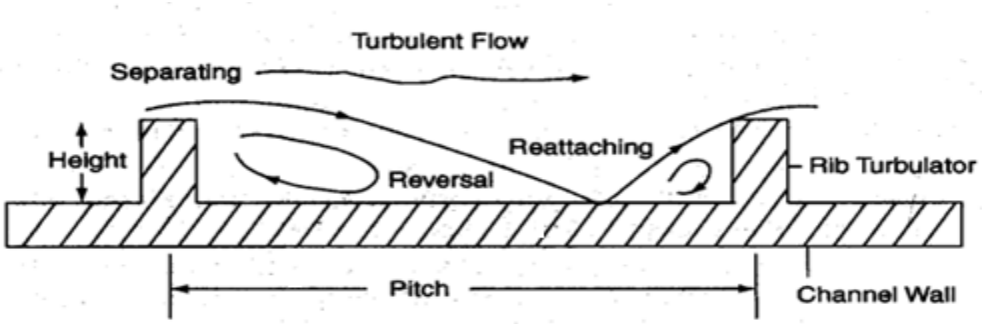

Figure 1.3: Schematic of flow over a ribbed surface (Han et al., 2000)

1.3.1.1 Effect of rib angle of attack: If the ribs are attached to the blade surface at an angle to the flow it produces secondary flow from one side to the other side. The interaction of this secondary flow with the main flow enhances heat transfer better than that of a transverse rib. Fann et al. (1994) explained the occurrence of higher heat transfer in angled ribs compared to the transverse ribs. They showed that for transverse ribs the vortices produced upstream and downstream of the ribs were stagnant and resulted in lower heat transfer close to the ribs. But for an angled rib the secondary flow causes the vortices to move along the angled ribs and join the main flow. This interaction causes high heat transfer enhancement on the blade surface. The concept of this flow behavior is shown in Fig. 1.4. Han et al. (1978) performed heat transfer and pressure drop studies using different rib spacing and angle of attacks for 45° and 90° angles placed in symmetric and staggered arrangements. A parameter called thermal performance is defined which takes into account both the heat transfer and pressure drop. The overall performance of a cooling system is characterized by the thermal performance factor. They

concluded that ribs with pitch/height ratio (P/e) of 10 with 45° angle of attack arranged in a staggered manner produced the highest thermal performance. Han (1984), Han and Park (1988) did extensive studies on stationary rib configurations and concluded that thermal performance primarily depended on the rib spacing, the channel aspect ratio, rib angle of attack and flow Reynolds number. They found that for square channel and 2:1 AR channel angle of attack α = 60° produced the highest heat transfer enhancement but α = 30° produced the highest thermal performance. Han et al. (1989) examined the effects of different angle of attack for narrow aspect ratio (AR = 1:2 and 1:4) channels. They concluded that the highest heat transfer was obtained utilizing an angle of attack of α = 60°, but the thermal performance was highest for α = 45°.

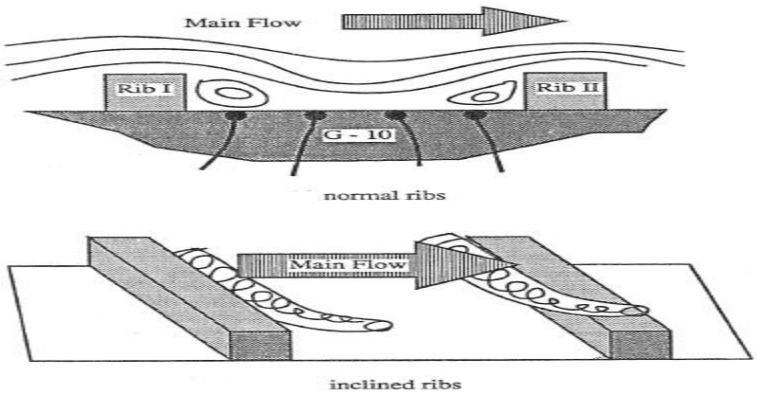

Figure 1.4: Formation of secondary flow in an angled rib channel (Fann et al., 1994)

Park et al. (1992) studied the effect of rib angle for 5 different aspect ratios (4:1, 2:1, 1:1, 1:2, and 1:4). They concluded that the narrow AR channels performed better than the wide AR channels for same angle of attack. They also found that α = 45° and α = 60° produced higher values of heat transfer enhancement for all rectangular channels except the 4:1 AR channel. For the narrow AR channel 1:4, highest heat transfer enhancement was obtained for α = 45°. The

detailed results are shown in Fig. 1.5. Fann et al. (1994) presented the effects of angle of attack and rib orientation with respect to the flow direction for a multipass channel with a square cross section. The results show that α = 45°, with right orientation, produce both the highest heat transfer enhancement and thermal performance. Kiml et al. (2001) studied a 2:1 AR channel for α = 45°, 60°, 75° and 90°. They concluded that, when averaging was done over all 4 surfaces of the channel, the 60° ribs produced the highest heat transfer enhancement and the 45° ribs produced the highest pressure drop. Bunker and Osgood (2003) tested the heat transfer performance of a square channel with ribs attached at a 45° angle of attack and leaning into and away from the flow. Rib lean angles tested were 45, 22.5, 0,-22.5 and -45 degrees. They concluded that the ribs with no leans produced the highest heat transfer enhancement.

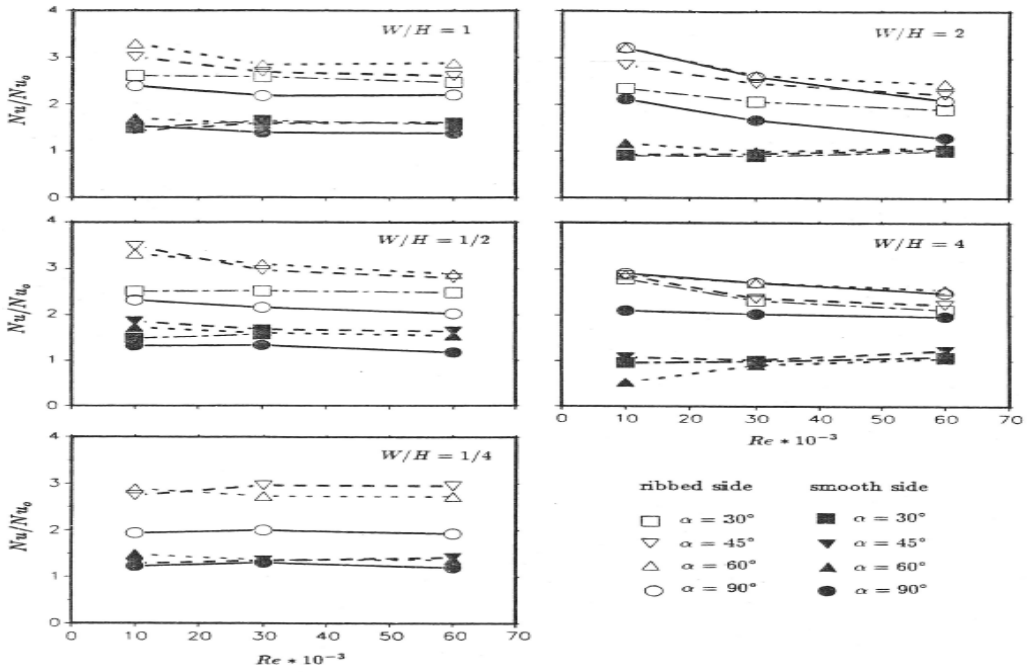

Figure 1.5: Effect of different angle of attack (Park et al., 1992)

1.3.1.2 Effect of rib pitch: The rib pitch has significant effect on the heat transfer enhancement of the blade surface. For smaller rib spacing, the reattachment of the flow on the blade surface

cannot occur and results in low heat transfer enhancement on the blade surface. For a rib spacing that is too large, a thick boundary layer is formed after the flow reattachment that causes lower values of heat transfer enhancement. Han and Park (1988) compared rib pitch to rib height (P/e) ratios of 10 and 20. They showed that P/e = 10 produced higher heat transfer enhancement than P/e = 20 for all aspect ratios. Park et al. (1992) also studied the effects of pitch by comparing P/e =10 with P/e =7.5 and found that P/e = 7.5 produced a higher heat transfer enhancement than P/e =10. Han et al. (1978) compared different rib pitches and concluded that P/e = 10 produced the optimum value of rib pitch. Figure 1.6 shows the effect of different rib pitches as shown by Han et al. (1978).

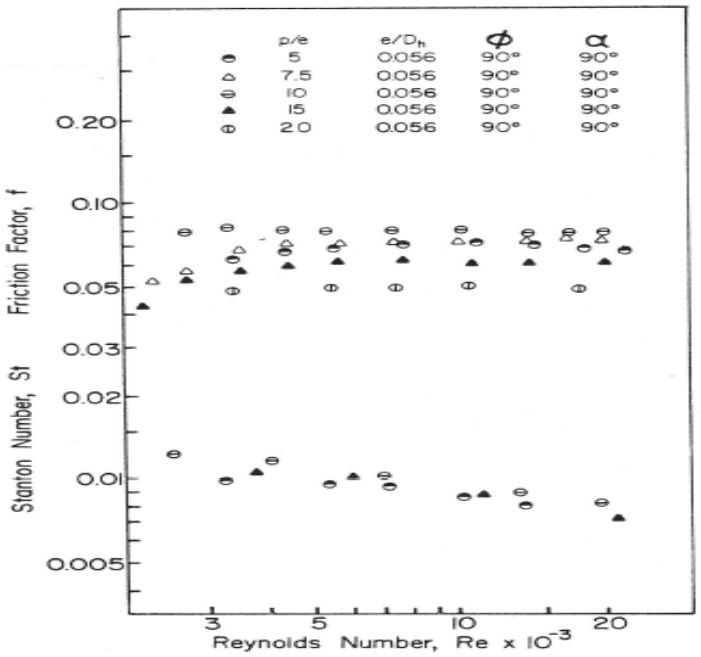

Figure 1.6 : Effect of different rib pitch (Han et al., 1978)

Taslim and Wardsworth (1997) and Taslim and Lengkong (1998) studied the heat transfer coefficient on the rib surface for three different rib spacing in a transverse and 45° ribbed

channel respectively. They showed that P/e =10 produced the highest thermal performance factor for both transverse and angled ribs.

1.3.1.3 Effect of rib height: Taslim et al. (1996) illustrated the effect of rib height by comparing 3 rib height/hydraulic diameter (e/D_h) ratios of 0.083, 0.125, and 0.167 for a square channel. They reported that the heat transfer was not sensitive to the rib height but the pressure drop increased largely due to the increase of rib height. They reported that for the 45° angled ribs, the highest thermal performance factor (TPF) was obtained for e/D_h = 0.125 when tested with Re= 5000-15000. As the Reynolds number increased, the ribs with e/D_h = 0.083 showed the highest thermal performance. A comparison between different rib heights studied is shown in Fig. 1.7.

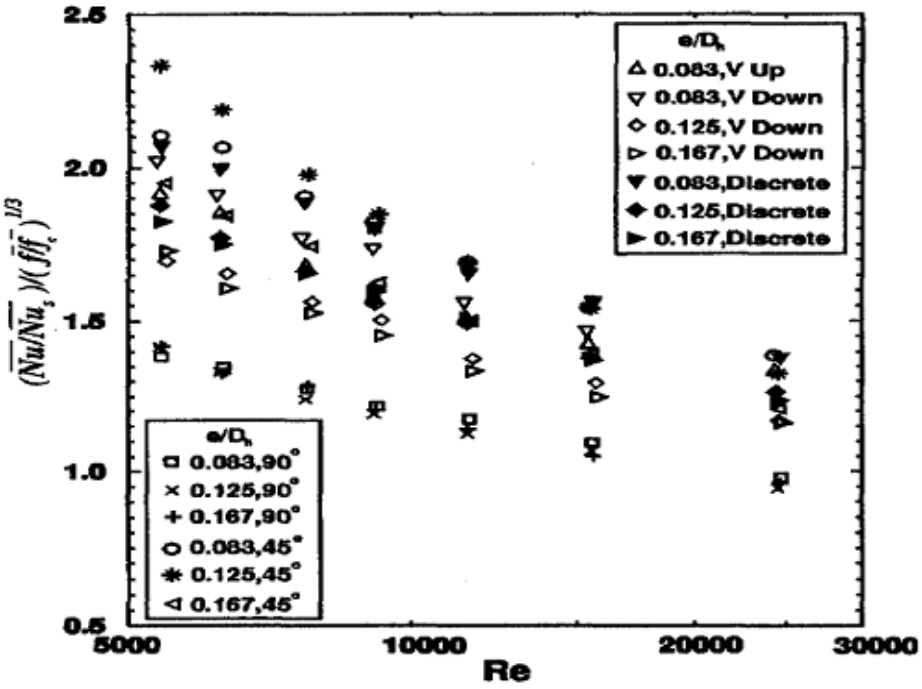

Figure 1.7: Comparison of different rib height (Taslim et al., 1996)

Han et al. (1978) also investigated the effects of rib height for e/D_h = 0.046, 0.056, and 0.076. They also found that the pressure drop increased largely with increase of rib height. Results of

Taslim and Wardsworth (1997) and Taslim and Lengkong (1998) on the rib surface heat transfer showed that the heat transfer enhancement on the rib surface was less affected by the rib height. However, the pressure drop increased substantially with rib height and as a result the lowest rib height configuration showed the highest thermal performance, based on the rib surface heat transfer coefficient. It can be seen from their results that for all rib spacing tested, the lowest rib height configurations produced the highest thermal performance.

1.3.1.4 Effect of channel aspect ratio: Park et al. (1992) studied five different Aspect Ratios (AR= 1:4, 1:2, 1:1, 2:1, and 4:1) channels with angle ribs. Their results showed that for 45 degree and 60 degree ribbed channels, the narrow AR channels performed better than the wide AR channels. Rhee et al. (2003) compared two V-shaped configurations at AR=3, 5, and 6.82. Their result also confirmed that higher AR reduced heat/mass transfer enhancement and thermal performance (Fig. 1.8).

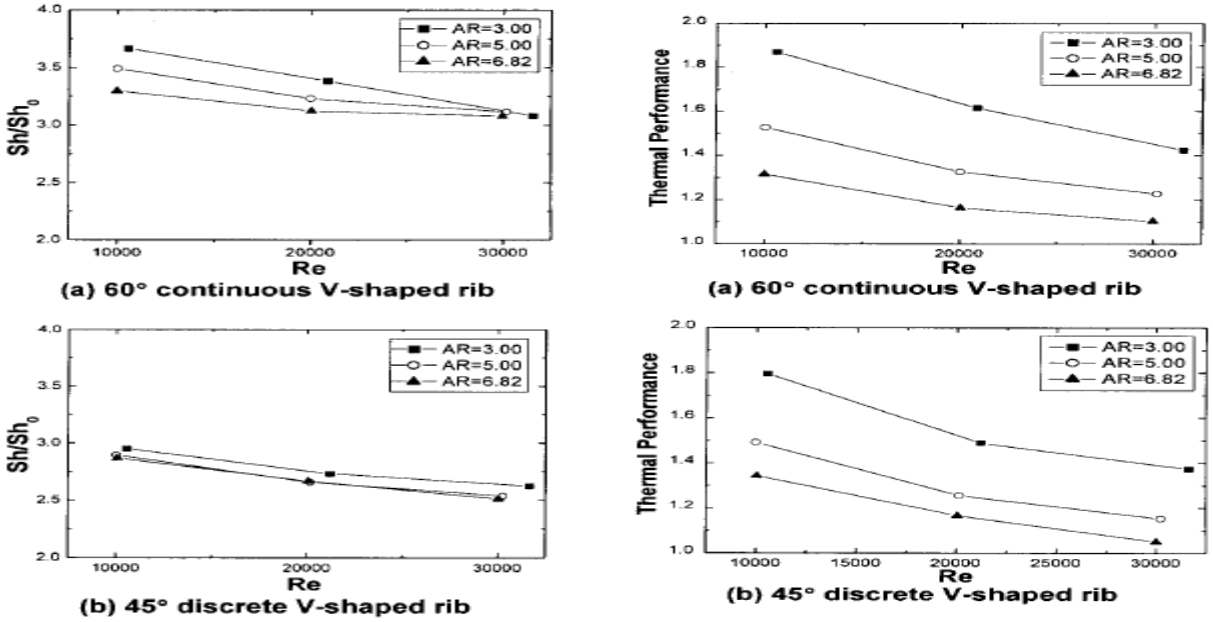

Figure 1.8: Comparison of channel AR for wide AR channels (Rhee et al., 2003)

Fu (2005) studied a 45° ribbed channel for four AR (AR = 1:4, 1:2, 1:1, and 2:1). The compiled result from their work is shown in Fig. 1.9. It can be clearly seen that the lower AR channels perform far better than the higher AR channels for the same set of Re.

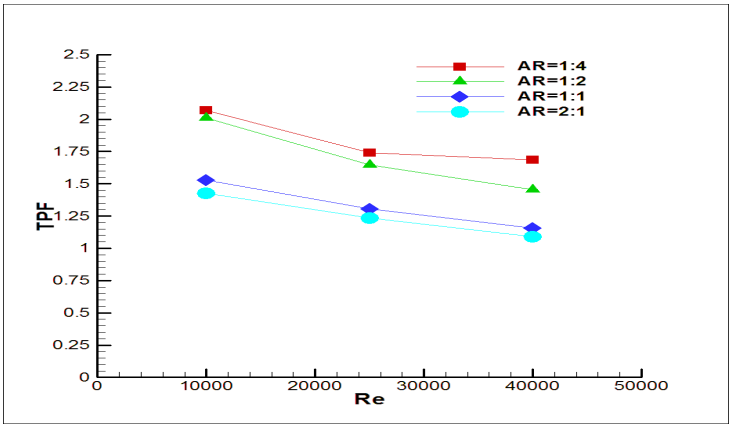

Figure 1.9: Aspect ratio comparison for a 45° ribbed channel (Fu., 2005)

1.3.1.5 Effect of rib orientation: Han et al. (1989) compared 45° and 60° parallel ribs with 45° and 60° crossed ribs. The study concluded that the heat transfer enhancement for crossed ribs could be as low as the 90° transverse ribs. The parallel ribs perform far better than the crossed ribs. Fann et al. (1994) also compared 60° parallel ribs with 60° crossed ribs in a left and right orientation. Results indicate that the 60° parallel ribs perform far better than the 60° crossed ribs for left and right orientation. They also showed that ribs with right orientation provide higher Nu ratio than ribs with left orientation. Al-Hadhrami and Han (2003) compared different 45° rib configurations under stationary and rotating conditions. The rib configurations studied are shown in Fig. 1.10. For the stationary channel, case e seems to be producing the highest enhancement for both the first and second pass. This is consistent with the finding of Fann et al. (1994), where also the right orientation produced the highest heat transfer enhancement.

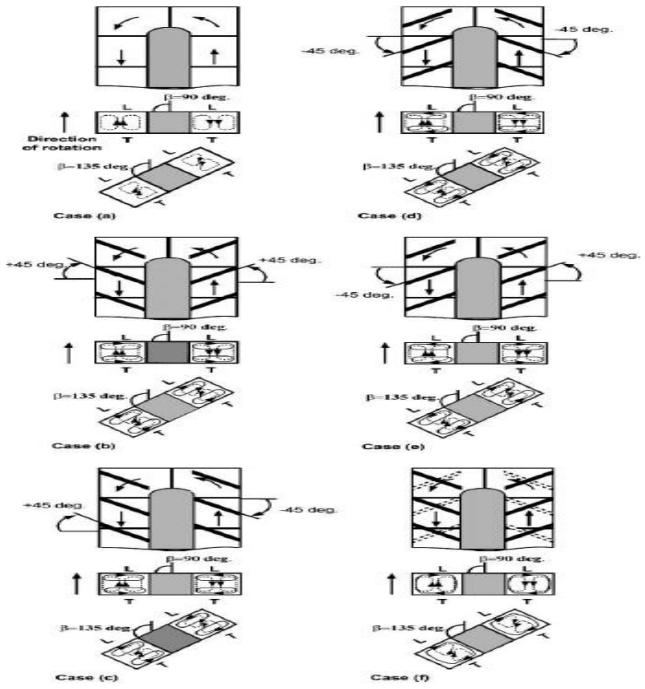

Figure 1.10 : Rib orientations used by Al-Hadhrami and Han (2003)

Han et al. (1978) compared inline symmetric ribs with staggered ribs. Their comparison seem to suggest that staggered ribs perform better than the symmetric ribs for P/e=5. Astarita and Cardone (2003) studied 30° and 45° ribs in inline and staggered arrangement for P/e =10, 20. Here the superimposed configuration showed higher values of heat transfer enhancement than the staggered ribs. Liou et al. (2006) showed that for ribs arranged in inline manner under rotation, the transverse mean velocities were directed towards the trailing wall for the 1st pass and leading wall for the 2nd pass because of the Coriolis force, but for ribs arranged in a staggered manner, the mean velocities showed a wavy pattern. They also showed that the regionally averaged heat transfer enhancement was higher for the staggered case than the inline case for 1st pass leading and trailing wall and 2nd pass leading wall. The pressure drop was also lower for the staggered case compared to the inline case.

1.3.1.6 Effect of different rib geometries: Han et al. (1991) compared parallel ribs with V-shaped ribs facing upstream and downstream. Their results showed that 60° and 45° V facing upstream produced the highest heat transfer enhancement for both the ribbed side and smooth side of the channel. Comparing friction factors, the 60° upstream facing V also produces the highest thermal performance. Han and Zhang (1992) studied 90°, 60°, and 45° parallel broken ribs and 60° and 45° broken ribs with upstream facing V and compared with the results for 60° and 45° continuous upstream facing V from Han et al. (1991). They showed that all the broken rib configurations showed higher thermal performance (higher Nu ratio and lower f ratio) than their corresponding continuous rib configurations. When comparing all configurations, the 60° broken V yields the highest thermal performance. Taslim et al. (1996) compared the effects of 45° upstream facing and downstream facing V and discrete ribs. Their discrete rib configuration performed poorly in terms of heat transfer enhancement when compared to downstream facing V or 45° staggered ribs. Comparing thermal performance they found that 45° staggered ribs performed the best, followed by the discrete ribs, downstream facing V and 90° staggered ribs. Liou et al. (2000) studied 12 different shaped ribs in a square channel. Among the 12 vortex-generator configurations studied, the 45° upstream facing V and delta wing facing upstream provided the highest pitch averaged Nusselt number ratio augmentation. Wright et al. (2004) investigated the effects of angled, V shaped, and W shaped continuous and discrete ribs for a 4:1 AR channel in a stationary and rotating frame. They concluded that discrete rib configurations were always better in terms of both heat transfer enhancement and thermal performance than the corresponding continuous ribbed cases. It was reported that discrete W shaped ribs produced the highest heat transfer but the discrete V shaped ribs produced the highest values of thermal performance factor. Han et al. (1993) studied heat transfer and pressure drop in a square channel

with wedge shaped and delta shaped ribs. They found that the delta shaped ribs produced higher heat transfer augmentation and lower pressure drop compared to the wedge shaped ribs. The backward aligned delta shaped rib produced the highest thermal performance. A comparison of thermal performance between these innovative rib designs are shown in Fig. 1.11. It can be seen from the plot that 60° broken V ribs and 45° parallel broken ribs produce the highest thermal performance.

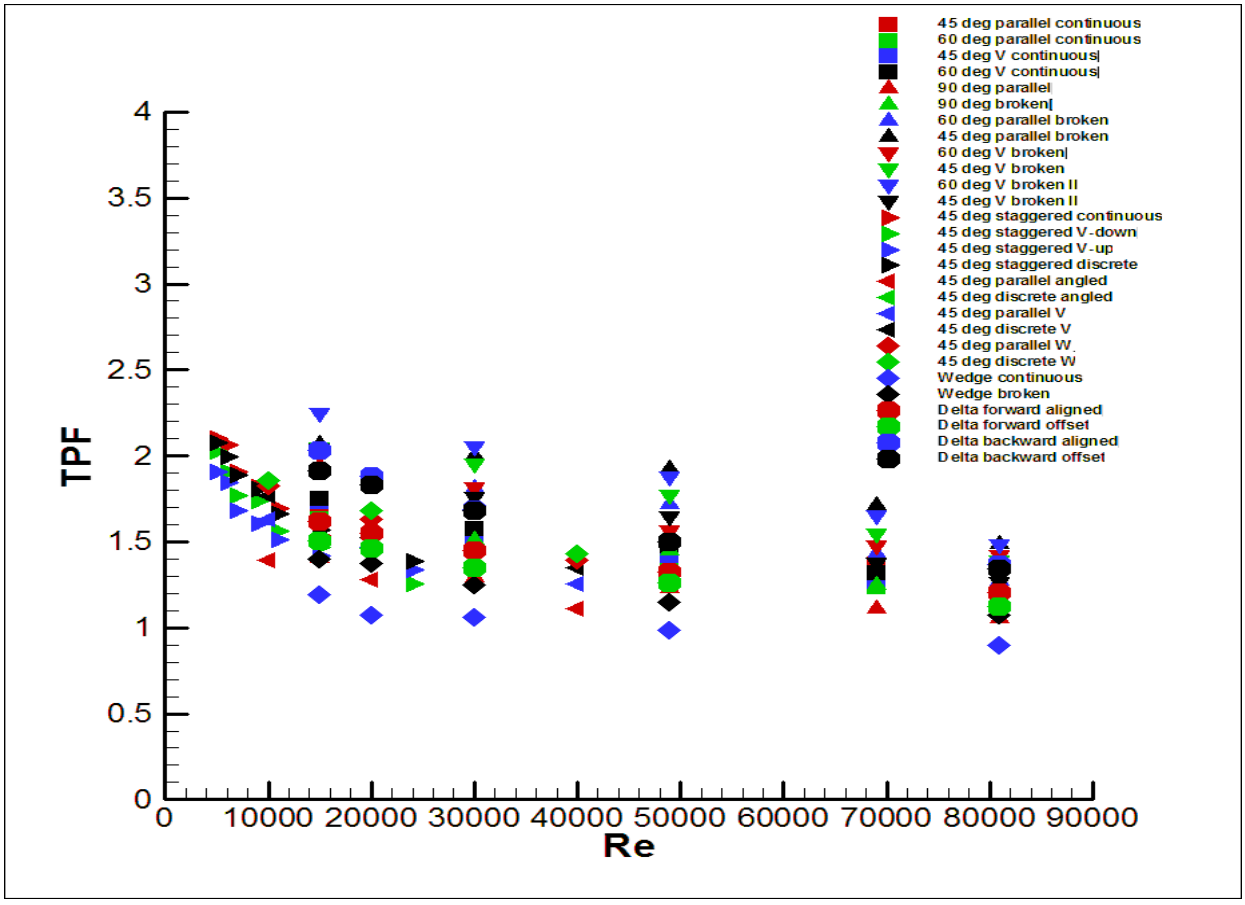

Figure 1.11: Comparisons of different rib geometries

1.3.2 Internal cooling channels under rotation: In the real world, the turbine blades rotate at high rotation speeds and hence it is necessary to test the internal cooling channels with

rotation. Coolant flow passing through the internal cooling channels experience two additional forces: 1) Coriolis forces, and 2) centrifugal buoyancy forces. These two forces combined generate secondary flow inside the cooling channel and the core flow gets redistributed asymmetrically. The following sections review the available literature on rotating smooth channels and rotating ribbed channels.

1.3.2.1 Rotation effect on flow field: Heat transfer on the coolant channel wall is dependent on the flow field inside the channel. Therefore it is necessary to understand the flow field under rotation to effectively design a cooling scheme in a turbine blade. A conceptual sketch of flow through a rotating channel is shown in Fig. 1.12. The Coriolis force is the cross product of the angular velocity of rotation and streamwise coolant fluid velocity. In the first pass, the direction of the coolant velocity is radially outward and as a result the Coriolis force acts towards the trailing surface pushing the core flow away from the leading surface. The direction of coolant velocity is opposite in the first and second pass but the direction of rotation remains the same. As a result, the Coriolis force in the second pass pushes the fluid towards the leading surface. The centrifugal buoyancy force tries to push the cooler, heavier fluid away from the rotation axis. Due to Coriolis forces, the cooler fluid in the first pass is more inclined towards the trailing surface. With the buoyancy force combined with the Coriolis force the fluid velocity close to the trailing surface increases in the first pass. So in the first pass, the centrifugal buoyancy force augments the Coriolis force and increases coolant velocity near the trailing surface. In the second pass, the Coriolis force makes the cooler fluid flow close to the leading wall. The buoyancy force combines with the Coriolis force and makes the velocity profile more uniform.

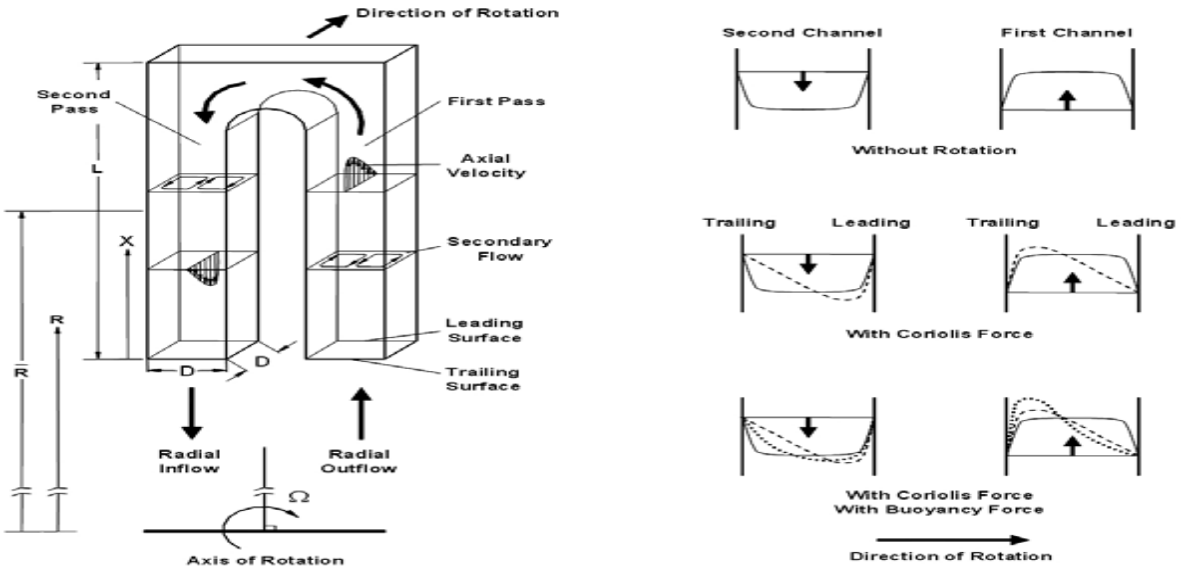

Figure 1.12: Conceptual sketch of the effects of rotation in a coolant channel (Han et al., 1993)

Velocity measurements inside a rotating multi-pass channel have confirmed the effects of Coriolis and centrifugal buoyancy forces. Bons and Kerrebrock (1999) did PIV measurements in a rotating, radially outward flow channel with and without heated walls. The results clearly showed the effects of rotation and buoyancy for a rotation number, Ro = 0.2 and density ratio, DR =0.27. Figure 1.13 shows the streamwise mean velocity and secondary velocity profile determined in this study. It is seen that for the outward flow, the combined effect of Coriolis and centrifugal buoyancy forces increase the streamwise velocity close to the trailing edge. The secondary velocity profile confirms the formation of two counter rotating vortices inside the channel.

Liou and Chen (1999) studied developing flow through a smooth two pass duct with 180° straight corner turn. Tests were done for Re = 14000 and Ro=0.082. The effect of density ratio

was not considered. The results indicate a strong separation bubble at the downstream corner of the divider wall.

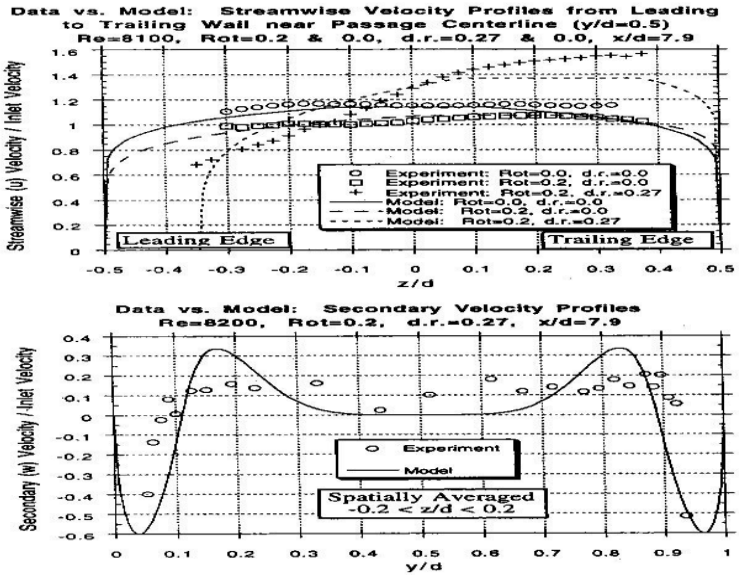

Figure 1.13: Velocity profile showing the effect of rotation and buoyancy (Bons and Kerrebrock., 1999)

As expected, the streamwise velocity profile is skewed towards the trailing wall for the first pass and towards the leading wall for the second pass. The Coriolis forces tend to affect the turbulence intensity profiles. In the first pass, the peak turbulence intensity shifts towards the trailing wall and the peak value is 1.5-2.2 times that shown in the stationary case. In the second pass right after the turn, the peaks of turbulence intensity are seen close to the trailing wall but as the flow progresses downstream, the peaks shifts towards the leading wall. Rotation also reduces the size of the separation bubble to 75% of the stationary case. Cheah et al.(1996) performed a Laser Doppler Anemometry (LDA) measurement in a U bend channel for two opposite directions of rotation at Ro = 0.2. In this case the curvature axis was parallel to the rotation axis, as compared with other cases where the curvature axis was perpendicular to the rotation axis.

They also showed the separation bubble downstream of the divider wall and concluded that a positive rotation increased the reattachment length but a negative rotation reduced the reattachment length.

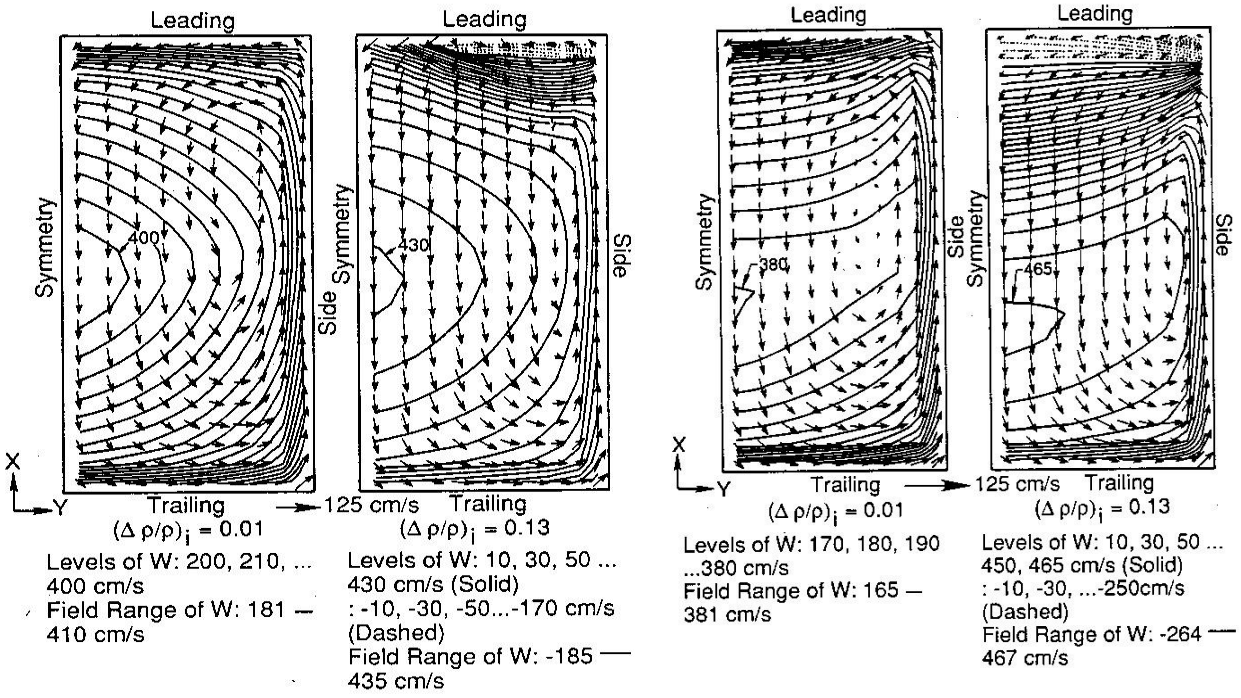

Figure 1.14: Streamwise velocity contour and cross stream velocity (Prakash and Zerkle., 1992)

Prakash and Zerkle (1992) did computational work on a radially outward flow rotating channel and considered both Coriolis and centrifugal buoyancy force. They presented data for Re=25000, Ro = 0.48, and DR = 0.01 & 0.13. They concluded that Coriolis forces produced a secondary flow from the leading to the trailing surface near the core and from the trailing to leading surface near the sidewall. The maximum streamwise velocity is near the center of the duct close to the duct inlet but as the flow progresses downstream the peak streamwise velocity shifts towards the trailing wall. Due to centrifugal buoyancy forces the fluid tries to increase the velocity of cooler

fluid near the trailing wall and reduces the velocity of warmer fluid near the leading wall. This effect becomes more significant as the density ratio increases. For the high density ratio case, a higher streamwise velocity is seen near the trailing wall and a reverse radial velocity is seen near the leading wall (Fig. 1.14).

Dutta et al. (1996) confirmed the formation of reverse flow close to the leading wall due to centrifugal buoyancy forces. They presented data for a radially outward flow duct with Re = 25000, Ro = 0.24, and DR = 0.07-0.22. As the DR increases, the flow close to the leading wall goes in the reverse direction. Dutta et al. (1996a) presented the effects of duct AR for Re = 25000, Ro = 0.5 and DR = 0.2. They presented data for radially outward flow for five different aspect ratios (AR = 4:1, 2:1 , 1:1 , 1:2, and 1:4). They concluded that the effect of centrifugal buoyancy reduced as the AR is reduced.

Real turbine blade internal cooling channels usually have ribs to enhance heat transfer. So the effect of rotation on ribbed channels is studied extensively. Iacovides et al. (1998) included transverse ribs in a staggered manner on the test section used by Cheah et al. (1996) and compared the effect of adding ribs on the flow field. They showed that the addition of ribs reduced the size of the separation bubble downstream of the divider wall. The reattachment length is about one hydraulic diameter for the ribbed case whereas it is about 2.2 diameters for a smooth case. It can be seen from their results that the rotation direction affects the flow in the first pass but the rotation direction does not have much effect in the second pass. Liou et al. (2002) conducted velocity and heat transfer measurements for a 90° ribbed square channel at Re =10000 and Ro = 0-0.2. They concluded that in the first pass, the maximum streamwise mean velocity and turbulence intensity of the ribbed duct flow increased up to 1.1 times and 2.5 times respectively, compared to the rotating smooth duct flow. The presence of ribs on both trailing

and leading walls decelerates the effect of Coriolis forces, and the profiles of the maximum streamwise mean velocity to average mean velocity becomes less skewed. The velocity and turbulence profile is shown in Figure 1.15. In the turn region, the Dean type vortex close to the trailing wall gets distorted by Coriolis forces. The majority of secondary flow is directed towards the leading wall due to a strong Dean type vortex on the leading wall side. Figure 1.16 shows the mean velocity vector plot around the turn for the first pass. In the second pass right after the turn, the direction of the Coriolis forces change and more flow is seen close to the leading wall (Fig. 1.17).

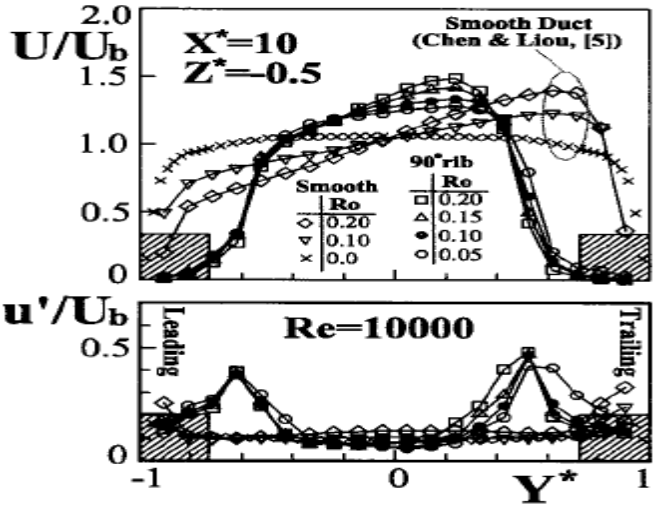

Figure 1.15: Variation of streamwise mean velocity and turbulence intensity profile with rotation number (Liou et al., 2002)

Velocity measurements were made in a longitudinal plane close to the divider wall to help understand the effect of ribs on the separation bubble. For the smooth case, the separation bubble is clearly visible. As the flow progresses further in the second pass, this bubble is absent and the main flow is skewed towards the leading wall. It seems that the introduction of the 90° ribs have eliminated the separation bubble downstream of the turn.

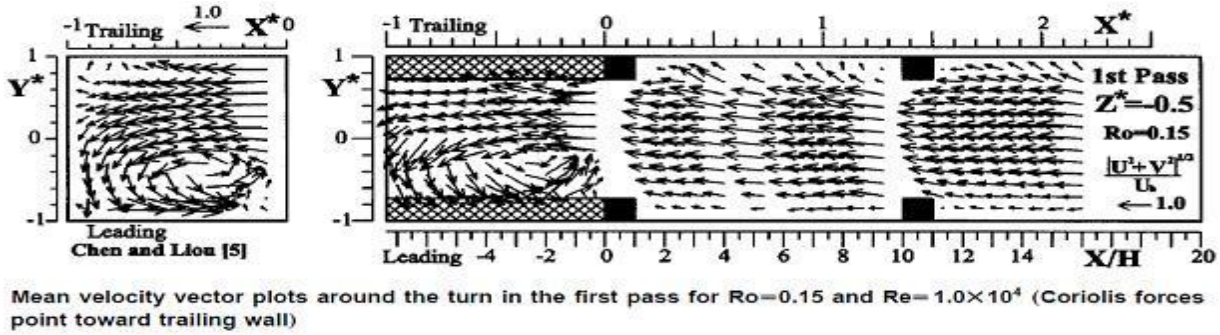

Figure 1.16: Mean velocity distribution for the 1st pass before the turn (Liou et al., 2002)

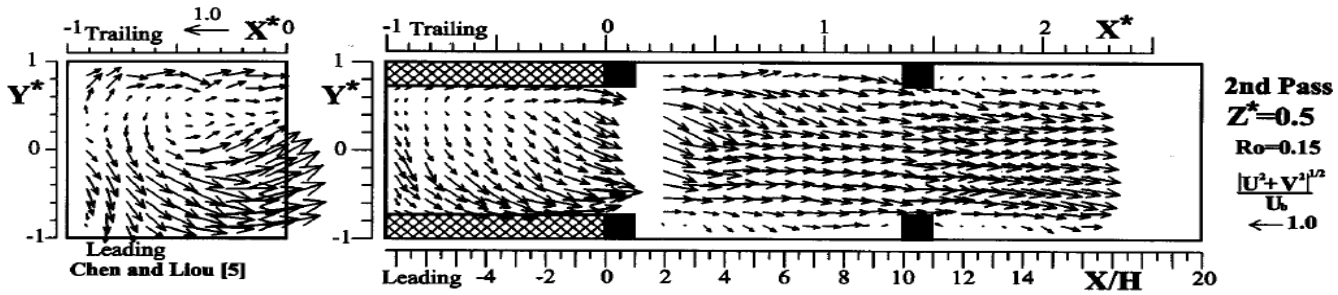

Figure 1.17: Mean velocity distribution for the 2nd pass right after the turn (Liou et al., 2002)

Liou et al. (2003) again tested a channel with 90° ribs detached from the leading and trailing walls. For the detached ribs, the magnitude of the maximum velocity and turbulence intensity is higher than the attached case (Liou et al., 2002). The flow separations downstream of the ribs are minimal. Liou and Dai (2004) tested a square channel under the same rotation conditions as Liou et al. (2001, 2002) but with 45° inline ribs. The inline ribs increase the magnitude of maximum velocity. In an angled ribbed channel secondary flow arises because of the angled ribs. Secondary flow due to Coriolis forces in the first pass try to push fluid towards the trailing wall near the center and vice versa near the outer and inner wall. The rib induced secondary flow tries to move the flow from outer to inner wall along the center plane and vice versa along the trailing and leading wall. The interaction of these two vortices cause the rib induced vortex to be more

dominant close to the leading wall and the rotation induced vortices to be more dominant close to the trailing wall. Figure 1.18 shows the secondary flow pattern for the first and second pass.

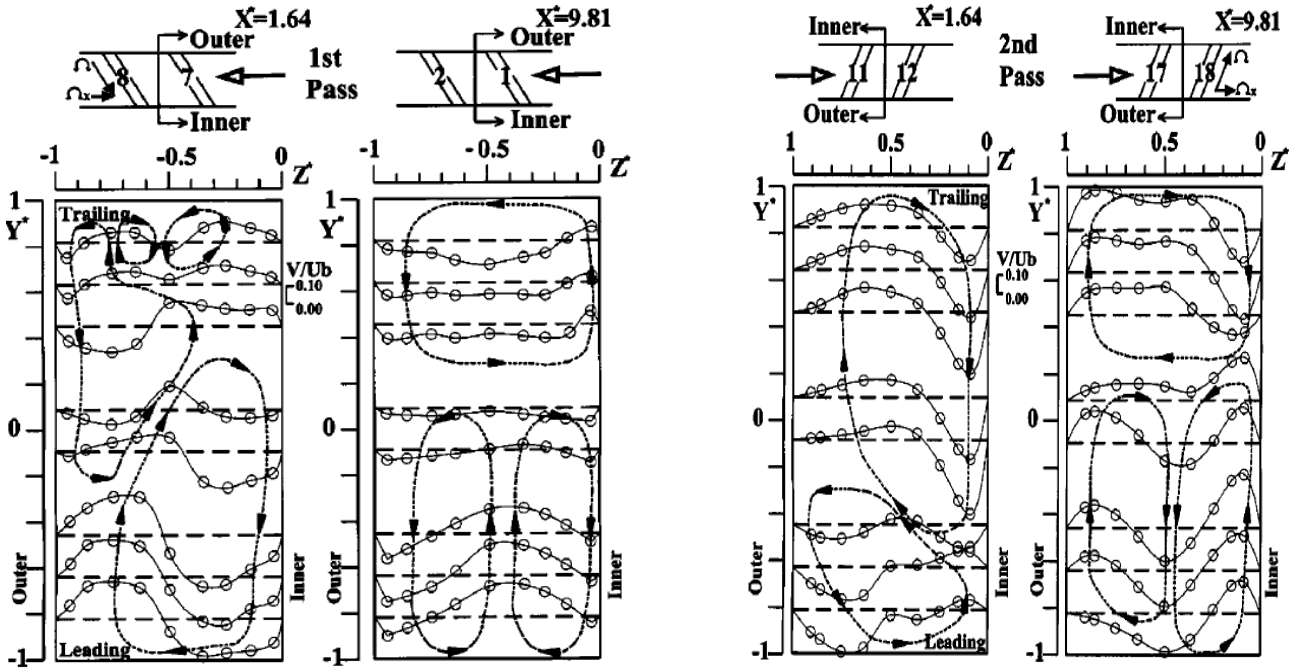

Figure 1.18: Transverse mean velocity distribution for the 1st and 2nd pass (Liou and Dai., 2004)

Iacovides (1998) performed numerical simulations for a 90° inline and a staggered ribbed channel. Al-Qahtani et al. (2002) studied a 45° ribbed channel at Re = 10000, Ro = 0.11, and DR = 0.115 for two channel orientation with respect to the rotation axis (β = 90° and 135°). The conceptual secondary flow profile by the ribs, rotation, and direction of rotation is shown in Figure 1.19. The angled ribs produce two counter rotating vortices and the rotation also produces two counter rotating vortices. For β = 90° the Coriolis force tries to push the cooler fluid from the core towards the trailing wall for the first pass and towards leading wall for the second pass.

For β = 135° the Coriolis force pushes the fluid from the inner–leading wall corner diagonally towards the center for the first pass and the opposite for the second pass.

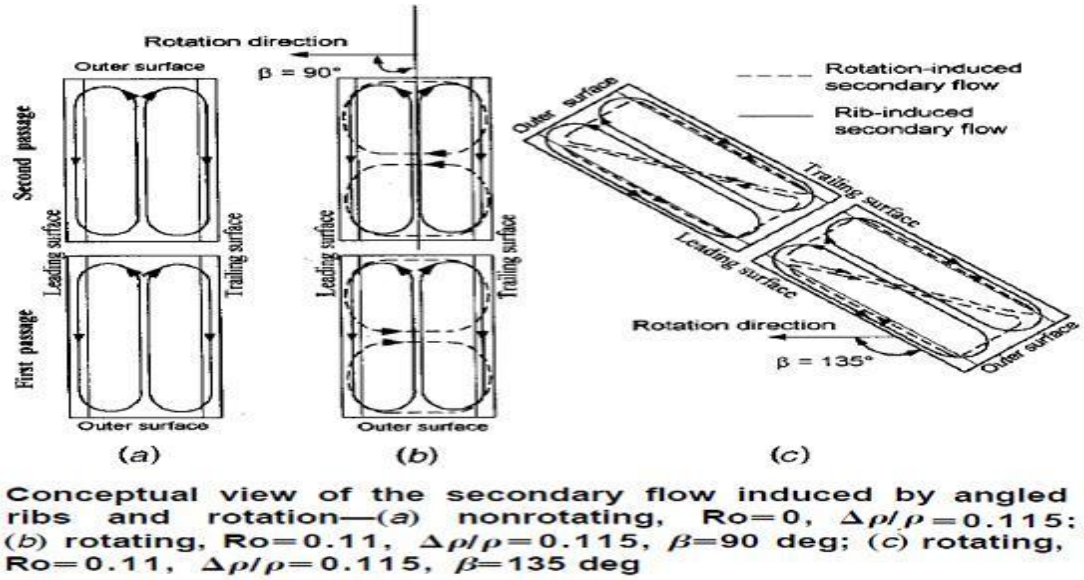

Conceptual view of the secondary flow induced by angled ribs and rotation—(*a*) nonrotating, Ro = 0, $\Delta\rho/\rho = 0.115$; (*b*) rotating, Ro = 0.11, $\Delta\rho/\rho = 0.115$, $\beta = 90$ deg; (*c*) rotating, Ro = 0.11, $\Delta\rho/\rho = 0.115$, $\beta = 135$ deg

Figure 1.19: Conceptual secondary flow pattern (Al-Qahtani et al., 2002)

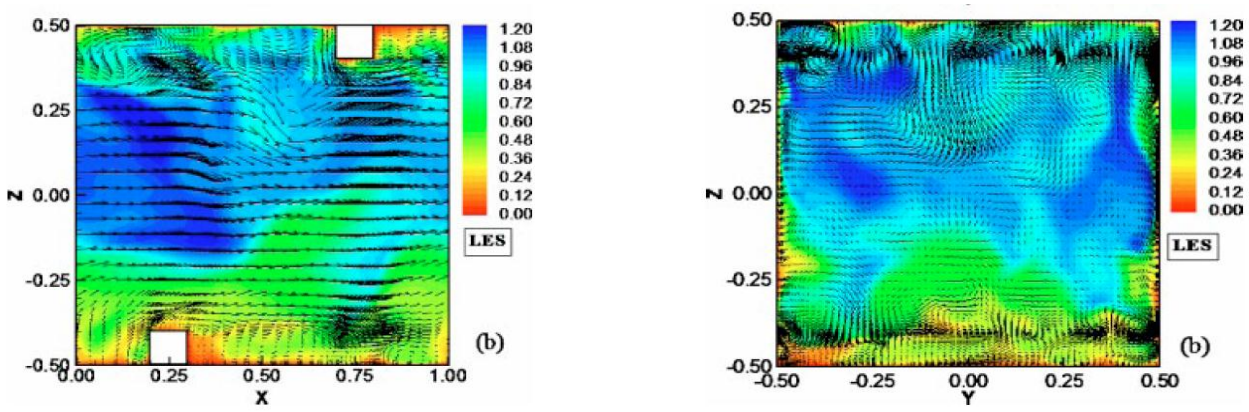

Figure 1.20: Streamwise velocity and secondary flow superimposed on temperature contour, Ro=0.12 and DR =0.13, Re=12500 (top: trailing wall; bottom: leading wall) (Saha and Acharya., 2005)

Saha and Acharya (2005) studied a transverse ribbed duct for Re = 12,500-100,000, Ro = 0-0.5, and DR = 0-0.5. Large Eddy simulation (LES) and Unsteady Reynolds Averaged Navier-Stokes

(URANS) were compared and found to give reasonable agreement with experimental heat transfer data. The instantaneous streamwise velocity and secondary velocity profiles are shown in Figure 1.20. The effects of varying Re, DR, and Ro on flow field and heat transfer are considered. The flow field does not change much with changes in Reynolds number.

1.3.2.2 Rotation effect on heat transfer: Heat transfer in a rotating channel is mainly affected by two factors: 1) Rotation number (Ro) and 2) Density ratio (DR). Rotation number signifies the strength of Coriolis force and Density ratio signifies the strength of centrifugal buoyancy force. Also, the heating condition of the wall (uniform wall temperature or uniform wall heat flux) can affect the heat transfer on the wall significantly.

1.3.2.2 a) Effect of rotation number : One of the first notable studies of heat transfer under rotation was done by Wagner et al. (1991).

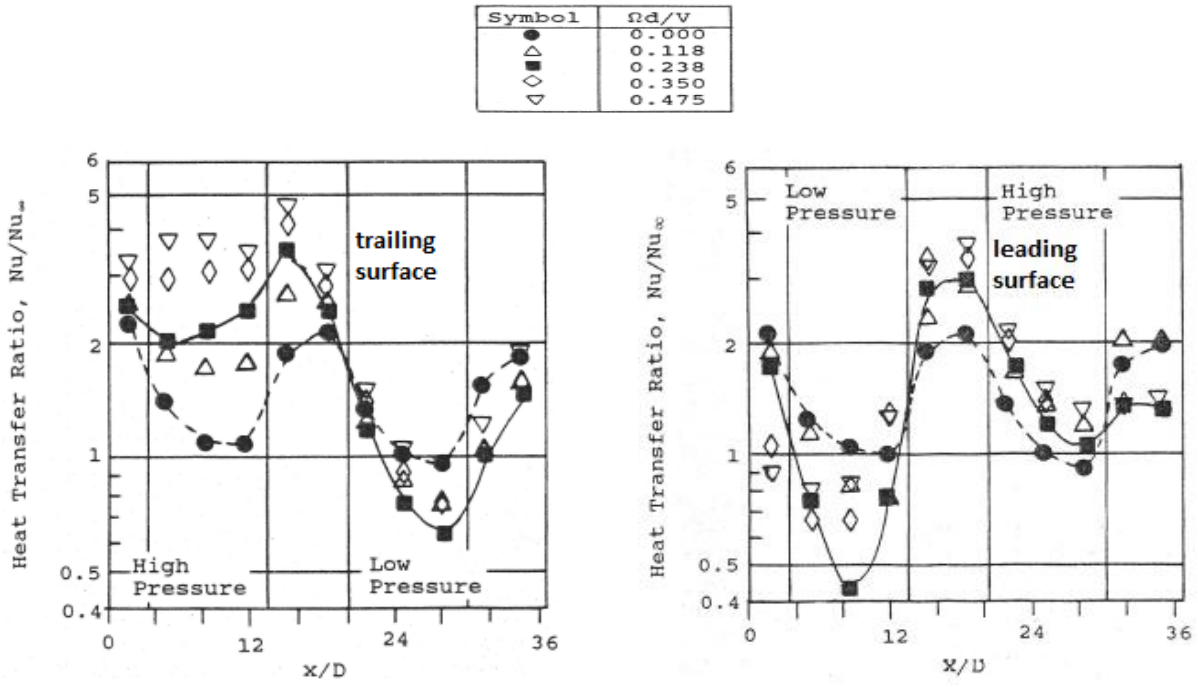

Figure 1.21: Effects of rotation number for smooth channel (Wagner et al., 1991)

They studied a four pass channel of which three were instrumented with heated copper elements and thermocouples. The test range was Re = 12,500-50,000, Ro = 0-0.48, and DR= 0.07-0.22. Figure 1.21 shows the Rotation number effect on heat transfer for the leading and trailing surface. For the highest Ro, heat transfer in the trailing surface of the 1st pass increases 3.5 times compared to the stationary value, but for the 2nd pass leading surface this increase is only about 50 percent. This difference in heat transfer for the 1st pass and 2nd pass is due to buoyancy effects.

Han and Zhang (1992a) studied three different wall heating conditions in a square, smooth two pass channel for Re = 2,500-25,000, Ro = 0-0.352. The heating conditions studied were A) Four walls at same temperature, B) Four walls at the same heat flux, and C) Leading and trailing walls hot and two sidewalls cold. They reported data only for the first pass. The leading and trailing wall data at different locations agreed well with Wagner et al. (1991) except at the entrance locations. A fully developed entrance was used by Han and Zhang (1992a) whereas a sharp 90° bend before the test section was used by Wagner et al. (1991), which probably contributed to the discrepancy in heat transfer enhancement values. It was reported that the channel-averaged Nu ratio for the trailing surface increased from 1.3 to 2.5 from the lowest to highest rotation number but the Nu ratio for leading surface reduced from 1.2 to 0.6 with increasing rotation number. Han et al. (1993) presented results for both the passes of the test section studied by Han and Zhang (1992a). It is seen that for the 2nd pass both leading wall and trailing wall Nu ratio increase with increasing rotation number except for case A (Four wall at same temperature) where the Nu ratio decreases and then increases with Ro. Mochizuki et al. (1994) studied a 3 pass channel and showed that effect of Coriolis force was present for all the 3 passes but for the 3rd pass (radially outward flow) the trailing and leading wall heat transfer values were not very far apart.

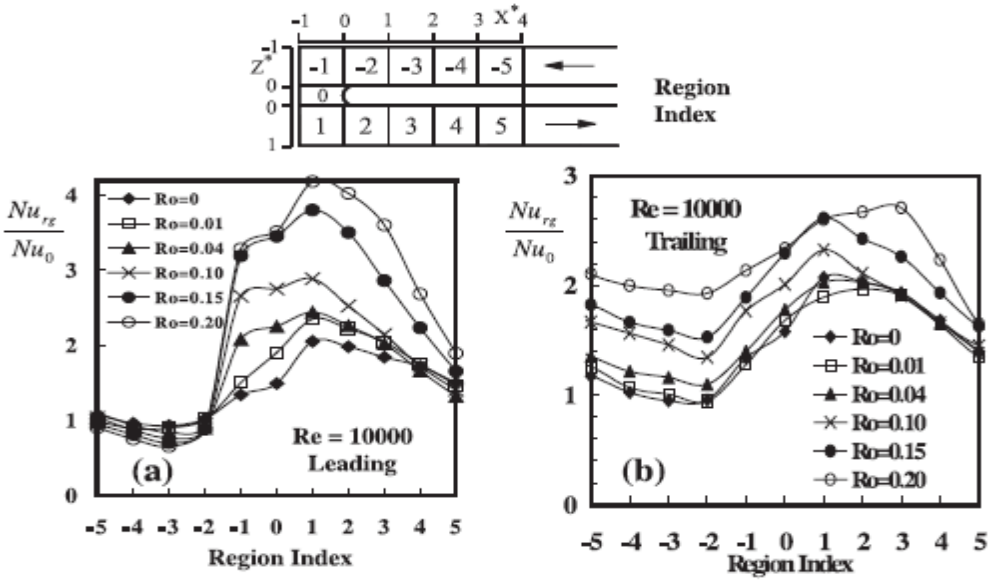

Figure 1.22: Regionally averaged Nu ratio distribution (Liou et al., 2001)

Liou et al. (2001) showed detail heat transfer data on the leading and trailing wall for Re = 10000 and Ro = 0-0.2. It can be seen from their heat transfer contour plots that as the rotation number increases, Nu ratio increases for both the leading and trailing wall in the second pass. In the first pass the leading wall Nu ratio increases and trailing wall Nu ratio decreases with increasing Ro. In the turn region the leading wall shows the highest heat transfer enhancement because the Dean type vortex gets pushed to the leading wall side in the turn region as observed in Figs. 1.16-1.17. Figure 1.22 shows the regionally averaged Nu ratio distribution. For the first pass leading wall, the Nu ratio is 5-15% lower than the stationary case but increases to 40-100% higher than the stationary case in the bend region. An interesting phenomenon is seen for the 2nd pass trailing wall which shows that for Ro <=0.1, the Nu ratio does not increase with increasing Ro. But above Ro = 0.1 Nu ratio increases with increasing Ro. So a critical range of Ro is defined ($0.10<Ro\leq0.15$) for which the effect of rotation is not present for the 2nd pass trailing wall. Zhou et al. (2007) studied a 4:1 AR channel for high range of Re and Ro (Re = 10000-150000 and Ro

= 0-0.6). Figure 1.23 shows the Rotation effect for the 4:1 AR channel. For a 4:1 AR channel Nu ratio is found to increase with rotation for both leading and trailing wall in the first pass. In contrast to a square channel a higher AR channel contains a multicellular secondary flow pattern which results in the leading side of the 1st pass also affected by the secondary flow. They also concluded that on the destabilized surfaces (trailing surface for the 1st pass and leading surface for the 2nd pass) Nu ratio increased up to a certain value of Ro and then reduced or flattened with Ro.

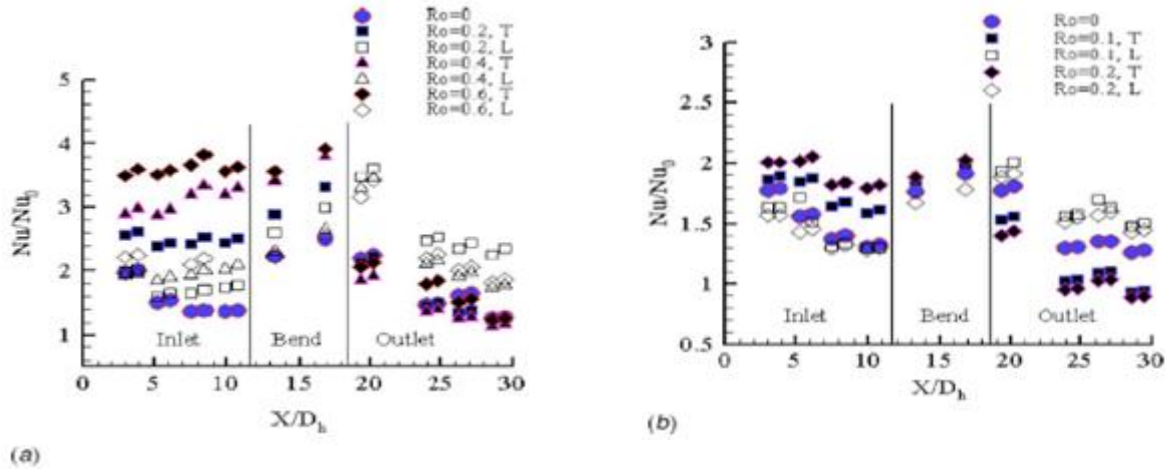

Figure 1.23: Rotational effect for DR = 0.1, a) Re = 10000 and b) Re = 40000 (Zhou et al., 2007)

Chen et al. (1999) showed detailed Nusselt number distribution for a U bend 2 pass channel. It is seen that for the leading surface of the 1st pass Nu ratio reaches a minimum value in the middle of the flow path and for the trailing surface of the 1st pass Nu ratio goes on increasing as the flow progresses towards the bend. The Nu ratio for the trailing surface is maximum at the inner bend but the leading surface shows the highest Nu ratio at the outer end of the 180° turn. The 2nd pass leading wall shows higher Nu ratio compared to trailing wall due to Coriolis force. This trend is consistent with the results of Liou et al. (2001). Taslim et al. (1991) studied a single pass square

cross section channel with 90° ribs in staggered arrangement with rotation. They found that the heat transfer coefficient under rotation on the trailing wall increases up to 45% compared to the stationary case and heat transfer coefficient on the leading wall decreases up to 6% compared to the stationary case. Wagner et al. (1992) and Johnson et al. (1994) studied the same four pass serpentine, square cross section channel used by Wagner et al. (1991) with 90° and 45° ribs on the leading and trailing wall. Figure 1.24 shows the effect of Ro on heat transfer of the 90° ribbed channels.

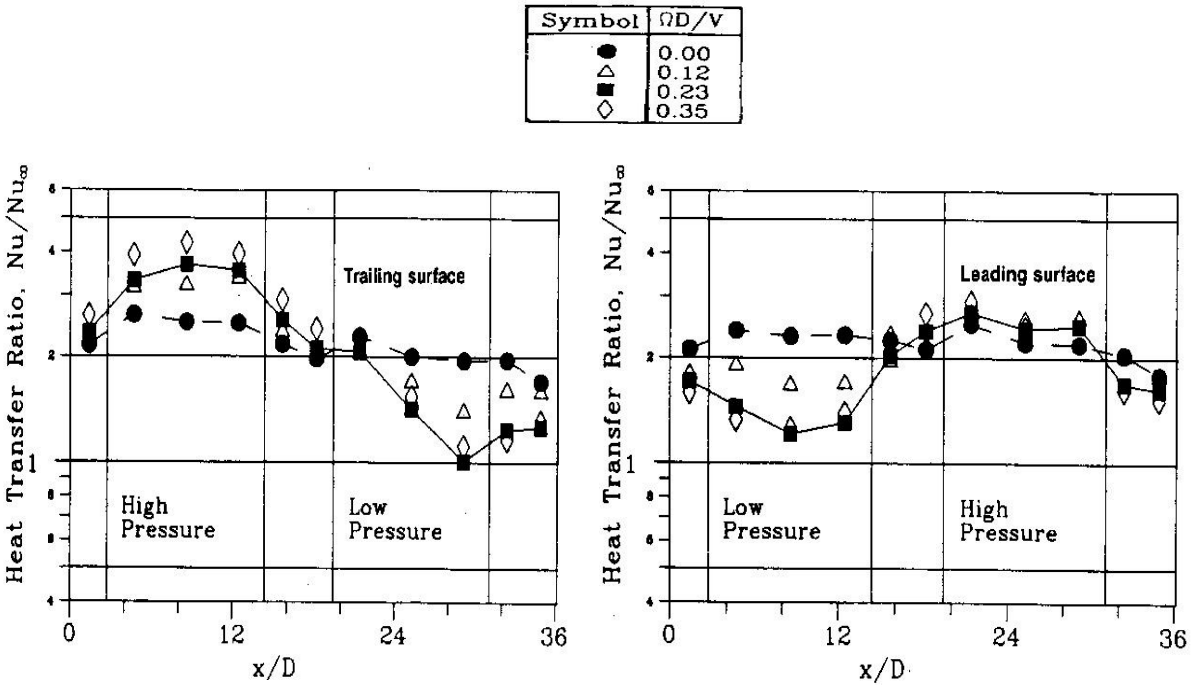

Figure 1.24: Effect of rotation number for a 90° ribbed channel (Wagner et al., 1992)

It is seen that the ribbed channels produces higher heat transfer enhancement for both leading and trailing wall of the two passes except at the turn region where the smooth case shows higher heat transfer enhancement. Both rib configurations show similar trends of heat transfer enhancement with the 45° skewed ribs showing higher values. For the 90° ribs, the heat transfer

enhancement on the trailing wall of the 1st pass increased by about 60% compared to the stationary case and for the 2nd pass leading wall it increased to about 10% compared to the stationary case. It can be said that the presence of ribs reduces the effects of rotation on both the walls and for the same set of Ro, the increase in Nu ratio was about 2.5 times for the smooth case with its corresponding stationary data. Parsons et al. (1994) and Zhang et al. (1995) studied a 90° ribbed channel and a 60° ribbed channel with the same heating conditions as Han and Zhang (1992a). For both the cases they concluded that rotating ribbed wall heat transfer enhancement values are 2-3 times higher than the rotating smooth wall heat transfer enhancement values for the same heating condition.

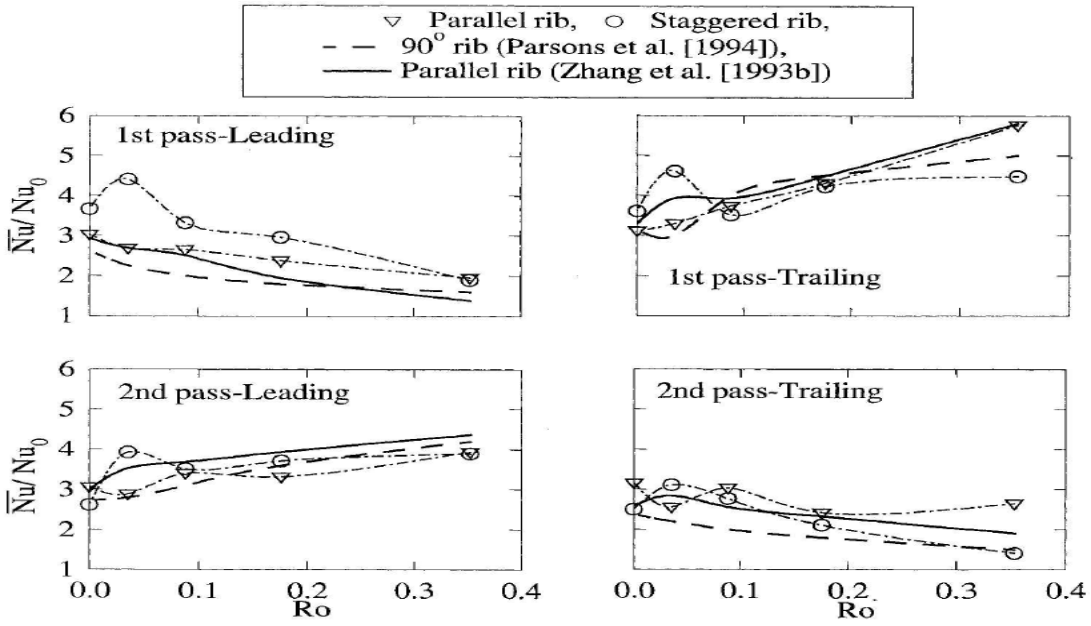

Figure 1.25: Comparison between different rib configurations under rotation (Dutta et al., 1995)

Dutta et al. (1995) studied a 60° parallel ribbed wall arranged in a different manner than Zhang et al. (1995) and a 60° staggered rib configuration and compared with the ribbed wall data from Parsons et al. (1994) and Zhang et al. (1995). Figure 1.25 shows the comparison between

different rib configurations. It is seen that the staggered ribs perform better for the low Ro for all the walls but as the Ro increases, the parallel ribs perform better than the staggered ribs for all the walls except the 1st pass leading wall. For the highest rotation number, the staggered ribs perform even worse than the 90° ribs. Therefore, parallel rib configuration is recommended compared to a staggered configuration in rotation.

Hsieh and Liu (1996) and Hsieh et al. (1997) examined a two pass square channel for uneven wall heat flux and uneven wall temperature respectively for Re = 5000-25000 and Ro =0-0.6152. In their data, the rotation axis was parallel to the curvature axis of the bend. Hsieh and Liu (1996) compared two different AR (AR = 1, 1.5) and two different heat flux ratio for two different Re. They suggested that heat transfer enhancement reduced when reducing Re for a fixed wall heat flux ratio and for all the Rotation numbers studied. It is also seen that the heat transfer enhancement reduced with increasing ratio of leading wall to trailing wall heat flux and for all the rotation numbers studied. It was found that lower AR increased heat transfer enhancement for all the rotation numbers studied. Liou et al. (2002) studied 90° ribs for the same flow and rotation condition as Liou et al. (2001). The wall average Nu ratio for the reported set of Ro was found to be in reasonable agreement with Parsons et al. (1994). Hwang et al. (2001) experimented a 4 pass serpentine passage with staggered half-V ribs for Re = 20000-40000 and Ro =0-0.21. Azad et al. (2002) studied a 2:1 AR channel with 45° parallel and 45° crossed ribbed configuration for Re = 5000-25000, Ro = 0-0.21, and DR=0.115. Figure 1.26 shows the effect of rotation number on the studied rib configurations. For both the rib configurations, the 1st pass trailing wall Nu ratio increases with increasing Ro. The 1st pass leading wall Nu ratio reduces with Ro and then reaches an asymptotic value. The same is seen for the 2nd pass trailing wall but the 2nd pass leading wall shows irregular dependence on Ro. It can be clearly concluded that the

parallel rib configuration produces higher heat transfer enhancement than the crossed rib configuration for all Ro. Griffith et al. (2002) studied a 4:1 AR channel with 45° ribs for Re=5000-40000, Ro = 0-0.3. It is seen from their results that both the trailing wall Nu ratio increases with increasing rotation. The leading wall shows an increase with Ro and then reaches an asymptotic value.

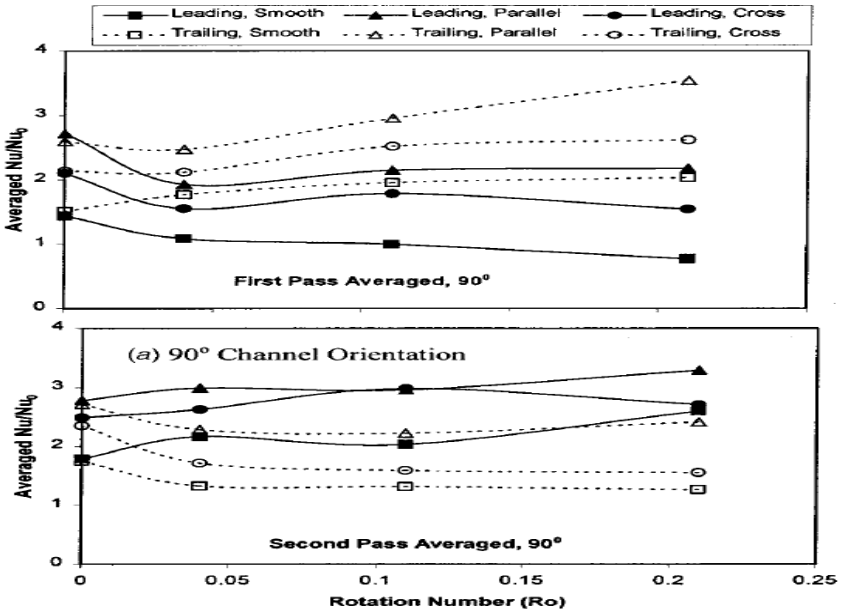

Figure 1.26: Effect of rotation number on different rib configuration (Azad et al., 2002)

Zhou and Acharya (2008) studied a 4:1 AR channel with 45° ribs for high rotation number range (Ro = 0-0.6). Figure 1.27 shows the effect of Ro for different Re. It is seen that rotation enhances Nu ratio on the 1st pass trailing wall significantly for all the Reynolds numbers studied but the 2nd pass leading wall does not show that much enhancement. Both the stabilized surfaces (1st pass leading and 2nd pass trailing) show reduction in Nu ratio with increasing Ro.

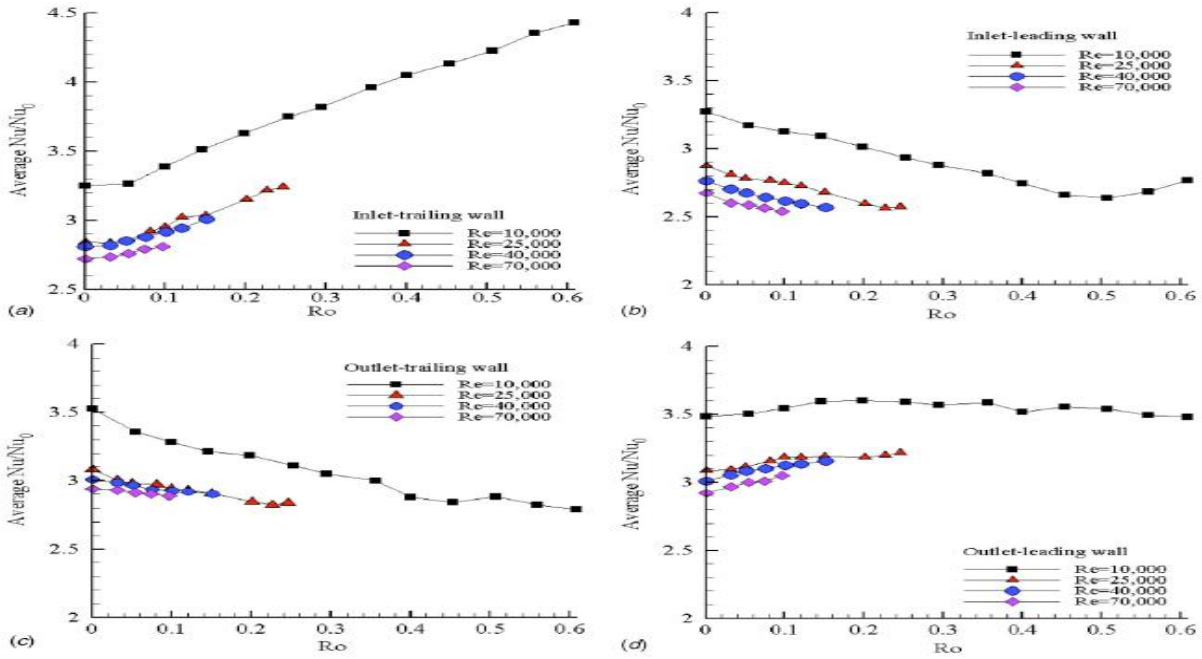

Figure 1.27: Effect of rotation number for a 4:1 AR channel (Zhou and Acharya., 2008)

Liou et al. (2007) studied a radially outward flow channel with Ro reaching values up to 2. The density ratio range was 0.07-0.28. They developed Nu correlations with Nu as a function of Re, Ro and Buoyancy number. Prakash and Zerkle (1995) examined the effect of rotation number for Ro = 0.06 and 0.12 computationally for a radially outward channel. Rotation increased Nu ratio for the trailing wall and reduced Nu ratio for the leading wall. Saha and Acharya (2007) did parametric studies for 3 Aspect ratios (AR = 1:1, 1:4 and 4:1) at Re = 25000-150000, Ro = 0-0.5, and DR = 0-0.5 for a radially outwards flow channel with transverse ribs. Figure 1.28 shows the effect of rotation number for different AR. It is clear that for all the AR studied, the leading wall heat transfer coefficient reduces with Ro, reaches a critical value of Ro and then Nu ratio remains constant. For the 4:1 AR channel the Nu ratio actually increases after the critical value of Ro. For the trailing wall, the Nu ratio goes on increasing with increasing Ro except for the 4:1

channel which shows a reduction in Nu ratio after Ro = 0.15. So a critical value of Ro exists at Ro =0.15.

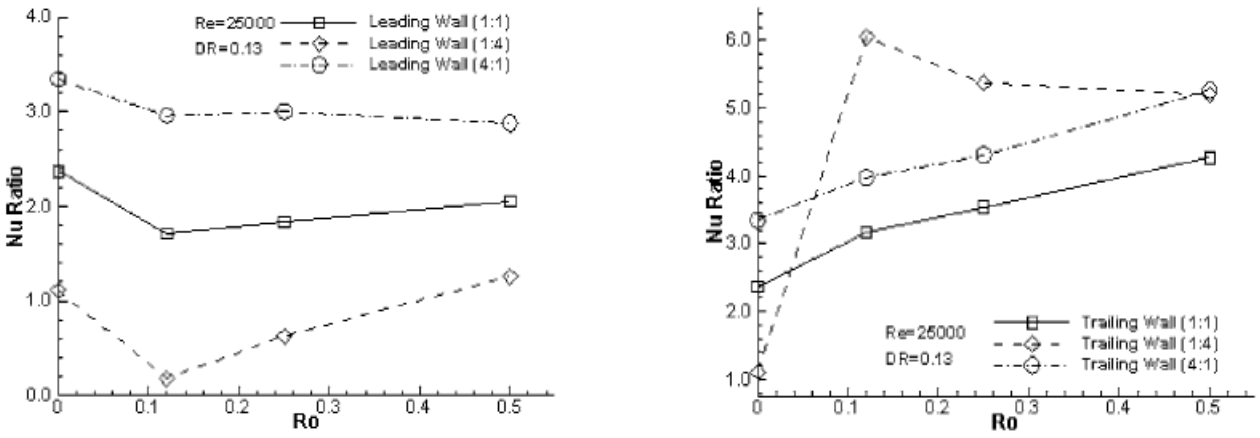

Figure 1.28: Rotation number effect for different AR (Saha and Acharya., 2005)

1.3.2.2 b) Effect of density ratio : Density ratio is another important parameter which signifies the strength of the rotational buoyancy force. For the 1st pass, the buoyancy force is in opposite direction to that of the inertia force of the fluid and in the 2nd pass it aids the inertia force of the fluid. Wagner et al. (1991) showed the effects of change in density ratio on leading and trailing wall heat transfer by varying the inlet density ratio from 0.07-0.22 in a square channel. Increasing the density ratio from maximum to minimum increased the 1st pass trailing surface heat transfer by 50% and the leading surface heat transfer by 100%. The 2nd pass heat transfer for both the leading and trailing surface increased by about 10-50 % for the range of density ratio considered. The high increase in heat transfer in the 1st pass leading wall can be attributed to the reverse velocity due to the centrifugal buoyancy force in the leading wall as explained by Prakash and Zerkle (1992). Zhou et al. (2007) studied the effect of DR by varying it from 0.1-0.2 in a 4:1 AR channel. Their heat transfer data shows similar trends as Wagner et al. (1991) as DR

is increased. Heat transfer increased for both leading and trailing wall for the 1st pass and 2nd pass. For the 2nd pass, a critical Ro is observed close to Ro = 0.1, after which the increase in Nu ratio for the leading wall and decrease in Nu ratio for the trailing wall is stopped (leading wall) or reversed (trailing wall).

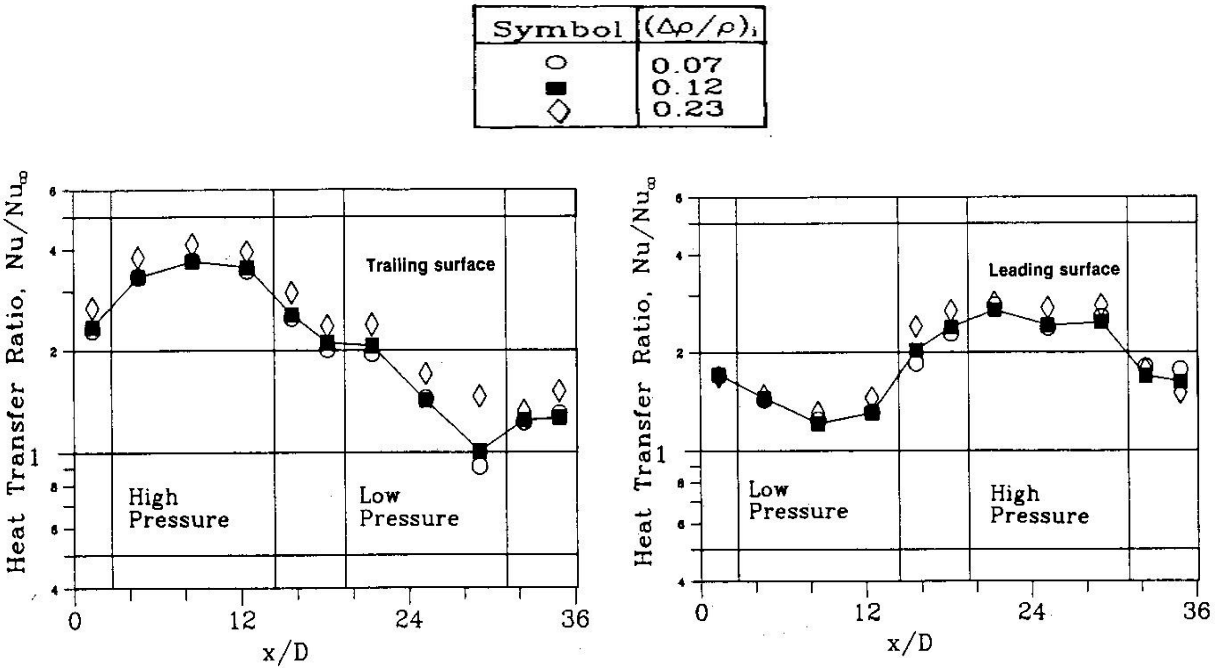

Figure 1.29: Density ratio effect for a transverse ribbed channel (Wagner et al., 1992)

Wagner et al. (1992) showed the effect of DR on heat transfer by varying the DR from 0.07-0.22. Their results are shown in Figure 1.29. Comparing with smooth channel case found in Wagner et al. (1991), it can be seen that the Nu ratio is higher for all the density ratios at a particular location due to the addition of the ribs. The Nu ratio still increases with DR for all the 1st and 2nd pass leading and trailing walls but the amount of enhancement with increased DR is reduced significantly. For the ribbed channel, the 1st pass trailing wall Nu ratio increases by only 25% (compared to 50% for the smooth case) and the leading wall Nu ratio increases by only about 20% (compared to about 100% for the smooth case) for the range of DR considered. So the

density ratio effect is more prominent in a smooth channel than in a ribbed channel. Johnson et al. (1994) performed tests with a 45° ribbed channel with the same set of flow and rotation conditions as Wagner et al. (1992). Their results show that the 45° ribs produce the highest heat transfer enhancement for all of the DRs studied. Heat transfer enhancement increases with DR like the smooth or transverse rib case but the effect of DR is diminished just like the transverse rib case. Zhou and Acharya (2008) used 45° ribs on the test section used by Zhou et al. (2007) and showed the effects of DR (Fig. 1.30).

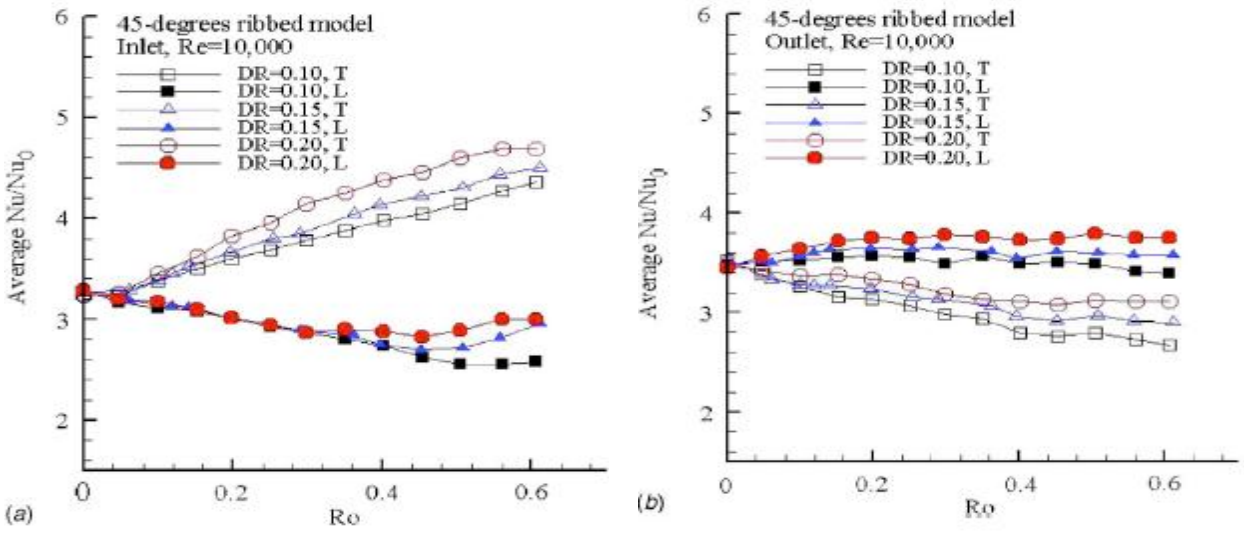

Figure 1.30: Density ratio effect for a 45° ribbed channel a) First pass and b) Second pass (Zhou et al. 2008)

It can be seen from the results that the 1st pass leading wall heat transfer is insensitive to DR up to a certain critical Ro and increasing Ro after this critical value shows an increase in Nu ratio for increasing DR. The 2nd pass trailing wall Nu ratio reduces with increasing Ro, reaches a critical Ro and then remains almost constant afterwards. Results from Saha and Acharya (2007) showed the effect of DR for different AR studied. It is seen that the heat transfer is almost insensitive to DR for 1:1 and 4:1 AR channels. It is seen from their results that for the 1:4 AR

channel, the leading wall Nu ratio reduces and trailing wall Nu ratio increases up to a critical value of DR (about 0.13) and then remains almost constant.

1.3.2.2 c) Effect of thermal boundary condition: Han et al. (1993) studied a two pass square smooth channel for three thermal boundary conditions: A) Four walls at the same temperature, B) Four walls at the same heat flux, and C) Trailing wall hotter than leading wall with side walls unheated. The case A is the most simplest one where the 1st pass trailing wall heat transfer increases with increase in rotation due to increase in both Coriolis and centrifugal buoyancy force. The leading wall side shows a decrease in Nu ratio up to a critical value of Ro after which the streamwise flow at the leading wall gets reversed and increases turbulence resulting in higher heat transfer. For both the asymmetrical temperature profile cases (case B and C), the secondary flow generated due to the uneven wall temperature interacts with the secondary flow generated due to Coriolis and centrifugal buoyancy force and increases the heat transfer on both the leading and trailing wall. The case B and C shows much higher level of heat transfer enhancement compared to case A. The difference becomes more prominent for the 1st pass leading wall and 2nd pass leading and trailing wall. Han et al. (1994) studied 4 different wall heating conditions for a smooth wall in a radially outward flow channel. The heating conditions were: 1) Four walls at uniform temperature, 2) Trailing wall at higher temperature than leading wall and the sidewalls at same temperature, 3) Trailing wall hot and the remaining 3 walls cold, and 4) Leading wall hot and the remaining 3 walls cold. It can be seen that when the trailing wall is hotter than the leading wall (case 2 & 3), the heat transfer on the trailing wall is lower compared to case 1. For this case, the cooler fluid stays close to the leading wall resulting in higher buoyancy force close to the leading wall and reduction in buoyancy force close to the trailing wall. This result in higher values of Nu ratio for the leading wall compared to case 1 and lower values of Nu ratio

for the trailing wall compared to case 1. So the local buoyancy condition due to uneven thermal boundary condition degrades the effect of centrifugal buoyancy.

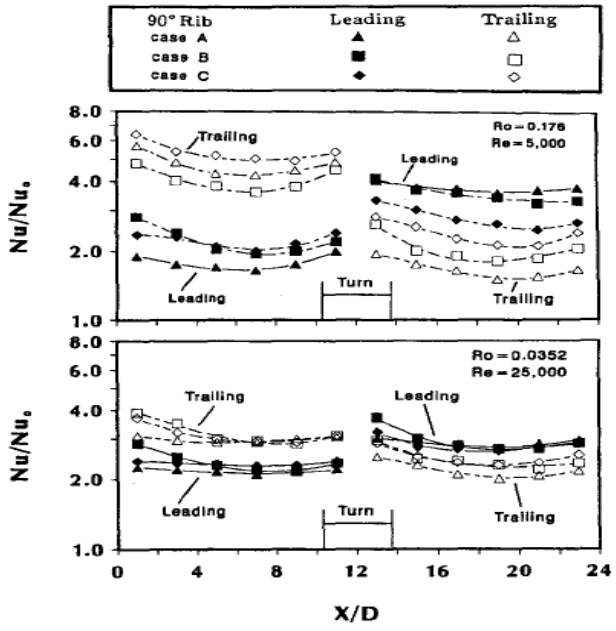

Figure 1.31 : Effect of wall heating on a 90° ribbed channel (Parsons et al., 1994)

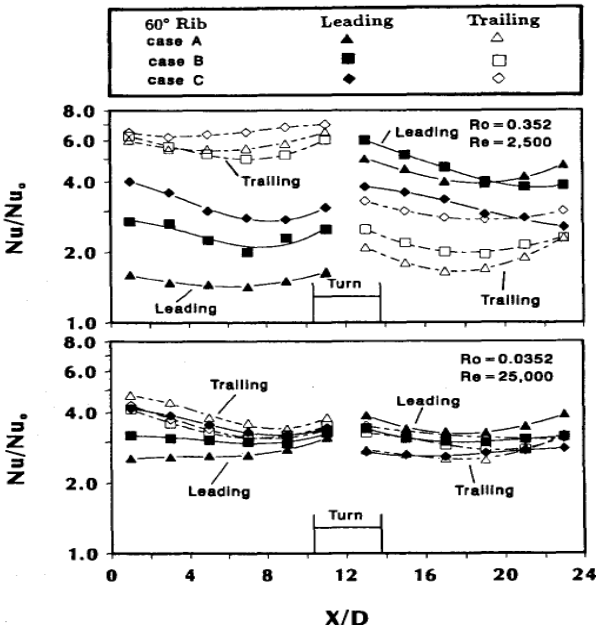

Figure 1.32 : Effect of wall heating on a 60° ribbed channel (Zhang et al., 1995)

Parsons et al. (1994) and Zhang et al. (1995) studied the same heating condition used by Han et al. (1993) with 90° and 60° ribbed channel respectively. The effects of heating condition for their geometries are shown in Figure 1.31-1.32. For the first pass leading wall, cases B and C show significant heat transfer enhancement than case A. The same is true for the 2nd pass trailing wall.

1.3.2.2 d) Effect of channel orientation with the rotation axis : Johnson et al. (1994) compared a square multipass serpentine channel with the channel oriented to 0° (the curvature axis perpendicular to the rotation axis) and 45° to the rotation axis. The first case is the most reported in open literature. In a real gas turbine cooling blade, the coolant can flow from the leading to trailing edge or from trailing to leading edge. The model was rotated in two directions to

simulate these two conditions. The Reynolds number, Rotation number, and Density ratio was fixed at Re = 25000, Ro = 0.24, and DR = 0.13. The effect of model orientation is shown in Figure 1.33.

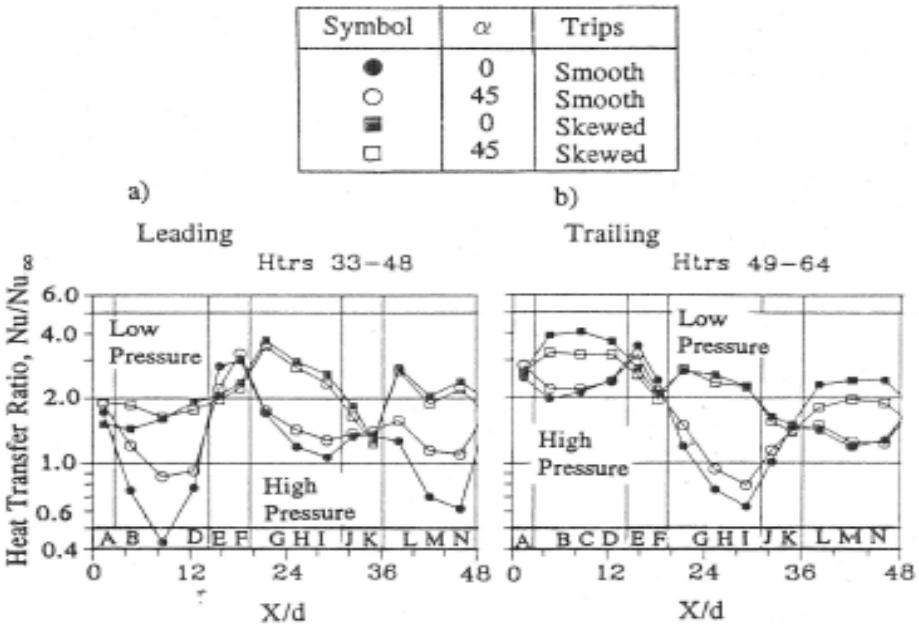

Figure 1.33: Effect of model orientation (Johnson et al., 1994)

It is seen that for the smooth channel, the 45° orientation shows higher heat transfer enhancement for both leading and trailing wall in all the passes. The difference is more for the leading wall than the trailing wall. The difference in heat transfer due to orientation is more prominent for the outward flow leading wall and inward flow trailing wall. But for the channel with 45° skewed ribs, the 0° orientation shows higher heat transfer enhancement. The difference is more prominent for outward flow trailing walls. They also studied the effect of direction of rotation on a smooth channel with two model orientations. It is seen from Figure 1.34 that for a same model orientation, rotation direction does not have much effect on the first pass heat transfer but the rotation direction effect is increasingly prominent for the 2nd and 3rd pass. Dutta and Han (1996)

studied a square channel with half V ribs with three channel orientations. The channel orientations were: A) Model in 0° with direction of rotation, B) Model in 90° with direction of rotation, and C) Model in 45° with direction of rotation. Figure 1.35 shows the comparison between the three model orientations with Ro.

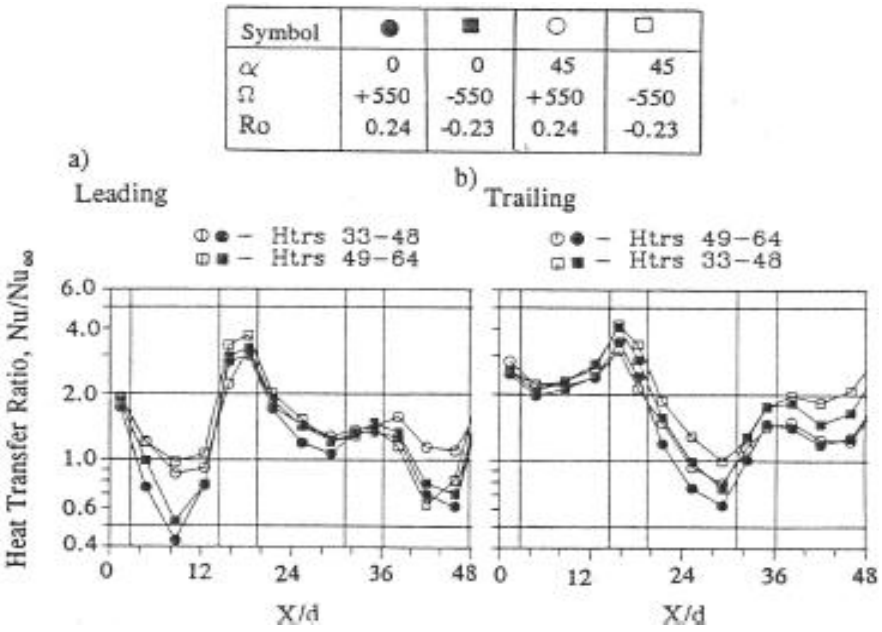

Figure 1.34: Effect of model orientation and rotation direction (Johnson et al., 1994)

Model A is the most common orientation reported in literature. For the 1st pass smooth case, Model A shows higher heat transfer enhancement than Model B for both leading and trailing wall. For the 2nd pass smooth case, Model A shows higher heat transfer enhancement for trailing wall but Model B performs better for leading wall. As expected the ribbed duct performs better than the smooth duct. For the ribbed case Model B performs better than Model A for both the passes and walls. For the leading wall in 1st pass and trailing wall in 2nd pass (destabilized surface) there exists a critical Ro up to which Nu ratio increases and then decreases. For the 2nd pass leading wall, the Model B performs better with increasing Re with values more than 50%

higher than Model A. Comparing between Model C and A, it is seen that for the 1st pass trailing wall, Model A performs better than Model C for both the smooth and ribbed case but for the leading wall Model C performs better. For the 2nd pass it seems that all the walls show higher Nu ratio for both smooth and ribbed case for Model C than Model A. Since the model C is a tilted orientation it shows less effects of rotation on Nu ratio.

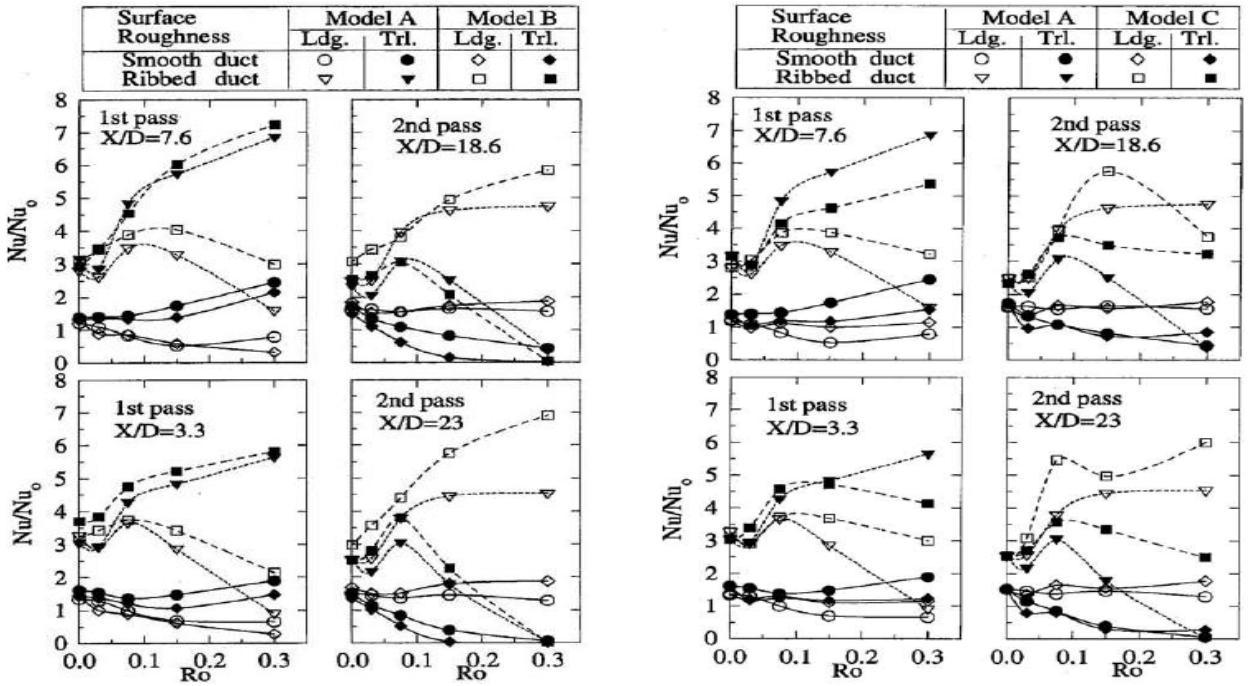

Figure 1.35: Comparison between three model orientations (Dutta and Han., 1996)

Park and Lau (1998) also did Naphthalene sublimation experiments for two channel orientations (0° and 45°) under Re =5500 and Ro =0.24 for a smooth channel. They also showed that for the 1st pass the effect of rotation is less for the diagonally oriented channel. The leading wall heat transfer for the 1st pass is almost the same as the stationary case. For the trailing wall, normally oriented channel shows higher Nu ratio than diagonally oriented channel. Azad et al. (2002) also did their tests for 0° and 45° model orientation and concluded that for the smooth channel, the

difference between the trailing and leading wall heat transfer is less for the 45° orientation case due to lesser effects of rotation.

1.3.2.2 e) Effect of channel aspect ratio : Dutta et al. (1996) studied 5 different AR (AR = 4:1, 2:1, 1:1, 1:2, and 1:4) for a radially outward channel numerically. The Coriolis force is less pronounced for the higher AR cases because the height H is small, but the centrifugal buoyancy effect is stronger for the higher AR cases. The effect of AR on Nu ratio for a fixed Re and Ro is shown in Figure 1.36.

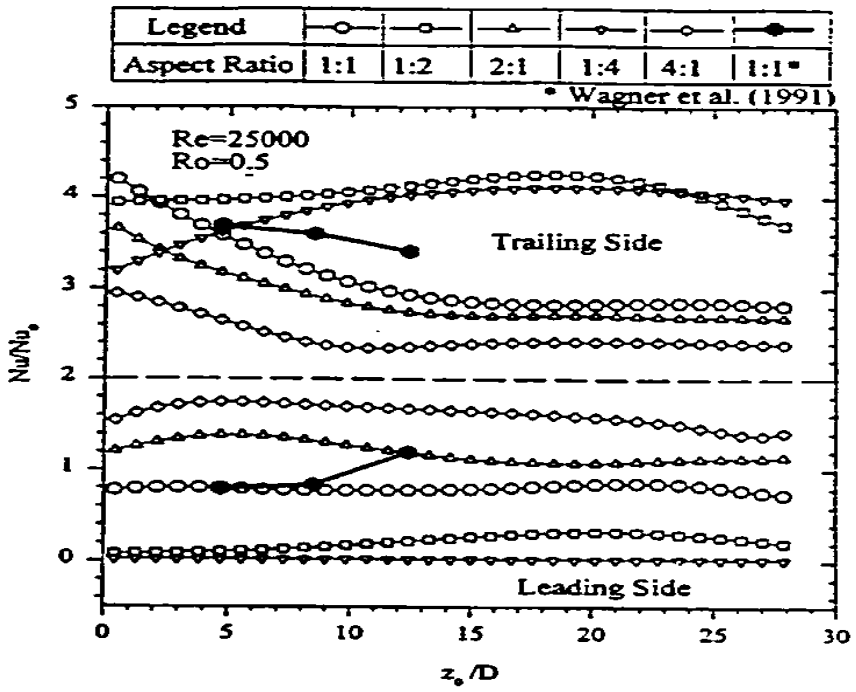

Figure 1.36: Effect of different AR under rotation (Dutta et al., 1996)

The lower AR channels show a wider difference of Nu ratio between trailing and leading wall. Saha and Acharya (2005, 2007) studied 3 aspect ratios (AR = 4:1, 1:1 and 1:4) for a radially outward channel. The Nu ratio and friction factor ratio for all the Re and Ro is tabulated in Table 1.1. It is seen that the 1:4 AR channel shows significantly low values of heat transfer in the

leading wall. This is probably due to a formation of a stagnation zone close to the leading wall. As Ro is increased, back flow starts which again increases Nu ratio. The backflow effect due to centrifugal buoyancy and corresponding increase in Nu ratio is seen for all the aspect ratios around Ro = 0.12. For the trailing wall, Nu ratio starts to decrease after Ro = 0.12. The 1:4 AR channel case shows the highest difference in trailing and leading wall heat transfer. This case also shows the highest pressure drop with pressure drop increasing with Ro. For the 4:1 AR channel, the trailing wall heat transfer goes on increasing with increasing Ro. The difference between trailing wall and leading wall heat transfer is the least for this case. The pressure drop for this case lies in between the other two channels.

Table 1.1: Nu and f ratio for different AR (Saha and Acharya., 2005)

Nusselt number and friction factor for the various cases

Aspect ratio	Rotation number	Nusselt number, *Nu*			Friction factor, *f* (per unit length)
		Side wall	Leading wall	Trailing wall	
1:1	0.00	1.14	2.37	2.37	0.1484
	0.12	1.46	1.71	3.16	0.1949
	0.25	1.54	1.84	3.54	0.3528
	0.50	1.63	2.05	4.27	1.128
1:4	0.00	1.88	1.11	1.11	0.0521
	0.12	2.68	0.18	6.05	0.1459
	0.25	2.46	0.63	5.37	0.4983
	0.50	2.66	1.26	5.20	1.7843
4:1	0.00	2.03	3.34	3.33	0.4786
	0.12	3.30	2.96	3.98	0.5576
	0.25	3.24	2.98	4.03	0.7503
	0.50	3.19	3.01	4.12	1.5300

1.4 Trailing edge cooling

Pin-fins are the most common cooling scheme used in the trailing region of the blade. Different configurations and shapes of pin-fins were tested over the years. A typical pin-fin configuration is shown in Figure 1.37.

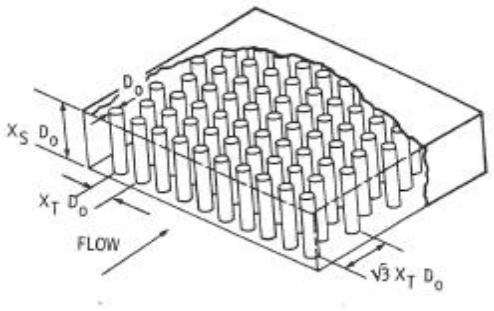

Figure 1.37: A typical Pin-fin configuration used by Brigham and Van Fossen (1984)

Metzger et al. (1982), Van Fossen (1982) studied staggered arrays of circular cross section pin-fins with different spacing between the arrays. Metzger et al. (1984) compared the heat transfer and pressure drop for different pin shape and orientation and found that oblong cross section of pin-fin enhanced heat transfer coefficient more compared to the circular cross section. The gain was offset, however, by a large increase in pressure drop for an oblong cross section. Chyu et al. (2007) compared different inclination angles of the pin-fins. They showed that increase in inclination angle reduced both the heat transfer and pressure loss and maximum thermal performance factor was obtained for the perpendicular fins. Chyu et al. (1999), Hwang et al. (1999) compared staggered and inline arrays of pin-fins and concluded that the staggered arrays of pin fins enhanced heat transfer more than the inline arrays. Chyu et al. (1998) compared different cross sections of pin-fins and concluded that the cubic shape pin-fins, perpendicular to the flow direction produced the maximum enhancement of heat transfer. Hwang and Lu (2000), Lau et al. (1989) measured heat transfer coefficient and pressure drop both for with and without lateral flow ejection and concluded that the overall heat transfer for a pin-fin channel with lateral flow ejection was less than that for a channel without lateral flow ejection. Hwang et al. (1999) and Hwang and Lu (2000) did tests in a trapezoidal duct simulating the actual shape of trailing edge channel more accurately. Uzol and Camci (2001) compared circular cross section pin-fins

with two different elliptical cross section pin-fins. They concluded that the circular pin-fins produced higher values of heat transfer enhancement compared to the elliptical pin-fins but the gain was offset by a huge pressure drop for the circular pin-fins compared to the elliptical ones. Overall, elliptical pin-fins give higher thermal performance than the circular pin-fins. In a typical gas turbine blade, the internal coolant flow comes from the hub of the blade. Some of the flow goes straight and exits through the holes in the tip of the blade and the rest of the flow exits through the trailing edge, where the exit flow is perpendicular to the main flow. Lau et al. (1989) studied the effects of different straight exit and lateral exit geometries in a rectangular channel. They showed that overall heat transfer coefficient values reduced by as much as 25 percent when the exit configuration was changed to no lateral ejection to full lateral ejection. Kumaran et al. (1991) studied a rectangular test section with short and long ejection holes. They found that the length of the ejection holes did not significantly affect the heat transfer in the pin fin channel. The heat transfer decreases rapidly as the flow proceeds to the straight exit. McMillin and Lau (1994) did naphthalene sublimation studies and pressure drop measurements on a rectangular test section with and without lateral ejection. They showed that the local pressure decreased continuously as the flow exited towards the straight exit without lateral ejection case, but when lateral ejection was present, the local pressure reached a constant value after eight pin rows and did not decrease further. Hwang et al. (1999) studied the effect of lateral ejection in a trapezoidal cross section channel. They varied the lateral flow rate to main flow rate ratio ε and found that as ε was increased from 0 to 0.2, the overall heat transfer coefficient values decreased but as ε is increased further up, the heat transfer values started increasing. The flow went through a converging cross section and exited laterally for their case. Increase in flow velocity due to converging cross section and flow turning increased heat transfer significantly when the lateral

flow rate was increased. Lau et al. (2008) studied a trailing edge channel with two sets of blockages and shaped exit slots. The averaged value of heat transfer was lower compared to a traditional pin fin channel.

1.5 Lattice structures used in internal cooling

A lattice-matrix structure, inserted between the suction and pressure side of an internal cooling channel, also has the potential to enhance heat transfer significantly. A schematic of the lattice structure is shown in Figure 1.38.

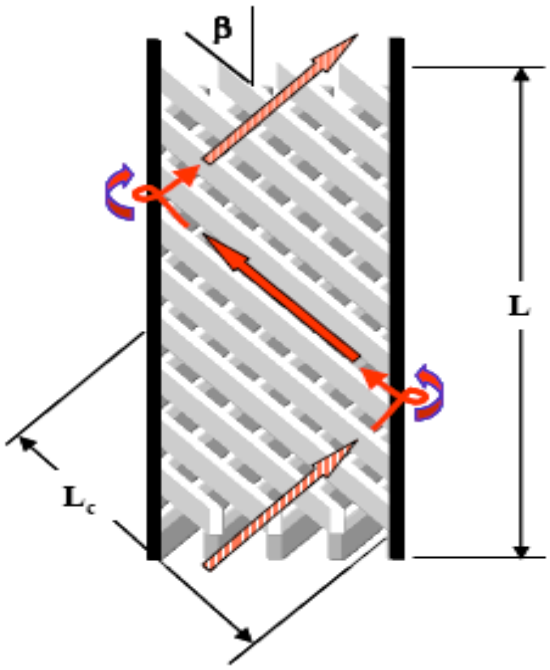

Figure 1.38: Schematic of a lattice structure (Bunker, 2004)

The serpentine flow passage increases turbulence to a high degree. In a lattice matrix structure the coolant flow continuously changes direction from one side of the blade to the other side (suction to pressure side or vice versa) while it is moving towards the exit. When the flow turns from one side of the blade to the other side, it produces impingement and as a result high heat

transfer zones. Flow turbulence is increased by interaction with the cross flow as well. The increased heat transfer area also causes an increase in a heat transfer area from the longitudinal ribs. Longitudinal ribs in lattice-matrix structures also increase the structural rigidity and therefore lattice structures are ideally suited for cooling regions where the airfoil cross sections are thin, e.g., the trailing edge of the airfoil. The lattice cooling technique has been used extensively in former Soviet Union-designed gas turbine engines. This is a relatively new concept in the West and information about this technique is limited. Goreloff et al. (1990) studied the overall cooling effectiveness of a turbine blade with leading and trailing edge lattice passages using the zinc melt technique. Bunker (2004) studied the heat transfer enhancement and pressure losses in rectangular lattice structures with orthogonal ribs. He found heat transfer enhancement to be 2.5-3. He also showed that less channel configuration produced higher values of heat transfer. Acharya et al. (2005) were the first to study a lattice structure with rotation and concluded that for low Reynolds number ($\leq$10000), rotation decreased heat transfer enhancement. For high Reynolds number ($\geq$ 20000) Reynolds number did not have much effect on heat transfer enhancement. Gillespie et al. (2000) measured the heat transfer coefficient values for flow in a trapezoidal cross section matrix structure with orthogonal ribs and flow ejection through film cooling holes on the trailing edge. Nagoga (1996) did extensive studies on different orientations of the matrix structure. He compared the lattice structures with a lattice with straight channels (i.e. parallel to the flow) rather than smooth duct and found that average heat transfer enhancement was in the range of 2-3.1 for different angles of the matrix channels. He found that channels at 45° to the flow directions enhanced the heat transfer the most. He studied the effects of different cooling methods on the blade life of the gas turbine and concluded that with the use of matrix structure, the operational blade life in high pressure turbine could

increase by 40 times, whereas the use of pin fins would increase the operational blade life only by 4 times.

1.6 Entrance geometry effect on internal cooling channel heat transfer

Most of the studies done on the internal cooling channel of the gas turbine blades consider fully developed flow at the inlet of the cooling channel. The coolant in actual gas turbine blades may be forced to flow through a complex curved channel within the hub of the blade before entering the actual blade cooling channel. Usually for actual blades, it is not possible to allow a long development length before entering the actual coolant channel and space limitation forces the coolant to flow through different entrance configurations. A typical s-shape fir-tree entrance configuration is shown in Figure 1.39.

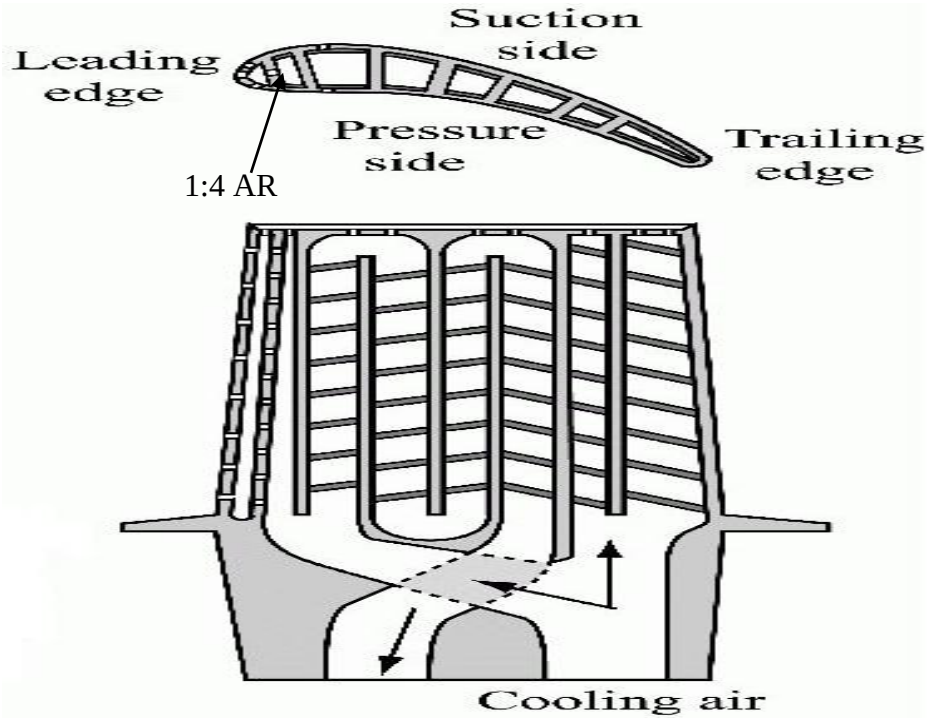

Figure 1.39: “Fir-tree” entrance configuration (Murata Lab)

A few studies have tried to investigate the effect of developing flow at the inlet of a cooling channel. Burggraf (1970) compared three different entrance geometries for a square channel with transverse ribs and without ribs in a stationary frame. His configurations were a long developing length before the test section, a plenum entrance with a short entry length, which forced a sudden contraction of the flow area and a 180° turn just before the entrance of the test section. The results showed a marked increase in heat transfer enhancement for the short entrance compared to the long entrance. The difference in heat transfer enhancement between the two channels reduces with increasing Reynolds number. Liou et al. (1992) studied an abrupt contraction entrance region before a square test section with transverse ribs in a stationary frame. They concluded that for the ribbed channel, the first 12-18% of the channel was affected by the sudden contraction. They developed a correlation for developing flow after a sudden contraction.

Wright et al. (2005) compared the effects of a sudden contraction and a partial sudden contraction in a rotating frame. The entrance configurations are shown in Figure 1.40. They studied the entrance configurations for a 4:1 AR channel with and without ribs. They showed that for the sudden contraction entrance, the values of heat transfer enhancement were higher than the fully developed entrance for the first 5 hydraulic diameters of the channel. The partial sudden contraction entrance shows higher heat transfer enhancement values compared to the fully developed entrance for the entire flow length. The entrance enhancement decreases with increasing rotation number. For the ribbed cases, the sudden contraction entrance and the partial sudden contraction entrance provide higher heat transfer enhancement than the fully developed entrance for the first 3 to 4 hydraulic diameters of the channel. The influence of the entrance geometry can be seen more for the smooth channel than the ribbed channel.

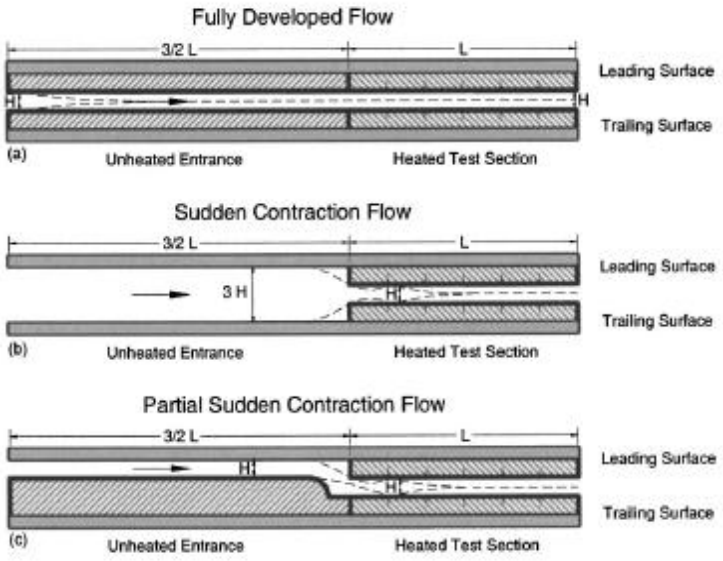

Figure 1.40: Entrance configurations tested by Wright et al. (2005)

Liu et al. (2008) studied a sharp 90° bend before the test section for a 1:4 AR channel at a high rotation number. They compared their data with Fu et al. (2005) who did tests on the same geometry with fully developed inlet. For stationary conditions, the sharp bend produced a 140% increase in heat transfer enhancement at the entrance of the test section compared to the fully developed case. After a length of 6 hydraulic diameters from the entrance, the difference is about 30%. The entrance effect reduced the effect of rotation in the first pass. As the rotation number increased, the rotation effect dominated over the entrance effect. Due to Coriolis force, the heat transfer enhancement on the trailing surface of the channel is always significantly higher than the leading surface for the first pass. But due to entrance effect, the leading and trailing surfaces showed almost the same heat transfer enhancement values for lower Rotation numbers. Huh et al. (2009) did tests with the same geometry as Fu et al. (2005) with the addition of angled ribs with high rotation. For the stationary case, the sharp bend with ribs produced about 50% higher heat transfer enhancement compared to fully developed entrance with ribs. As the flow progresses further in the first pass, the entrance effect dies down. Huh et al. (2009a) studied a

sudden expansion from a smaller diameter circular channel to a smooth rectangular 2:1 AR channel with high rotation. For the stationary case, the sudden expansion entrance almost doubled the heat transfer enhancement when compared with the 2:1 AR channel with fully developed entrance studied by Fu et al. (2005). It is also seen that the entrance effect dominates the rotation effect for low Rotation numbers as found by Liu et al. (2008).

1.7 Bend effect in two-pass channel

Metzger et al. (1984a) studied pressure loss through a sharp 180° turn smooth channel. They varied the channel width and compared the pressure drops. Their results showed that the effect of changing channel width did not have significant influence on the pressure drop for the range of parameters considered. Ekkad and Han (1995) used a transient liquid crystal technique to find a detailed heat transfer coefficient distribution in a 180° bend. Their results showed that the highest heat transfer enhancement was achieved near the outer wall away from the divider. There is another high heat transfer zone at the downstream corner of the turn due to flow impingement and a low heat transfer zone at the downstream corner of the tip due to flow separation. Schabacker et al. (1998) did PIV tests to capture velocity and turbulence profile in the sharp bend. Their results confirmed the separated zone in the downstream corner of the divider wall. They also showed the formation of two counter-rotating Dean type secondary vortex on the bend region. Liou et al. (1999) did LDV tests to study the effects of different divider wall thickness for a square channel. They observed that the turbulence level after the turn decreased with increasing divider wall thickness and flow uniformity after the turn increased with increasing divider wall thickness. The velocity vector profile and TKE contour plot is shown in Figures 1.41-1.42.

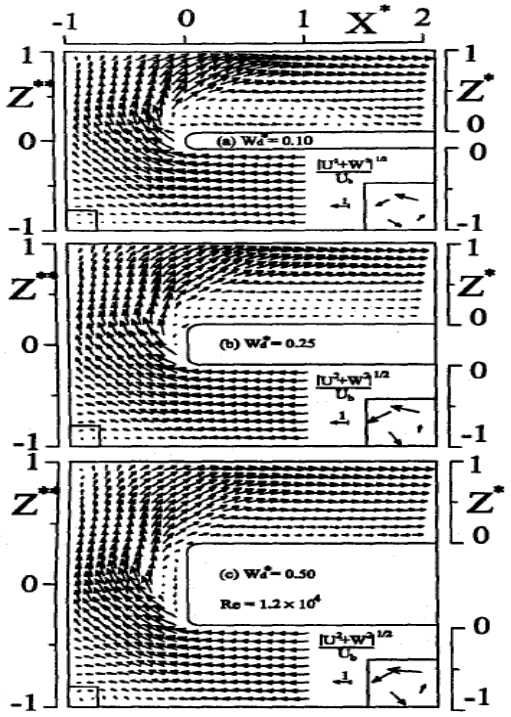

Figure 1.41 : Velocity vector plot for 3 different divider wall thickness(Liou et al., 1999)

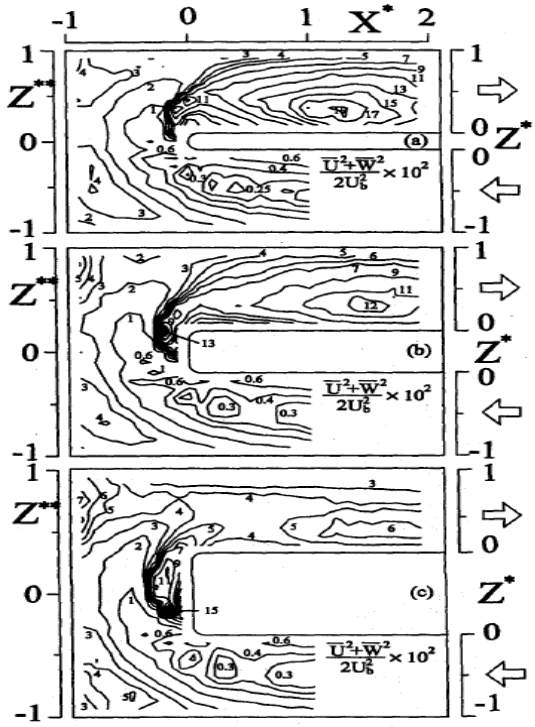

Figure 1.42 : TKE contour plot for 3 different divider wall thickness(Liou et al., 1999)

Liou et al. (2000) again did transient liquid crystal tests on the same geometries in Liou et al. (1999) and found that the heat transfer coefficient became more uniform with increasing divider wall thickness. Son et al. (2002) performed PIV experiments in a two-pass square channel with a smooth wall and a 90° ribbed wall. They compared their velocity data with heat transfer data from Ekkad and Han (1997). They concluded that flow impingement is the primary factor in heat transfer enhancement in the bend region versus the flow turbulence. Hirota et al. (1999) carried out mass transfer and pressure tests to study the effects of different turn clearances for a 2:1 AR channel. They showed that the lowest turn clearance enhanced heat/mass transfer the most but it also had the highest pressure drop. Nakayama et al. (2006) did LDV studies for the same geometry used in Hirota et al. (1999) and found that the turn clearance had significant effect on

the separation bubble formation on the downstream corner of the divider tip. The height of the separation bubble increases as the turn clearance decreases and reattachment length from the divider tip also increases as the turn clearance decreases. Wang and Chyu (1994) studied the effects of 3 different turning configurations computationally. The studied configurations included a straight corner turn, a rounded corner straight turn and a circular corner turn. Their results suggested that there exists a recirculation zone at the upstream outer corner for the first 2 geometries but it is absent for the circular turn and the circular turn provides the smoothest turning possible. The zone of low heat transfer coefficient downstream of the turn and attached to the divider tip is largest for the straight corner turn followed by rounded corner turn and circular turn. In the turning region heat transfer enhancement is highest for the straight corner turn and lowest for the circular corner but in the second pass, the circular corner turn provides the highest heat transfer enhancement. From the point of more uniform heat transfer enhancement and lowest pressure drop, the circular corner provides the highest thermal performance.

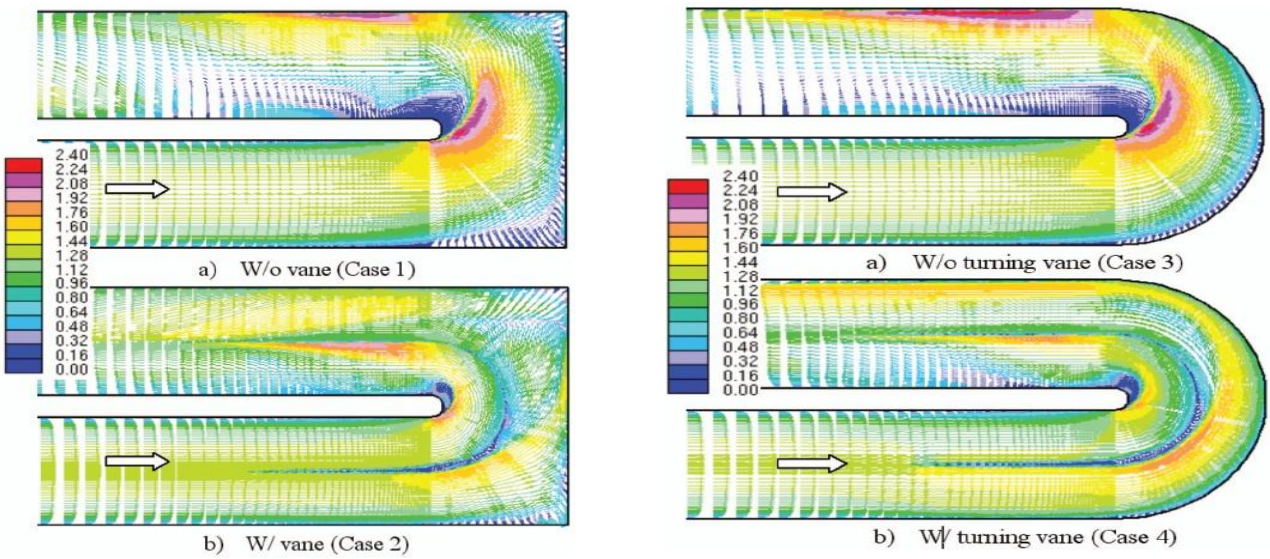

Figure 1.43: Velocity contour map by Luo and Razinsky (2009)

Metzger and Plevich (1990) studied the effects of turn region inserts on pressure drop through a sharp 180° channel with 90° ribs. The inserts included corner fillets, radial ribs, and turning vanes. Their results show that the inclusion of turning vanes reduces the pressure drop through sharp 180° bend channel significantly. Rao et al. (2004) performed an experimental study on various turning vanes inside a sharp 180° bend. They observed that shape, number, and position of turning vanes significantly affected the pressure loss through the bend. Luo and Razinsky (2009) studied a straight corner turn and rounded corner turn with turning guide vanes computationally. The velocity vector map is shown in Figure 1.43. It can be seen that the introduction of the guide vane reduces the size of the separation bubble at the downstream corner of the divider tip for both the geometries. It is also seen that without the guide vane, the region of high mean velocity at the downstream corner of the bend remains for both straight corner and round corner duct. Introduction of guide vane smoothens the velocity profile for the round corner duct more than the straight corner duct. Namgoong et al. (2008) did an optimization study to determine a 180° bend shape with the lowest pressure drop. They modified the shape of the divider wall between the two channels and calculated the pressure drop from the inlet to the exit of the channel. Chang and Cai (2010) studied a ribbed two-pass channel with and without bleeds from the bend. They found that the introduction of bleed in the bend region increased heat transfer enhancement and reduced pressure drop in the bend region. It was found that the thermal performance factor of the ribbed channel increases with increasing bleed mass flow rate. Schüler et al. (2011) studied the effect of turning vane configuration in a 45° ribbed channel, both experimentally and numerically. Their result show that with proper usage of turning vane, the pressure drop can go down to about 25% but the heat transfer values also go down in the second pass due to the use of turning vanes. Chen et al. (2011) compared a ribbed U-bend channel with a

turning vane and a turning vane-rib combination configuration experimentally and numerically. The turning vane configuration reduced the pressure drop significantly and the vane-rib combined configuration also reduced the pressure drop, but the heat transfer enhancement was still the highest for the baseline ribbed U-bend channel.

1.8 Dimple cooling

Sometimes instead of having protrusions in the flow (ribs), it is beneficial to add indentations on the inside surface of gas turbine blade internal cooling channel. These indentations on blade surfaces are called dimples. The dimples present in a channel produce local vortices in the indentation region which enhances the local Nusselt number considerably. Another favorable aspect of a dimpled channel is that the dimples do not protrude into the main flow like a ribbed channel and hence they do not produce pressure drops due to boundary layer separation from the protrusions, and the overall pressure drop is much lower than a conventional ribbed channel. The dimpled channels present a suitable alternative to the engine designers where they have a limited pressure budget and moderate level of heat transfer is needed. Different shapes of dimples have been used by researchers like spherical, cylindrical, conical, or tear drop shapes in stationary condition. Ligrani et al. (2001), Mahmood et al. (2001) showed the formation of instantaneous vortex pairs by smoke wire flow visualization. The schematic of time-dependent vortex shedding event is shown in Figure 1.44. Mainstream flow goes inside the indentation and as time progresses fluid packets are ejected out of the dimples. Two counter rotating vortex cells are generated inside the dimple and they go outward from the dimple. Due to the presence of the mainstream flow, these counter rotating vortices are advected downstream. It can be seen that the vortices gets elongated and gets shortened in cross section as these are advected downstream.

Fresh fluid packets arrive at the dimple again and this periodical cycle of vortex shedding continues from a dimple surface.

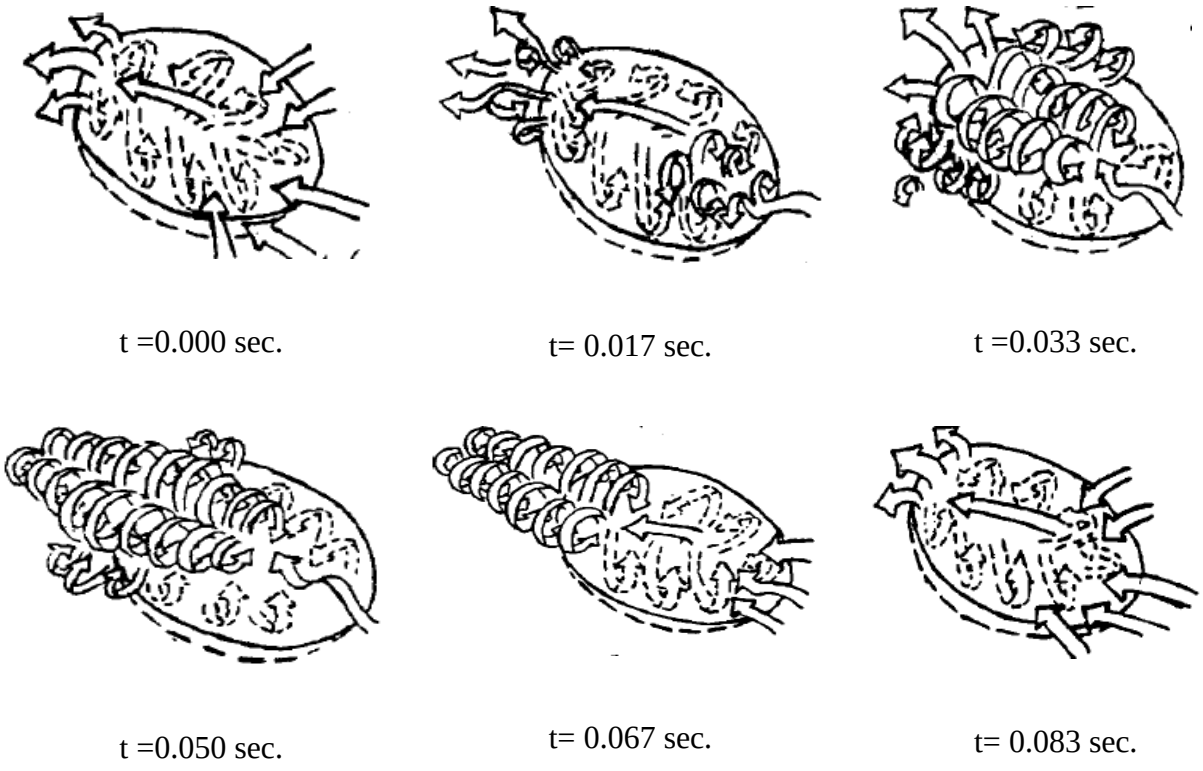

Figure 1.44: Schematic of instantaneous vortices around a dimple (Ligrani et al., 2001)

Ligrani et al. (2003) provided an extensive literature review of flow structure and heat transfer in a dimpled channel under stationary conditions. Won et al. (2005) studied flow structure in a dimpled channel with three different dimple depths. The strength of the primary vortex pair ejecting from the dimple increases with increasing dimple depth resulting in higher turbulence transport and turbulence production. The vortex shedding frequency is independent of the dimple depth. Burgess and Ligrani (2005) studied the overall thermal performance of a channel with different dimple depths. They showed that both overall averaged Nusselt number and friction

factor increases as the dimple depth is increased but the thermal performance also goes up with increasing dimple depth. Hwang and Cho (2006) reported heat transfer and pressure drop data in a channel with dimples and protrusions. They showed that the thermal performance for a channel with dimples on both surfaces was higher than dimples on a single surface or protrusion surfaces. Samad et al. (2008) did an optimization study on different dimple parameters for highest heat transfer and lowest pressure drop. The optimization variables chosen were Channel height/Dimple print diameter, Dimple depth/Dimple print diameter, and Dimple print diameter/Dimple pitch. Two optimum designs were obtained; one for high heat transfer and high-pressure drop and another for low heat transfer and low-pressure drop. The first optimal design increased the thermal performance by more than 2 times and the second optimal design increased it by about 50%.

1.9 Flow through a grooved channel

Extensive work has been done over the years on heat transfer and pressure drop through a ribbed channel. Ribs produce local flow separation and reattachment to the blade wall resulting in efficient mixing and better heat transfer from the wall but as the ribs protrude into the main flow, the pressure drop penalty is also high. Surface modifications in the form of grooves can also produce local turbulence close to the wall and enhance heat transfer. As they do not protrude into the mainstream flow, the pressure drop penalty is also lesser than a ribbed channel. Studies on heat transfer on grooved channels in turbulent flow are limited in open literature. Zhang et al. (1994) examined the combined effect of rectangular ribs and V- shaped grooves on heat transfer and pressure drop of a 10:1 AR channel. The grooves were placed in the mid-pitch spacing between the ribs and the six different rib spacings were used (P/e=8, 10, 15, 20, 25, 30). The rib-

groove combination channel performed better than a ribbed channel and produced heat transfer enhancement ratio of 3.4 and friction factor ratio of 6 for Re=12000, which finally produced the highest thermal performance for all the rib-groove combination in the range of Reynolds numbers studied. Lorenz et al. (1995) conducted Infrared Thermography measurements in a channel with periodic transverse grooves. In their case, the space between the grooves had the same width as the grooves themselves. The Nusselt number enhancement ratio obtained was in the range of 1.52-1.75. Eiamsa-ard and Promvonge (2008) investigated the flow in a channel with transverse periodic grooves numerically for different groove width to channel height ratios (B/H=0.5 to 1.75). The highest thermal performance factor of 1.33 was obtained for B/H=0.75. Bilen et al. (2009) compared the effect of different groove shapes (circular, trapezoidal and rectangular) on heat transfer and pressure drop for a grooved tube. The circular groove shape produced the highest thermal performance followed by trapezoidal and rectangular shape. Eiamsa-ard and Promvonge (2009) examined three types of transverse rib-groove arrangements: rectangular rib-triangular groove, triangular rib-rectangular groove, and triangular rib-triangular groove for three different pitch ratios (P/e =6.6, 10, and 13.3). The triangular rib-triangular groove combination produced the highest thermal performance in the range of 0.95-1.1.

1.10 Objectives of the study

It is important to understand the flow behavior in the internal cooling channels of a gas turbine blade to design it more efficiently. Engine designers need a thorough knowledge of flow behavior and heat transfer coefficient distribution inside a cooling channel. New cooling techniques may be needed where the blade is vulnerable to thermal failure like the trailing edge of the blade. There is need for understanding of complete flow behavior in the complex entry

structures of a coolant channel rather than idealized entry structures. The coolant has to go through multiple serpentine channels to fully utilize the cooling potential of the cold air drawn from the compressor. There is some pressure drop involved due to multiple flow turns inside the blade. It is of utmost importance that the pressure drop be reduced as much as possible so that less air mass will be used for the coolant circuit and more air is used for operating the engine, which will result in higher efficiency. Sharp turn-induced separations can produce local "hot spots" where the heat transfer from the blade wall to the coolant air is less and can lead to local failures of the blade. The present research has four primary objectives.

1) The first objective of the present research is to study the prospects of a new turbulence promoter in the trailing edge region rather than the standard pin-fins used in industry. Heat transfer and pressure drop tests will be done on two converging lattice structures that can be directly used in the trailing edge cooling channels and their performance will be compared with a typical pin-fin configuration. Another constant cross section area lattice structure, suitable for endwall cooling applications, will be also tested to see the effects of number of sub-channels in lattice structures.
2) Due to space limitation inside the blade, the coolant may have to flow through several different complex geometries before entering the actual coolant channel. The second objective is to study the flow physics and heat transfer inside some entrance geometries closely simulating the actual entrance geometries found in the hub section of the turbine blade before the coolant enters the coolant channels. Heat transfer, pressure, and velocity measurements will be done to completely understand the coolant flow through these entrance geometries. Numerical simulations will be done under rotating condition to

understand the interaction of the entrance geometry generated flow and the rotation induced flow.

3) The third objective is to design a sharp 180° bend geometry that reduces the pressure drop through the bend and at the same time does not reduce the heat transfer from the bend region. Most of the bend geometries studied in open literature focus on reducing the pressure drop. While some reported modifications of the bend geometry reduced the pressure drop significantly (e.g., turning vanes), they also decreased the overall heat transfer enhancement. While the reduction in pressure drop is of interest to an engine designer, the reduction in overall heat transfer due to the change in bend geometry is not always acceptable. In this study, bend geometries with the highest thermal performance factors (TPF) that give a unified measure of heat transfer and pressure drop are explored.
4) The fourth and final objective is to study some grooved channel at an angle to the flow direction. The goal of the grooved channel is to disturb the flow close to the blade wall resulting in inhibition of thick boundary layer development and better mixing causing higher heat transfer from the wall. Making the grooves at an angle to the main flow direction is supposed to promote a secondary flow along the groove and better mixing with the mainstream flow, which results in higher heat transfer close to the wall. A combination of angled grooves and ribs are tested to get the benefit of both the surface turbulators to further enhance heat transfer.

CHAPTER 2: EXPERIMENTAL SETUP AND PROCEDURES

2.1 Experimental setup

The schematic of the stationary test setup is shown in Fig. 2.1.

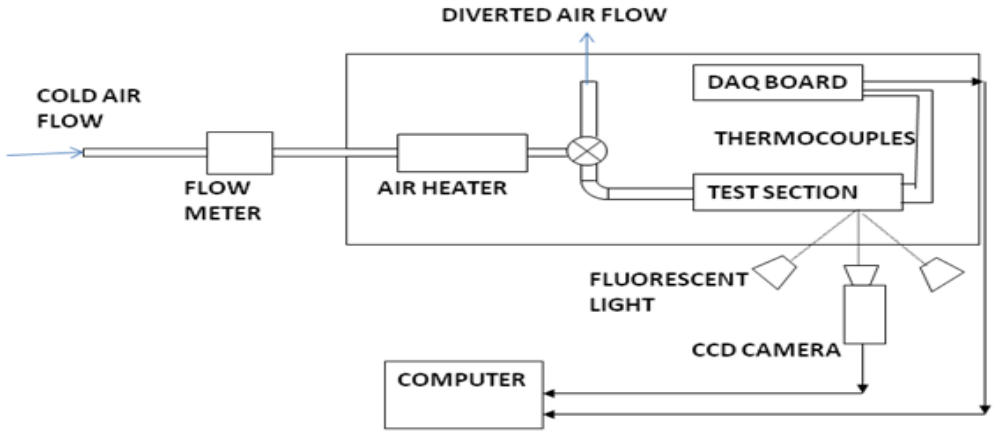

Figure 2.1: Schematic of the stationary setup

Compressed air is supplied from an Atlas Copco GA-315 compressor. Air is metered by a Omega FLR-87-25D flowmeter. The range of the flowmeter is 25-250 SCFM. Air coming to the test section is heated by an inline air heater to provide the temperature gradient for heat transfer between air and test section. The air coming out of the inline air heater is initially bypassed to the atmosphere through a three-way ball valve until it reaches a steady temperature and flow rate. When the air reaches a steady temperature, the experiment is started by suddenly turning the ball valve to allow hot air to pass through the test section. An analog CCD camera, placed at a right angle to the test section, records the images of the test section during the test. Two fluorescent lights are placed at 45^0 angles to light up the test section. The analog video signal acquired from the CCD camera is digitized and stored as individual frames with the help of a NI PCI-1411 Frame grabber card. T-type thermocouples are used to measure the mainstream air temperature and wall temperature. Thermocouple data are recorded by an Agilent hp-34970a data acquisition

unit. A code is written in Labview to simultaneously acquire images and record thermocouple data after the start of the test. A picture of the stationary test setup is shown in Figure 2.2.

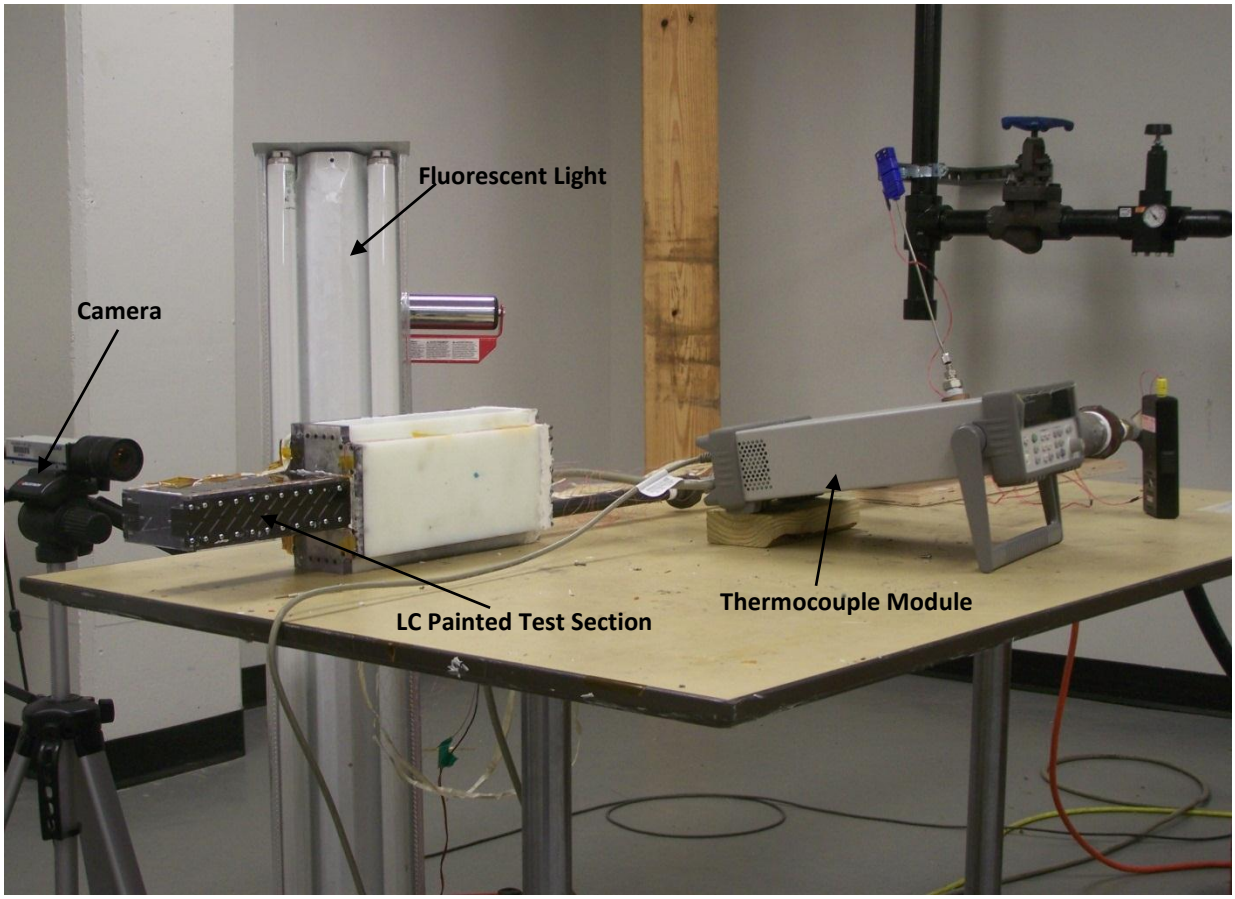

Figure 2.2: Picture of the stationary test setup

2.2 Heat transfer theory

The test section wall is assumed as an infinitely thick flat plate where the heat flux does not penetrate. The schematic of the plate is shown in Figure 2.3. The flat plate is assumed to be in uniform temperature T_0 at the start of the test. Suddenly the mainstream flow at temperature T_∞ is allowed to pass over the flat plate. Now it is assumed that the heat is transferred only in x direction. So, the 1-D heat conduction equation becomes

$$\frac{\partial^2 T}{\partial x^2} = \frac{1}{\alpha}\frac{\partial T}{\partial t} \qquad (2.2)$$

Now we need two boundary conditions and one initial condition to solve this equation. If we assume the semi-infinite condition, the boundary conditions become

$T(\infty,t) = T_0$ (2.3)

$$-k\frac{\partial T}{\partial x} = h(T_\infty - T(0,t)) \qquad (2.4)$$

The initial condition is, $T(x, 0) = T_0$ (2.5)

Now the semi-infinite condition means that the heat flux does not penetrate the other side of the flat plate during the duration of the test. Two steps are taken to ensure that the heat flux does not penetrate the thickness: 1) The test section is made of low thermal conductivity plastic to increase penetration time, and 2) The test duration is kept very small. According to Vogel et al. (2001), the semi-infinite assumption is valid until $\tau_d = \frac{\alpha t}{d^2} < \frac{1}{4}$ (2.6)

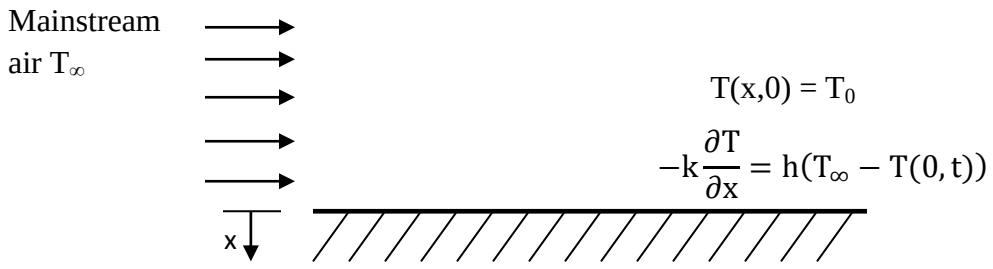

Figure 2.3: Schematic of flow over a flat plate

Low thermal conductivity acrylic of thickness ½ inch (12.7 mm) is chosen to build the test section and the test duration is kept within 80 seconds. So the criterion by Equation 2.3 is safely obeyed.

Equation 2.2 is solved using Equations (2.3)-(2.5). The solution is given by

$$\frac{(T_w - T_0)}{(T_\infty - T_0)} = 1 - \exp\left(\frac{h^2 \alpha\, t}{k^2}\right) erfc\left(\frac{h\sqrt{\alpha\, t}}{k}\right) \qquad (2.7)$$

However, in actual experiments, a perfect step change of the mainstream air temperature is usually not possible. Since the mainstream air temperature is a function of time, the solution in Equation 6 has to include the time-variance of the mainstream temperature. This is resolved by modifying Equation 6 using Duhamel's superposition theorem. The new solution is given by

$$T_w - T_0 = \sum_{j=1}^{N} \left[1 - exp\left(\frac{h^2 \alpha (t - \tau_j)}{k^2}\right) \times erfc\left(\frac{h\sqrt{\alpha (t - \tau_j)}}{k}\right) \times \left(\Delta T_{\alpha(j, j-1)}\right) \right] \qquad (2.8)$$

where ΔT_∞ is the step change in mainstream air temperature.

In Equation 2.8, T_w is the liquid crystal color change temperature which is previously calibrated. The initial uniform temperature T_0 is obtained from surface thermocouple mounted on the test section wall. History of the mainstream temperature T_∞ is recorded with fine wire thermocouples. Equation 2.8 is solved iteratively by Newton's method to find *h*. A guess value of h_0 is chosen first and it is continuously modified like $h_{n+1} = h_n - \frac{f(h_n)}{f'(h_n)}$ until $|h_{n+1} - h_n| \leq e$, where *e* is a small error value.

2.3 Liquid crystal thermography

Liquid crystal is a substance that is an intermediate phase between solid and liquid that occurs in some organic compounds. Molecules of the polymer in liquid crystal phase retain their orientational order but lose positional order. Because of the positional order, they display many

optical properties of the crystalline solid but the lack of orientational order contributes to their fluidity.

2.3.1 Classification of liquid crystals: Different classifications of the liquid crystalline phase are shown in Figure 2.4. ***Thermotropic*** liquid crystals are solids formed by heating the liquid to a certain temperature above which the crystal structure of the solid is no longer stable but still behaves as liquid crystal. ***Lyotropic*** liquid crystals are formed by mixing some compound with a solvent. The compound does produce a complete solution and shows characteristics of the liquid crystal state.

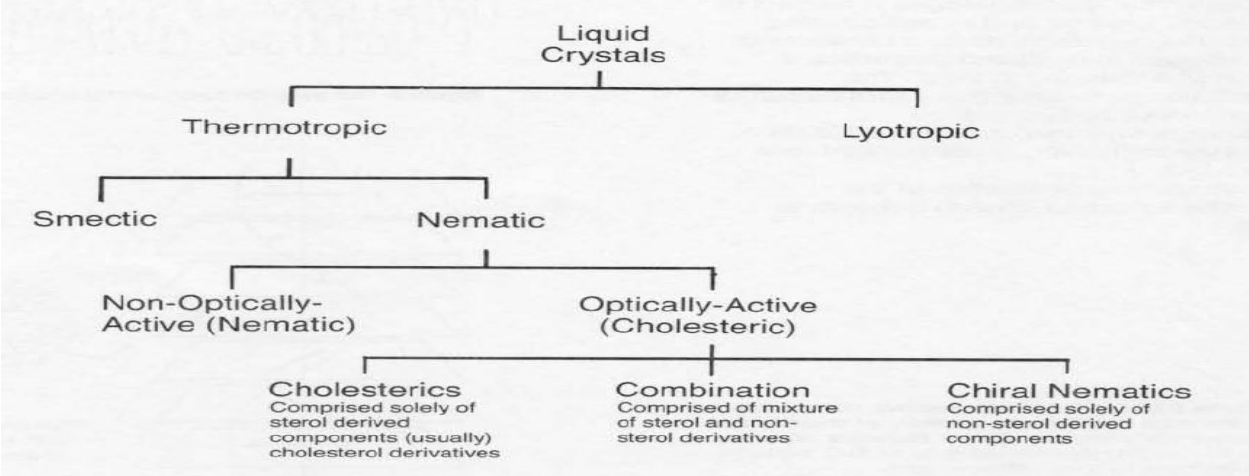

Figure 2.4: Different classifications of liquid crystal (Hallcrest Inc. Handbook)

The ***Thermotropic*** liquid crystal phase can be subdivided into two mesophases : ***smectic*** and ***nematic***. Schematics of the molecules in both phases are shown in Figures 2.5a & 2.5b. In the ***smectic*** phase, the molecules are layered with the long axis perpendicular to the plane of the layer. In the ***nematic*** phase the molecules are not as ordered as the ***smectic*** phase. As shown in Figure 2.5b, the long axes are parallel, but the molecules are not layered. A director ***n*** describes the average molecular orientation.

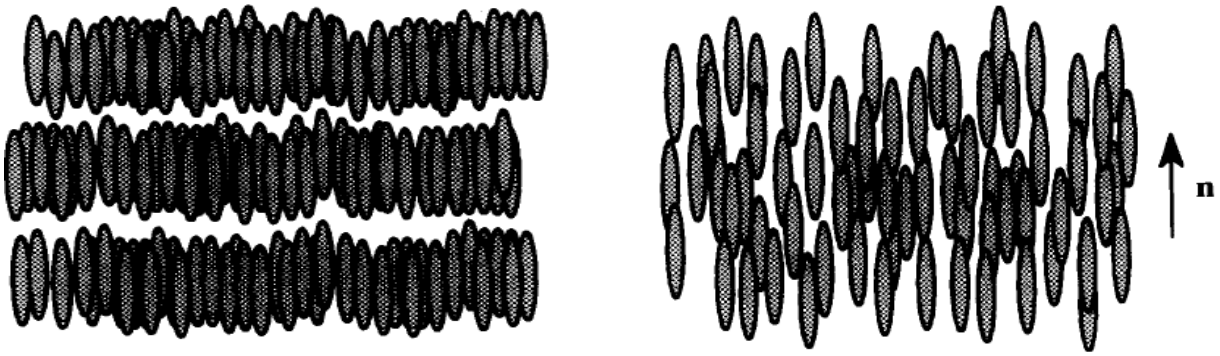

a) b)

Figure 2.5: Schematic of molecules in a) Smectic b) Nematic liquid crystal phase (Hallcrest Inc. Handbook)

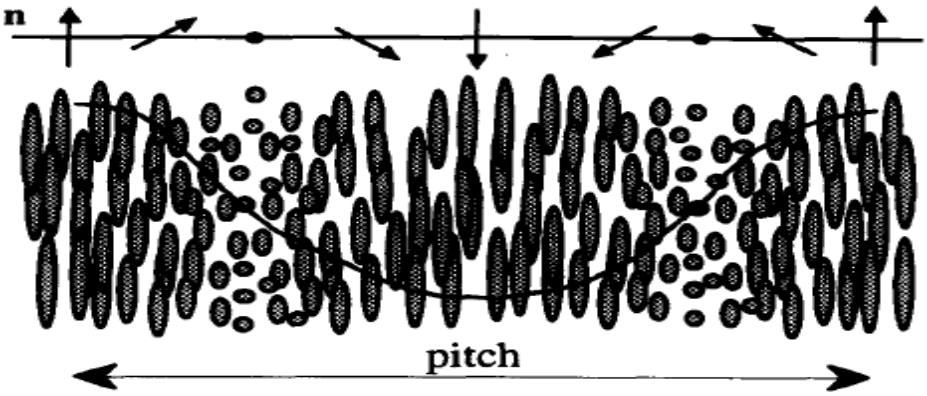

Figure 2.6: Schematic of chiral nematic liquid crystal phase (Hallcrest Inc. Handbook)

If the molecules in the liquid crystal phase are not symmetrical about its long axis, it is ***chiral***. Here the intermolecular forces cause each molecule to be rotated slightly with respect to the adjacent molecules and as a result the director n traces a helical path as shown in Fig. 2.6. Here n is parallel to the direction of the major axes of the long ellipses. With rotation of the molecules, n changes direction from parallel to the plane of the paper to perpendicular to the plane of the paper. The pitch p of a ***chiral nematic*** liquid crystal is defined as the distance over which n rotates through 360°.

The liquid crystals can be also classified according to use:

1) Unsealed liquids: In the unsealed form, the liquid crystal droplets are not surrounded by any protective coatings. Films of unsealed liquid crystal are vulnerable to atmosphere, chemicals, grease and common organic solvents. The presence of these impurities can severely affect the Color-Temperature relationship of the liquid crystal. However, once applied they produce brilliant color display. Because of the contamination issues, the lifetime of the unsealed liquid is rather short, from a matter of a few hours to a few days depending on the application.

2) Microencapsulated coatings: To use the liquid crystal for a longer time and to maintain the Color-Temperature relationship, the liquid crystal droplets are covered with a protective barrier. A microcapsule is a small sphere of liquid crystal polymer which is covered by a uniform thickness of protective polymer around it. Microencapsulated coatings can be available in an aqueous sprayable solution, which is easy to use and store. The typical diameter of the microcapsule is in the range of 5-10 μm. Microencapsulated liquid crystals of different color play range can be mixed together to watch temperature change of a substance for longer temperature range.

3) Liquid crystal coated sheet: In liquid crystal sheets, a thin film of liquid crystal is sandwiched between a transparent polymer substrate and a black background. This is the most easy to use form of liquid crystal.

2.3.2 Color play properties of liquid crystal:

Temperature sensitive liquid crystals have a range of temperature between which it shows optical properties. A typical reflected wavelength pattern is shown in Fig. 2.7. The COLOR PLAY of a liquid crystal is defined either by specifying the Red color start or by specifying the Green color start and by specifying the Bandwidth. The Bandwidth is defined as the difference between the Blue start temperature and

the Red start temperature. Depending on the Bandwidth, a liquid crystal can be called Wide band or Narrow band. Liquid crystal having bandwidths greater than 5° C is called Wide band liquid crystal and the ones with bandwidths less than 2° C are called Narrow band liquid crystals. A liquid crystal with the designation R30C1W means it has a Red start temperature at 30° C and a bandwidth of 1° C. Commercial liquid crystals are available with red appearance temperature ranging from -30° C to 120° C.

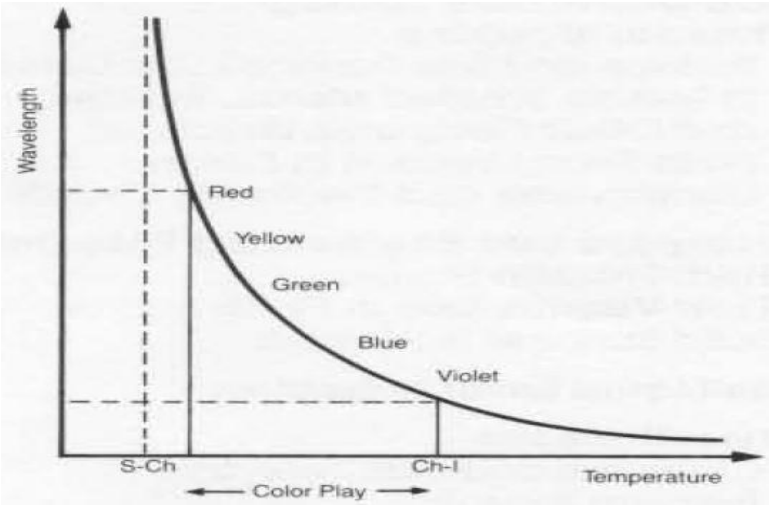

Figure 2.7: Reflected wavelength to temperature response for a typical liquid crystal (Hallcrest Inc. Handbook)

2.3.3 Liquid crystal calibration techniques: In a liquid crystal thermography experiment, the image of a test section painted with liquid crystal is recorded with a camera. The color data obtained from the image has to be calibrated to temperature. Any color data can be represented as a combination of three primary colors- Red(R), Green (G) and Blue(B). The RGB color system can be described in a Cartesian system by Fig. 2.8. Black color is the origin and each point of the cube is a unique color. Any color can be represented as a combination of RGB.

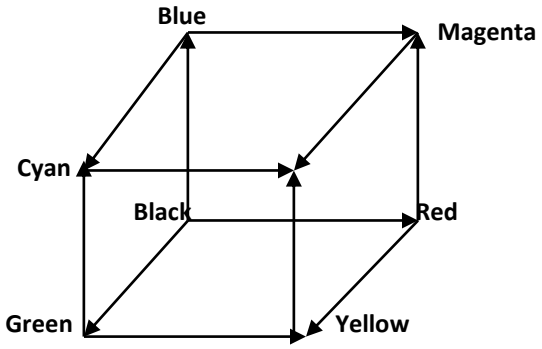

Figure 2.8: RGB color representation

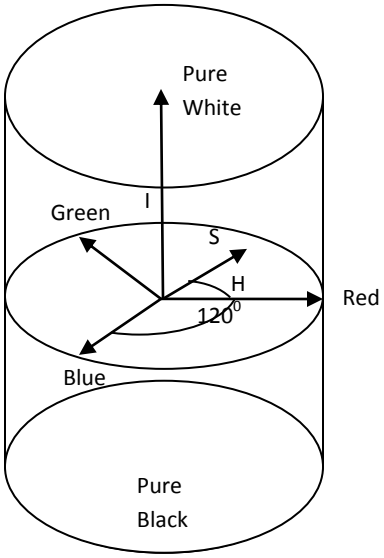

Figure 2.9: HSI color representation

The HSI color model can be represented on a cylindrical coordinate system. The schematic of HSI representation is shown in Fig. 2.9. The Hue means the basic color and Saturation means the representation after adding white to the basic color. The HSI model can separate the color information, which is a combination of Hue and Saturation, from Intensity. Hue (H) is defined by an angular value. Saturation(S) is the angular distance from the center of the cylinder. Intensity (I) is the height of the cylinder. The HSI conversion from RGB is given below.

$$H = \cos^{-1}\left[\frac{0.5\{(R-G)+(R-B)\}}{\{(R-G)^2+(R-B)(G-B)\}^{1/2}}\right] \quad (2.9)$$

$$I = \frac{1}{3}(R+G+B) \quad (2.10)$$

$$S = 1 - \frac{Min(R,G,B)}{I} \quad (2.11)$$

Han et al. (2000) describes all the calibration techniques used in the past. Some of the widely used calibration techniques are discussed below.

Steady state HSI technique: In this technique the color range parameter hue is calibrated with temperature during a calibration experiment. The test section is painted with a wide band liquid crystal. A thermocouple is mounted on the test section to measure the wall temperature at a particular point of the test section. A region of small area is chosen around the thermocouple bead and the average value of the hue is calculated for the region. The heat input is varied and the test section is allowed to reach steady state before noting another value of temperature and hue. The property hue shows a repeatable set of values over a range of temperature. A direct relation between the wall temperature and hue is obtained in this way. A typical Hue-Temperature calibration curve is shown in Fig. 2.10. After the calibration test, the test section is supplied with a constant heat flux and allowed to reach steady state. A steady color pattern is observed and recorded with a camera. The hue value at each pixel is transferred to a wall temperature value from the calibration curve. The heat transfer coefficient is obtained by,

$$h = \frac{q}{T_w - T_\infty} \quad (2.12)$$

where T_∞ is the mainstream temperature. This technique is very sensitive to lighting conditions and camera angle. If there is any change in the lighting condition or camera angle from the calibration test to the actual test, a new calibration curve has to be generated. The duration of this test is about 2-3 hours.

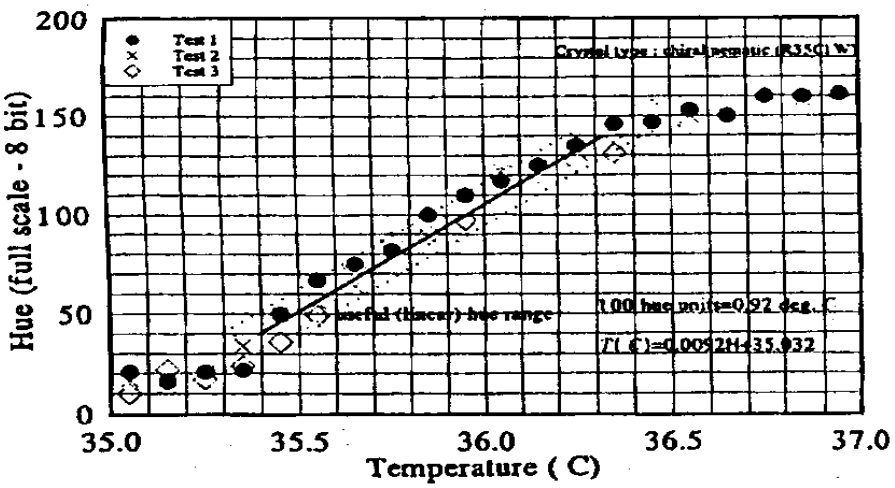

Figure 2.10: A sample hue-temperature calibration curve (Han et al., 2000)

Transient HSI technique: In this technique, the calibration process remains the same as the steady state HSI technique. Change in camera angle and lighting still affect the calibration during this technique but the advantage is the shorter duration of tests. The test section is initially kept at uniform temperature. The test section is usually made of low thermal conductivity plastic to maintain the semi-infinite assumption. 1-D heat conduction equation with semi-infinite boundary is solved to obtain relationship of heat transfer with temperature. The solution is given in Equation 2.7. After the start of the test, images of the test section are recorded at certain intervals with accurate time stamps. An image processing system converts the RGB image to HSI image for all the images. At a particular time *t*, the wall temperature T_w is obtained from a calibration curve like Fig 2.10. The time *t* in Equation 2.7 is obtained from the time stamp of the image.

Knowing the mainstream air temperature T_∞ and the thermophysical properties of the test section material, the heat transfer coefficient h can be obtained.

Transient single-color capturing technique: In this technique, the time of appearance of a particular color band at every pixel of the test section is observed during a transient experiment. The particular color value is associated with a predefined temperature. In this technique the image processing system looks for a definite value of color at every image taken during the test and the time is obtained from the time stamp of the image. But in the transient HSI technique the time is kept constant and the wall temperature spatial variation is obtained from the calibration curve. Bunker and Metzger (1990) used the appearance of green color as the predefined color. According to them the change of color from red to green shows a strong intensity which is more accurate to track. Vedula and Metzger (1991) also used the same technique for simultaneous measurement of heat transfer coefficient and film cooling effectiveness. The calibration procedure is not as rigorous as the other methods and is insensitive to camera angle and lighting.

2.4 Experimental procedures

The walls surrounding the test section are painted with a thin coating of narrow band liquid crystal of 1° C bandwidth. The walls are then painted with a black paint over the liquid crystal to enhance contrast of the images. Before the test, the test section is kept at ambient temperature. The experiment is initiated by suddenly allowing the hot air, which is above the temperature of the liquid crystal color change temperature, to flow through the test section. Image and thermocouple data acquisition are also started with the start of the test. The color change of the liquid crystal on the test section is recorded with a CCD camera at 5 frames/second and mainstream and wall temperature are recorded with T-type thermocouples during the test.

Images are saved in BMP format and divided into their constituent Red, Green and Blue colors. The time required for the green color to appear in the images is used for the data analysis. When the liquid crystal color changes from red to green, it produces a strong change in intensity which is easily and accurately tracked. A calibration test is run in laboratory lighting condition to verify the color change temperature and the same lighting conditions are used during the tests. This work uses the green band tracking technique used by Vedula and Metzger (1991), Metzger et al. (1991).

2.5 Uncertainty analysis

The uncertainty analysis in this work is done based on the methodology by Kline and McClintok (1953). For finding the uncertainty of a result, one needs to find the uncertainties of the measurements affecting the results. Let's assume that $x_1,x_2,x_3,\ldots\ldots..,x_n$ are some independent variables which are measured in the Laboratory. R is a quantity which is found by using the independent measurements $x_1,x_2,x_3,\ldots\ldots..,x_n$. R is expressed in terms of the independent variables as

$$R = f(x_1,x_2,x_3,\ldots\ldots..,x_n) \qquad (2.13)$$

For small variations of the variables δx_i, the variation in the result δR is given by

$$\delta R = \frac{\partial R}{\partial x_1}\delta x_1 + \frac{\partial R}{\partial x_2}\delta x_2 + \frac{\partial R}{\partial x_3}\delta x_3 + \ \ldots\ldots + \frac{\partial R}{\partial x_n}\delta x_n \qquad (2.14)$$

If R is a linear function of n independent variables, then the uncertainty of R is given by

$$u_R = \sqrt{\left(\frac{\partial R}{\partial x_1}u_{x_1}\right)^2 + \left(\frac{\partial R}{\partial x_2}u_{x_2}\right)^2 + \ \ldots\ldots\ldots\ldots + \left(\frac{\partial R}{\partial x_n}u_{x_n}\right)^2} \qquad (2.15)$$

The relative uncertainty of R is given by

$$\frac{u_R}{R} = \sqrt{\left(\frac{\partial R}{\partial x_1}\frac{u_{x_1}}{R}\right)^2 + \left(\frac{\partial R}{\partial x_2}\frac{u_{x_2}}{R}\right)^2 + \ldots\ldots\ldots + \left(\frac{\partial R}{\partial x_n}\frac{u_{x_n}}{R}\right)^2} \qquad (2.16)$$

In the experiments done in this work, the intended result is the heat transfer coefficient *h*. It is related to the other variables by Equation 7.

$$\frac{(T_w - T_0)}{(T_\infty - T_0)} = 1 - \exp\left(\frac{h^2 \alpha\, t}{k^2}\right) erfc\left(\frac{h\sqrt{\alpha\, t}}{k}\right)$$

or, $h = f(T_w, T_0, T_\infty, \alpha, k, t)$ (2.17)

Uncertainty in T_w is not considered since the liquid crystal is factory calibrated and it is obtained from the factory calibration. The properties of the test section like α and k are taken from tabulated value and as a custom a relative uncertainty of 3% is assumed for those variables.

The uncertainties for all the variables are as follows

$u_{T_0 = \pm 0.5^0 C}$

$u_{T_\infty = \pm 0.5^0 C}$

$\frac{u_\propto}{\propto} = \frac{u_k}{k} = \pm 0.03$

$u_t = \pm 0.2\ s$

From Equation 2.16, the relative uncertainty of h will be

$$\frac{u_h}{h} = \sqrt{\left(\frac{\partial h}{\partial t}\frac{u_t}{h}\right)^2 + \left(\frac{\partial h}{\partial T_0}\frac{u_{T_0}}{h}\right)^2 + \left(\frac{\partial h}{\partial T_\infty}\frac{u_{T_\infty}}{h}\right)^2 + \left(\frac{\partial h}{\partial \propto}\frac{\propto}{h}\frac{u_\propto}{\propto}\right)^2 + \left(\frac{\partial h}{\partial k}\frac{k}{h}\frac{u_k}{k}\right)^2}$$

$\frac{u_h}{h} = 0.101$ or 10.1%

This value calculated is the maximum uncertainty for all the tests. This is the case with the lowest heat transfer coefficient. For other values of heat transfer coefficient and time, the value of relative uncertainty is lower.

Similarly the uncertainty in Reynolds number is also calculated and the maximum uncertainty in Reynolds number comes out to be about 2.2 %.

CHAPTER 3: LATTICE STRUCTURE RESULTS

3.1 Converging lattice structures

3.1.1 Geometries used during the test: To enhance structural rigidity and heat transfer in the trailing edge of the region, the lattice structures can be incorporated in the trailing edge cooling channel. A schematic of some lattice structures in the trailing edge region is shown in Fig. 3.1.

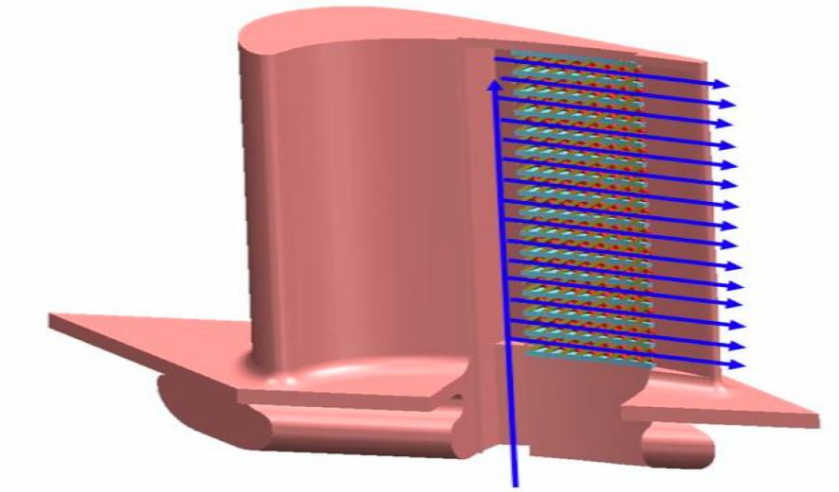

Figure 3.1: Lattice structures in trailing edge of gas turbine blade

The trailing edge of the blade reduces in cross section towards the trailing edge direction. To accommodate a lattice structure in that region, the cross section of the lattice structure decreases from flow inlet to exit. The majority of the work reported in the literature deals with rectangular aspect ratio channels with radial entry and exit. In a trailing edge, the channel cross-section is typically trapezoidal, and in specific design configurations the entry flow can be chordwise with a 90-degree flow turn at the entry (see Fig. 3.1). The flow may have to go through a converging channel before exiting the trailing edge of the blade. Studies done on lattice structures in open

literature also focused on constant cross-section lattice structure. So a combination of a 90 degree turn, converging cross-section in trailing edge region and a lattice structure incorporated inside the converging channel is quite a unique geometry. These geometrical issues and their impact on the lattice cooling heat transfer have not been reported in the archival journal and represent the primary focus of the present work.

To closely simulate the theoretical drawing, a test section is built with development length of the flow before the entrance to the lattice structure. The air flow enters the test section from a ½ inch NPT pipe. The test sections are made of acrylic sheet, while the lattice cores are made of a copolymer material commonly called ABS (Acrylonitrile Butadiene Styrene). The air flows through the test section and takes a 90° turn to enter the test section. The flow direction is shown in Fig. 3.2. After taking a 90° turn, the flow enters the lattice structure, goes through the inlet channels and hits the side walls. After it hits the side wall the flow is diverted from one side of the blade to the other side and proceeds downstream along a sub-channel until it hits the opposite wall where the flow undergoes up- or down-turning and impingement on the opposite wall. The target surfaces are the front and back walls of the trailing edge model that supports the lattice structure. From a design perspective, it is anticipated that the lattice–structure studied will form a radial section of the trailing edge passage, as shown in Fig. 3.1, and several of these sections will make up the full trailing edge. Two converging lattice structures are tested to see the effect of number of entry channels on the heat transfer enhancement and thermal performance. A transient liquid crystal technique is used to determine the heat transfer coefficient for the two lattice geometries, and four values of Reynolds number ($4000<Re<20000$).

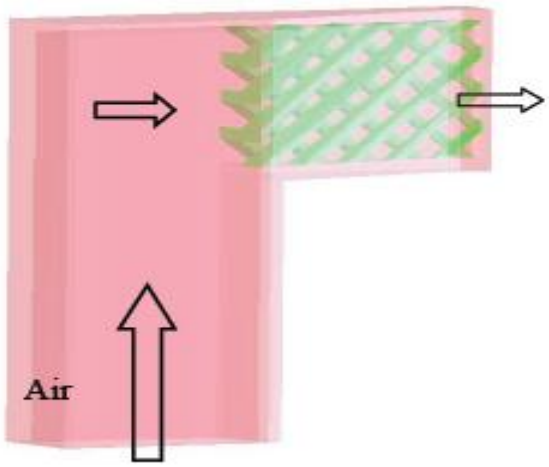

Figure 3.2: Flow direction for the converging lattice structure

The lattice structures are shown in Figs. 3.3-3.4. The ribs are inclined at an angle 45° to the flow direction. One side of the lattice is straight and the other side of the lattice is at a 15° angle with the straight side. The lattice with four inlet channels changes cross section from 2.46:1 Aspect ratio (AR) to 11:1 AR. The lattice with two inlet channels changes cross section from 1.12:1 to 5:1 AR. The flow direction through the lattice is shown below in Figs. 3.5-3.6.

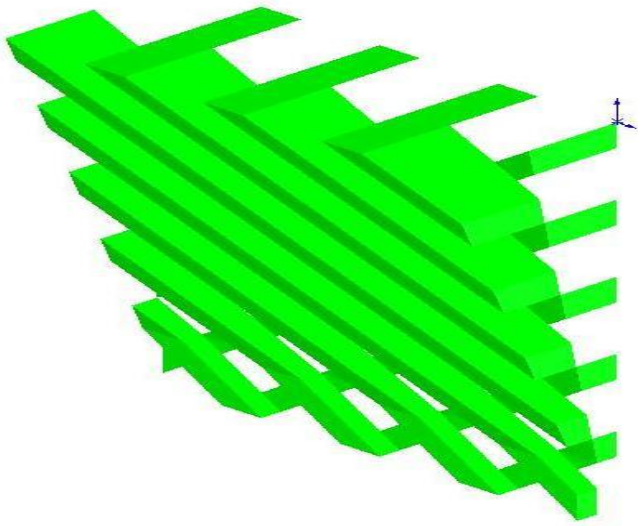

Figure 3.3 : Four inlet channel lattice structure

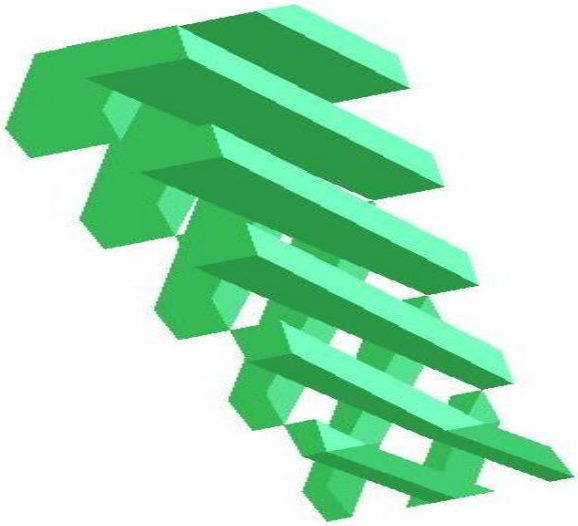

Figure 3.4 : Two inlet channel lattice structure

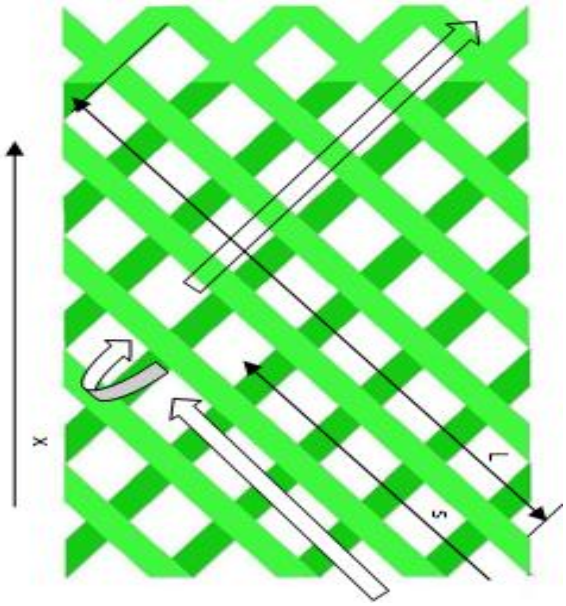

Figure 3.5 : Flow directions of the four inlet channel lattice

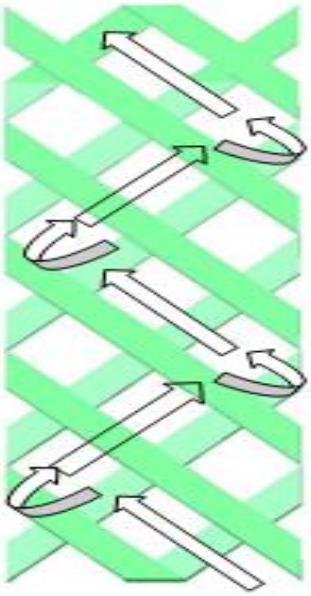

Figure 3.6 : Flow directions of the two inlet channel lattice

Tests were done at four Reynolds number at Re=4,400, Re=7,800, Re = 13,000 and Re=20,000, based on the hydraulic diameter D_{in} of the entry sub channel at inlet. Tests were done for the straight and inclined side of the lattice and heat transfer map for surface is obtained for different Reynolds number. Nusselt number is obtained from the heat transfer coefficient. This Nusselt number is compared with the Nusselt number (Nu_0) for a simple smooth channel in turbulent flow. The characteristic dimension for calculating the Reynolds number and the Nusselt number for each channel is the hydraulic diameter of each sub-channel at inlet. The dimensions for calculating the hydraulic diameter of a channel is shown in Fig. 3.7. Here H is the height of the sub-channel at inlet and W is the channel width. Since the channel is converging, H changes for different channels as the flow progresses towards the exit. As a result each channel have different hydraulic diameter.

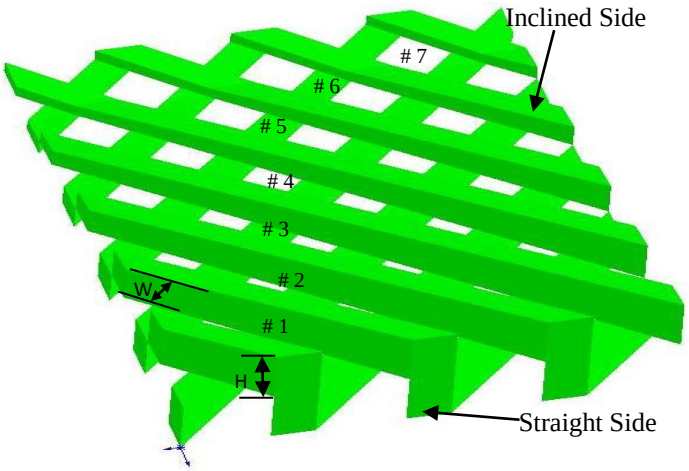

Figure 3.7: Dimensions used for calculation of hydraulic diameter of a sub-channel at inlet

The Nusselt number is normalized by the Dittus-Boelter correlation (1930).

$$Nu_{0_s} = 0.023.{Re_s}^{0.8}.Pr^{0.4} \qquad (3.1)$$

where Re_s is based on the dimension of each sub-channel at the inlet. The Reynolds number at the entry of each sub-channel is different than the Re at inlet of the entry sub-channel. As a result Nu_{0s} for the middle and the exit channels of the lattice are also different than the entry channel. Table 3.1 and 3.2 shows different Re_s values for the 4 entry channel lattice and 2 entry channel lattice structure respectively.

Table 3.1: Reynolds number at inlet of different sub-channels for four inlet channel lattice

	Re=4400	Re = 7800	Re=13000	Re=20000
Channel #	Re_s	Re_s	Re_s	Re_s
1	4400	7800	13000	20000
2	4400	7800	13000	20000
3	4400	7800	13000	20000
4	4759	8436	14059	21630
5	5394	9562	15936	24518
6	6225	11035	18392	28296
7	7359	13046	21742	33450

Table 3.2: Reynolds number at inlet of different sub-channels for two inlet channel lattice

	Re=4400	Re = 7800	Re=13000	Re=20000
Channel #	Re_s	Re_s	Re_s	Re_s
1	4400	7800	13000	20000
2	4743	8408	14013	21559
3	5380	9538	15896	24455
4	6213	11014	18357	28241
5	7351	13031	21719	33413

3.1.2 Results: Figure 3.8 shows the contour plot of the Nusselt number enhancement ratio for the two sides of the lattice structure for the two converging lattice geometries at Re = 4400. The Nu ratios at the other Reynolds numbers show similar trends for the heat transfer with the values being lower for increasing Reynolds number. Figures 3.8(a)-(b) show the Nu contours for the inclined or converging side of the channel while Figs. 3.8(c)-(d) exhibit the contours for the straight/flat side. For identifying the different sub-channels, they are numbered starting from the inlet to the exit of the lattice in Fig. 3.8. The flow direction is also shown in Fig. 3.8. Flow enters and flows along the sub-channel and undergoes a 90-degree turn and impinges on to other side of the channel at its termination point along the sidewall. The heat transfer coefficient decreases in the sub-channels with increased distance from the impingement or the entry point. Some localized regions of high heat transfer coefficients are also observed along the flow direction which is due to the turbulence created by the cross flow from other side of the lattice. For both the cases, the entry channels (Channels 1-3 for the four entry channel and channel 1 for the two entry channel) show the lowest values of heat transfer coefficient. The flow takes a 90° turn before entering the entry sub-channels. The low values of heat transfer at the entry channel are probably due to flow separation after the 90° turn of the flow.

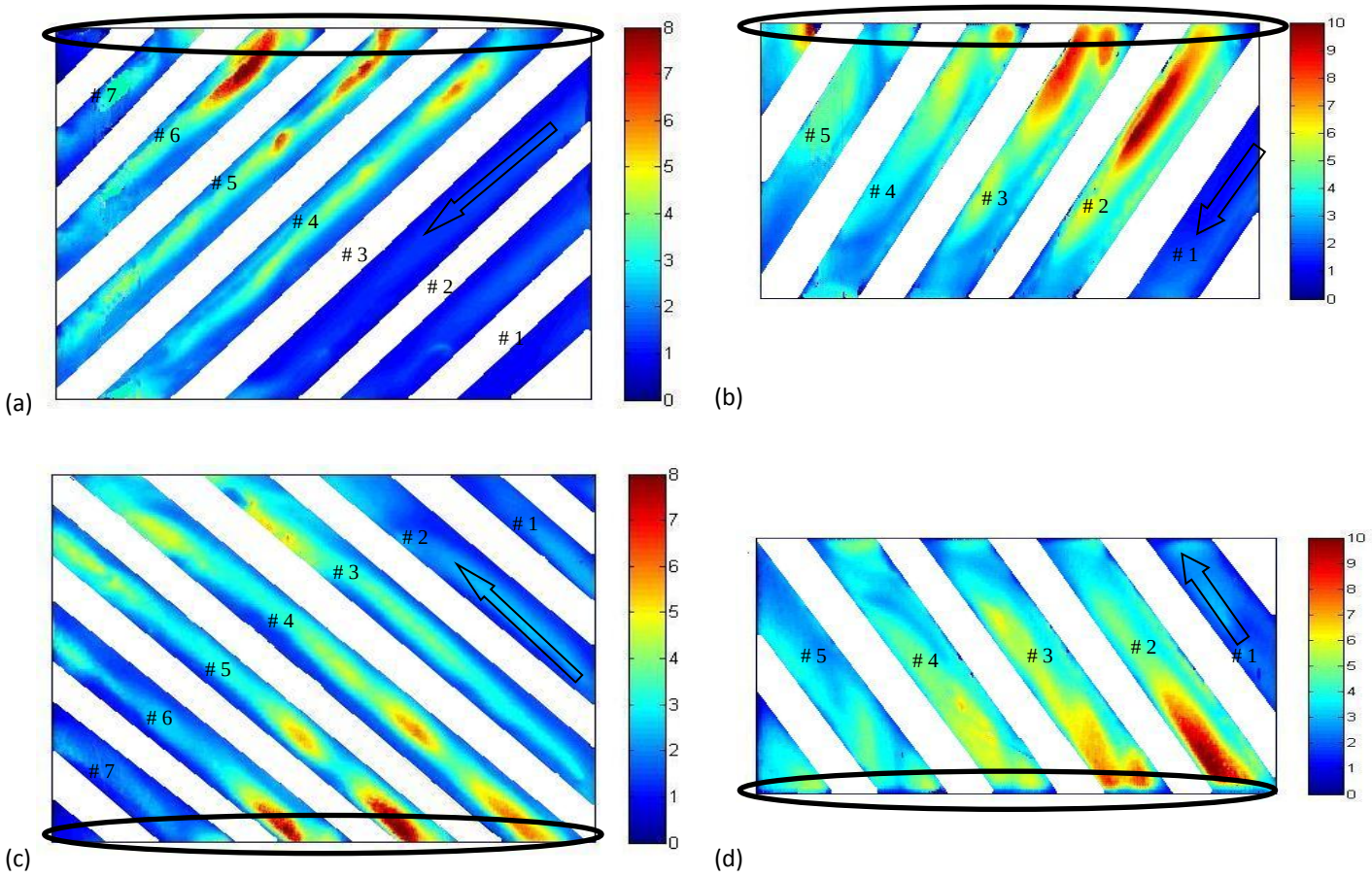

Figure 3.8 : Detailed local Nu/Nu_0 distribution for Re =4400; (a) Inclined side, four-inlet-channel, (b) Inclined side, two-inlet-channel, (c) Straight side, four-inlet-channel, (d) Straight side, two-inlet-channel

Figure 3.9 shows the Nu/Nu_0 line plot along streamwise direction for the straight side at Re = 4400 and Re =13000. The inclined side shows similar trends. Here ***s*** is the distance along the flow path and ***L*** is the length of the channel as shown in Fig. 3.5. For the inlet channels (#1-#3 for the four-channel case, and #1 for the two-channel case), the Nusselt number ratio profiles are relatively flat, near 2 for the lower Re and about 1.5 for the higher Re. These values are representative of a standard turbulated channel, albeit a bit lower, since the turbulators are on the opposite wall of the channel (and the turbulators are non-conducting). For the downstream channels (#4-#7 for the four-pass configuration and #2-#5 for the two-pass configuration), the

heat transfer coefficient enhancement value is maximum at the impingement zones for all the channels. Then it decreases and attains a uniform value throughout the channel. Heat transfer coefficient enhancement is reduced with increase of Reynolds number which is common for internal cooling applications. For the four-inlet-channel case, channels 4, 5 and 6 show the highest values of heat transfer enhancement, reaching values as high as 5 in the impingement region at the lower Re. Beyond the impingement location, the heat transfer ratios decay down to a range of about $Nu/Nu_0 \sim 2$ in the latter-halves of the sub-channels. It is noteworthy that downstream of the impingement point there is some non-monotonicity particularly for channels 4 and 5 characterized by the strongest impingement. These are presumably reflective of the complexity in the flowfield at the Reynolds numbers considered. For the two-inlet-channel case, channel 2 shows the highest value of Nu enhancement factor (about 6 for channels 2 and 3 and lower for other channels) and the profiles tend to be more monotonic with a decay from the impingement location downstream.

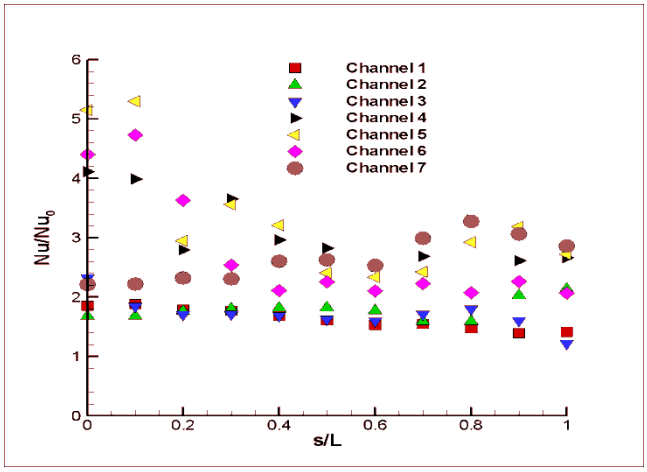

(a)

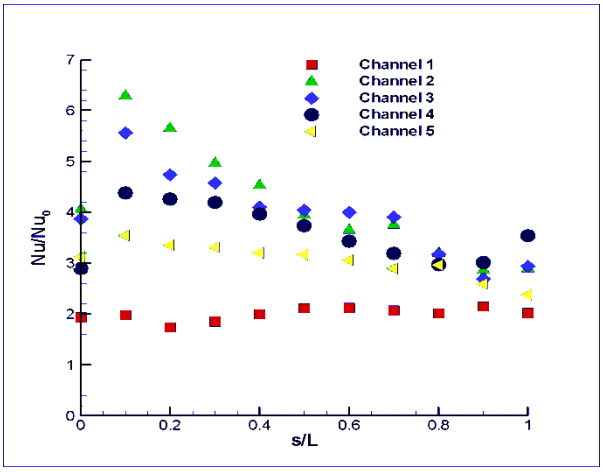

(b)

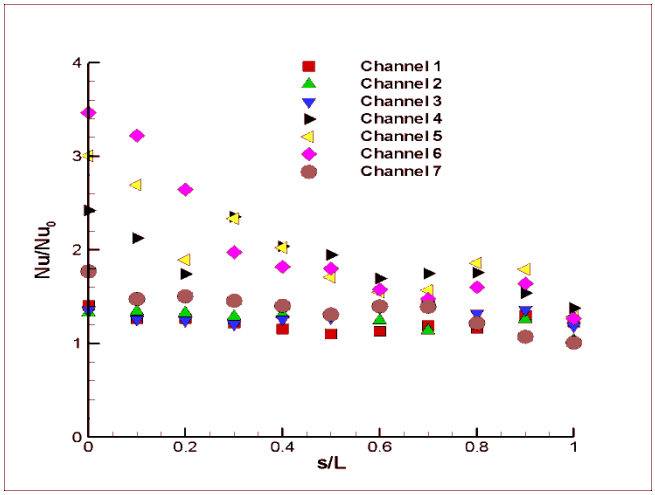

(c)

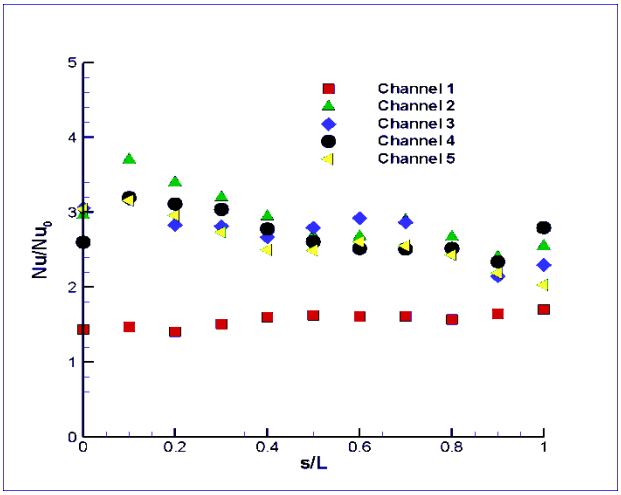

(d)

Figure 3.9: Nu/Nu_0 line plot along streamwise direction; (a) Re =4400, four-inlet-channel, (b) Re =4400, two-inlet-channel, (c) Re =13000, four-inlet-channel, (d) Re = 13000, two-inlet-channel

Figure 3.10 shows the averaged Nu/Nu_0 plot for each sub-channel of the straight and inclined side which is plotted as a function of the distance ***x/D*** which represents the mid-point of the sub-channel measured axially from the inlet of the lattice geometry as shown in Fig. 3.5. As expected, channels 5 and 6 (x/D of 4.4 and 5.2) produces the highest averaged heat transfer enhancement values for all the Reynolds number in case of the four-inlet-channel lattice. A significant Reynolds number effect is observed with the Nu ratios decreasing 30-80% (depending on the channel number) with Reynolds number. For the two-inlet-channel case the highest value of heat transfer is obtained for channel 2 (x/D=2). The heat transfer enhancement reduces as the flow progresses further towards the exit. Here also a strong Re dependence is observed with a decrease in Nu ratio as high as 78% with increasing Reynolds number. The straight side and the inclined side shows similar averaged Nu/Nu_0 values for both the lattice cases.

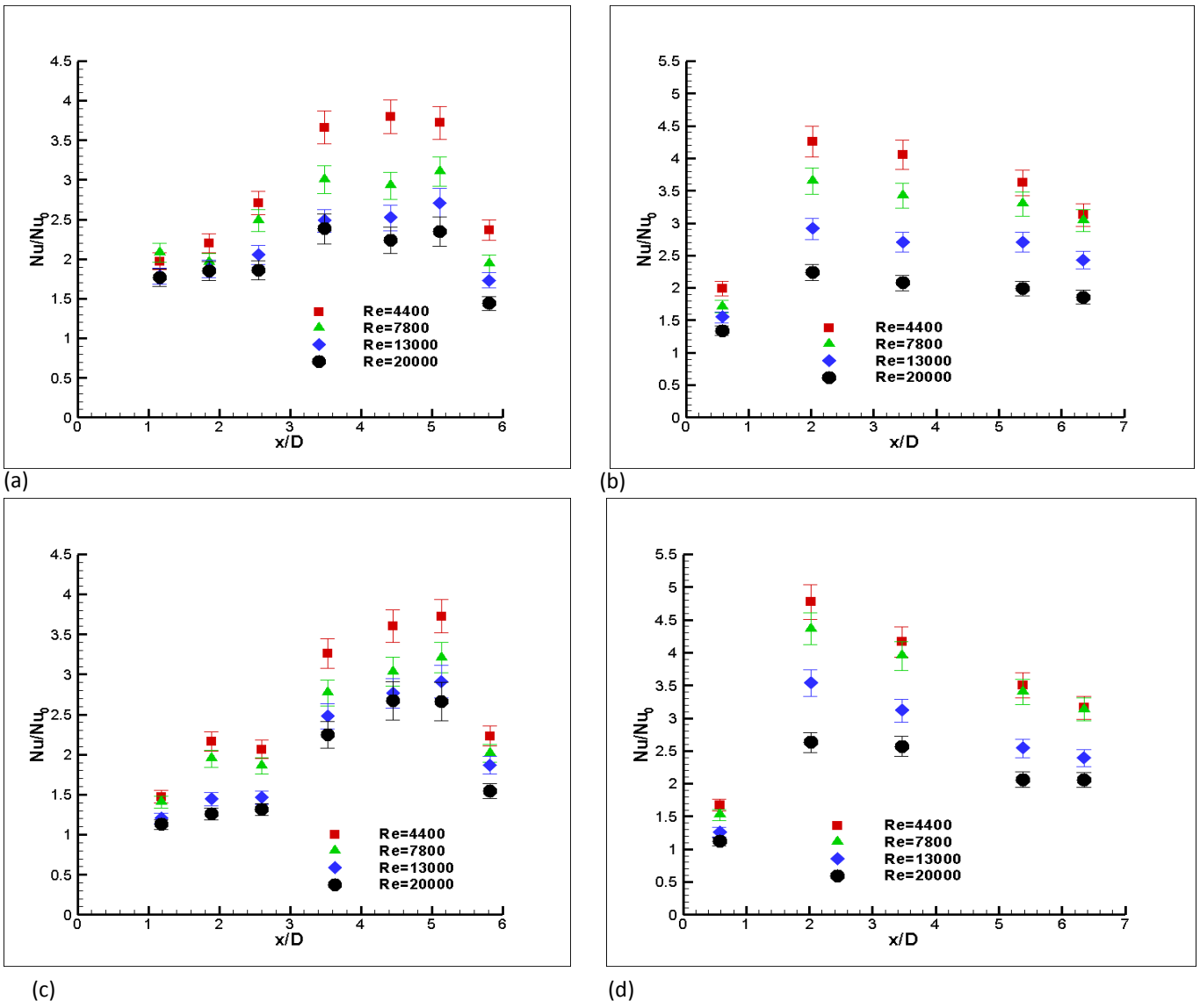

Figure 3.10: Averaged Nu/Nu_0 plot; (a) Four-inlet-channel lattice-straight side, (b) Two-inlet-channel lattice-straight side, (c) Four-inlet-channel lattice-inclined side, (d) Two-inlet-channel lattice-inclined side

To compare the performance of lattice structure against a standard cooling technique in the trailing edge region, heat transfer enhancement and pressure drop are compared with the pin fin data from Metzger et al. (1984a). The pin fin configuration used for comparison is shown in Fig. 3.11.

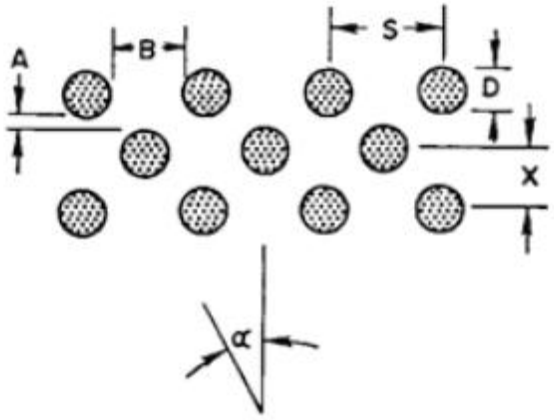

Figure 3.11: Pin fin configuration used by Metzger et al. (1984a)

The heat transfer performance of a pin fin configuration depends on different parameters like the pin fin height, arrangement of the pin fins, cross section of the pin fins etc. For the current set of Reynolds number, a staggered array of pin fin with $\alpha = 0°$, studied by Metzger et al. (1984a), produced the highest Thermal Performance Factor. Results in the current study are compared with the results of Metzger et al. (1984a) with $\alpha = 0°$, S/D = 2.5, X/D=2.5, A/D = 0.5 and B/D = 1.5.

Figure 3.12 shows the comparison of average Nu ratio of the two lattice structures with the pin fin configuration used by Metzger et al. (1984a). It is seen that the pin fins produce the lowest value of heat transfer enhancement (Nu/Nu_0 values in the range 1.7-2.2). This is followed by the four-inlet-channel lattice which shows Nu/Nu_0 values in the range 1.9-2.8. The two-inlet-channel lattice performs the best in terms of heat transfer enhancement (Nu/Nu_0 values in the range 2.1-3.4). For the same Reynolds number, the two entry channel lattice shows higher heat transfer coefficient than the other one. This is consistent with the findings of Bunker (2004), who also observed that the channel lattice configuration with fewer sub-channels enhances the heat transfer coefficient more. It is also to be noted the heat transfer enhancement value reported here

is based on the heat transfer on the lattice supporting straight and inclined walls only. In the current tests the lattice structures are made of low thermal conductivity plastics. In actual gas turbine airfoils they are cast integrated with the internal cooling channels of the airfoil. They can provide additional heat transfer area compared to the pin fins and can greatly enhance the overall heat transfer from the airfoil surface.

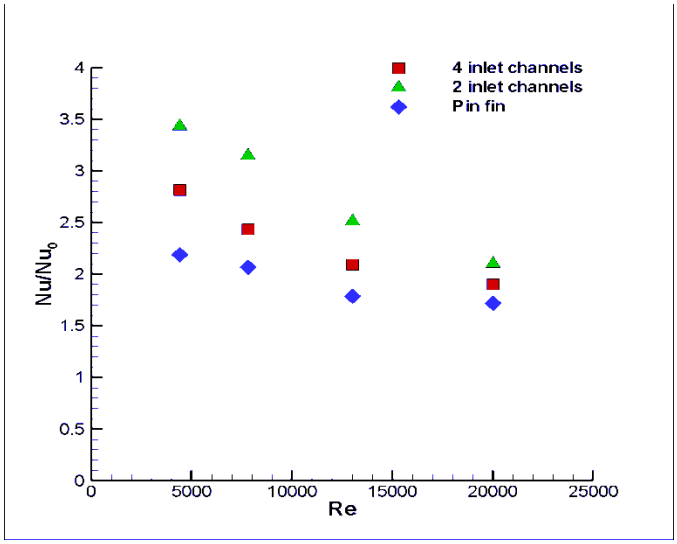

Figure 3.12: Comparison of the lattice structures with the pin fin (Metzger et al., 1984a)

Pressure data: Pressure data are taken at selected pressure tap points following a channel from the inlet to the exit. The pressure tap points for the four-inlet-channel and two-inlet-channel lattice are shown in Fig. 3.13. The pressure drop profile is plotted following a flow channel with the flow turnings. In other words, the pressure taps are located on both sides of the lattice structure and follow a particular flow channel on both sides. The white pressure taps are the pressure taps on one side of the lattice (straight side) and the grey pressure taps are on the other side of the lattice.

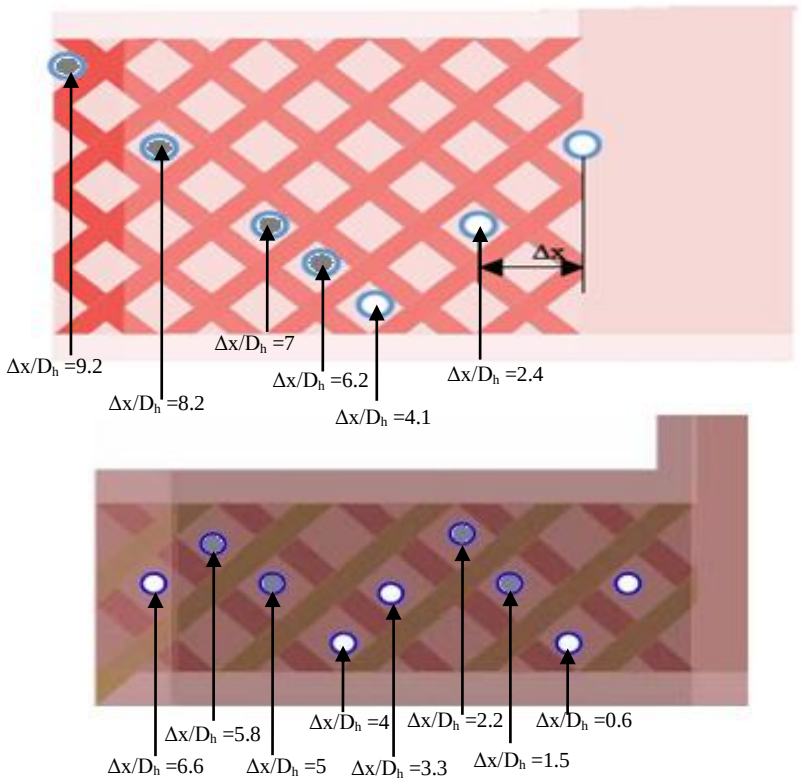

Figure 3.13: Pressure taps for the lattice structures

A non-dimensional pressure drop p* is plotted with the distance Δx in Fig. 3.14 for the four and two-inlet-channel lattice structures, where Δx is the distance between two pressure tap locations as shown in Fig. 3.13.

$$p^* = \frac{\Delta p}{\frac{1}{2}\rho V_{in}^{\ 2}} \qquad (3.2)$$

where V_{in} is the velocity at the entry sub-channel of the lattice at inlet. The first pressure tap point at the inlet is chosen as the reference point. For all the subsequent points, pressure drop is calculated with reference to that point and Δx is the distance, measured in the streamwise direction, between the corresponding pressure tap and the inlet pressure tap.

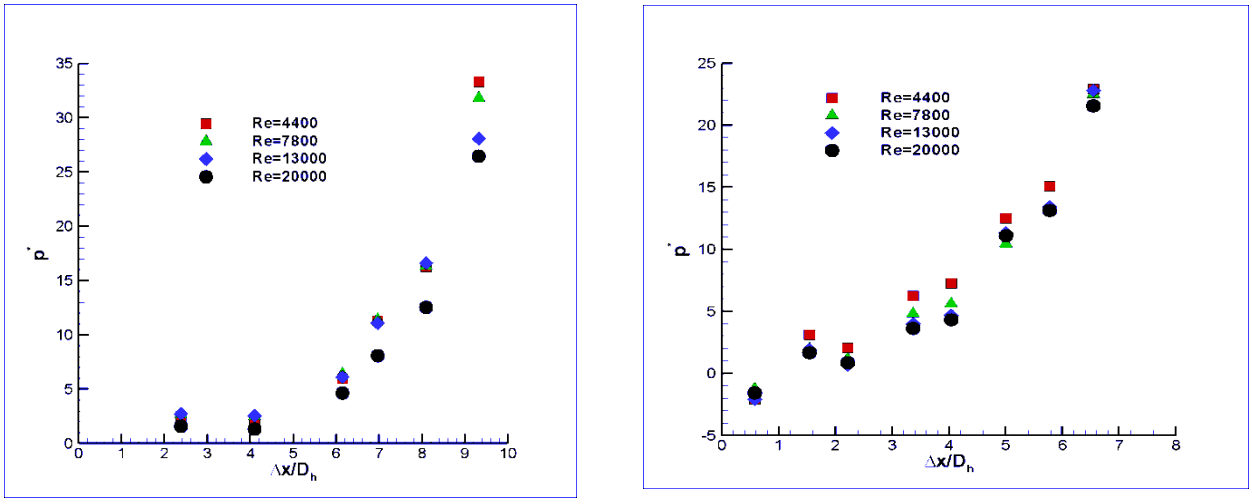

(a) (b)

Figure 3.14: Detailed pressure drop following a channel; (a) Four-inlet-channel lattice, (b) Two-inlet-channel lattice

The majority of the pressure drop occurs because of the flow turning from one side of the test section to the other side and due to the vortex formed due to the interaction of the straight channel flow and cross flow coming from the other side. This is observed in Fig. 3.14 by the slope of the pressure curve which is high across the pressure taps around each turn and relatively flat in the sub-channel itself. There is a slight pressure recovery at the impingement region ($\Delta x/D_h$ =4.1 for the four inlet channel lattice and $\Delta x/D_h$ =0.6, 2.2 for the two inlet channel lattice). This is due to the formation of a stagnation zone in the impingement region which produces some pressure recovery. This trend of pressure recovery close to the wall is consistent with the findings of Bunker (2004). For the other impingement regions in case of the two-inlet-channel lattice ($\Delta x/D_h$ =4, 5.8), there is no measurable pressure recovery. After the flow turn the pressure drop increases steeply for all the channels. The four-inlet-channel shows higher pressure drop than the two-inlet-channel lattice.

Thermal Performance Factor (TPF) calculation: Though the heat transfer enhancement produced by the lattice structures are higher than the pin fins, the pressure drop involved in the

lattice structures are also pretty high because of multiple flow turnings and cross flow interactions. Therefore to see the relative importance of the lattice structures in actual gas turbine airfoils, there is a need to compare both heat transfer enhancement and pressure drop. Thermal Performance Factor (TPF) is a parameter which describes the overall cooling efficiency. It is a measure of heat transfer enhancement per unit of frictional drop compared to a smooth channel duct.

A non-dimensional friction factor is defined for the calculation of TPF. The pressure drop between the reference and the exit pressure tap is used as the overall pressure drop for calculation of the friction factor. The friction factor is defined as

$$f = \frac{\Delta p / 0.5\rho {V_m}^2}{4\Delta x / D_m} \qquad (3.3)$$

For the converging lattice structures, the cross section of the channel changes continuously. As a result velocity and hydraulic diameter also changes. The velocity and hydraulic diameter at the middle of the lattice structure in the streamwise direction is taken for the calculation of friction factor.

The friction factor is normalized by the Karman-Nikuradse equation (Kays and Crawford,1993).

$$f_0 = 0.046 Re^{-0.2} \qquad (3.4)$$

Thermal performance factor is calculated for both the lattice structures and it is compared with the TPF for the pin fin structure used in Metzger et al. (1984a) to understand the overall importance of the lattice structure. For the calculation of an overall thermal performance, heat transfer enhancement is compared for a constant pumping power and surface area. The thermal

performance factor (TPF) is calculated from the method used by Webb (1981), Gee and Webb (1980) and is defined as

$$TPF = \frac{Nu/Nu_0}{f/f_0^{\frac{1}{3}}} \qquad (3.5)$$

Figure 3.15 shows the TPF comparison of the lattice structures with the pin fin configuration. It is seen that the four channel lattice structure performs poorly among all. For the lower Reynolds number cases, the two-inlet-channel lattice performs the best. As we go to the higher Reynolds number, the pin fin performs better than the two lattice structures.

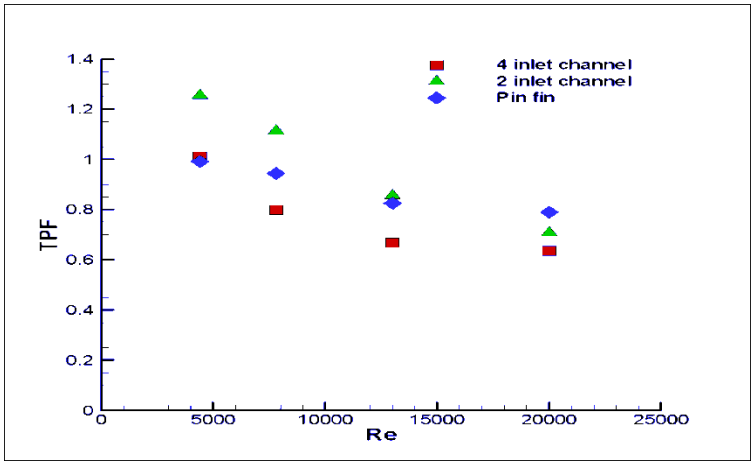

Figure 3.15: TPF comparison with pin fins (Metzger et al., 1984a)

3.1.3 Conclusions: Two converging lattice structures suitable for use in the trailing edge region of a gas turbine airfoil are tested. Detailed heat transfer and pressure drop measurements are taken and performances of the structures are compared with standard pin fin structures in trailing edge applications. The conclusions from the study are:

1) Introduction of the lattice structures enhances heat transfer significantly. The maximum enhancement is observed in the impingement region, where the flow turns from one sub-channel to the other, and peak heat transfer enhancement values close to 8 are observed.

2) Averaged heat transfer enhancements are in the range of 2-3.5 with the higher enhancements at the lower Re, and these values are all higher than that of the pin fin published data that fall in the range of 1.7-2.2.
3) Pressure drop increases in the streamwise direction except in impingement region close to the wall, where a pressure recovery is observed. The turning of flow from one side of the lattice to the other side, and the interaction with the cross flow produces high pressure drop in the sub-channel.
4) The TPF for the four-inlet-channel lattice is low compared to the other two structures. TPF for the two-inlet-channel lattice is comparable and sometimes higher (for Re =4400-7800) than the TPF obtained from the pin fins. In the current study, the lattice structure was made of a material of low thermal conductivity. In actual gas turbine blades the lattice structure can be cast integrated with the internal cooling channel of the blade. So it can provide additional fin area compared to a conventional pin fin channel, resulting in higher heat transfer from the hot blade to the internal coolant flow. Thus, a lattice structure with a lower number of inlet channels can be a good alternative to pin fins in trailing edge applications particularly since they provide high levels of structural support and additional heat transfer surface area.

3.2 Constant cross section lattice structure

3.2.1 Geometry: A constant cross section lattice with some exit bleed holes is tested. This lattice structure also has two inlet channels. The channel in which it is inserted is a 7:1 AR channel. A schematic of the straight lattice test section is shown in Fig. 3.16. The test section is made using 0.006 m thick Acrylic sheets. The lattice core is made of the polymer material ABS.

The lattice is 0.402 m in length and 0.084 m in width. The height of the total lattice is 0.012 m with each set of sub-channels occupying half the height. Each sub-channel has a cross section of 0.0297 m by 0.006 m. These dimensions are used for the calculation of hydraulic diameter D_h of the sub-channel and used throughout the paper. The ribs of the lattice are placed at an angle 45° to the flow.

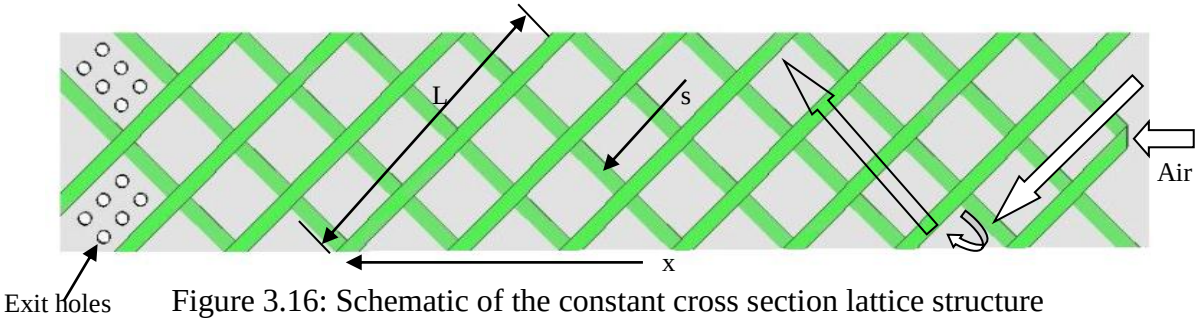

Figure 3.16: Schematic of the constant cross section lattice structure

Air from the lab air supply comes through a diverging plenum and enters the test section straight. The diverging plenum is 0.254 m in length and changes cross section from a 0.03175 m square cross section to a cross section of 0.012 m by 0.084 m, which is the test section dimension. A straight entrance length of 0.0762 m is provided downstream of the diverging plenum before the flow encounters the lattice structure. Air enters the lattice through the entry sub-channels at the inlet, then follows the serpentine pathway and finally exits through the bleed holes located at the exit of the test section. It is assumed that the flow enters the lattice structure and gets evenly distributed among the four entry sub-channels (two on each side) of the lattice structure. Each of the bleed holes has a diameter of 0.0048 m.

3.2.2 Results: Tests were done for Re=5500, Re= 9000, Re=14500 and Re= 22000, based on the hydraulic diameter of the sub-channel. The side with the bleed holes is referred to as front side while the other side is referred to as the back side. Figure 3.17 shows the heat transfer

enhancement contour plots of the constant cross section lattice for Re = 5500. The other Reynolds numbers show similar results with different Nu/Nu_0 values.

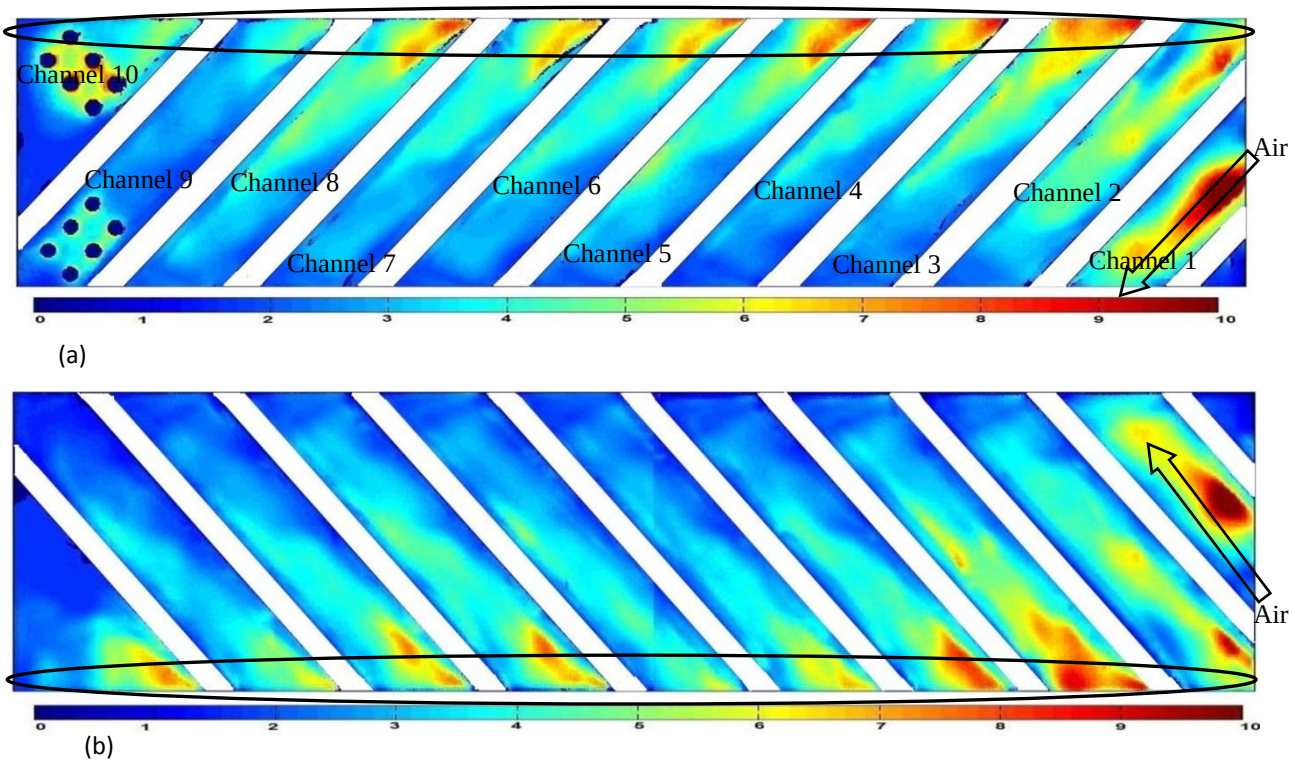

Figure 3.17: Nu/Nu_0 contour plot (Re=5500) a) Front side b) Back side

The sub-channels are termed as channel 1-10 from the inlet to the exit of the lattice as shown in Fig. 3.17a. From the contour plots it can be seen that the heat transfer coefficient is highest at the impingement zones (shown by the encircled zones in Fig. 3.17a) and at the entry channel. After the flow passes from the inlet of a sub-channel (say a sub-channel on the front side) to the exit, it hits the bounding sidewall and has to flow towards the other side of the lattice (i.e. a sub-channel on the back side). The flow takes a 90° turn and impinges on the wall at the entrance of a sub-channel on the other side of the lattice. Impingement is associated with a formation of a stagnation point, and the thin viscous sub-layer at the stagnation zone contributes to very high heat transfer coefficient values. The heat transfer coefficient decreases with increased distance

from the stagnation point. After impinging on the inlet wall of a sub-channel the flow progresses through the sub-channel and the heat transfer coefficient decreases as the flow progresses towards the exit of a sub-channel. On the front side walls the channels 3-8 show quite similar trends and magnitudes. While the trends are quite similar, the peak magnitudes decay from about 8-9 at the lowest Reynolds number to about 3-4 at the highest Reynolds number. Also for the front side, the heat transfer coefficient is high close to the exit bleed holes, but for the back side, the region opposite from the bleed holes produce the lowest Nu/Nu_0 values in the whole lattice structure. The Nu/Nu_0 values close to the bleed hole regions are typically of the order of (but lower than) the impingement Nu/Nu_0 values.

The line plots of heat transfer enhancement factors along the sub-channels are shown in Figs. 3.18-3.21. In these plots the Nu/Nu_0 ratio is plotted along the length of the sub-channel from the impingement location towards the end of the sub-channel where the flow turns toward the sub-channel along the opposite wall. Figure 3.18 shows that for each sub-channel, the highest values are close to the beginning of the channel where the flow is impinging or entering the channel. In general, the earlier channels (e.g., 1, 2, 3) have the highest Nu ratios (as high as 6-8) while the channels at the end (e.g., 9 and 10) have the lowest values (in the range of 2-3). It can be seen that channels 9 and 10 show a large peak corresponding to the coolant extraction holes through which the flow exits. In Figure 3.19, corresponding to the back side without the coolant extraction holes, while the general trends are similar as for the front side, the increase in Nusselt numbers corresponding to the coolant extraction in channels 9 and 10 are not observed. For channel 10, the combined effect of impingement and flow extraction increases the Nu/Nu_0 values to about 6 (Re =5500) whereas flow extraction only (channel 9) increases the Nu/Nu_0 values to about 4. Channel 1 (the entry channel) on both walls has high Nusselt number ratios, of the order

of 9 at a Re=5500 (Fig. 3.18) and decreasing to 5-6 at a Re=14500 (Fig. 3.20). Channels 2-8 have somewhat similar trends and values, and in general, they all fall within a narrow band of values. Channels 9 and 10 have the bleed holes, and exhibit high Nu ratios in the vicinity of the bleed holes. For channel 9, an increase in the Nu ratio is observed past s/L of 0.75 on the front wall (the back wall without the bleed holes shows no effect). At the lower Reynolds number, this bleed-induced heat transfer increase can be significant (nearly a doubling of the Nu ratio at Re of 5500), while at the higher Reynolds number this enhancement is reduced. For channel 10, the bleed holes occupy much of the channel, and the corresponding Nu ratios are higher in this region. A combination of impingement and bleed hole extraction increases the Nu/Nu_0 values close to 6 (Re=5500) in the bleed hole vicinity. Beyond this (s/L>0.6-0.65), there is a sharp drop off in the Nu ratio, as seen in Fig. 3.18. Figures 3.20 and 3.21 show the Nusselt number ratios at the higher Reynolds number of 14500. There appears to be a considerable Reynolds number effect with the Nu ratios now in the range of 4-5 at its highest and about 1.5-2 at its lowest. However, the channel-to-channel differences in Nu between inlet and exit is reduced for both the front and back surfaces at the higher Re. However, the peak associated with coolant extraction in channels 9 and 10 is still present and distinct.

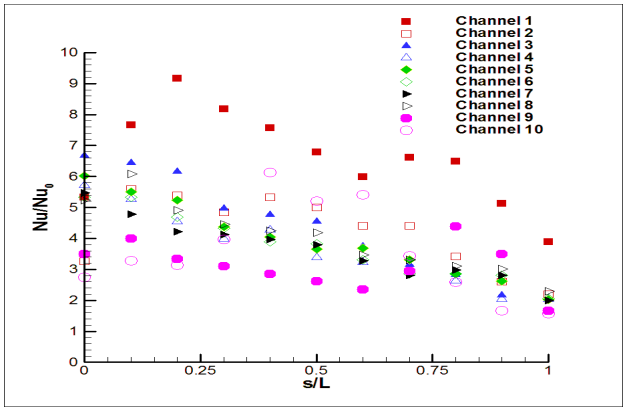

Figure 3.18: Nu/Nu_0 line plot for the front side (Re =5500)

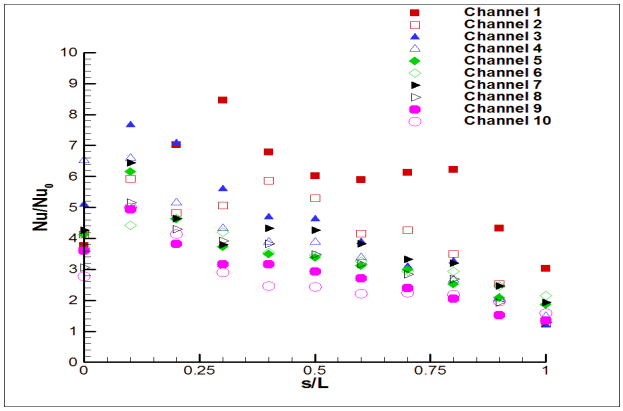

Figure 3.19: Nu/Nu_0 line plot for the back side (Re =5500)

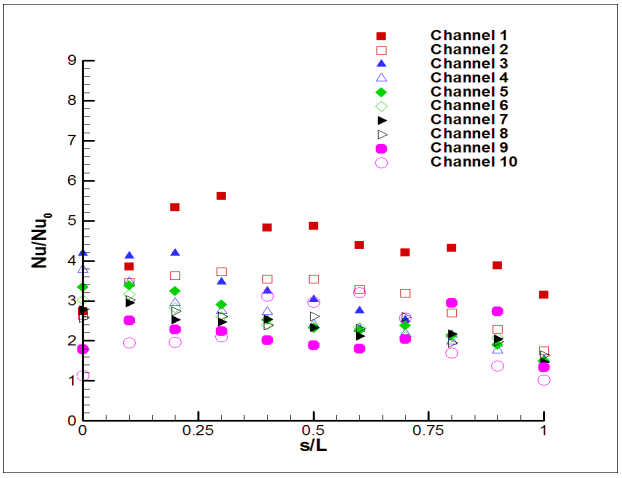

Figure 3.20: Nu/Nu_0 line plot for the front side (Re =14500)

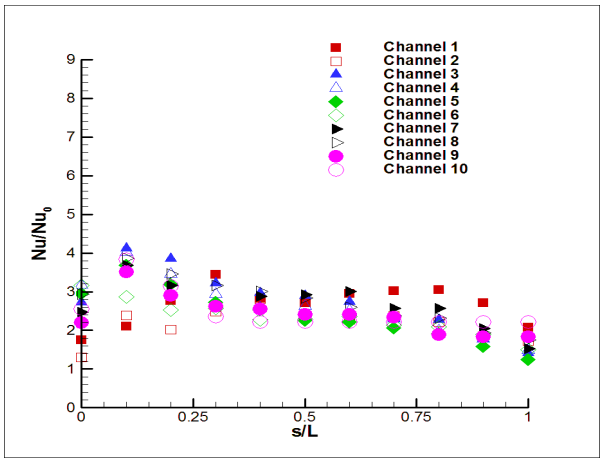

Figure 3.21: Nu/Nu_0 line plot for the back side (Re =14500)

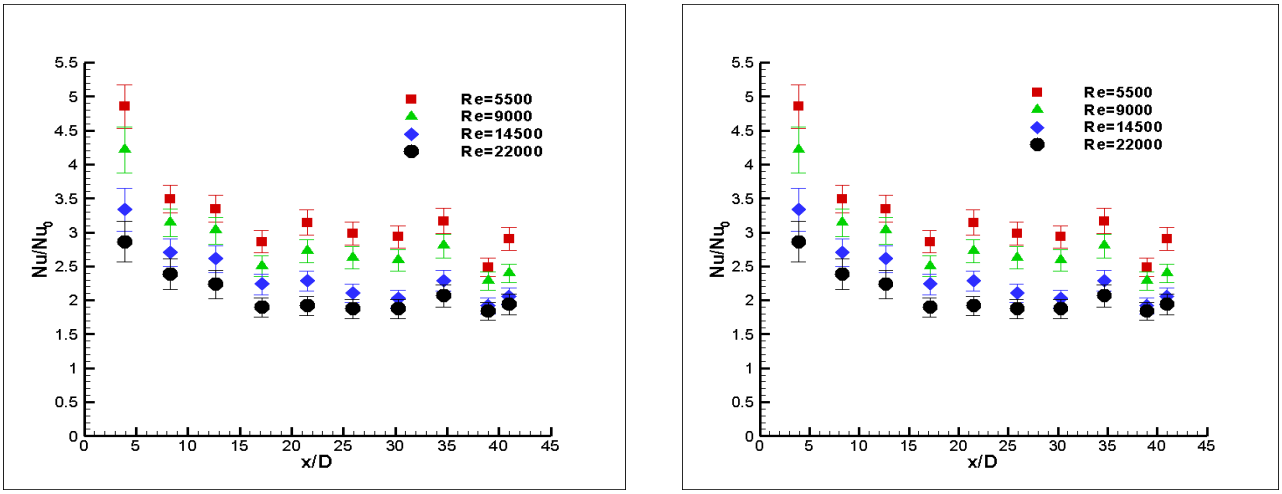

(a) (b)

Figure 3.22: Channel averaged Nu/Nu_0 plot for a) Front side b) Back side

The channel-averaged Nu enhancement factor plotted with respect to the axial direction (x) is shown in Figs. 3.22 for the front and back side. Here, the Nusselt number in each sub-channel is averaged and is plotted with respect to the sub-channel midpoint x value. For the channels with bleed holes, (channel 9 and 10) the bleed hole area is not considered at the time of averaging. In general, the front and back sides exhibit similar Nu ratios, with the Nu ratios decreasing from the

entry regions (values in the range of 2.5-4.5 with the higher values at the lower Re) and reaching asymptotic values in the range of 2-3 around x/D of 15.

The overall heat transfer enhancement factor (averaged over the front and back side wall area) for the whole test section is shown in Fig. 3.23 as a function of the Re. At Re=5500, these ratios are in the neighborhood of 3, while at the higher Re value of 22000, the enhancement ratio drops to about 2.25. It may be argued that these numbers are typically of the same range as commonly used 45 degree rib turbulators (Park et al., 1992). Also, for the current study, the lattice structure was made of low thermal conductivity plastic. Typically in a gas turbine blade internal cooling channel, they will be cast integrated with the internal cooling channel. Thus, the lattice structure can provide additional heat transfer area compared to a standard turbulated channel (ribs or pin fins). Further, as seen in Fig. 3.22, the entry effects are generally limited to an x/D of about 10-15, where D here represents the sub-channel dimension. This entry effect is lower compared to a typical turbulated channel.

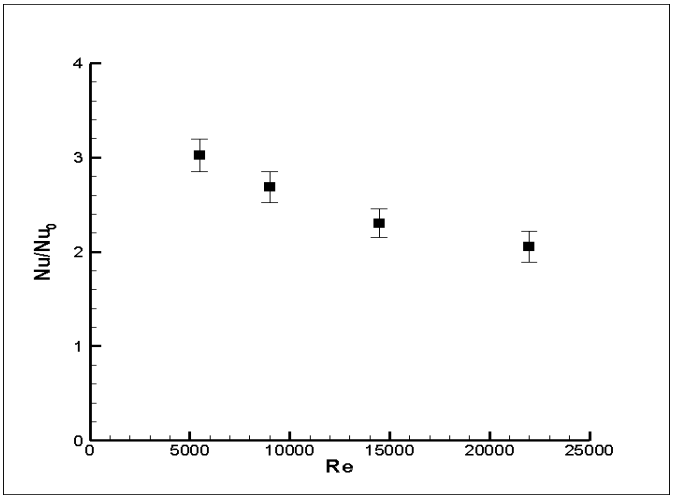

Figure 3.23: Overall heat transfer enhancement factor for the whole test section

Pressure drop between the inlet and exit of the lattice is taken for calculation of the thermal performance factor. The friction factor is defined by Equation 3.3 and is normalized by a friction factor for smooth pipe flow as defined by Equation 3.4. The friction factor ratio is plotted in Fig. 3.24. The friction factor increases with increasing Reynolds number.

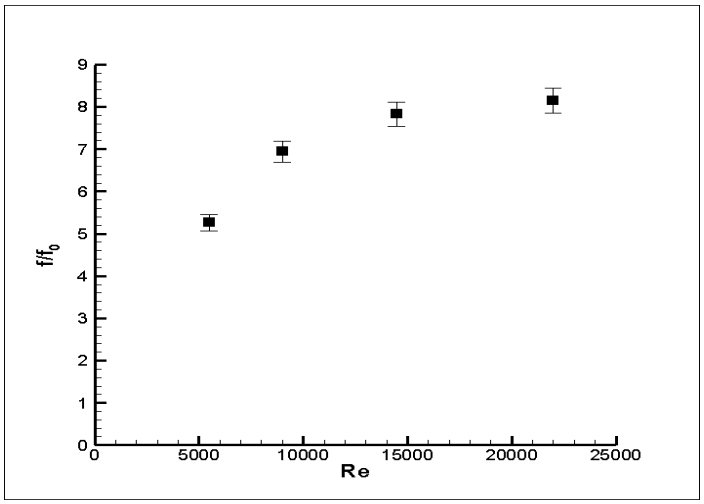

Figure 3.24: Friction factor ratio for different Re

The TPF is defined by Equation 3.5. It is a measure of heat transfer enhancement per unit of frictional drop compared to a smooth channel duct. The thermal performance factors for different Reynolds numbers are shown in Fig. 3.25, and are in the range of 1-1.65. The TPF values are in the same range as a conventional 45 degree rib turbulator channel, which showed values of 1.3-1.4 at a range of Re=10000-20000 (Wright et al., 2004) for a 4:1 AR channel. The lattice structure, due to its multiple twists and turns produces significantly higher pressure drop than a ribbed channel. In this study, the full pressure drop due to the lattice structure has been taken into account but the full heat transfer enhancement potential of the lattice structure has not been realized as the lattice was made of a low thermal conductivity plastic. This study provides the information of heat transfer distribution through a lattice channel with bleed holes. Future study

is needed for documenting the full potential of the lattice structure with both the test section and lattice made of conductive material.

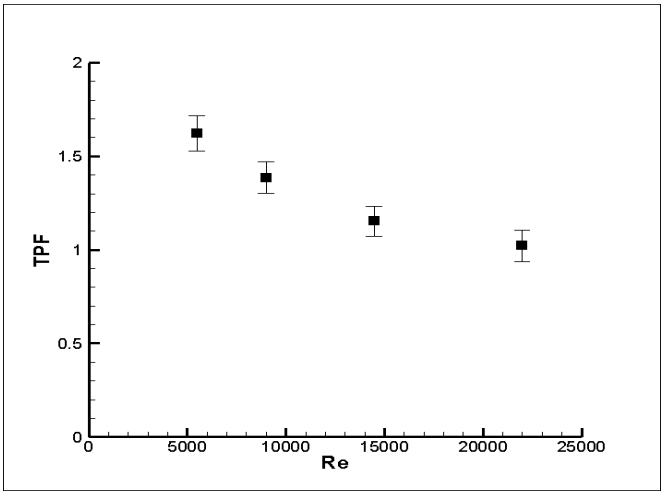

Figure 3.25: Thermal Performance Factor for different Re

3.2.3 Conclusions: Measurements of heat transfer and pressure drop are reported for a lattice channel with constant cross section and bleed holes on one wall close to the exit. Data was taken at four Reynolds number ranging from 5500 to 22000. The following were the main observations of the study.

1. High heat transfer coefficients are obtained in the impingement regions with peak Nusselt number ratios (Nu/Nu_0) in the range of 7-8 at Re=5500 and 3-4 at Re=22000.

2. The Nu distributions reached constant values within 10 sub-channel hydraulic diameters and remained nearly constant over the rest of the channel.

3. High heat transfer coefficients (Nu/Nu_0 in the range of 3-4 at Re =5500) were observed in the vicinity of the bleed holes for channel 9 indicating that coolant extraction favorably

improved the Nusselt numbers. A combination of impingement and bleed hole extraction increased the Nu/Nu_0 values to about 6 (Re =5500) for the channel 10 extraction holes.

4. Channel-averaged Nu/Nu_0 was in the range of 2-3, and thermal performance factors in the range of 1-1.6 with the higher Nu and TPF occurring at the lower Reynolds number.

3.3 Concluding remarks

Three lattice structures were tested for a range of Reynolds number. The heat transfer enhancements and the TPF are summarized in table 3.3 below.

Table 3.3: Comparison of the Lattice Structures Used

	Constant cross section	Converging, 2 inlet channel	Converging, 4 inlet channel
Nu/Nu_0	2.25-3.1	2.1-3.4	1.9-2.8
TPF	1-1.65	0.7-1.25	0.63-1

It is clear that lattice channels with lesser number of channels have higher efficiency. For the same number of channels, a constant cross section lattice performs better than a converging cross section lattice. Flow turning has significant effect on the heat transfer enhancement of the lattice structures for the converging cases. It is seen that the flow turning produces the lowest values of heat transfer enhancement for the entry channels in the converging cases. Straight inlet produces highest values of heat transfer enhancement for the constant cross section lattice because of flow development at the inlet.

CHAPTER 4: BEND GEOMETRY RESULTS

4.1 Numerical simulation

4.1.1 Geometries used during the test: A total of ten geometries with a square cross-section were tested numerically including the baseline case of a traditional U-Bend. The schematic of the various geometries tested are shown in Fig. 4.1.

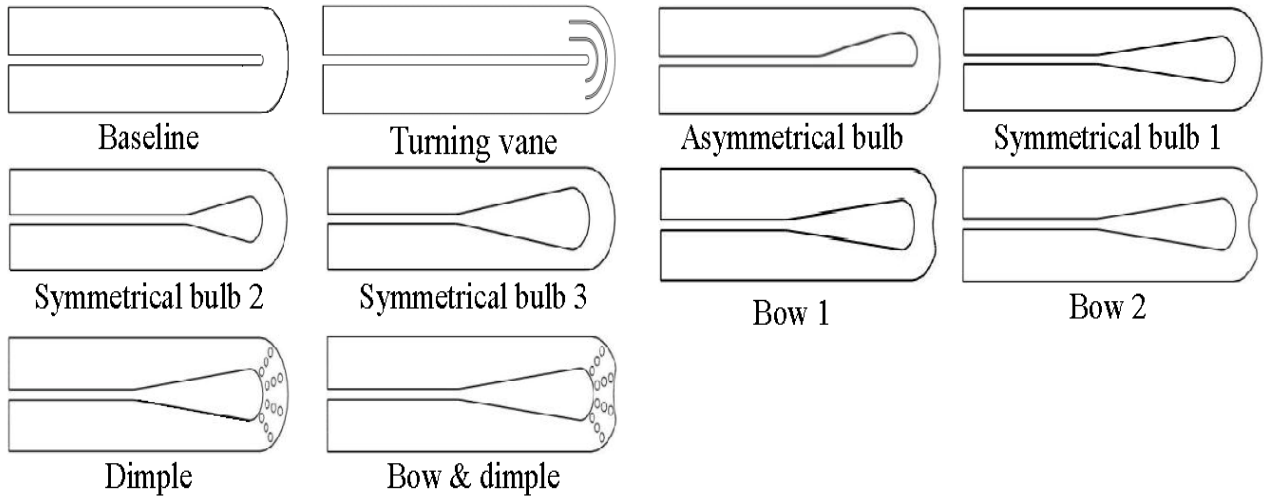

Figure 4.1: Schematic of the bend geometries studied

The various geometrical configurations for the bend mostly centered around the idea of using a bulb that could eliminate the separation past the sharp corner. A turning vane design with two turning vanes at the bend region is also studied. Both asymmetrical and symmetrical bulbs were studied, and bulb thickness and length varied. The idea of adding a bow to the outer turn is new and was explored as a means for locally accelerating the flow to increase the heat transfer. Finally the effect of adding dimples in the bend was studied as a means of increasing heat transfer with minimal pressure drop penalty.

The specific test section chosen for the study is a square cross section with H=W=0.03048 m. The baseline test section was 10W long upstream of the bend. The bend radius was chosen so that a uniform bend clearance of W is achieved. The constant divider wall thickness was chosen to be 0.2W. For the turning vane case, the flow channel is divided into three passages, each with a width of 0.3W. The vanes are made 0.05W thick and extended to a length of 0.625W in the second pass. The shape and size of the asymmetrical bulb was obtained from the computed dimensions of a separation bubble formed at the tip of the divider wall for the baseline simulation. The asymmetrical bulb started at a distance of 6.3W from the test section entrance and the maximum thickness of the bulb was 0.48W measured from the divider wall. Since the separation bubble contributes to the bulk of pressure drop, it was thought that eliminating the separation bubble would improve the performance of the two-pass channel significantly. For the symmetrical bulb 1 and 2 the bulb radius was the same and equal to 0.5W. The bulb length of the symmetrical bulb 1 was 5W and for the symmetrical bulb 2, it was 3W. The symmetrical bulb 3 had the same length as symmetrical bulb 1 but its radius was 0.667W. Different dimensions of symmetrical bulb were tried and it was found that the symmetrical bulb 1 provided the highest thermal performance without any flow separation. So bulb 1 was used for the subsequent modified geometries. For the bow cases, bow shapes area contractions were introduce in the bend region to accelerate flow and increase heat transfer in the bend region. For the bow 1 case, the minimal bend clearance was 0.75W and for the bow 2 case, the minimal bend clearance was further reduced to 0.5W. The dimple depth δ was chosen as 1.524×10^{-3} m and the dimple print diameter D was chosen as 5.08×10^{-3} m so that δ/D ratio was 0.3. Burgess and Ligrani (2005) showed that a δ/D ratio of 0.3 provides the highest performance. The dimple spacing in an array was 8.128×10^{-3} m. The arrays of dimples were arranged in a radial manner with an angle of 30°

between two arrays. For the case with both bow and dimples, the bow geometry is the same as the bow 1 case.

4.1.2 Grid generation and computational setup: Tetrahedral unstructured meshes were generated using ANSYS ICEM CFD. The grid topology for the baseline geometry is shown in Fig. 4.2.

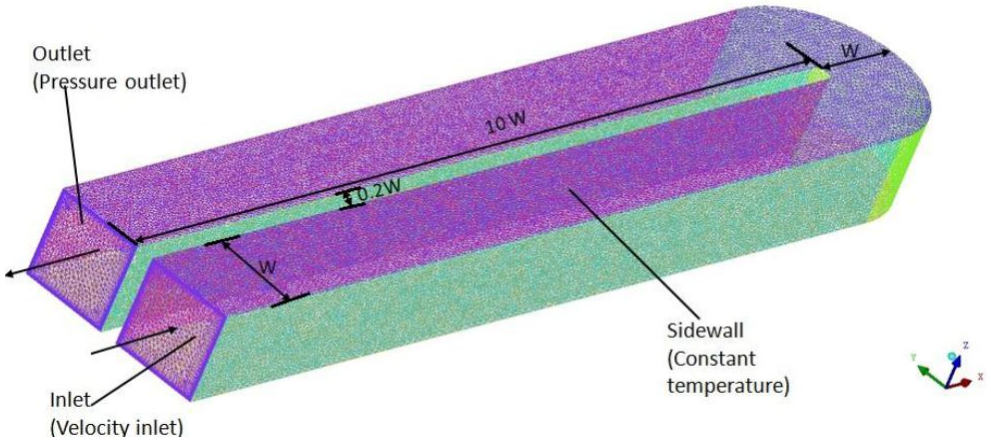

Figure 4.2: Tetrahedral mesh with prism layers (baseline geometry)

The main flow volume was meshed using tetrahedral meshes and the near wall was meshed using prism layers. RANS equations were solved using a low-Re realizable k-ε model. To maintain the requirement of the turbulence model, a y+ value of 0.5 was chosen for the first grid point near the wall, and the near-wall region was represented by 24 prism layers that are generated close to the wall. A total number of 3.2-3.6 million cells were used for the simulations. For the dimple geometries, an additional mesh refinement with comparable mesh sizes as the near-wall prismatic layers was done near the dimple surfaces.

Previous studies by researchers have shown that the RANS formulation gives reasonable agreement with the experimental data (Schüler et al. 2011, Chen et al. 2011, Schüler et al. 2011a) and it takes much less computational time than RSM or LES. In this study, the low-Re realizable

k-ε model (Wilcox, 2006) with enhanced wall treatment was used in the commercial finite volume solver FLUENT (Fluent Inc., 2006) as a compromise between computational time and accuracy. Air was used as the working fluid. A steady state pressure based solver was used in FLUENT for the solution and pressure-velocity coupling was handled by the SIMPLE (Acharya et al., 2007) algorithm. To achieve fully developed boundary condition at the inlet of the two-pass channel, a separate simulation was run with a channel of length 15 times the hydraulic diameter. The velocity, temperature and the turbulence field obtained from this simulation was used as the inlet boundary condition to the two pass channel. Constant wall temperature of T_w=298 K was chosen for all the channel walls. The outlet boundary condition was fixed to the atmospheric pressure of P =101325 Pa. The Reynolds number based on the hydraulic diameter of the channel was 25000. Typical converged solutions were obtained after about 4000-5000 iterations. For convergence criteria, the residuals are chosen as 10^{-6} for the continuity, the momentum and the turbulence equations and 10^{-9} for the energy equation. The average heat transfer coefficient on wall was also used as an additional convergence criterion.

Data reduction: The wall heat flux and the local bulk air temperature were obtained from the numerical solution, and the heat transfer coefficient was then obtained by

$$h = {q_w}/{(T_w - T_\infty)} \qquad (4.1)$$

where q_w is the wall heat flux, T_w is the constant wall temperature and T_∞ is the mainstream air temperature. The Nusselt number is obtained from the heat transfer coefficient as

$$Nu = {hD_h}/{k} \qquad (4.2)$$

where k is the thermal conductivity of air.

To present the results, the Nusselt number was normalized using the Dittus Boelter correlation (1930).

$$Nu_0 = 0.023.Re^{0.8}.Pr^{0.4} \quad (4.3)$$

Friction factor is defined as

$$f = \frac{\Delta p / 0.5\rho V^2}{4\Delta x / D_h} \quad (4.4)$$

The friction factor is normalized by Karman-Nikuradse equation (Kays and Crawford, 1993).

$$f_0 = 0.046.Re^{-0.2} \quad (4.5)$$

The thermal performance factor is then defined with a constant pumping power assumption from the method used by Webb (1981), Gee and Webb (1980) and is defined as

$$TPF = \frac{Nu / Nu_0}{\left(f / f_0\right)^{1/3}} \quad (4.6)$$

4.1.3 Results: For all the cases studied, detailed Nu/Nu_0 contour maps along one wall, velocity contours and streamlines along the midplane, and secondary flow profile at different planes perpendicular to the main flow are presented. As metrics of interest to the designer, the overall pressure drop and heat transfer coefficient for all the geometries are shown along with the thermal performance factor.

In order to validate the simulations, the predicted results are compared with the heat transfer experimental data obtained for the baseline geometry. For the measurements, a thermochromic liquid crystal (TLC) technique is used to determine the heat transfer coefficient. Details about the

experimental procedure and the setup are provided in Saha and Acharya (2011). Figure 3 shows the average Nu/Nu_0 comparison between the measurements and the simulations.

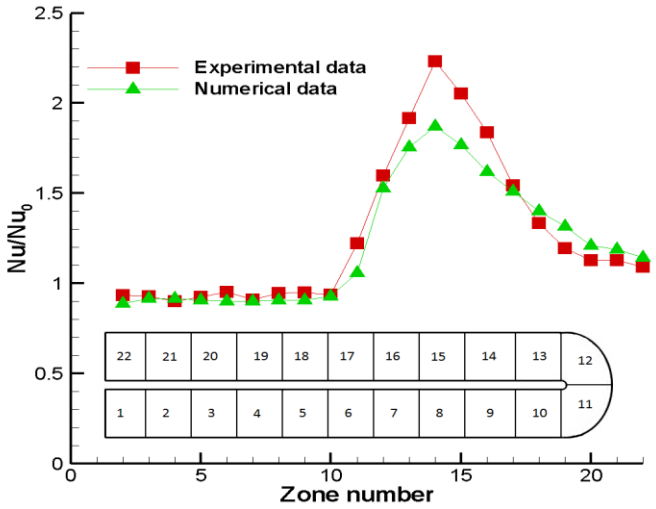

Figure 4.3: Nu/Nu_0 comparison with experimental data

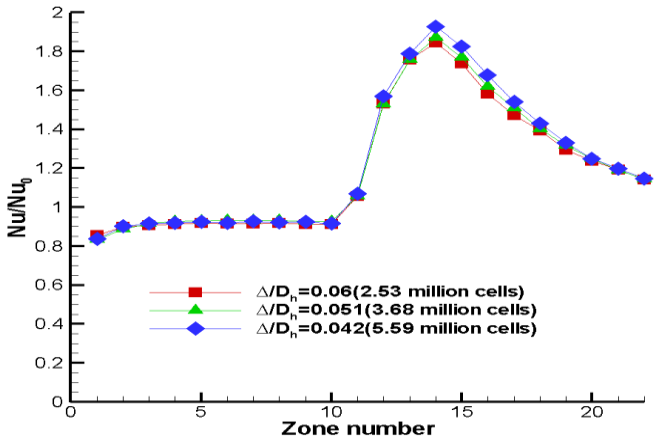

Figure 4.4: Grid independence study

The numerical value deviates from the experimental value by a maximum 16% in the impingement region downstream of the turn. Except near this peak location, the agreement at all other locations is generally excellent. A grid independent study is also performed with three different tetrahedral element sizes of maximum dimensions Δ/D_h =0.042, 0.051 and 0.06 leading to grid sizes of 5.59 million cells, 3.68 million cells and 2.53 million cells respectively. The

result of the grid independent study is shown in Fig. 4.4. It can be seen changing the tetrahedral size does not have much effect on the heat transfer on the wall (within 3%).

4.1.3.1 Baseline: The streamline profile for the baseline geometry on the symmetry plane is shown in Fig. 4.5(a). The separation bubble starts at the divider tip and the flow reattaches to the divider wall after about 3.5 times the hydraulic diameter of the channel. The height of the separation bubble is close to half the width of the channel. An impingement zone is observed close to the outer wall of the second pass. Secondary flow profiles are plotted along two planes perpendicular to the mainstream flow and shown in Figs. 4.5(b)-4.5(c).

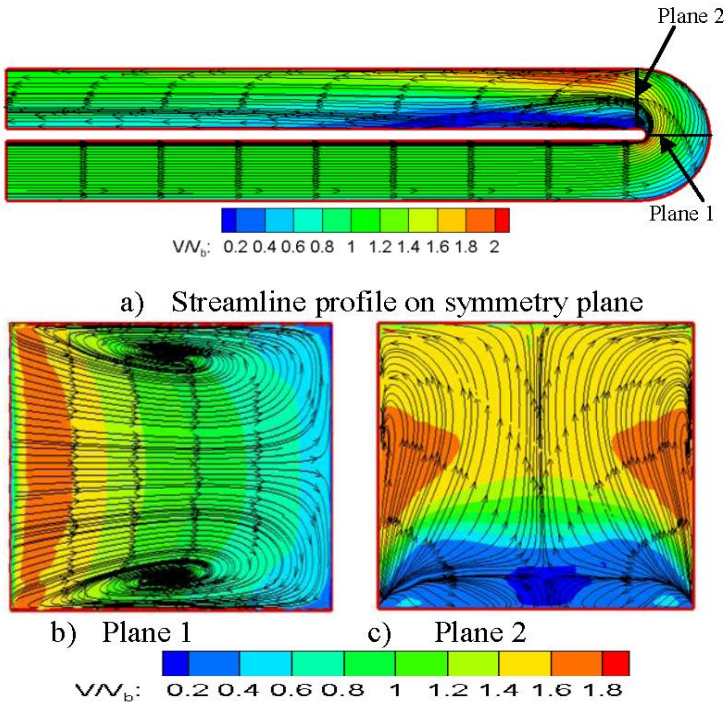

Figure 4.5: Velocity profile on different planes for baseline case

Centrifugal force is generated due to streamline curvature in the bend region which directs the fluid away from the divider wall. On the other hand the pressure on the outer wall is higher than

the pressure on the divider wall side which tries to push the fluid towards the divider wall. A combination of centrifugal force and pressure force takes the fluid from the core of the channel to the sidewalls and forms Dean type vortices (Dean, 1928). In plane 2, the centrifugal forces drive most of the fluid towards the outer wall resulting in high velocity (and therefore high heat transfer) close to the outer wall. The heat transfer enhancement contour map is shown in Fig. 4.6.

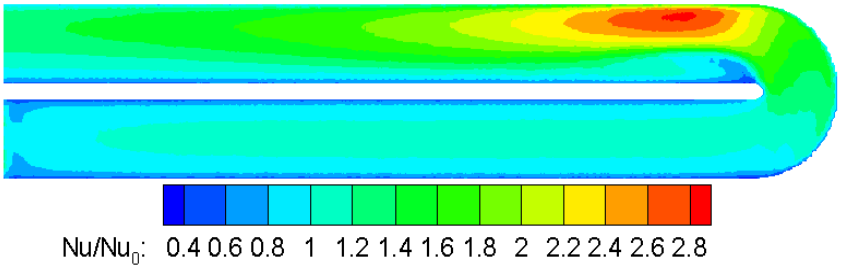

Figure 4.6: Nu/Nu_0 contour map for the baseline case

The heat transfer coefficient is highest (Nu/Nu_0~3) at the outer wall of the second bend due to the high velocities and the associated impingement effect. The presence of the separation bubble at the divider wall tip reduces the heat transfer coefficient close to the divider wall significantly for several hydraulic diameters from the divider wall tip.

4.1.3.2 Turning vanes: Turning vanes in the bend region avoid flow separation and reduce the pressure drop significantly. The streamline profile on the symmetry plane is shown in Fig. 4.7 (a). While the separation bubble is not totally eliminated, the height of the separation bubble is only about 0.06 W. Flow impingement on the outer wall of the second pass is absent and the flow profile is smooth throughout the second pass. The secondary flow velocity (as seen in Figs. 4.7(b)-(c)) in the bend region is much smaller than the baseline case. The strength of the Dean type vortices are reduced in both Plane 1 and Plane 2 which results in lower heat transfer coefficient values for the sidewall.

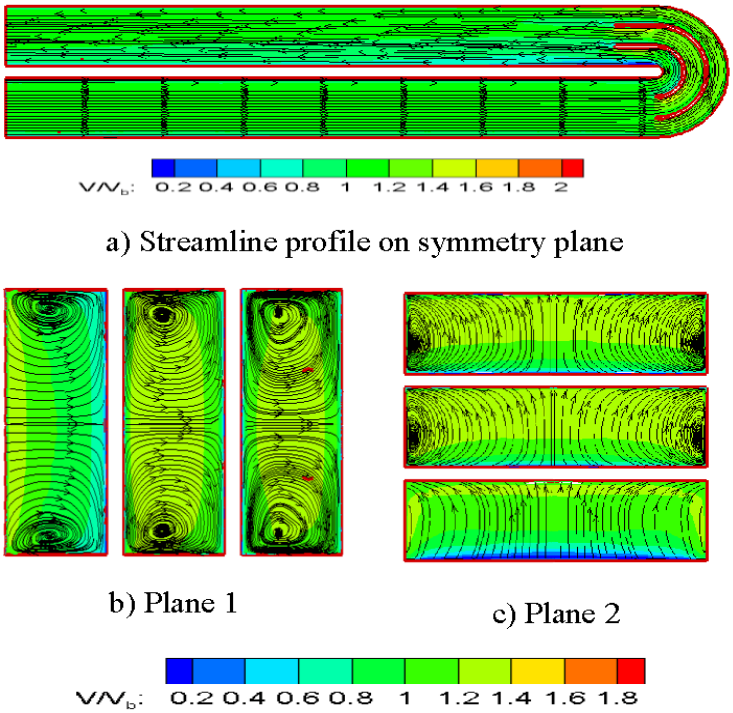

Figure 4.7: Velocity profiles on different planes for turning vane case

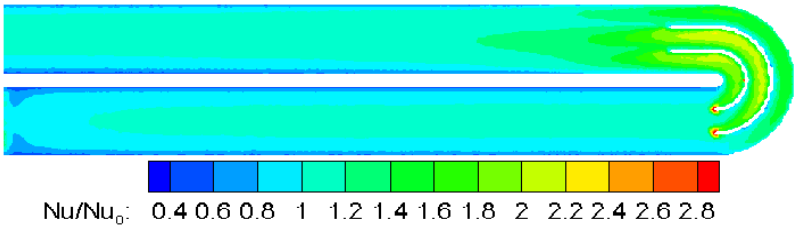

Figure 4.8: Nu/Nu_0 contour map for the turning vane case

Figure 4.8 shows the heat transfer enhancement contour map for the turning vane case. Impingement at the 1st pass turning vane tip raises the localized Nu/Nu_0 values to about 3 over a small region. Outer bend of the turning vanes produce Nu/Nu_0 values close to 2. Impingement zone heat transfer enhancement is completely absent in the second pass and the Nu/Nu_0 values are uniform throughout the width of the passage. Averaged Nu/Nu_0 values are 14-30% lower throughout the second pass compared to the baseline case.

4.1.3.3 Asymmetrical bulb: The asymmetrical bulb was studied to eliminate the portion from the flow channel which contained the separation bubble for the baseline case.

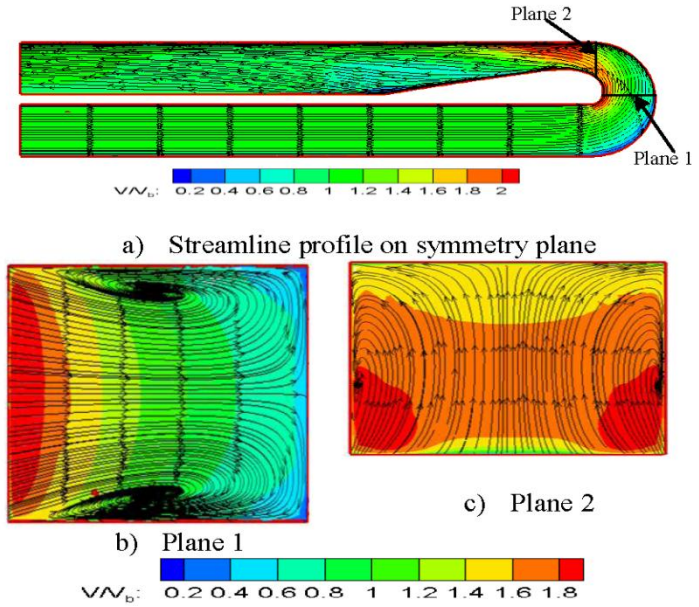

Figure 4.9: Velocity profile on different planes for asymmetrical bulb case

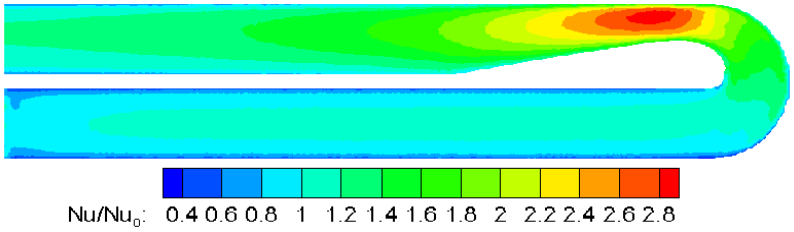

Figure 4.10: Nu/Nu_0 contour map for the asymmetrical bulb case

From Fig. 4.9 (a), it can be seen that the separation bubble has been eliminated and the flow profile is smooth after the bend. As seen in Fig. 4.10, the low heat transfer zone associated with the baseline separation past the divider wall tip in the second pass is now no longer present for the asymmetrical bulb. The streamwise velocity in the impingement zone (V/V_b ~2) is about the same for the asymmetrical bulb and baseline case, and therefore high heat transfer coefficients (Nu/Nu_0~3) are observed in Fig. 4.10 along the outer wall of the bend at the beginning of second

pass. The secondary flow velocity profile is almost the same as the baseline case on plane 1 (Fig. 4.9(b)) with little influence of the asymmetrical bulb downstream. It can be seen from the secondary velocity profile on plane 2 (Fig. 4.9(c)) that since the effect of the separation bubble is completely eliminated, and the cross-sectional area reduced in the bulb region, the secondary flow velocity is higher compared to the baseline case. Thus, overall heat transfer values in the second pass are slightly enhanced (about 3%) compared to the baseline case.

4.1.3.4 Symmetrical bulbs: For the symmetrical bulbs 1 and 2, the maximum bulb diameter was the same as the channel width. For bulb 3, the radius is 0.667W and the channel has a narrower cross-section at the entry and exit into the bend region. The length of the bulb was same for bulb 1 and bulb 3 (5W), but for bulb 2 it was 3W.

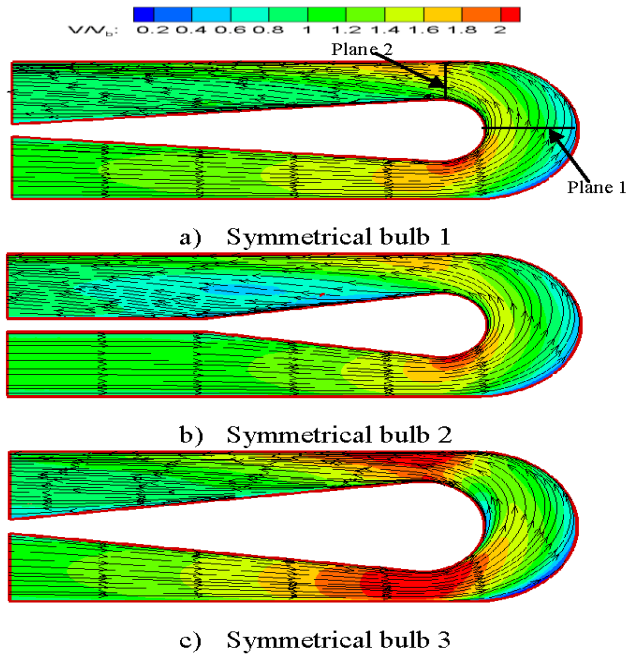

Figure 4.11: Streamline profile on symmetry plane for the symmetrical bulbs

The streamwise velocity profile on the symmetry plane for the three symmetrical bulb cases are shown in Fig. 4.11. For clarity, the contour plots are only shown from a length of 5W from inlet

of the channel. The separation bubble is absent for all the symmetrical bulb cases and the flow profile is smooth after the bulbs (no separation). Here the impingement zone velocity for the bulb 1 and bulb 2 cases (V/V_b ~1.6) are lower than the baseline and asymmetrical bulb cases (V/V_b ~2) but the velocity in the turn region is higher due to flow-area contraction. The velocity in the impingement zone for bulb 3 (V/V_b ~2.4) is higher than the other two bulbs and also the baseline and asymmetrical bulb cases.

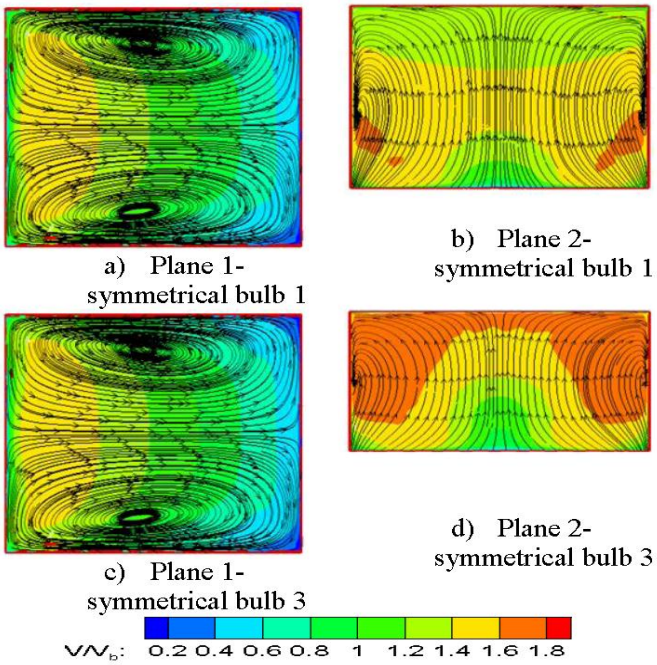

Figure 4.12: Secondary velocity profile on planes perpendicular to the streamwise flow for symmetrical bulb cases

The secondary flow profiles at two different cross-sectional locations are shown in Fig. 4.12. The secondary velocity profile for bulb 1 and bulb 2 case (not shown) are same on both plane 1 and plane 2 but a slight increase in secondary flow velocity is seen for the bulb 3 case on plane 1 and a more increased secondary flow velocity is seen on plane 2 because of the reduced cross

section at plane 2. Secondary flow velocity on plane 2 for the bulb 1 and bulb 2 cases are about 22% lower and for the bulb 3 case it is 11% lower than the asymmetrical bulb case.

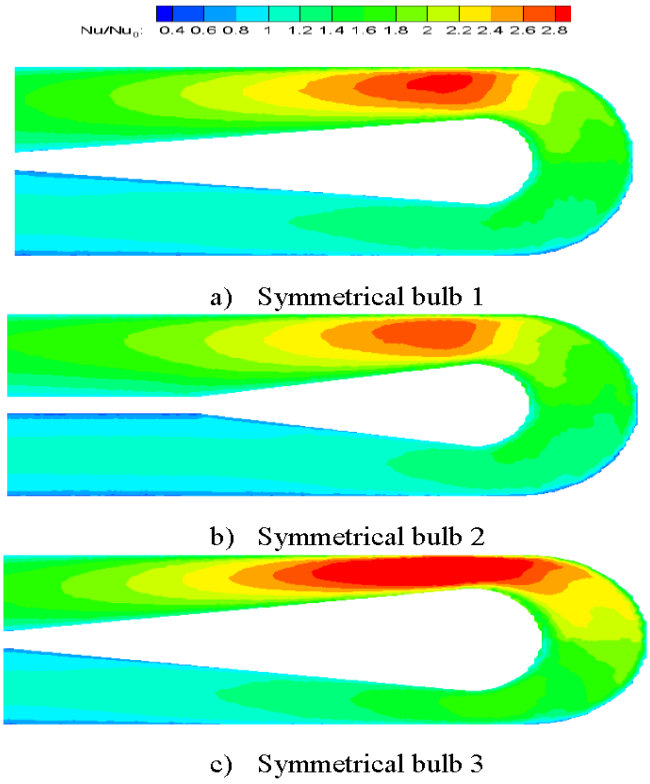

Figure 4.13: Nu/Nu_0 contour map for the symmetrical bulb case

The heat transfer enhancement contour map for all the symmetrical bulb cases are shown in Fig. 4.13. The symmetrical bulb 1 case shows slightly lower heat transfer enhancement values than the asymmetrical bulb case in the second pass (due to the larger flow cross-section for the symmetrical bulb), but the heat transfer is increased in the 1st pass due to the area convergence and in the bend compared to the asymmetrical bulb case. The bulb 2 case shows lower Nu/Nu_0 values in the impingement region but Nu/Nu_0 values are roughly the same level elsewhere. The bulb 3 case shows significant increase in Nu/Nu_0 values in the bend region and in the

impingement zone after the bend (about 20% greater Nu value right after the turn compared to the other symmetrical bulb cases). This can be attributed to the higher level of flow convergence just after the turn which leads to increase in impingement zone velocity and heat transfer.

4.1.3.5 Bow design: The purpose of the bow design is to introduce a converging-diverging nozzle-type effect to the main flow to increase the velocity and heat transfer in the bend-throat region. Two different bow geometries are tested. For bow 1, the turn clearance is reduced by 25%, and for bow 2, the turn clearance is reduced by 50% at plane 1(Fig. 4.11(a)). The streamwise velocity profiles on the symmetry planes are shown in Fig. 4.14.

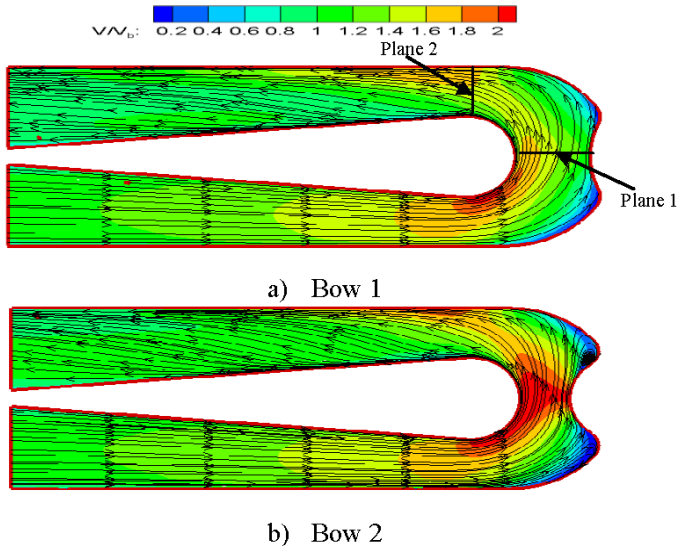

Figure 4.14: Streamline profile on symmetry plane for the bow design cases

The streamwise velocity in the bend region does not increase to a great extent for the bow 1 case except along the inner bend, and the streamwise velocity is low before and after the bow shape due to flow separation before and after the flow contraction. As noted, a slight increase in streamwise velocity is seen at the lowest cross section of the bend due to flow convergence at this section. The bow 2 design increases the streamwise velocity significantly at the lowest cross

section of the bend. Flow separation and recirculation areas are seen before and after the flow contraction. The secondary flow velocity profiles at cross sectional planes are shown in Fig. 4.15.

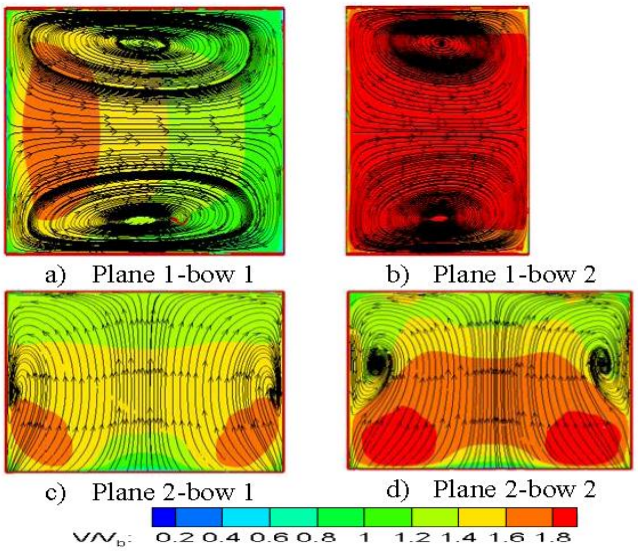

Figure 4.15: Secondary velocity profile on planes perpendicular to the streamwise flow for bow design

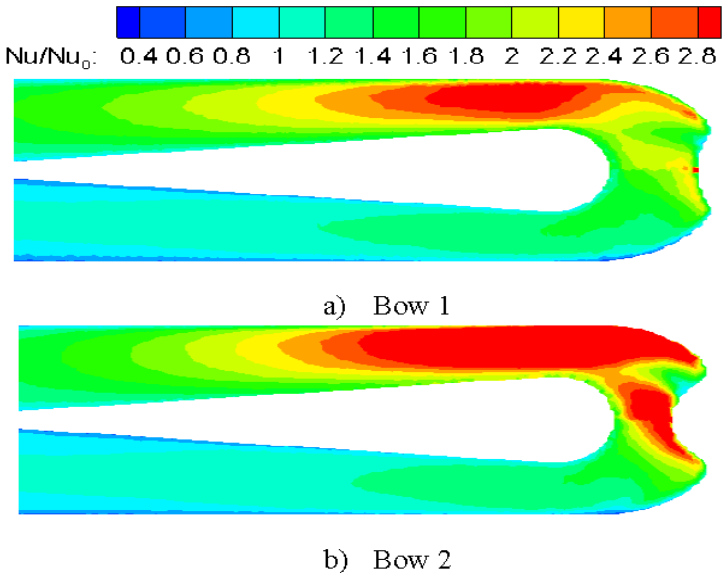

Figure 4.16: Nu/Nu_0 contour map for the bow design cases

For the bow 1 case, the secondary flow velocity goes up to 1.6 V_b and is about 14% higher compared to the bulb 1 case. The secondary flow velocity on plane 1 for the bow 2 case is significantly higher and goes up to 2.2 V_b close to the divider wall, while on plane 2 it goes up to 1.8 V_b close to the divider wall and the velocity close to the sidewalls is higher compared to the bulb 1 case by about 12-14%.

The heat transfer enhancement contour maps for the two bow designs are shown in Fig. 16. For the bow 1 case, the Nu/Nu_0 values go up to 3 in the impingement region. In the bend region itself, the heat transfer enhancement values go up to 40% higher compared to the bulb 1 case. For the bow 2 case, impingement zone Nu/Nu_0 goes up to a value of 4.4. The bend region heat transfer enhancement is almost double the values compared to the symmetrical bulb 1 case. The heat transfer enhancement for the bow 2 case is higher compared to the bulb 1 case till the end of the bulb region.

4.1.3.6 Dimple design: The idea behind using dimple in the bend region is to promote localized eddies close to the sidewall so that the heat transfer coefficient on the sidewall increases without affecting the main bulk flow field. Dimple geometries are known to increase heat transfer moderately with little increase in pressure drop across a flow channel. Radial arrays of dimples are placed at an angle of 30° on both sidewalls in the bend region. The streamline profile on the symmetry plane of the dimple geometry is the same as the symmetrical bulb 1 case and it is not affected by the dimple produced secondary flows close to the sidewalls.

Figure 4.17 shows the Nu/Nu_0 contour map with the dimpled wall. In the dimples and close to the dimples, the Nu/Nu_0 values can go up to 4. The impingement zone heat transfer is not much affected by the presence of the dimples. The secondary profile at various cross flow locations are

shown in Fig. 4.18 where they are also compared with the secondary profiles at corresponding locations in the symmetrical bulb 1 case.

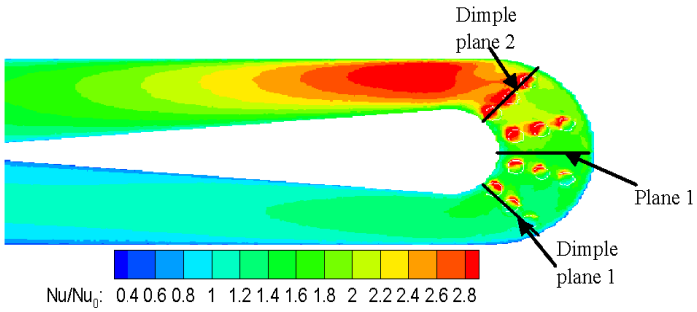

Figure 4.17: Nu/Nu_0 contour map for the dimple case

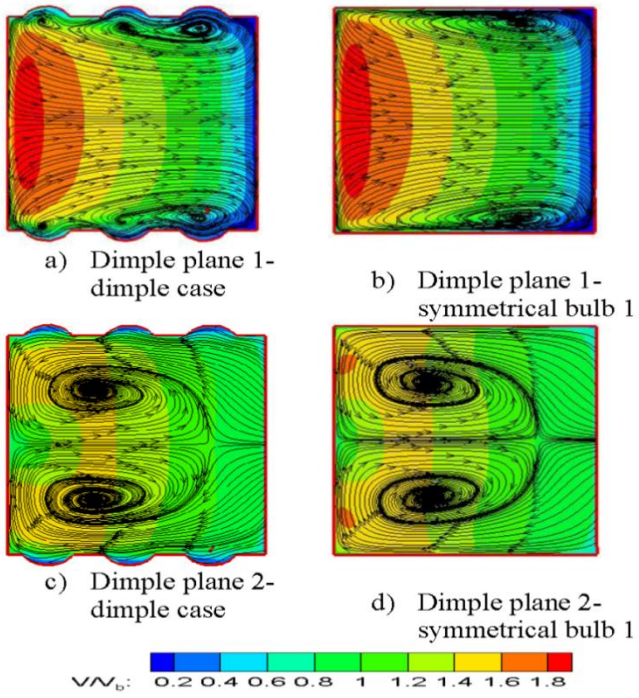

Figure 4.18: Comparison of secondary velocity profile with dimple case and without dimple case

It can be seen that the main secondary flow is not at all affected by the introduction of the dimples except in a very small region close to the dimples. The dimples produce localized circulations which increase the heat transfer close to the dimple but do not affect the overall

flowfield. Secondary velocity profile at any other cross location for the dimple case is the same as the bulb 1 case.

4.1.3.7 Dimple & bow combined design: For the dimple design, local high heat transfer enhancement values were obtained in the bend region and the bow design increases the Nu/Nu_0 values as well due to flow convergence. The goal is to combine these two advantageous features to increase Nu/Nu_0 values significantly without increasing the pressure drop too much. Dimple configuration is the same as the previous dimple case and the bow configuration is the same as Bow 1. The Nu/Nu_0 contour map is shown in Fig. 4.19. The dimples increase the heat transfer enhancement more in the bend region compared to the bow design in other areas surrounding the dimples. In the dimple regions the Nu/Nu_0 values go as high as 4.6. The secondary velocity profiles for this case (not shown) at dimple plane 1 & 2 (as shown in Fig.4.17) is the same as the bow 1 case except close to the dimples.

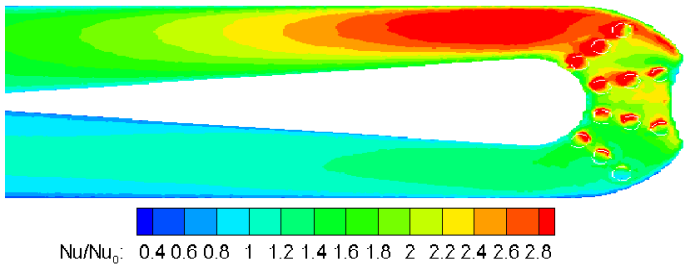

Figure 4.19: Nu/Nu_0 contour map for the bow & dimple case

4.1.3.8 Averaged heat transfer enhancement: Zone averaged heat transfer enhancement is shown in Fig. 4.20. Each of the zonal segments is $1D_h$ long in streamwise direction. The bulb starts from zone 6 for the symmetrical bulb 1 case, and from zone 8 for the symmetrical bulb 2 case.

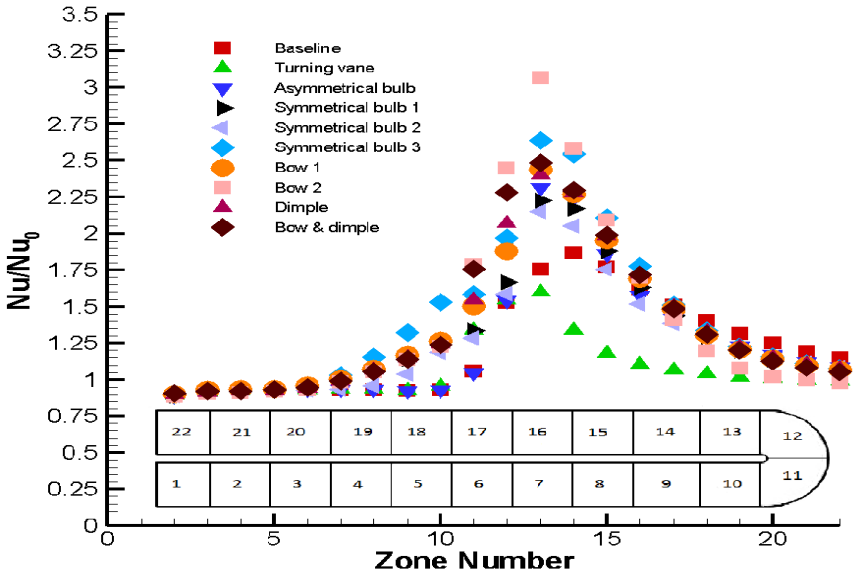

Figure 4.20: Zone averaged Nu/Nu_0 for all the configurations

The turning vane geometry reduces the heat transfer coefficient throughout the 2nd pass compared to the other cases. Just after the bend (zones 14-15), Nu/Nu_0 values are about 30% lower compared to the baseline case. For all the geometries with the symmetrical bulb 1, the averaged Nu/Nu_0 values just before the turn (zone 10) goes up to a value that is 33% higher compared to the baseline case. The bend region heat transfer for bulb 1 case is about 15% higher than the baseline, and in the impingement region (zone 13-14) it is about 21% higher compared to the baseline case. After the end of bulb in the second pass (zone 18) the average Nu/Nu_0 values are up to 10% higher for the baseline case. The heat transfer enhancement values for the symmetrical bulb 2 case around the bend are slightly lower than the bulb 1 case. For symmetrical bulb 3, this enhancement value can reach 65% higher values compared to the baseline case, and the averaged value is about 19% higher in the bend region than the bulb 1 case. In the impingement region, the Nu/Nu_0 values are about 17% higher for the bulb 3 case compared to

the bulb 1 case. For the bow 1 case, Nu/Nu_0 is about 13% higher than the bulb 1 case in the bend region and remains slightly higher in zones 13-15 (about 4-9%). The bow 2 design shows an increase in Nu/Nu_0 of about 42% in the bend region compared to bulb 1 case and in the impingement region it is about 28% higher. With the dimples present, the bend region heat transfer goes up to 21% higher values but the impingement region heat transfer is only about 5% higher compared to bulb 1 case. With both bow and dimple present, the bend region heat transfer goes up to 35% higher values and the impingement zone heat transfer is about 8% higher compared to bulb 1 case. Thus, in the bend region bow 2 design produces the highest heat transfer enhancement followed by the bow & dimple case. The impingement zone heat transfer is also highest for the bow 2 case followed by symmetrical bulb 3 case.

4.1.3.9 Overall thermal performance: For calculation of overall thermal performance, heat transfer enhancement values are averaged from zone 6-17 and pressure drop in the flow path between zone 6 and 17 is calculated to find the overall thermal performance factor.

The averaged Nu/Nu_0, f/f_0 and TPF values for all the geometries are listed in Table 4.1. For convenience of readers, the percentage changes of the parameters for different geometries with respect to the baseline case are shown in parenthesis. The bow 2 case shows the highest heat transfer enhancement which is about 28% higher than the baseline but the pressure drop is also about 9% higher leading to a TPF increase of 24% compared to baseline case. The highest reduction in pressure drop is obtained in the case of turning vane case where a pressure drop reduction of 51% compared to the baseline case is achieved but the heat transfer enhancement for this case is the lowest among all the geometries (about 9% lower compared to baseline) leading to a TPF increase of about 13% compared to baseline. The highest TPF increase is obtained for the bow-dimple combination (increase of 41%) followed by the dimple case

(increase of 38%). The bow-dimple combination case provides comparable levels of heat transfer enhancement like the bow 2 with significantly low pressure drop.

Table 4.1: Overall performance comparison of different bend geometries studied

	Nu/Nu_0	f/f_0	TPF
Baseline	1.29	4.52	0.78
Turning vane	1.15(-11 %)	2.20(-51%)	0.88(13%)
Asymmetrical bulb	1.32(2%)	2.59(-43%)	0.96(23%)
Symmetrical bulb 1	1.46(13%)	2.70(-40%)	1.04(33%)
Symmetrical bulb 2	1.38(7%)	2.50(-45%)	1.01(29%)
Symmetrical bulb 3	1.63(26%)	4.27(-5%)	1.00(28%)
Bow 1	1.53(19%)	2.95(-35%)	1.07(37%)
Bow 2	1.65(28%)	4.95(9%)	0.97(24%)
Dimple	1.55(20%)	2.99(-34%)	1.08(38%)
Bow & dimple	1.62(25%)	3.19(-29%)	1.10(41%)

4.1.4 Conclusions: Heat transfer coefficients and pressure drops are numerically calculated for a two pass channel with different bend geometries. The objective of the current study is to determine the best geometry with the greatest thermal performance factor. A total of 10 geometries are studied to determine the effect of different bend geometry parameters on the overall performance of the two pass channel. The main conclusions from this study are as follows.

1) Turning vanes reduces the overall pressure drop most (about 51% compared to baseline) among all the geometries but the absence of impingement zone in the 2nd pass results in lower overall Nu/Nu_0 values, about 11% lower compared to the baseline case.
2) Adding an asymmetrical bulb based on the shape of the separation bubble at the divider wall tip in the second pass reduces the overall pressure drop by about 43%, with a modest heat transfer enhancement that is due primarily to the removal of the low heat transfer zone in the separation bubble.
3) Adding a symmetrical bulb to the divider wall also removes the separation bubble from the divider wall tip. Highest pressure drop reduction is obtained with the bulb with shortest length (symmetrical bulb 2) where a pressure drop reduction of 45% is achieved. In terms of heat transfer enhancement, the bulb with higher bulb thickness (symmetrical bulb 3) delivers the best results producing about 26% increase in averaged Nu/Nu_0 values but the pressure drop reductions are not as significant (only a reduction of 5%) compared the other symmetrical bulb cases. Symmetrical bulb 1 gives the highest thermal performance which is about 33% higher than the baseline case.
4) Adding a bow shape to the bend region has the effect of increasing the bend region heat transfer enhancement significantly and also increases the overall heat transfer enhancement. The bow shape with the higher flow blockage in the bend region (bow 2) produces the highest heat transfer enhancement amongst all the geometries (28% increase compared to the baseline), but for this case the pressure drop is even higher than the baseline case. The bow 1 design seems to be a better option as it produces a 19% increase in Nu/Nu_0 and about 35% reduction in pressure drop leading to a increase in TPF of about 37% compared to the baseline case.

5) Addition of dimples in the bend is effective in increasing the bend region heat transfer significantly without adding much pressure drop penalty. The bend region heat transfer for the dimple geometries are only second best to the bow 2 geometry with significantly lower pressure drop. The bow-dimple combination provides the highest TPF amongst all the geometries which is about 41% higher than the baseline case.

4.2 Experimental study on down selected geometries from numerical simulation

4.2.1 Geometries: For the experimental study, the down selected geometries are (1) the symmetrical bulb with length 5W and radius 0.5W and (2) the bow with minimal bend clearance of 0.75W. In this paper, measurements of pressure drop and detailed heat transfer coefficient values with the transient liquid crystal technique are obtained for four Reynolds number ($10000<Re<55000$). The goal is to examine if the bend geometry modifications can increase the overall TPF in the bend region, and to report on the magnitude of this increase. The test section chosen for study is a square cross section with H =W = 0.03048 m. Two modifications of the bend geometry are studied (Fig. 4.21) and they are compared with a standard U-bend which is chosen as the baseline. The baseline test section is 10W long upstream of the bend. The bend radius is chosen so that a uniform bend clearance of W is achieved. The constant divider wall thickness is chosen to be 0.2W. The first modified bend geometry involves a symmetrical bulb positioned at the end of the divider wall (Fig. 4.21b) to eliminate the separation bubble in the baseline geometry due to the sharp turning into the second pass. The bulb radius is 0.5W and the bulb length is 5W. A second modification is done by introducing a bow shaped area contraction on the outer bend wall (see Fig. 4.21c), opposite to the bulb region, to initially accelerate the

flow into the bend and increase the heat transfer in the bend region. The minimal bend clearance at the bend is set to 0.75W for the bow-bulb combination case. As noted earlier, the bulb and the bulb-bow geometry are selected from the numerical earlier screening study that utilized a Reynolds-averaged turbulence model. The numerical study showed that the current bulb and bulb-bow geometries produced significant improvement in TPF over the baseline case (order of 30%), but these numerical studies were done at a single Reynolds number. This experimental study extends the numerical work to a range of Reynolds numbers and examines if the improvements observed in the numerical study are achieved experimentally.

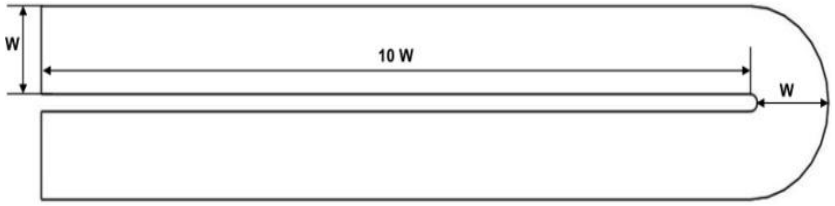

a) Baseline geometry

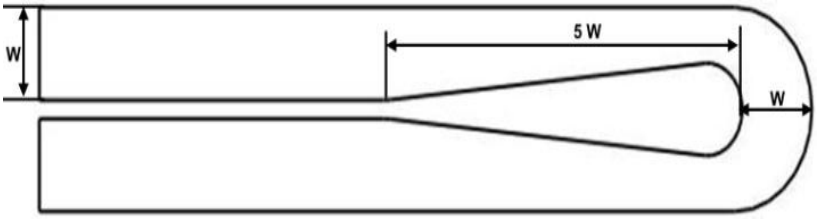

b) Symmetrical bulb

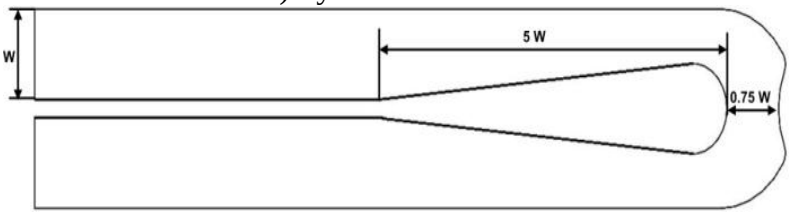

c) Bow-bulb combination

Figure 4.21: Schematic of the bend geometries

For the calculation of Reynolds number and all other temperature dependent properties, the mean mainstream air temperature during the experiment is used. The flow conditions are shown in Table 4.2 below.

Table 4.2: Flow conditions during experiments

Mean mainstream air temperature (K)	Mass flow rate (kg/s)	Re
335	0.006241	10000
320	0.014968	25000
315	0.023666	40000
310	0.032195	55000

4.2.2 Results: Detailed heat transfer coefficient contour maps are obtained for the test section on three different walls simulating the leading/trailing wall (same here since test section is non-rotating) and the 1st pass and 2nd pass sidewalls. Tests were done at Re =10000, 25000, 40000 and 55000 based on the fluid properties at the inlet of the test section. Nusselt number is obtained from the heat transfer coefficient and normalized with the Nusselt number (Nu_0) for a simple smooth channel given by the Dittus-Boelter correlation (Equation 4.3).

In presenting the results, the heat transfer enhancement contour map is shown for a single Reynolds number (Re =25000). Other Reynolds number show similar trends with different values, and therefore Reynolds number effects are presented in the averaged line plots. Flow streamlines are shown in planes perpendicular to the mainstream flow for capturing the secondary flow behavior.

4.2.2.1 Baseline: The heat transfer enhancement factor (Nu/Nu_0) contour map for the baseline case is plotted in Fig. 4.22. As the flow enters and progresses through the 1st pass, it shows fully developed Nu/Nu_0 values close to 1 over most of the channel length indicating fully developed conditions. For a fully developed turbulent flow in a smooth round pipe the Nusselt number value is represented by Eq. 4.3, and the Nu/Nu_0 ratio should be 1. The Nu/Nu_0 value of 1 in the 1st pass of the test section for the current case indicates that the flow coming in is fully

developed and also provides an additional measure of validation to the present experimental data. As the flow moves into the bend, secondary flows start generating leading to increases in Nusselt numbers seen immediately downstream of x/D_h of 10. The flow into the bend first strikes the outer wall, skirting alongside it, leading to higher heat transfer in the outer wall region (Nu/Nu_0 ~1.8) compared to the divider wall side (Nu/Nu_0 ~1.2). A recirculation zone is formed as the flow negotiates the tip of the divider wall because of the inability of the flow to take a sharp turn which reduces the Nu/Nu_0 values at the divider wall tip and around the inner corner in the second pass.

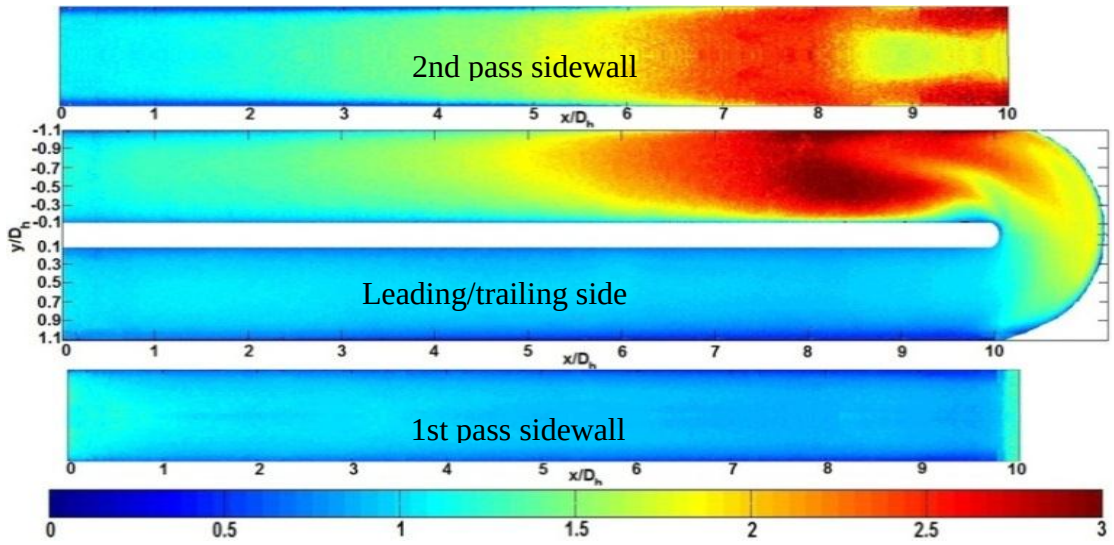

Figure 4.22: Nu/Nu_0 contour map for the baseline case (Re =25000)

This can also be seen in the secondary flow patterns in Fig.4.23b where a three-dimensional separation is evident along the inner (divider) wall in the 2nd passage. The outer flow impinges on the 2nd pass sidewall leading to high Nu/Nu_0 values (Nu/Nu_0 ~3) in the impingement region. A lower Nu region (~1.8-2) can be seen embedded in the sidewall impingement region reflecting the three dimensional nature of the secondary flow as it negotiates the bend (Fig. 4.23b). As

shown in Fig. 4b, the secondary flow patterns show streamline convergence towards the corners (higher heat transfer in the corners). Flow fully reattaches after about 2 times the hydraulic diameter from the entrance of the 2nd pass, leading to greater spatial homogeneity in the Nu/Nu_0 distributions and values close to 3 in that region. Along the leading/trailing walls, the Dean type vortices (Dean,1928) that are formed(Fig. 4.23a) and strengthened in the bend region lead to the high Nu/ Nu_0 values observed in Fig. 3 that show the peak values about 2 hydraulic diameters downstream of the far-end of the bend and then decay slowly towards the exit of the second passage. Values of Nu/Nu_0 as high as 2 are seen $5D_h$ into the second passage. In Fig.4.23a, the Dean vortex rolls do not close up along the divider wall, reflecting the flow separation developing along the divider tip and the three-dimensional nature of the flow. Studies by Kobayashi et al. (1994), Ligrani and Hedlund (1998,2004) showed that due to the effect of the curvature, large scale eddies form near the outer wall and small scale eddies form near the inner wall. The large scale eddies near the outer wall augment heat transfer in that region because of increased turbulent diffusion and as a result higher Nu/Nu_0 values are seen close to the outer wall, which is confirmed by the current experimental data.

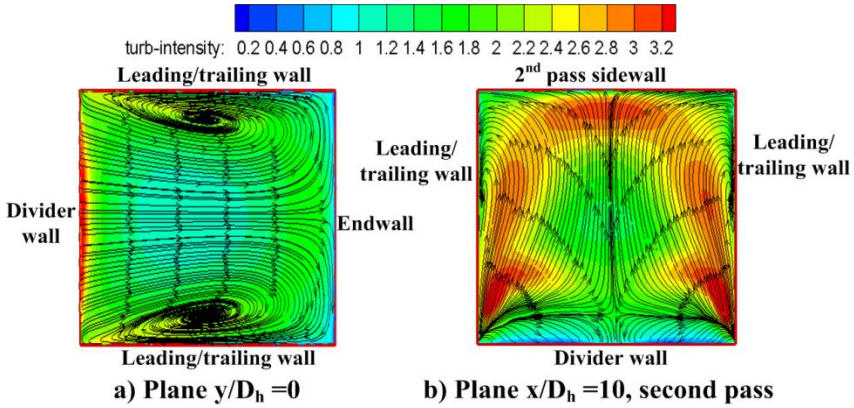

Figure 4.23: Streamline pattern at different planes perpendicular to the flow direction (baseline)

4.2.2.2 Symmetrical bulb: From the Nu/Nu_0 contour map of the symmetrical bulb case (Fig. 4.24), it can be seen that the 1st pass heat transfer coefficient values are about the same as the baseline case.

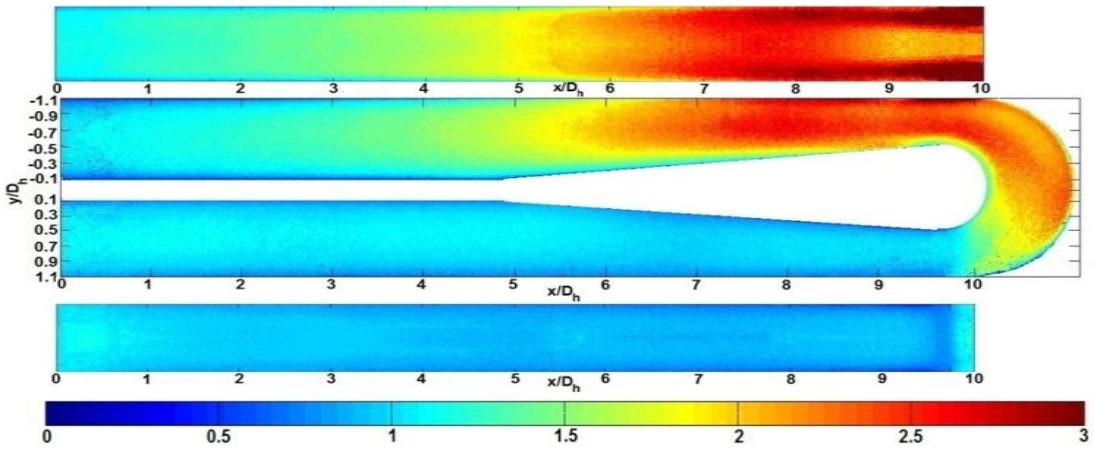

Figure 4.24: Nu/Nu_0 contour map for the symmetrical bulb case (Re =25000)

The flow velocity after the bulb increases due to the flow area contraction. As a result, higher values of Nu/Nu_0 close to 2.4 are observed throughout the bend region. The separation zone at the divider wall tip is completely absent due to the presence of the bulb, and relative to the baseline case, more uniform Nu/Nu_0 distributions are observed in the bend and in the beginning regions of the 2nd pass. An impingement zone is still present in the 2nd pass sidewall, and due to flow contraction, both the streamwise velocity and the secondary flow velocity from the divider wall side to 2nd pass sidewall is also higher, leading to higher Nu/Nu_0 values in the second pass. The 2nd pass sidewall shows higher values of Nu/Nu_0 up to about 5 D_h from the entrance of the 2nd pass. Figure 4.25 does not show a three-dimensional separation along the outer side wall of the second passage, as in the baseline case, and therefore the spanwise non-uniformity in the Nusselt numbers on the side wall is considerably lower for the bulb case relative to the baseline. However, there is a variation in the magnitude of the secondary and streamwise velocity along

the side wall with streamline convergence toward the corners still evident in Fig.4.25b. Hence, higher Nu/Nu_0 values are still seen in the corners of the sidewall in the second passage which quickly decay from the start of the passage leading to nearly spanwise uniformity within 1.5 hydraulic diameters. After the end of the bulb, Nu/Nu_0 slowly decays but the effect of the bend persists till nearly the end of the passage. At the bend mid-plane (Fig. 4.25a), the Dean vortices show fully closed streamlines in that plane, implying the absence of any separation along the inner divider wall.

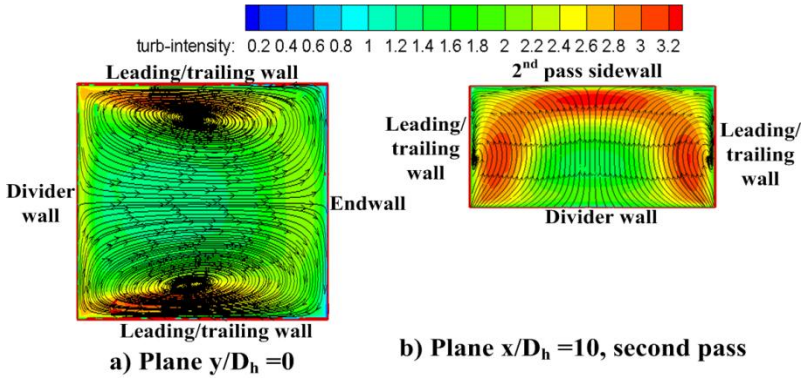

Figure 4.25: Streamline pattern at different planes perpendicular to the flow direction (symmetrical bulb)

4.2.2.3 Bow bulb combination: The Nu/Nu_0 contour map with the combination of bulb and bow is shown in Fig. 4.26.

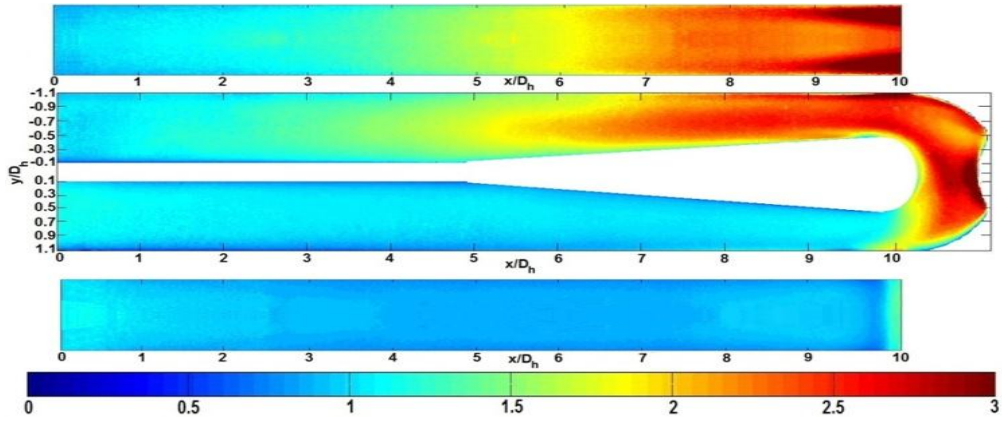

Figure 4.26: Nu/Nu_0 contour map for the bulb-bow combination case (Re =25000)

Heat transfer enhancement values in the 1st pass are in the same range as the previous two cases. In the bend and second pass regions the general trends appear to be similar to the symmetric bulb case with differences in magnitude and detail. A significant increase in Nu/Nu_0 values are seen as the flow enters the bend. Before the bow shaped contraction, Nu/Nu_0 values are in the range of 2.5 which is higher than the symmetrical bulb case by about 20%, and is reflective of the upstream effect of the bow as the flow senses the contraction and begins to accelerate even upstream of the geometric contraction. Heat transfer value is highest in the bend portion with the lowest flow area, where Nu/Nu_0 values about 3 are observed. Flow contraction and increased turbulence (as observed from the simulations) have a significant impact on increasing the overall heat transfer in the bend region. The second pass Nu/Nu_0 values are about the same for the bulb case and the bulb-bow combination case with relative uniform spanwise distributions, peak Nu/Nu_0 values of around 3 in the corners at the start of the second passage and absence of 3D separation along the outer wall (which was seen in the baseline case).

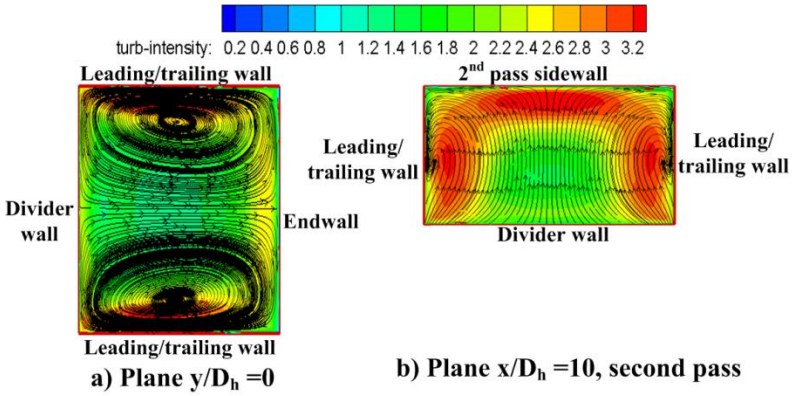

Figure 4.27: Streamline pattern at different planes perpendicular to the flow direction (bow-bulb combination)

The streamline pattern at the middle of the bend (Fig. 4.27a) and end of the bend (Fig. 4.27b) for the bow-bulb combination is similar to the symmetrical bulb case, and indicates that the positive effects of the symmetric bulb are preserved. The numerically-simulated turbulence intensity

close to the leading/trailing wall is higher than both the baseline and the symmetrical bulb case. The fully closed streamlines in Dean type vortices implies the absence of any separation along the divider wall. The Dean type vortex formation is hindered because of the curtailed space at the middle of the bend but still flow convergence in the bend region increases the streamwise velocity and heat transfer from the leading/trailing wall.

4.2.2.4 Average Nu/Nu_0 comparison: Zonal averaged heat transfer enhancement values at Re =25000 are shown in Fig. 4.28. Each of the zones is 1 D_h long in the streamwise direction as shown in Fig. 4.28. For the 1st pass, averaging is done on the 1st pass sidewall and the 1st pass of the leading/trailing side. For the 2nd pass, averaging is done on the 2nd pass leading/trailing side and the 2nd pass sidewall. Averaging is done by dividing the summation of Nu/Nu_0 values for each pixel in a given zone by the number of pixels in that zone. Each zone includes both the leading/trailing surfaces as well as the side walls.

It can be seen from the line plot that the averaged Nu/Nu_0 values in the 1st pass do not change much among different geometries until zone 9 even though the bulb starts from zone 6. The Nu/Nu_0 values start increasing from zone 10 and it is about 16% and 30% higher compared to the baseline case for the symmetrical bulb case and bow-bulb combination respectively. In the bend region (zone 11-12), the Nu/Nu_0 values can go as high as 37% and 61% compared to the baseline case for the bulb and bow-bulb combination cases. Impingement occurs in the 2nd pass and impingement zone (zone 13) Nu/Nu_0 value is about 9% and 21% higher than the baseline case for the two bend modifications. Reattachment occurs for the baseline case after the impingement zones due to the 3D flow separation along the outer endwall (Fig. 4)resulting in slightly higher Nu/Nu_0 values for the baseline cases in these zones (zone 14-15) compared to the

modified bend geometries. Second pass Nu/Nu_0 values in zones 16-22 are almost the same and reach an asymptotic value for all the geometries.

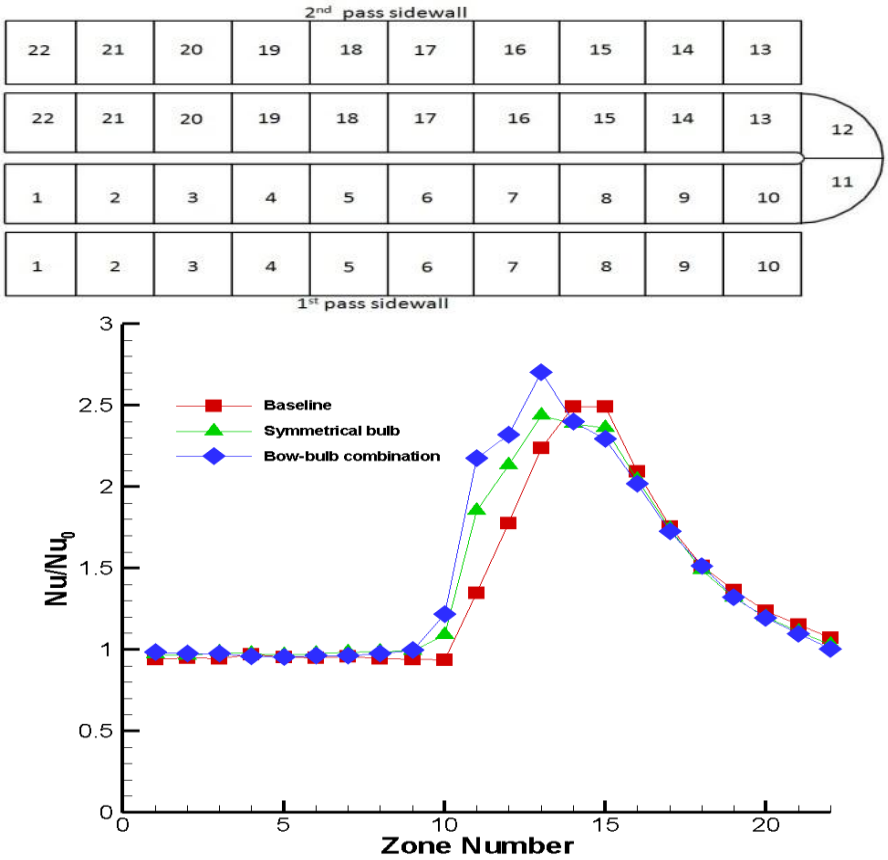

Figure 4.28: Zone averaged Nu/Nu_0 for the configurations tested (Re =25000)

4.2.2.5 Overall performance comparison: For calculation of overall performance, and assessing the bend effects with clarity, the averaged Nu/Nu_0 values are calculated for only the bulb region (zone 6-17) and pressure drop is calculated between the entrance of zone 6 and exit of zone 17. This is done because Nu/Nu_0 values before and after the bulb is almost the same for all the geometries and the goal is to see the performance of the bend modifications which only starts from zone 6 and ends at zone 17.

The friction factor is calculated from the pressure drop from zone 6 to 17. It is given by Equation 4.4. Friction factor is normalized by Equation 4.5. For calculation of a performance criterion, the

heat transfer enhancement for the geometries are compared for a constant pumping power and constant surface area. The thermal performance factor (TPF) is defined by Equation 4.6.TPF is widely considered to be a direct measure that combines both the heat transfer augmentation and pressure drop into a single performance metric.

The experimental data is compared with the numerical work at Re=25000. It is to be noted that the overall Nu/Nu_0 reported in the numerical work considered only the leading/trailing wall and for one to one comparison the averaging is done in Table 4.3 for only the leading/trailing wall. Table 4.3 shows the excellent comparison between the experimental and numerical data.

Table 4.3: Comparison between the numerical and experimental data

	Nu/Nu_0	f/f_0	TPF
Baseline-experimental	1.31	4.2	0.81
Baseline-numerical	1.29	4.52	0.78
Symmetrical bulb-experimental	1.43	2.67	1.03
Symmetrical bulb-numerical	1.46	2.70	1.04
Bow-bulb- experimental	1.55	2.85	1.09
Bow-bulb-numerical	1.53	2.95	1.07

The total averaged Nu/Nu_0 plot is shown in Fig. 4.29 as a function of the Reynolds number. Here the averaging is done for all walls including the leading/trailing wall, 1^{st} pass and 2^{nd} pass sidewalls. The heat transfer enhancement values for the symmetrical bulb case are 6-10% higher compared to the baseline case for the range of Reynolds number considered and it is about 12-19% higher for the bow-bulb combination. It should be noted that even if these increases in the averaged Nusselt numbers are modest, the bend modifications have a greater effect in the

pressure drop (discussed next), and in the absence of any negative effect on the heat transfer, result in the desired TPF enhancements.

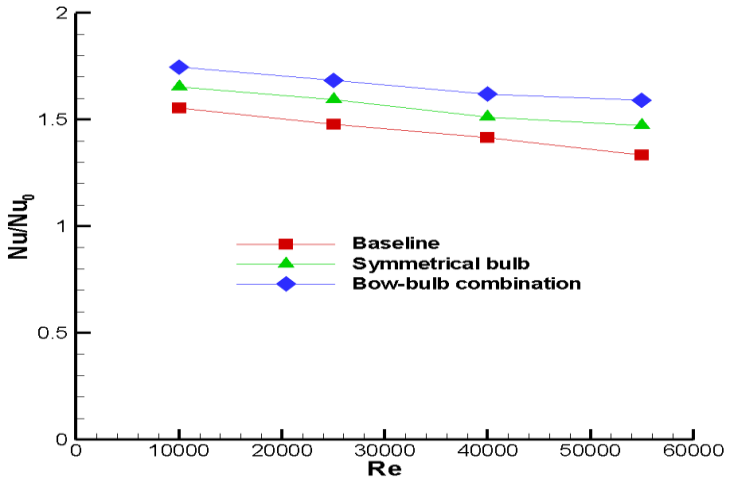

Figure 4.29: Total averaged Nu/Nu_0 comparison

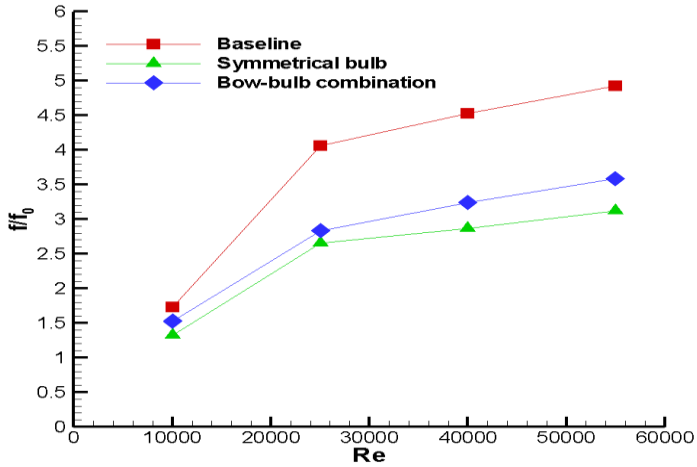

Figure 4.30: Total friction factor ratio

The friction factor ratio is plotted in Fig. 4.30 for the range Reynolds numbers considered. As expected, the baseline case shows the highest pressure drop due to the separation in the 2nd pass. The symmetrical bulb case shows the lowest pressure drop which is about 23-37% lower compared to the baseline case with the larger improvements at the higher Reynolds numbers. These improvements in the pressure drop are a direct consequence of eliminating the separation

bubble that forms in the second passage downstream of the sharp divider tip. Adding a bow at the bend increases the overall pressure drop slightly compared to the symmetrical bulb case but still the pressure drop is about 11-27% lower compared to the baseline case.

Figure 4.31 shows the TPF for the three geometries considered here. Total averaged Nu/Nu_0 obtained from Fig. 4.29 is used for the calculation of TPF. Adding the bow at the end along with a bulb at the divider wall produces the highest TPF among the range of Reynolds number studied. The 16-29% increase in TPF for the symmetrical bulb case is mainly due to the significant reduction in pressure drop compared to the baseline case. The higher enhancement levels obtained are at the higher Reynolds numbers of about 55000 which are representative of many modern engines. Adding the bow increases the overall heat transfer and pressure drop compared to the bulb only case but still produces the highest TPF which is about 17-33% higher compared to the baseline case.

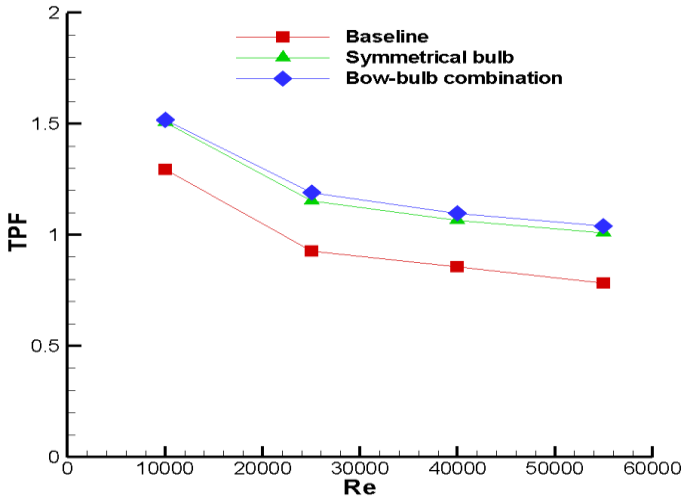

Figure 4.31: TPF comparison

4.2.3 Conclusions: Three bend geometries in a two-pass internal cooling channel of a gas turbine airfoil are studied in a stationary frame. The geometries are a baseline U-shaped bend with a rectangular dividing wall, a dividing wall with a symmetrical bulb at the end, and a bend

with a bulb on the divider and a bow on the outer end wall. Detailed and averaged heat transfer data are presented for a smooth test section with the three bends. Pressure drops are measured and the overall thermal performances are calculated for the bend geometries. The following major conclusions are obtained from the study

1) For the baseline case, the source for the high pressure drop and lower heat transfer after the bend is the separation bubble in the 2nd pass along the divider wall.
2) Adding a long symmetrical bulb (length of 5 D_h and bulb radius of 0.5 D_h) completely eliminates the separation bubble induced by the sharp turn of the divider tip and increases the Nu/Nu_0 values in the bend region. Overall Nu/Nu_0 values are about 6-17% higher compared to the baseline case with the higher enhancements at the higher Reynolds numbers.
3) Adding a bow with the existing bulb has the effect of creating a nozzle effect in the bend region, leading to greater increases in heat transfer values in the bend region. Heat transfer coefficient values in the region just after the turn are slightly higher than the bulb only case. The bow-bulb combination case increases the overall Nu/Nu_0 values by 12% at the lower Reynolds number (10000) and 19% at the higher Reynolds number (55000) compared to the baseline case.
4) Since both the geometries eliminate the separation bubble in the second pass, overall pressure drops are significantly reduced compared to the baseline case.
5) The highest thermal performance factor is achieved by the bow-bulb combination which is about 17-33% higher than the baseline case depending on the Reynolds number. The symmetrical bulb only case shows very comparable enhancements in the range of 15-29%. In both cases, the TPF enhancements increase with Reynolds number. Such a high

increase in TPF without any associated reduction in the overall heat transfer values may make this design a desirable candidate for integration in actual gas turbine blade internal cooling designs.

4.3 Bend geometries under rotation

Two of the modified bend geometries are tested numerically under rotation to see their effectiveness in rotating condition and they are compared with the baseline case. The geometries studied are the symmetrical bulb and the bow-bulb combination case. The goal is to see if the degree of performance benefit found in the stationary case is still present in rotating condition and also to see the effect of rotation on bend generated secondary flows. The rotating cases are run for the three geometries at Re =25000, Ro =0.2 and DR =0.2.

4.3.1 Results: Streamline profiles are presented for the midplane and close to the leading and trailing wall to see the effect of rotation. Secondary flow profiles are also presented at different cross-sectional planes. Heat transfer contour maps are shown for the leading and trailing walls and the overall normalized Nu ratio is calculated over the leading and trailing walls to find the overall heat transfer enhancements. Pressure drop is calculated from the inlet to the exit of the bend to calculate the overall thermal performance and they are compared with the stationary performance.

4.3.1.1 Baseline case under rotation: The streamline profiles at different streamwise planes are shown at Fig. 4.32. The planes are plotted at a distance of z/D_h =0.2 from the leading and trailing wall and at an equidistance plane (midplane) from both the walls.

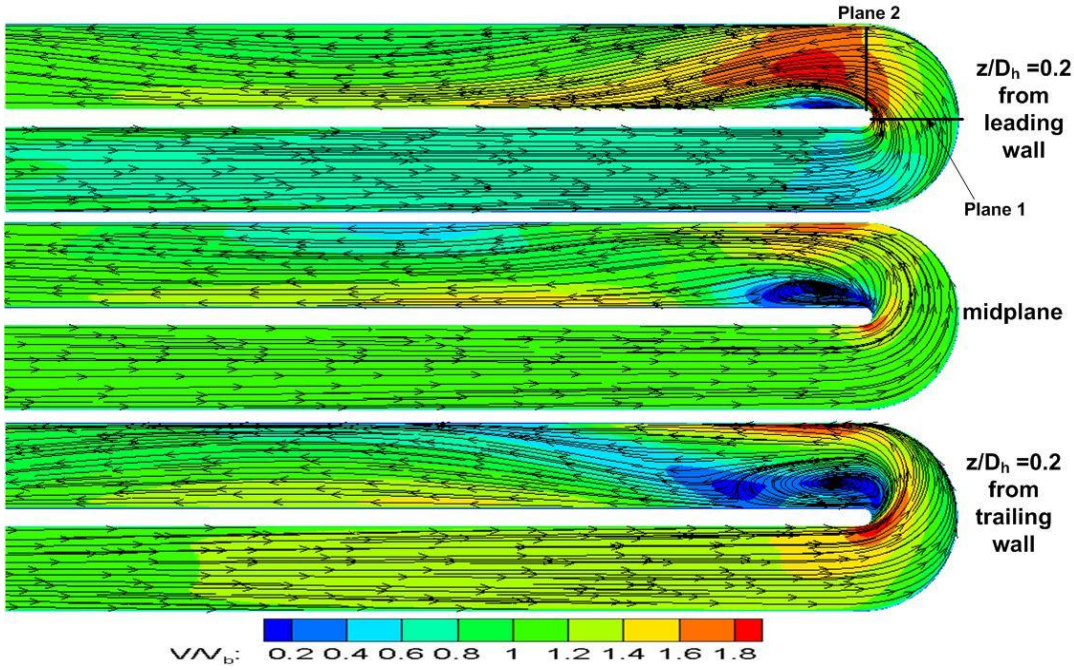

Figure 4.32: Streamline pattern at different streamwise planes (baseline)

From the streamline plots, it can be seen that the size of the separation bubble after the bend reduces as we go towards the leading wall and increases as we go towards the trailing wall. The streamwise velocity close to the leading wall is about $V/V_b \sim 2$ and it encompasses the whole region outside the separation bubble. The height of the separation bubble is about 0.2 times the hydraulic diameter of the channel. For the midplane, the bubble height is about 0.4 times the hydraulic diameter of the channel. Increase in streamwise velocity magnitude ($V/V_b \sim 2$) is only seen in the impingement region. The separation bubble height close to the trailing wall is about 75% the width of the channel and it spreads to about 3 D_h downstream from the bend inside the second pass.

Figure 4.33 shows the secondary velocity patterns at different planes perpendicular to the mainstream flow.

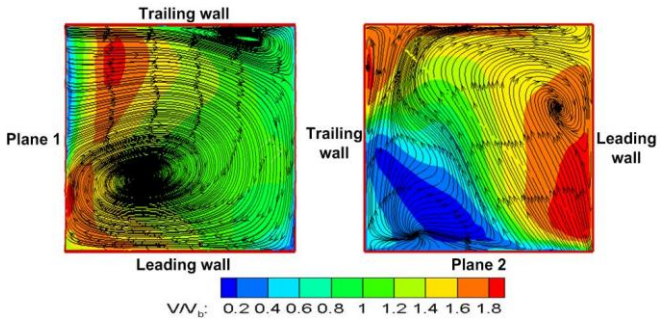

Figure 4.33: Secondary velocity profile at different cross sectional planes (baseline)

The Dean type vortices are not closed at the center of the bend (plane 1), indicating 3 dimensional flow pattern and separation at the divider wall size. The Dean type vortex close to the leading wall almost occupies the whole channel width and the vortex close to the trailing wall is very small. In the first pass, most of the flow is driven towards the trailing wall due to the combination of Coriolis force and centrifugal buoyancy force but as the bend is approached, the flow is reversed and more flow is driven towards the leading wall in the second pass. The bend region shows this transition and as a result the vortex close to the leading wall occupies most of the channel width. For the plane 2, it can be seen that the separation bubble is almost absent close to the leading wall side and the separation bubble size is larger close to the trailing wall. So, rotation has significant effect on the extent of separation and pressure drop compared to the stationary case. The vortex close to the leading wall occupies most of the channel width like plane 1 and velocity close to the leading wall is higher compared to the velocity close to the trailing wall.

The Nu ratio contour maps for the leading and trailing walls of the baseline case are shown in Fig. 4.34. As the Dean type vortex close to the leading wall is stronger compared to the trailing wall side, the heat transfer values at the bend close to the leading wall is about 20% higher compared to the trailing wall side. The reduction in heat transfer values due to the presence of

separation bubble at the divider wall tip is absent on the leading wall but the separation bubble related reduction in heat transfer values is present on the trailing wall. Nu ratio values as high as 2.8 are seen in the impingement zone of the leading wall and second pass Nu ratio values downstream of the bend are of the order of 1.2. The trailing wall shows a slight increase in Nu/Nu_0 values in the reattachment zone after the separation bubble where values of the order of 1.6 are seen. The rest of the trailing wall side shows Nu/Nu_0 values in the range of 0.8-1.2.

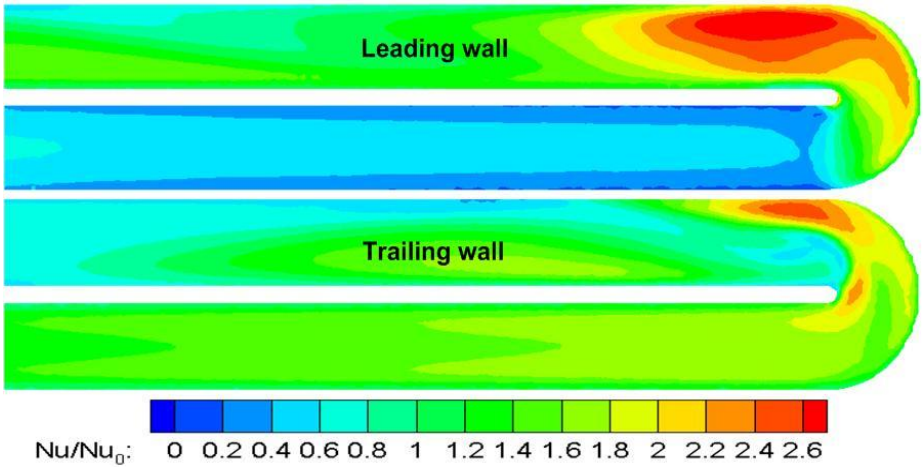

Figure 4.34: Nu/Nu_0 contour map for the baseline case

4.3.1.2 Symmetrical bulb case under rotation: The streamline profiles at different streamwise planes are shown at Fig. 4.35. It can be seen from the streamline profiles that the separation bubble is completely absent for all the planes. The streamwise velocity in the first pass close to the trailing wall is about 50-100% higher compared to the leading wall side, indicating the dominance of rotation induced Coriolis and centrifugal buoyancy force which pushes the fluid towards the trailing wall. Also this difference in velocity is higher compared to the baseline case. So a combination of flow convergence and rotation induced flows increases the streamwise velocity close to the leading wall compared to the trailing wall. As the flow moves into the

second pass, the flow pattern due to rotation is reversed and higher velocity is seen close to the leading wall ($V/V_b \sim 2$) after the bend.

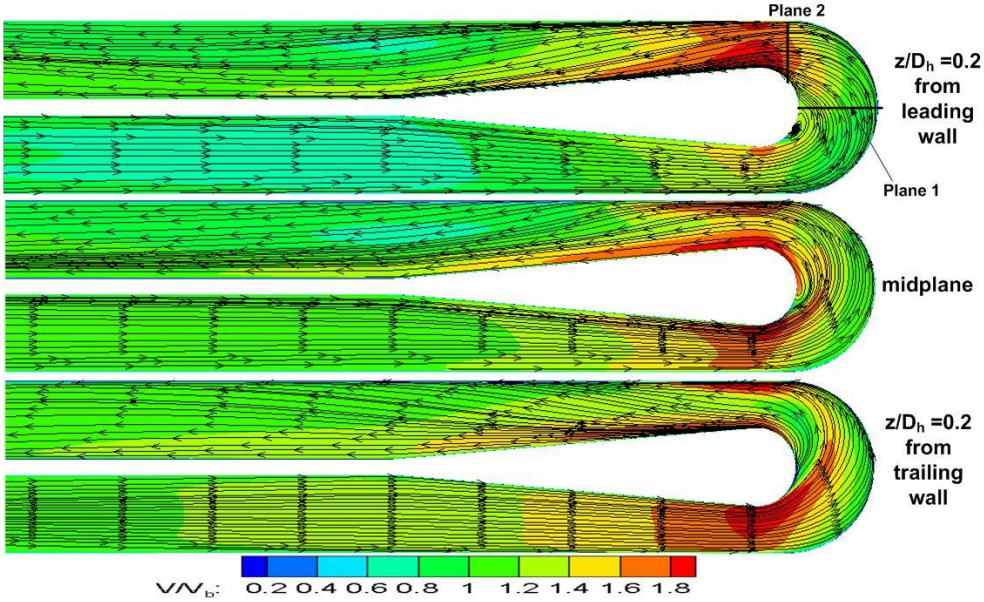

Figure 4.35: Streamline pattern at different streamwise planes (symmetrical bulb)

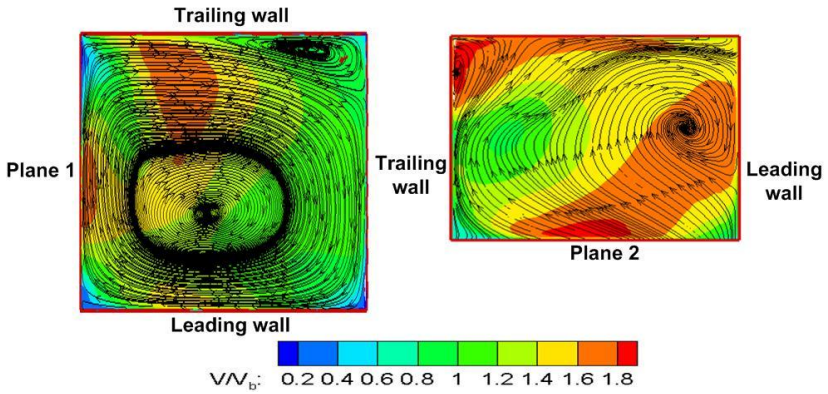

Figure 4.36: Secondary velocity profile at different cross sectional planes (symmetrical bulb)

Figure 4.36 shows secondary velocity profiles at different planes perpendicular to the mainstream flow. The streamlines at plane 1 are fully closed, indicating the absence of any separation bubble at the inner divider wall. Rotation increases the strength of the vortex close to the leading wall as it occupies almost the whole flow width and the vortex close to the trailing

wall is small in size. This trend persists up to plane 2 and the leading wall side velocity is mostly higher than the trailing wall side velocity. The separation bubble is completely absent for both the leading and trailing wall side.

The Nu/Nu_0 contour map for the symmetrical bulb case is shown in Fig. 4.37. A separation bubble induced low heat transfer zone was seen on the trailing wall for the baseline case but this is completely absent here. Due to the introduction of the bulb, Nu/Nu_0 values on the leading wall in the 1st pass can increase by 50-100% compared to baseline. There is about 20% increase in Nu/Nu_0 values on the trailing wall in the 1st pass compared to baseline. The leading wall side Nu/Nu_0 values for the 2nd pass are about the same as the baseline case but the trailing wall values are about 25-35% higher compared to baseline.

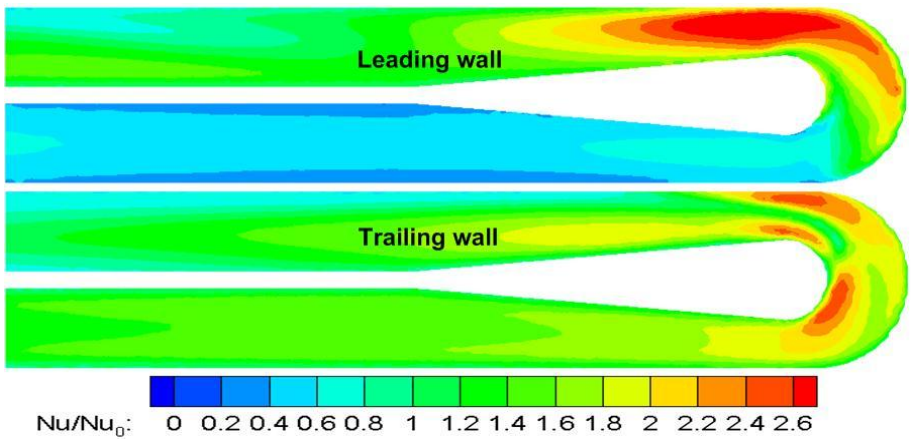

Figure 4.37: Nu/Nu_0 contour map for the symmetrical bulb case

4.3.1.3 Bow- bulb combination case under rotation: The streamline profiles at different streamwise planes are shown at Fig. 4.38. The streamline profile is almost the same as the symmetrical bulb case. There is a small separation zone present downstream of the bow close to

the leading wall. The midplane streamwise velocity is slightly higher than the symmetrical bulb case.

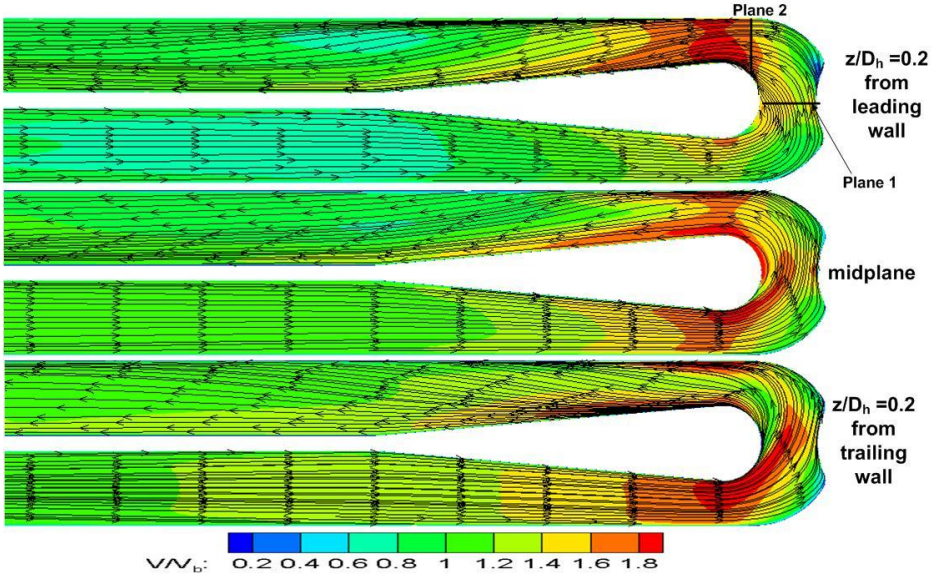

Figure 4.38: Streamline pattern at different streamwise planes (bow-bulb combination)

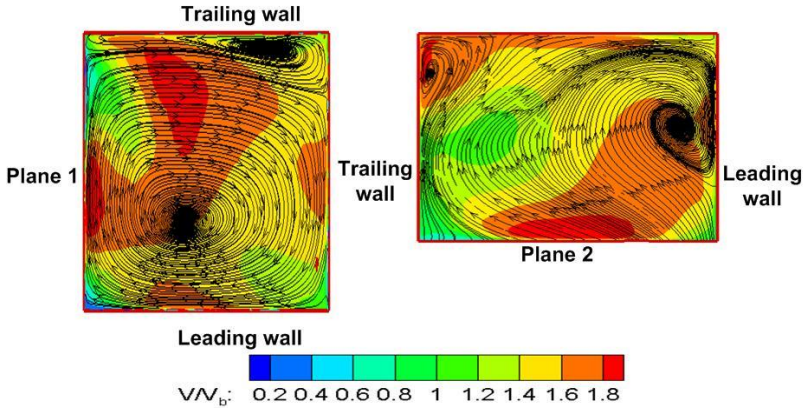

Figure 4.39: Secondary velocity profile at different cross sectional planes (bow-bulb combination)

Secondary flow velocity is shown at Fig. 4.39 for the bow-bulb combination case. Due to the presence of the bow, plane 1 velocities are about 10-12% higher compared to the symmetrical bulb case. The streamline pattern is the same as the symmetrical bulb case indicating the absence

of separation bubble at the divider wall tip. For the plane 2, magnitude and the streamline patterns are exactly the same as the symmetrical bulb case.

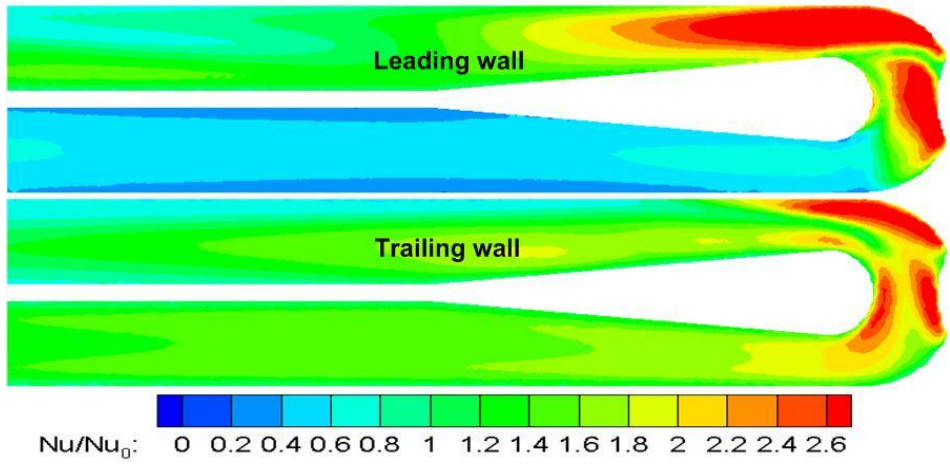

Figure 4.40: Nu/Nu_0 contour map for the bow-bulb combination case

The Nu/Nu_0 contour map for the bow-bulb combination case is shown in Fig. 4.40. The immediate effect of the bow geometry is to increase the bend zone heat transfer values significantly, both for the leading and trailing wall. Bend region Nu/Nu_0 values can reach as high as 3 for both the leading and trailing wall and the values can be about 30-50% higher compared to the symmetrical bulb case. The Nu/Nu_0 values are higher than the symmetrical bulb case in 2nd pass for first few hydraulic diameters and as the flow progresses downstream the symmetrical bulb value and bow-bulb combination value become the same.

4.3.1.4. Average Nu/Nu_0 distribution: Zonal averaged heat transfer enhancement values at Re =25000 and with rotation are shown in Fig. 4.41. Each of the zones is 1 D_h long in the streamwise direction as shown in Fig. 4.41. Averaging is done by dividing the summation of Nu/Nu_0 values for each pixel in a given zone by the number of pixels in that zone.

The trailing wall Nu/Nu_0 values are about the same for all three geometries in the 1st pass but for the leading wall, Nu/Nu_0 values of the bulb cases can be about 60% higher compared to the baseline case. Inside the bend region and downstream of the bend region, both the baseline and symmetrical bulb cases show similar levels of heat transfer enhancement. The highest heat transfer enhancement for the leading wall is seen at the start of the 2nd pass (zone 13), where the Nu/Nu_0 value is about 17% higher than the baseline and symmetrical bulb case. The highest Nu/Nu_0 value for the trailing wall is seen just downstream of the bow (zone 12) where the value is about 26% higher compared to the baseline case. Trailing wall side Nu/Nu_0 values for both the bulb cases are about the same from zone 13 onwards and are about 15-45% higher compared to the baseline case.

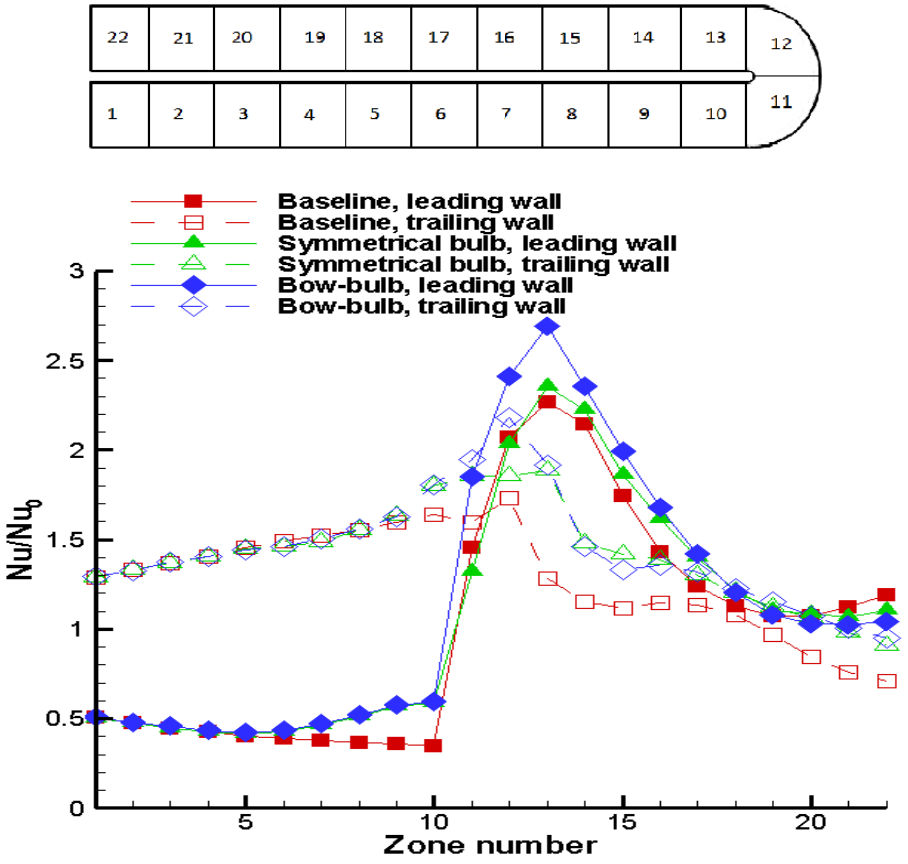

Figure 4.41: Zonal averaged Nu/Nu_0 values for the leading and trailing walls under rotation

4.3.1.5 Overall performance comparison: Heat transfer enhancement values are averaged over the leading and trailing wall to find the overall heat transfer performance of the three geometries under rotation. The averaged Nu/Nu_0 values are calculated for only the bulb region (zone 6-17) and pressure drop is calculated between the entrance of zone 6 and exit of zone 17. The friction factor is calculated from the pressure drop from zone 6 to 17. It is given by Equation 4.4. Friction factor is normalized by Equation 4.5. For calculation of a performance criterion, the heat transfer enhancement of the geometries are compared for a constant pumping power and constant surface area. The thermal performance factor (TPF) is defined by Equation 4.6.

Table 4.4 shows the performance comparison of the three geometries under rotation.

Table 4.4: Comparison of the bend geometries under rotation

	Nu/Nu_0 (Leading wall)	Nu/Nu_0 (Trailing wall)	Nu/Nu_0 (Overall)	f/f_0	TPF
Baseline	1.18	1.41	1.295	2.86	0.91
Symmetrical bulb	1.27	1.58	1.425 (10%)	2.11(-26%)	1.11(22%)
Bow-bulb combination	1.39	1.61	1.5 (15.8%)	2.34(-18.2%)	1.13(24.2%)

The performance of the two geometries with bulbs under rotation is not as good as in the stationary case but still the improvement in TPF is present. As seen with the stationary case, the highest thermal performance is achieved with the bow-bulb combination case which increases the TPF by about 24% compared to the baseline case.

4.3.2 Conclusions: Two bend geometries are tested numerically under rotation and their performance is compared with a baseline geometry. Numerical simulations are run for each case at Re =25000, Ro =0.2 and DR =0.2. Detailed and averaged heat transfer data are presented for a smooth test section with the three bends. Pressure drops are measured and the overall thermal

performances are calculated for the bend geometries. The following major conclusions are obtained from the study

1) For the baseline case, the separation bubble at the 2nd pass divider wall tip is present but it shifts towards the trailing wall side. The size of the separation bubble is very small close to the leading wall and grows in size towards the trailing wall.
2) Inside the bend, the Dean type vortex close to the leading wall almost occupies the whole channel width and the vortex close to the trailing wall side is very small in size. This effect is present at the beginning of the second pass as well. Reduction in heat transfer values due to the presence of separation bubble at the divider wall tip is absent for the leading wall side but is present for the trailing wall.
3) Separation bubble is completely absent for the symmetrical bulb and bow-bulb combination case. Due to the combination of flow convergence and rotation induced flows, the 1st pass streamwise velocity close to the trailing wall is about 50-100% higher than the leading wall side. This is also reflected in the heat transfer contour map where the 1st pass leading wall Nu/Nu_0 values after the bulb are about 50-100% higher than the baseline case.
4) Introduction of the bow shape at the center of the bend increases the local streamwise velocity at the bend. The local Nu/Nu_0 values also increases by about 30-50% compared to the symmetrical bulb case.
5) Performance enhancement due to the modified geometries with rotation is not as high as the stationary condition. The bow-bulb combination case shows the best performance with a TPF increase of 24% compared to the baseline case.

4.4 Concluding remarks

Several modifications in standard U-bend geometries are made for maximizing the thermal performance of the bend. The goal is to find a geometry which reduces the pressure drop and increases the heat transfer performance as well. A total of 10 geometries are studied numerically at a single Reynolds number (Re=25000) to find a geometry with the highest thermal performance. A combination of a symmetrical bulb at the divider wall, a bow shaped area contraction and an array of dimples in the bend region increased the TPF value to 41% compared to the baseline case. Two geometries are down selected from the numerical study (symmetrical bulb and bulb-bow combination) and tests are performed on them to find the thermal performance for a range of Reynolds number ($10000<Re<55000$). It is found that for the range of Reynolds number studied, the bow-bulb combination increased the TPF by 17-33% compared to the baseline case. Numerical simulations are run on this two geometries at Re =25000, Ro =0.2 and DR =0.2 to see the benefit in actual rotating condition. It is seen that the degree of of TPF increase with rotation is not as great as the stationary case. While the above conclusions apply for smooth channels, and an improved bend geometry for such channels has been found, future work will be directed at turbulated channels where the flow features are likely to be different than those of a smooth channel.

CHAPTER 5: GROOVED CHANNEL RESULTS

5.1 Geometries used during the tests

The quest to discover a geometry that enhances heat transfer from hot gas turbine blade to internal coolant channel flow with minimal pressure drop penalty is endless. Extensive work has been done on different combinations of ribs and it is the most common turbulence promoter used in modern gas turbine blades. A turbulence promoter on the internal surface of the blade in the form of a groove can also improve the heat transfer from the blade. Instead of protruding into the flow like a rib, a groove is indented to the surface. As they do not protrude into the flow, the pressure drop penalty associated with these turbulence promoters are also smaller compared to a ribbed channel. Some work has been done by previous researches on transverse grooved channel (Lorenz et al., 1995, Eiamsa-ard and Promvonge, 2008, Bilen et al., 2009) or combination of transverse groove and transverse ribs (Zhang et al., 1994, Eiamsa-ard and Promvonge, 2009). Making the groove angled to the flow direction can produce some secondary flow along the groove and this, in combination with the mainstream flow and the upwash flow coming from the groove, can increase local turbulence and enhance heat transfer from the wall. In the present work, a total of seven geometries are studied. The geometries are: 1) 45° V groove with the V facing upstream flow, 2) 45° V groove with the V facing downstream flow, 3) 45° angled groove with smaller pitch, 4) 45° angled groove with larger pitch, 5) combination of 45° angled groove with 45° angled rib, 6) combination of 45° angled groove with transverse rib, and finally, 7) combination of V groove and V rib facing upstream flow. The schematic of the various geometries tested are shown in Figure 5.1. The flow direction is shown by the arrows.

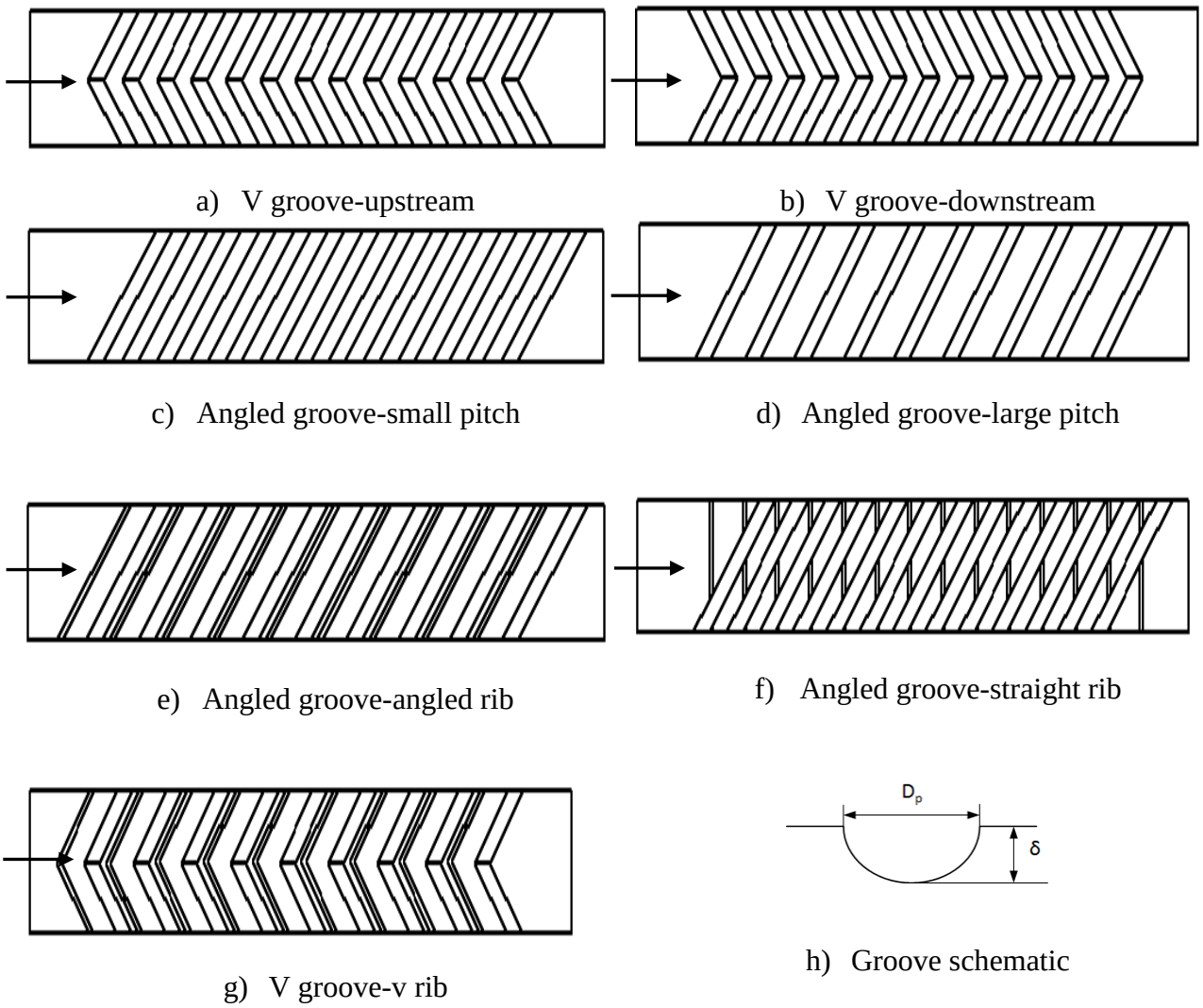

Figure 5.1: Schematic of the geometries studied

The test section is a square cross section channel with the sides being H=W=0.03048 m. A long entrance geometry is used before the actual test section to attain fully developed profile before the test section. The grooves and ribs are mounted on the wall simulating the leading/trailing wall (same as the test is stationary). The cross section of the groove is circular and for all the groove geometries the groove depth (δ) is kept at 0.06 in (0.001524 m). The groove print diameter (D_p) is kept at 0.2 in (0.00508 m). A screening study was done numerically for the optimum δ/D_p ratio and δ/D_p =0.3 was found to be the one producing highest thermal

performance. For the upstream and downstream facing V grooves (Fig. 5.1 (a)-(b)), the groove pitch (p)/groove depth (δ) ratio is kept at 10. For the angled groove-small pitch case (Fig. 5.1 (c)) the p/δ ratio is kept at 10. The angled grooves are at an angle 45° to the mainstream flow. The p/δ ratio is 15 for the angled groove-large pitch case (Fig. 5.1 (d)). The ribs used in this study are all square cross section rib with a rib height (e) of 0.06 in (0.001524 m). The groove geometry used for the angled groove-angled rib combination case (Fig. 5.1 (e)) is the angled groove with p/δ =15. For the angled groove-angled rib combination, the 45° ribs are placed at a distance of p/e =5 downstream of the groove. The distance from one rib to the next downstream groove center is kept at p/e =10. The groove geometry used for the angled groove-straight rib combination case (Fig. 5.1 (f)) is the angled groove with p/δ=10. The groove pitch for the v groove-v rib combination case is kept at p/δ =15. The V ribs are placed at a distance of p/e =5 downstream of the V groove. The distance from one rib to the next downstream groove center is kept at p/e =10.

5.2 Results

Detailed heat transfer coefficient contour maps are obtained for the test section on the leading/trailing wall. Tests were done at Re =13000, 25000, 40000, and 55000 based on the fluid properties at the inlet of the test section. Nusselt number is obtained from the heat transfer coefficient and normalized with the Nusselt number (Nu_0) for a simple smooth channel given by the Dittus-Boelter correlation.

$$Nu_0 = 0.023.Re^{0.8}.Pr^{0.4} \quad (5.1)$$

In presenting the results, the heat transfer enhancement contour map is shown for Reynolds numbers 13000 and 40000. Other Reynolds number show similar trends with different values,

and therefore Reynolds number effects are presented in the averaged line plots. Line plots of Nu/Nu_0 at different streamwise locations are shown at Re=25000 to understand the flow development as the flow interacts with the grooved and rib-grooved geometries. Overall averaged Nu/Nu_0 values are calculated and the pressure drop from inlet to the exit of the channel is also calculated to find the thermal performance factor.

5.2.1 V groove upstream: The heat transfer enhancement contour map for the V-groove upstream case at Re =13000 and Re =40000 is shown in Figure 5.2.

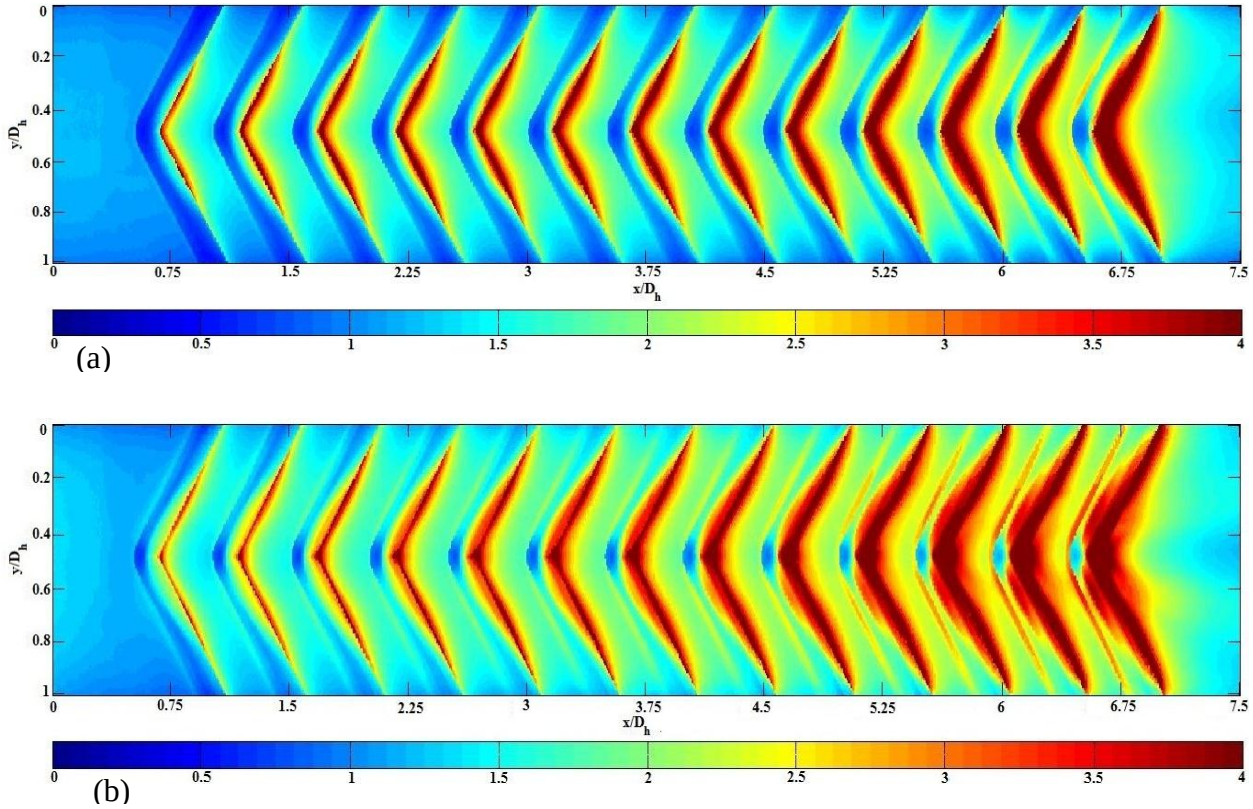

Figure 5.2: Nu/Nu_0 contour map for the V-groove upstream case (a) Re =13000, (b) Re =40000

Fully developed Nu/Nu_0 values close to 1 are seen at the entrance of channel (x/D_h =0-0.5). For a fully developed turbulent flow in a smooth round pipe the Nusselt number value is represented

by Eq. 5.1, and the Nu/Nu_0 ratio should be 1. The Nu/Nu_0 value of 1 in the 1st pass of the test section for the current case indicates that the flow coming in is fully developed and also provides an additional measure of validation to the present experimental data. A small separation zone is formed at the upstream nose of the V groove where Nu/Nu_0 values are pretty low (Nu/Nu_0 ~0.6-1). There is a development of secondary flow along the grooves which, in interaction with the mainstream flow raises the in-groove Nu/Nu_0 values close to 2-2.5. As the secondary flow progresses along the groove, it losses strength as it gets washed by the mainstream flow and as a result low values of Nu/Nu_0 are seen (Nu/Nu_0 ~0.7-1) towards the end of the groove (y/D_h=0, 1). The highest Nu/Nu_0 values are seen in the upwash region of the grooves showing a Nu/Nu_0 value of 4. Flow attains periodically developed condition at around x/D_h =6 and in-groove Nu/Nu_0 values close to 3-3.5 are observed and Nu/Nu_0 values close to 5 is observed in the upwash region downstream of the V nose. Both the Reynolds numbers show similar trends of heat transfer with the heat transfer value higher for the higher Reynolds number. This is in contrast with the common ribbed channel where higher Nu/Nu_0 values are typically achieved with lower Reynolds number.

Figure 5.3 shows the spanwise Nu/Nu_0 distribution at different x/D_h locations at Re =25000. For all the locations plotted, the highest Nu/Nu_0 values are seen at y/D_h =0.1, 0.9. The upwash from the groove combined with the mainstream flow results in high Nu/Nu_0 values (Nu/Nu_0 ~4) in this region. Another feature to be noted is the low heat transfer value in the upstream nose of the V groove (y/D_h =0.5) where Nu/Nu_0 value of about 1 are seen at locations x/D_h =3-6. This is because of the small separation zone at the nose of the groove where the flow first enters the groove. This separation zone is present throughout the test section for all the grooves downstream as well. It is also to be noted that the Nu/Nu_0 values close to the sidewalls (y/D_h =0,

1) have increased to about 2 for x/D_h =7 whereas for the other streamwise locations it is close to 1.

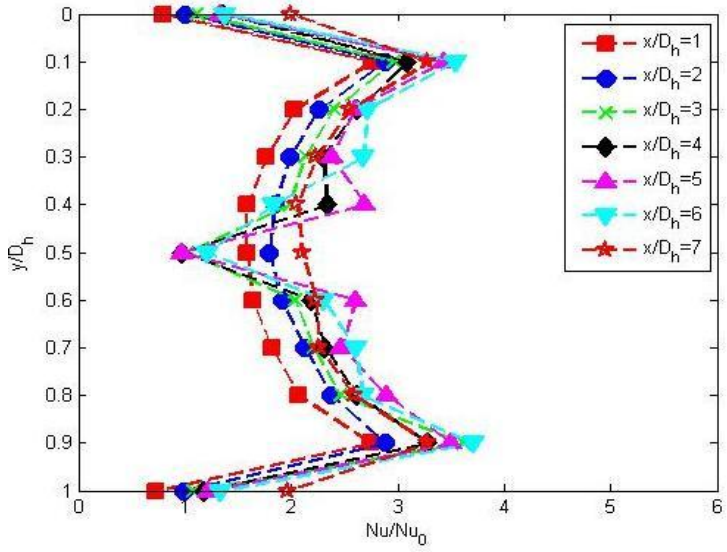

Figure 5.3: Spanwise Nu/Nu_0 distribution at different streamwise locations for V-groove upstream case (Re =25000)

5.2.2 V groove downstream: The heat transfer enhancement contour map for the V-groove upstream case at Re =13000 and Re =40000 is shown in Figure 5.4. It can be seen from the contour map that putting the V-groove in downstream direction has some detrimental effect on overall heat transfer values. The corner of the V-groove close to the sidewalls (y/D_h =0, 1) show Nu/Nu_0 values lower than 1. The secondary flow moves along the groove from the sidewall side towards the center but never really meet at the groove nose and advect by the mainstream flow towards the intra-groove spacing. The groove nose Nu/Nu_0 values are of the order of 1. The highest Nu/Nu_0 values (Nu/Nu_0 ~4) are observed just downstream of the grooves at a zone spanning from the sidewall to the center of the channel. The flow attains periodically fully developed condition after about x/D_h =3. It is also seen that the Nu/Nu_0 values at the surface between the grooves are lower than the V-groove upstream case.

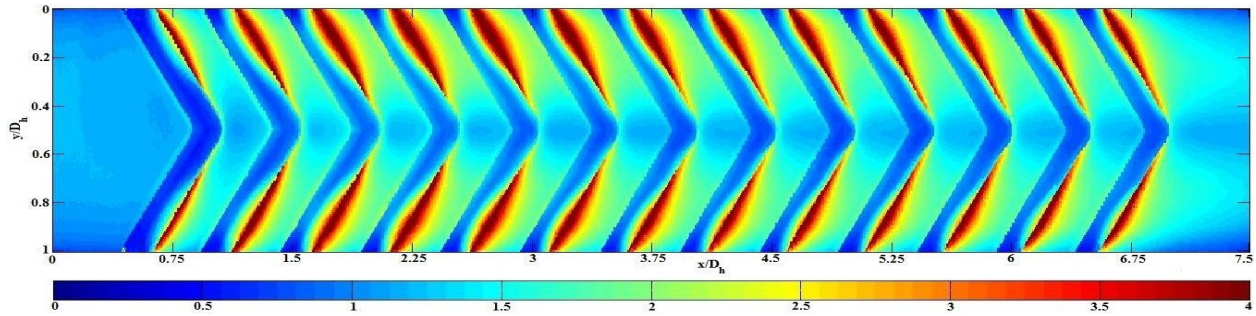

(a)

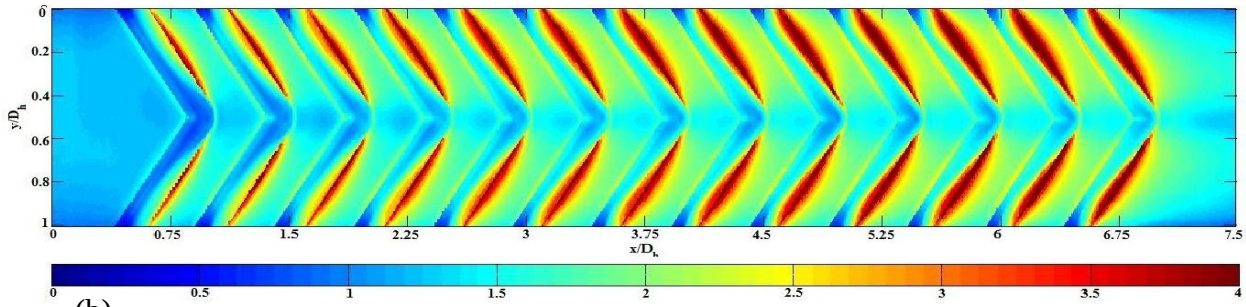

(b)

Figure 5.4: Nu/Nu_0 contour map for the V-groove downstream case (a) Re =13000, (b) Re =40000

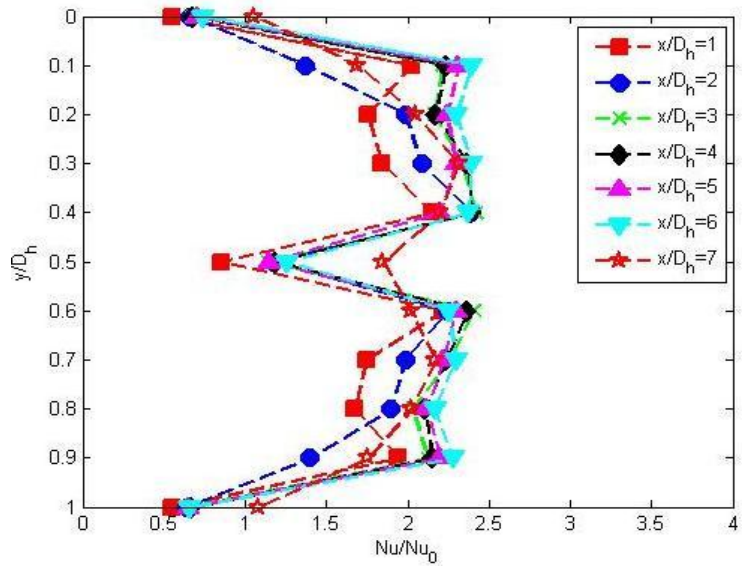

Figure 5.5: Spanwise Nu/Nu_0 distribution at different streamwise locations for V-groove downstream case (Re =25000)

The spanwise Nu/Nu_0 development in the streamwise direction is shown in Figure 5.5. In general, the Nu/Nu_0 values at a same streamwise location can be about 22-50% lower compared

to the V-groove upstream case. The Nu/Nu_0 values at x/D_h =3-6 is almost same which signifies the periodically developed flow condition. The curve is flat for y/D_h =0.1-0.4 signifying the same level of heat transfer enhancement for the intra-groove spacing. The V nose Nu/Nu_0 values are about 1 which is in the same range as the V-groove upstream case.

5.2.3 Angled groove–small pitch: For the angled groove-small pitch case, the pitch is kept at p/δ =10. The heat transfer enhancement contour map for this case at Re =13000 and Re =40000 is shown in Figure 5.6.

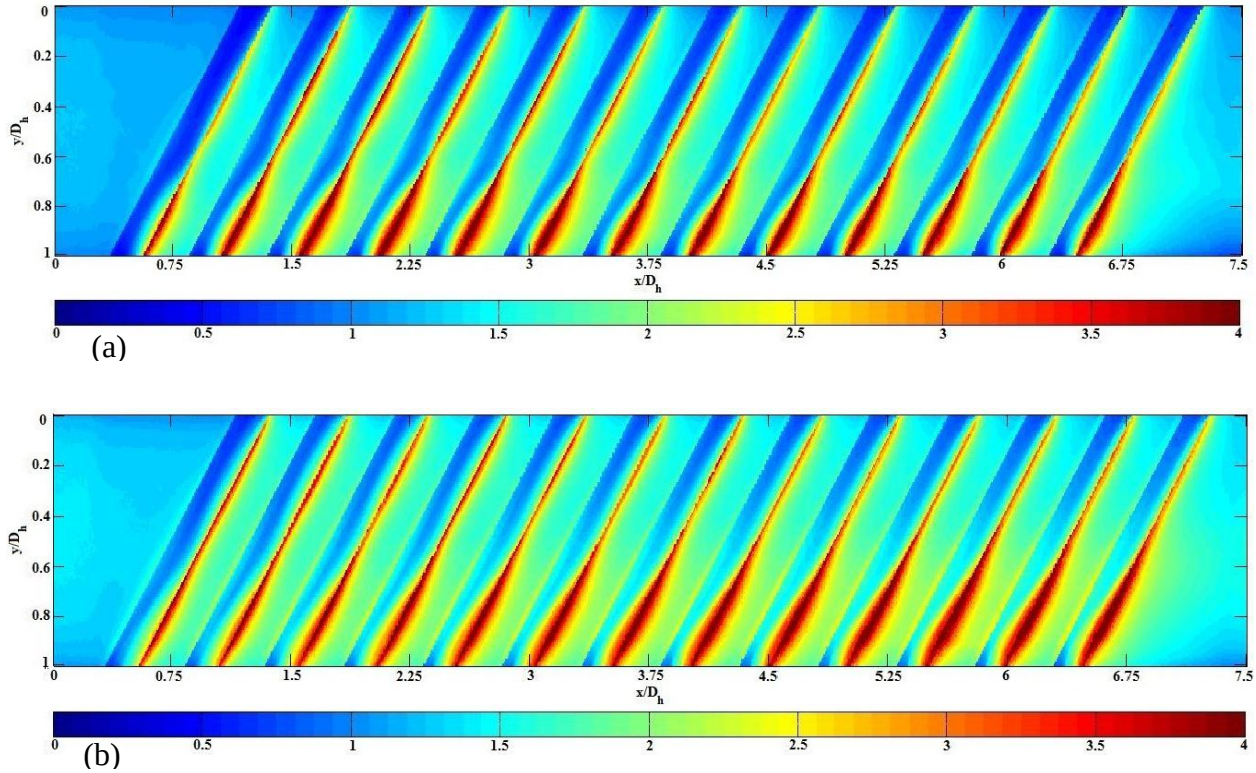

Figure 5.6: Nu/Nu_0 contour map for the angled groove-small pitch case (a) Re =13000, (b) Re =40000

In this case, the upstream corner of the angled groove (y/D_h =1) shows a slight separation related low heat transfer zone. As the flow progresses through the groove from y/D_h =1 to y/D_h =0, this separation zone grows in size as lesser amount of secondary air is available along the groove and

most of it gets swept away by the mainstream flow. The highest Nu/Nu_0 values (Nu/ Nu_0 ~4) are seen downstream of the groove at the y/D_h =1 side. For other spanwise locations downstream of the groove, Nu/Nu_0 values close to 3 are seen. This is expected since the secondary flow losses strength as it is gets swept by the mainstream flow continuously and close to y/D_h =0, the interaction with the upwash secondary flow and mainstream flow is not very strong. Periodically developed condition is achieved after about x/D_h =3.

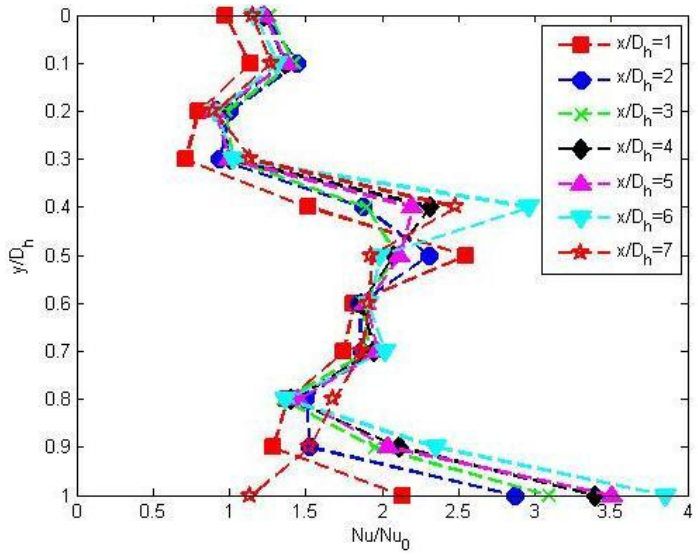

Figure 5.7: Spanwise Nu/Nu_0 distribution at different streamwise locations for angled groove-small pitch case (Re =25000)

The spanwise Nu/Nu_0 distribution is shown in Fig. 5.7. As expected highest value of Nu/Nu_0 is seen close to y/D_h =1 for the streamwise locations x/D_h =3-6. The intra-groove spacing Nu/Nu_0 values are of the order of 2-2.5.

5.2.4 Angled groove–large pitch: For the angled groove-small pitch case, the pitch is kept at p/δ =15. The space between the grooves for the insertion of a rib is very small and for this reason a grooved channel with a larger pitch will be used for the groove-rib combination case. The heat transfer enhancement contour map for this case at Re =13000 and Re =40000 is shown

in Figure 5.8. The heat transfer contour shows similar trend as the small pitch case. The main difference is the level of heat transfer enhancement in the intra-groove spacing. Since the spacing between the grooves is larger than the previous case, the intra-groove Nu/Nu_0 values close to y/D_h =0 can be about 50% lower than the small pitch case. The highest Nu/Nu_0 values (Nu/ Nu_0 ~3.5) are seen downstream of the groove at the y/D_h =1 side like the small pitch case. The inner groove Nu/Nu_0 values are similar to the small pitch case and decreases along the secondary flow direction.

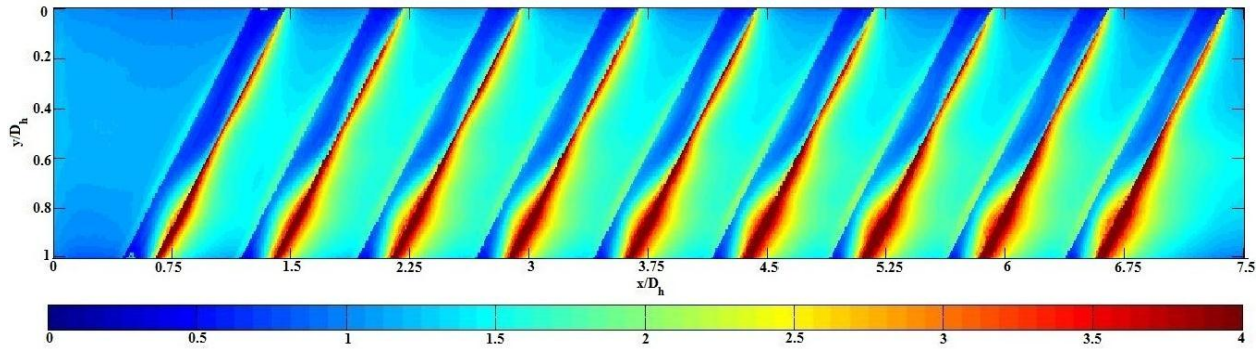

(a)

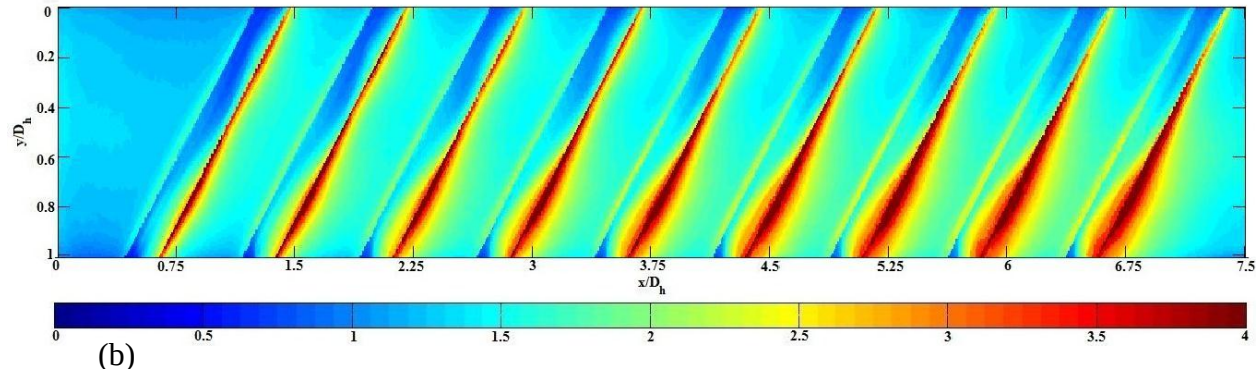

(b)

Figure 5.8: Nu/Nu_0 contour map for the angled groove-large pitch case (a) Re =13000, (b) Re =40000

Figure 5.9 shows the spanwise Nu/Nu_0 distribution for the angled groove-large pitch case. The locations x/D_h =3 and x/D_h =6 are the positions just downstream of a groove and shows the highest Nu/Nu_0 values at x/D_h =0.9. For other locations like x/D_h =1,4,7 , the high Nu/Nu_0 value

just downstream of the groove is about 3 (location x/D_h =0.6) and for locations x/D_h =2 and 5 it is about 2.5. This shows that as the strength of the secondary flow reduces along the groove from y/D_h =1 to y/D_h =0 side, the high Nu/Nu_0 value just downstream of the groove also reduces. The inner groove Nu/Nu_0 value at y/D_h =0 side inside the groove can be as low as 0.7.

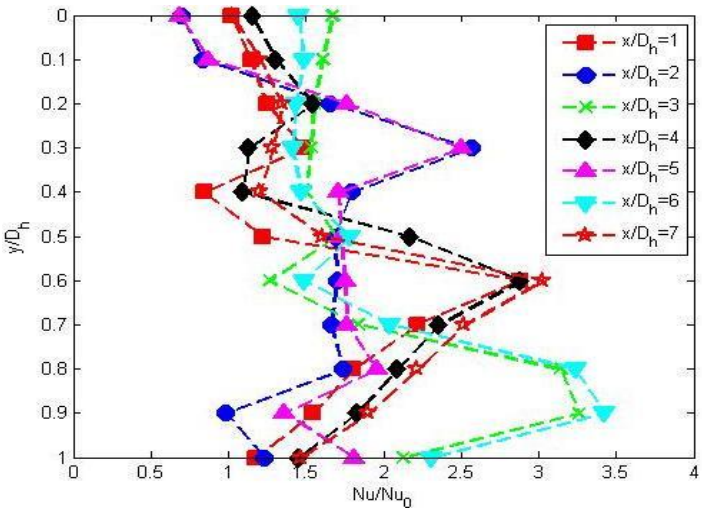

Figure 5.9: Spanwise Nu/Nu_0 distribution at different streamwise locations for angled groove-large pitch case (Re =25000)

5.2.5 Angled groove – angled rib: The thought behind inserting some ribs in the intra-groove spacing comes from the fact that the intra-groove Nu/Nu_0 values for the angled groove-large pitch case is not very high and if a rib can be inserted in that space, the flow may reattach before the groove or inside the groove to increase Nu/Nu_0 values significantly. The height of the rib is kept low (e/D_h =0.5) and the ribs are placed just after one groove (at a distance of p/e =5 downstream of the groove center) so that the flow can reattach before it encounters the next groove.

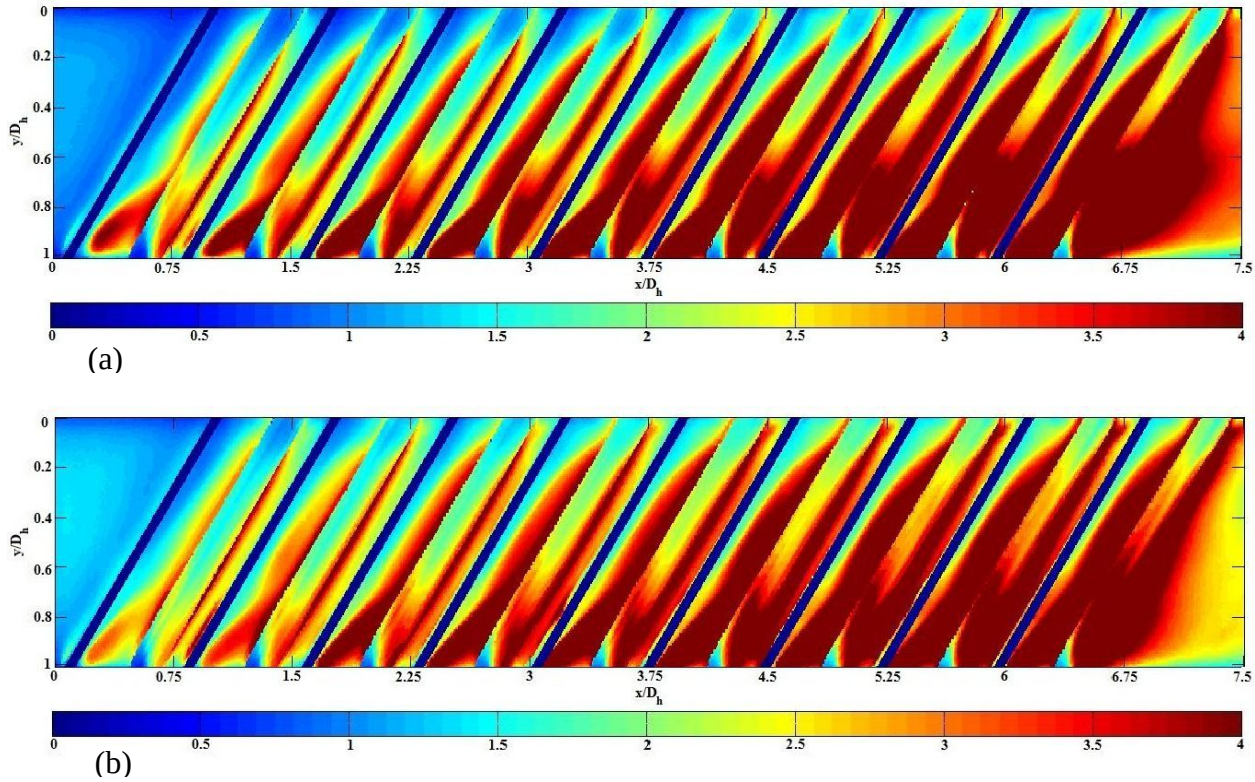

Figure 5.10: Nu/Nu_0 contour map for the angled groove-angled rib case (a) Re =13000, (b) Re =40000

Figure 5.10 shows the heat transfer enhancement contour map for this case at Re =13000 and Re =40000. It can be readily seen that the Nu/Nu_0 levels throughout the span has increased drastically compared to the without rib case. The flow development happens at larger x/D_h values compared to the without rib case. The periodically developed flow condition occurs after about x/D_h =5. The low Nu/Nu_0 values (Nu/Nu_0 ~1) at the downstream side of the groove (y/D_h =0 side) is still seen up to about 4-5 ribs but as the flow progresses further, this value goes up to about 2.5. This value is about the lowest Nu/Nu_0 in the whole span. The highest Nu/Nu_0 values are seen just downstream of the grooves at y/D_h =1 side where Nu/Nu_0 values as high as 8 can be seen. It is the interaction of the flow reattachment after the rib and the interaction of the groove generated secondary flow that takes the Nu/Nu_0 values to such a high level. A small separation

zone at the upstream corner of the groove (y/D_h =1 side) is still present which shows Nu/Nu_0 values around 1 as in the previous cases.

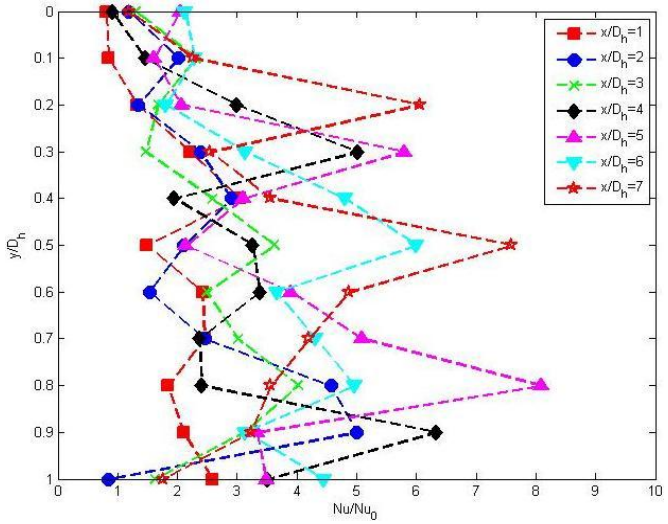

Figure 5.11: Spanwise Nu/Nu_0 distribution at different streamwise locations for angled groove-angled rib case (Re =25000)

Figure 5.11 shows the spanwise heat transfer distribution for the angled groove-angled rib case. The highest levels of heat transfer enhancement is always seen downstream of the groove where the interaction of rib produced flow reattachment, groove produced upwash flow, and mainstream flow is present. An interesting fact to be noted is that the enhancement in heat transfer values due to rib generated flow reattachment can take the Nu/Nu_0 values to about 6 (locations like x/D_h =4, y/D_h =0.9; x/D_h =6, y/D_h =0.5; x/D_h =7, y/D_h =0.2) but the interaction with the groove generated secondary flow can take the values over 8 in the affected zones. The intra-groove Nu/Nu_0 values are also very higher compared to the without rib case.

5.2.6 Angled groove – straight rib: For the angled groove-straight rib case, the groove geometry is the one with the smaller pitch. Ribs angled perpendicular to the flow is placed over the grooves. It is thought that the flow will go under the ribs through the grooves and interact with the mainstream flow to enhance Nu/ Nu_0 values.

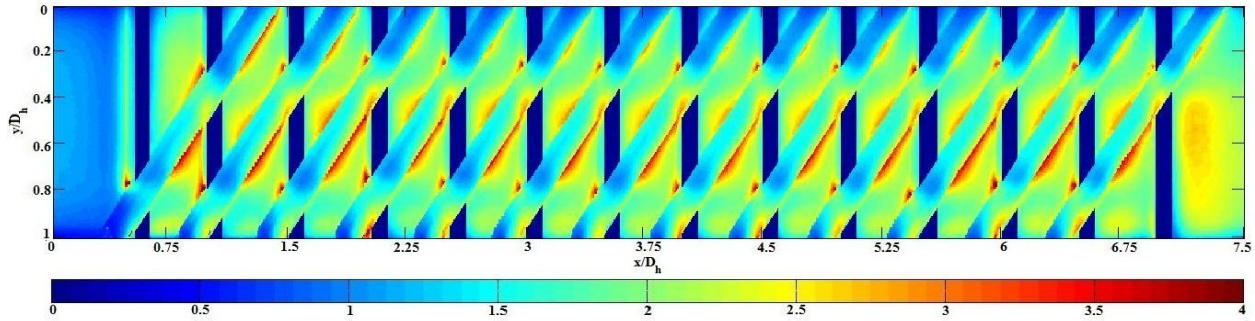

(a)

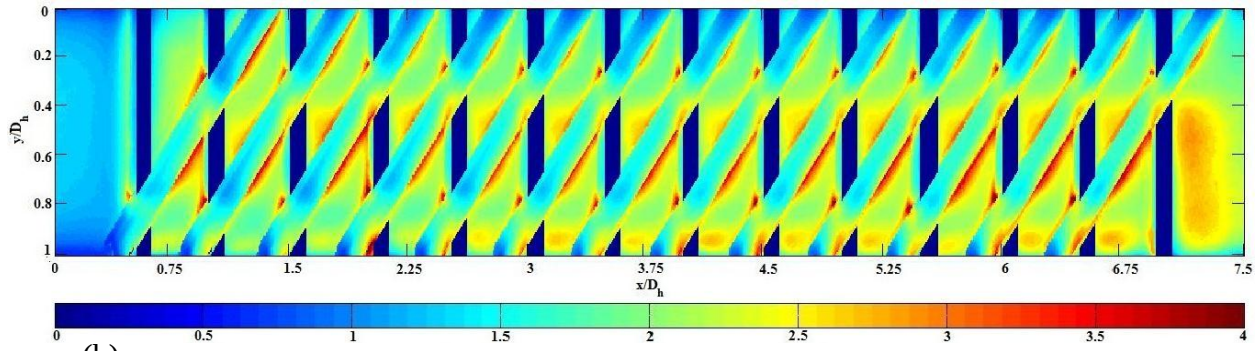

(b)

Figure 5.12: Nu/Nu_0 contour map for the angled groove-straight rib case (a) Re =13000, (b) Re =40000

The heat transfer enhancement contour map for this case at Re =13000 and Re =40000 is shown in Figure 5.12. It can be seen that the enhancement level produced by this case is not as high as the angled groove-angled rib case. The enhancement level is in the same range as the without rib case. The zones insides the grooves, under the rib shows about 50-80% increase in Nu/Nu_0 values. The Nu/Nu_0 values downstream of the grooves are about the same level as the without rib

case. The inner-groove Nu/Nu_0 values at the y/D_h =0 side are also same level as the without rib case.

Figure 5.13 shows the spanwise heat transfer distribution for the angled groove-angled rib case.

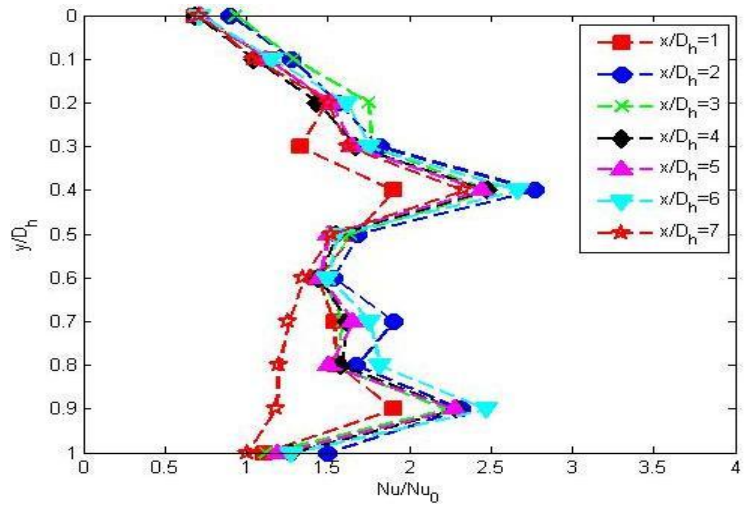

Figure 5.13: Spanwise Nu/Nu_0 distribution at different streamwise locations for angled groove-straight rib case (Re =25000)

It is seen that the highest Nu/Nu_0 (Nu/Nu_0 ~2.5-3) occurs in the zones below the straight rib inside the grooved surface (y/D_h =0.4, and y/D_h =0.9). Other than that the inter-groove Nu/Nu_0 values are in the range 1.5-2 and do not show drastic enhancement.

5.2.7 V groove-v rib: The last geometry tested in this study is a combination of v rib and v groove. The angled groove-angled rib combination showed significant enhancement of heat transfer and the v groove only case showed higher level of enhancement compared to the angled groove only case. So, it is thought that the combination of v groove and v rib should enhance the heat transfer to a higher level compared to the angled groove-angled rib case. The height of the rib is kept low (e/D_h =0.5) and the ribs are placed just after one groove (at a distance of p/e =5

downstream of the groove center) so that the flow can reattach before it encounters the next groove.

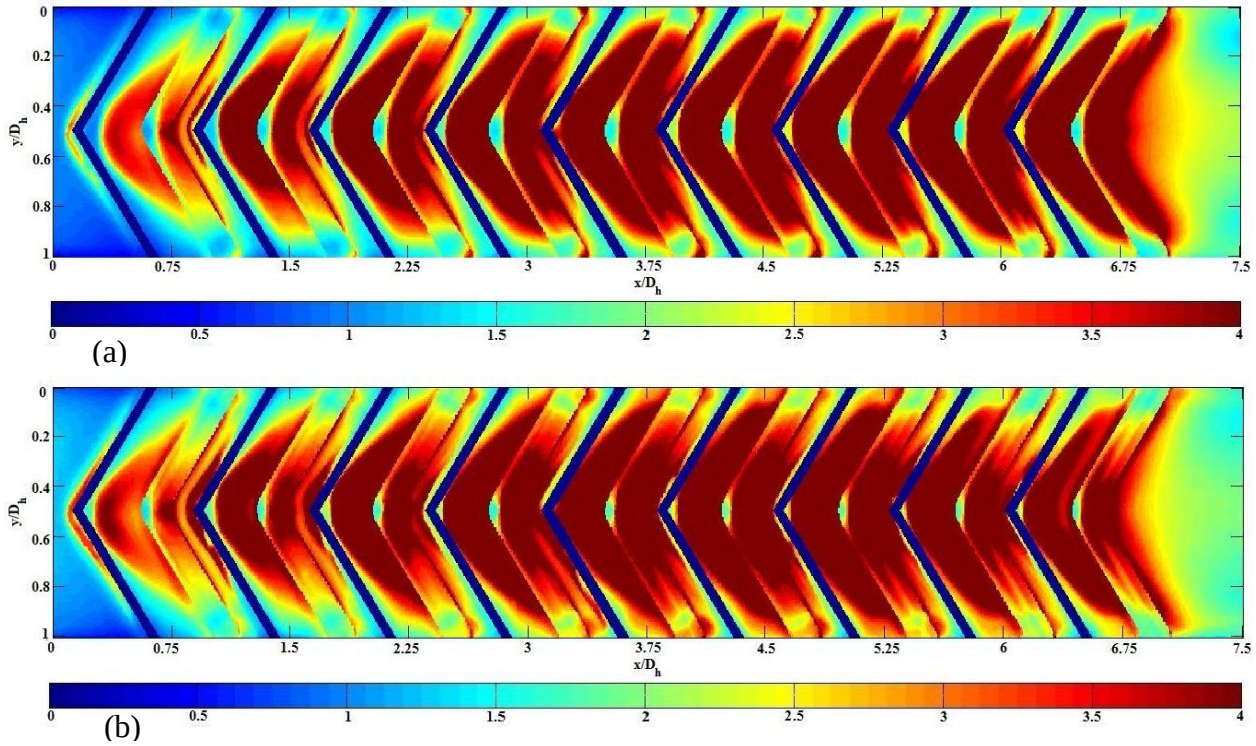

Figure 5.14: Nu/Nu_0 contour map for the V groove-v rib case (a) Re =13000, (b) Re =40000

Figure 5.14 shows the heat transfer enhancement contour map for this case at Re =13000 and Re =40000. It is clear that zones of high Nu/Nu_0 values are present throughout the span for this case compared to the angled groove-angled rib case. Highest Nu/Nu_0 values (Nu/Nu_0 ~9-10) are seen just downstream of the groove at the center of span (y/D_h =0.5). Without the ribs, the Nu/Nu_0 values in these regions were about 4 but the presence of rib generated reattachment, groove generated upwash flow and the mainstream flow takes the Nu/Nu_0 values to such a high level. Heat transfer value is lower at the sidewall sides (y/D_h =0,1) as the secondary flow moves along the v groove and loses strength as it goes on. A low heat transfer zone is also seen at the nose of the v groove where Nu/Nu_0 values close to 2 are seen.

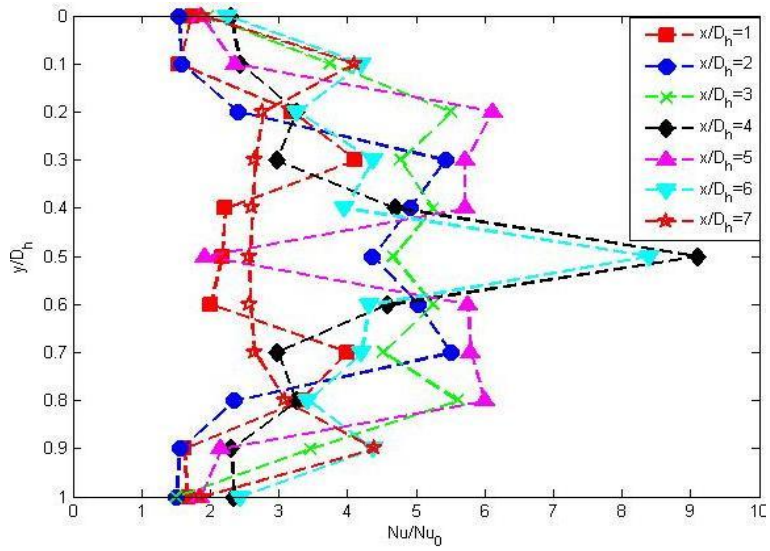

Figure 5.15: Spanwise Nu/Nu_0 distribution at different streamwise locations for V groove-v rib case (Re =25000)

Figure 5.15 describes the spanwise heat transfer distribution for the angled groove-angled rib case. It can be seen that for the center location (y/D_h =0.5), the Nu/Nu_0 value can go as high as 9 if it is just downstream of the groove. It can be as low as 2 as well when the point is at the nose of the groove. Rib generated flow reattachment can increase the local Nu/Nu_0 values to about 5-6. The low Nu/Nu_0 values, which were seen close to the sidewalls inside the groove (Nu/Nu_0 ~1) for the v groove only case, have increased to about 2.

5.2.8 Averaged Nu/Nu_0 comparison: The zonal averaged Nu/Nu_0 is shown in Figure 5.16. The averaging is done over a zone length of 1.5 D_h and the values are plotted at the center of the zone. It is seen that the angled groove cases show averaged Nu/Nu_0 values in the range 1.5-1.7. The introduction of 90° ribs on top of the angled groove does not improve the averaged value of heat transfer. The V groove-downstream case produces averaged Nu/Nu_0 values in the range 1.6-2.2. The best performer among the groove only geometries is the V groove-upstream

geometry. Here zonal averaged Nu/Nu_0 values can go to about 2.9. The introduction of the ribs with the angled groove enhances the zonal averaged Nu/Nu_0 values up to about 100% compared to the without rib case. After about 5 hydraulic diameters, the zonal averaged Nu/Nu_0 values reach about 3.8. The highest level of heat transfer enhancement is seen with the v groove-v rib case. Averaged Nu/Nu_0 values as high as 4.5 are seen. For the last zone (x/D_h =6-7.5), the effect of rib dies out and the average value drops down to about 4.

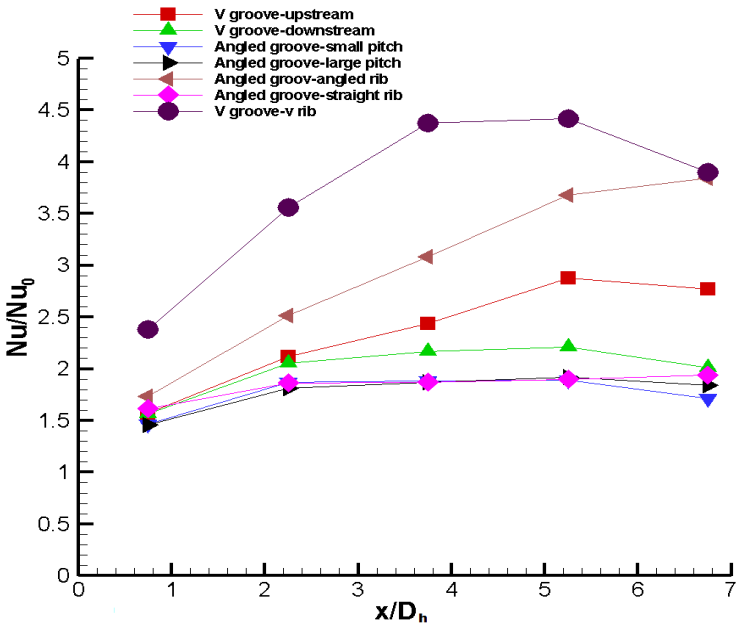

Figure 5.16: Averaged Nu/Nu_0 for the configurations tested (Re =25000)

5.2.9 Overall performance comparison: For calculating the overall performance, the Nu/Nu_0 values are averaged throughout the test section and pressure drop from inlet to the exit of the test section is calculated. Friction factor is defined as

$$f = \frac{\Delta p / 0.5\rho V^2}{4\Delta x / D_h} \qquad (5.2)$$

The friction factor is normalized by Karman-Nikuradse equation (Kays and Crawford, 1993).

$$f_0 = 0.046.Re^{-0.2} \quad (5.3)$$

The thermal performance factor is then defined with a constant pumping power and constant surface area assumption from the method used by Webb (1981), Gee and Webb (1980) and is defined as

$$TPF = \frac{{}^{Nu}/_{Nu_0}}{\left({}^{f}/_{f_0}\right)^{1/3}} \quad (5.4)$$

The total averaged Nu/Nu_0 plot is shown in Figure 5.17 as a function of the Reynolds number. The Reynolds number dependence is weak for all the cases. The angled groove cases without the ribs produces Nu/Nu_0 in the range of 1.6-1.9. The angled groove-straight rib case and the V groove-downstream case come next with averaged Nu/Nu_0 values 1.8-2.1. The V groove-upstream case enhances heat transfer values to about 8-16% compared to the V groove-downstream case. The angled groove-angled rib case produces averaged heat transfer values of about 3.1-3.2. The best performer among the group is the combination of V groove and v rib case which produces Nu/Nu_0 in the range of 3.6-3.8.

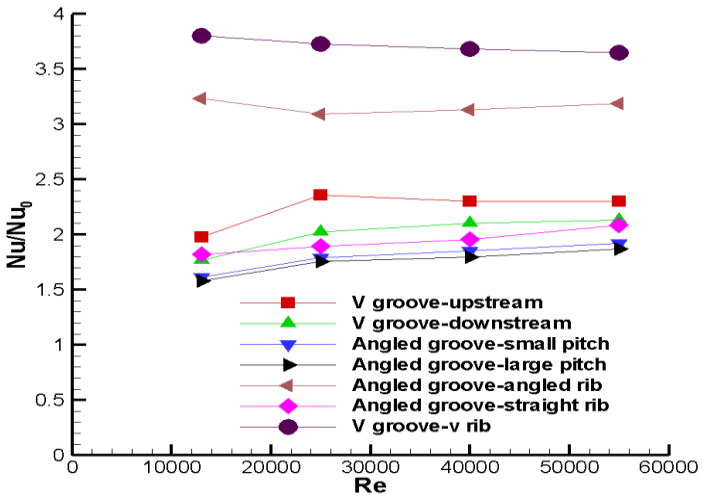

Figure 5.17: Total averaged Nu/Nu_0 comparison

The pressure drop is calculated from the inlet to the exit of the test section and friction factor ratio is plotted with Re (Fig. 5.18).

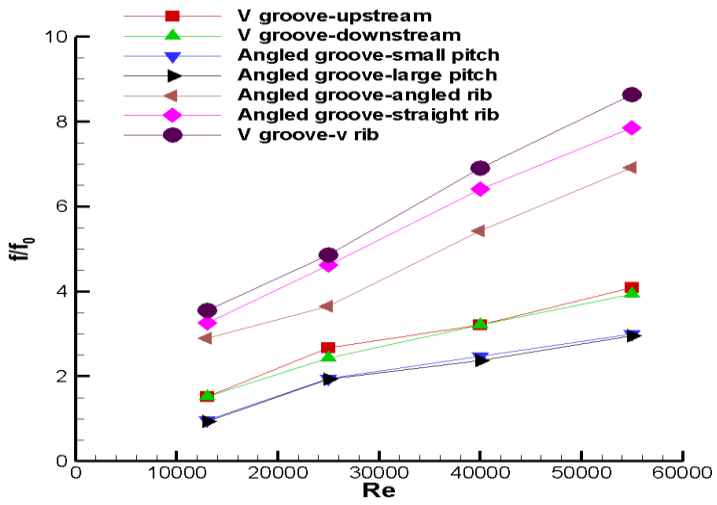

Figure 5.18: Total friction factor ratio

It can be seen from the friction factor plot that the introduction of the ribs increase the pressure drop to 2-3 times compared to the without rib case. The highest pressure drop is seen with the V groove-v rib case. Even though the heat transfer performance of the angled groove-straight rib case is poor, the pressure drop is quite high, which is almost the same level as the V groove-v rib case. The friction factor increases with increasing Reynolds number but the rate of increase is higher for the cases with ribs.

Figure 5.19 shows the overall TPF of the seven geometries considered here. The highest TPF is observed with V groove-v rib case which shows TPF values in the range of 1.8-2.5 for the range of Reynolds number considered (13000<Re<55000). The angled groove-angled rib case comes second with TPF values 1.7-2.3. Among the cases without the ribs, the V groove-upstream geometry is the best performer (TPF ~1.4-1.7). The angled groove-straight rib case performs the

worst (TPF ~1-1.2) as it produces very high pressure drop without much heat transfer enhancement. The other cases produce TPF values in the range of 1.3-1.6.

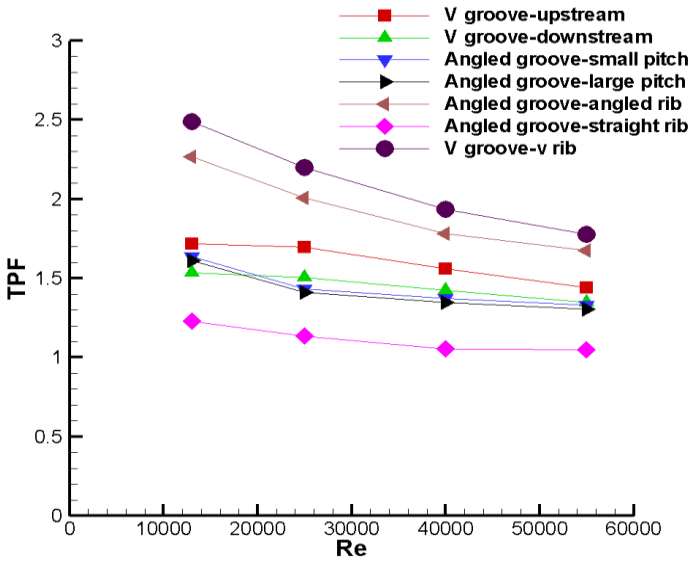

Figure 5.19: TPF of the geometries studied

The TPF values obtained in the current study are fairly high and it is important to compare the performance values with the performances of some standard and innovative rib geometries, which is the common standard in gas turbine blade internal cooling channels. The rib geometries considered for comparison are 1) 90°, 45°, and 60° parallel angled continuous ribs; 45° and 60° V continuous ribs from Han et al. (1991), 2) 90°, 45°, and 60° parallel angled broken ribs; 45° and 60° V broken ribs from Han and Zhang (1992), 3) Wedge and Delta arrangements from Han et al.(1993), and 4) 45° continuous and discrete W from Wright et al. (2004). The two geometries used for comparison from the current study are the angled groove-angled rib and V groove-v rib case as they perform the best among the current group. Figure 5.20 shows the comparison TPF plot.

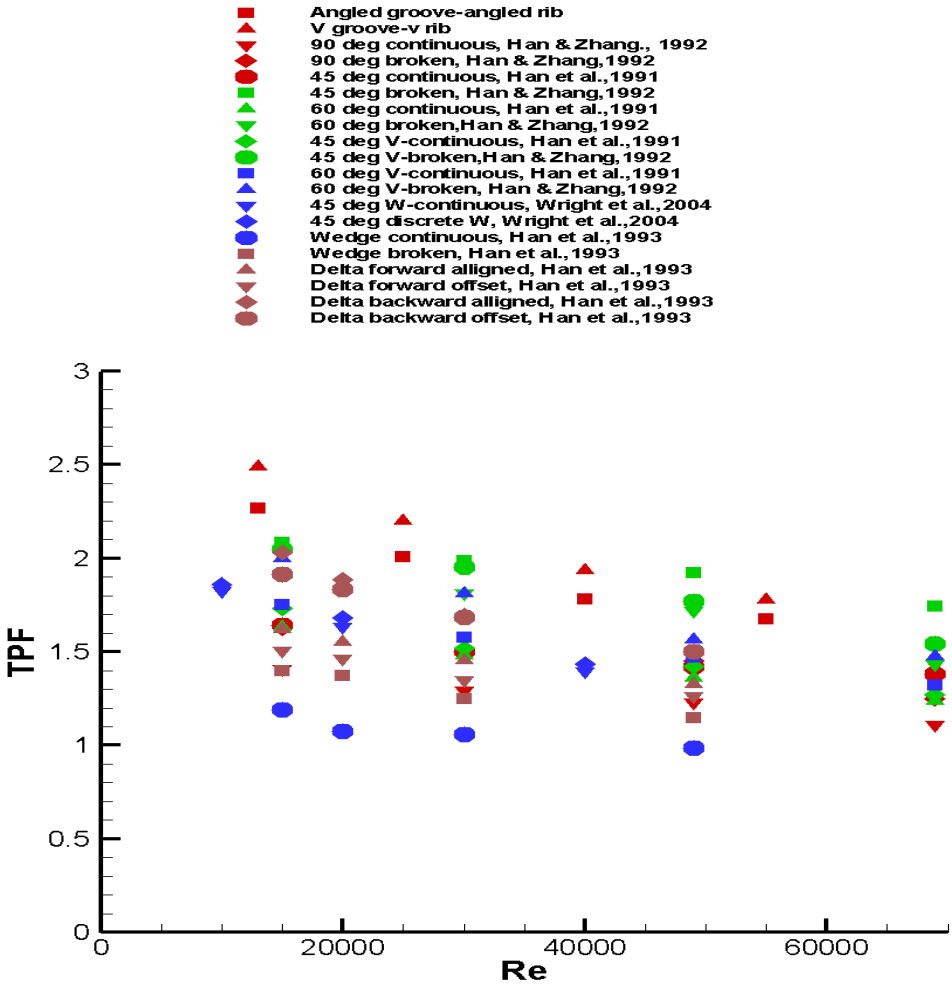

Figure 5.20: TPF comparison with some common and innovative rib geometries

It is seen that the V groove-v rib case in the current study performs the best for the low Re region (Re<40000). At higher Reynolds numbers, 45° broken rib configuration from Han and Zhang (1992) produces higher TPF.

5.3 Conclusions

The idea of using groove as turbulence promoter to enhance the surface heat transfer from the blade is explored. Some 45° angled parallel and V grooves are studied and 45° ribs are also

introduced in combination with the grooved geometries to enhance heat transfer more. The following major conclusions are obtained from the study:

1) The angled grooves produce secondary flow along the grooves. The secondary flow weakens along the angled groove as the flow is swept away by the mainstream flow. The interaction of the mainstream flow and the upwash flow from the grooves enhances heat transfer significantly at the downstream side of the groove. A separation zone exists at the upstream side of the groove where low values of Nu/Nu_0 are seen. This separation zone grows in size along the groove from the nose to the leg of the groove.
2) The Nu/Nu_0 values just downstream of the grooves can be as high as 4. The intra-groove Nu/Nu_0 values reduces in the streamwise direction until the next groove is reached. Same level of heat transfer enhancement is seen in the zones just downstream of the grooves and inside the grooves for different pitches of grooves but the intra-groove Nu/Nu_0 values are generally lower for the higher pitched groove cases.
3) The introduction of the angled ribs in conjunction with the angled grooves produces very high levels of heat transfer enhancements. The interaction of rib produced flow reattachment, groove produced upwash flow and mainstream flow increases the Nu/Nu_0 values to as high as 8. Without the groove effect, the interaction of rib produced flow reattachment and the mainstream flow increase the Nu/ Nu_0 values to about 6. The straight 90° ribs, when introduced on top of the angled groove, does not produce much heat transfer enhancement as the angled groove-angled rib case. As the flow goes under the ribs, the heat transfer values inside the groove become more uniform but the enhancement level is not much higher. Highest value of heat transfer enhancement is seen for the V groove-v rib case where local Nu/ Nu_0 values can go to as high as 9-10.

4) Averaged heat transfer value is highest for the V groove-v rib case which is in the range of 3.6-3.8. The angled groove-angled rib case comes second with values of about 3.1-3.2. The angled groove-straight rib case performs poorly.
5) The TPF obtained for the V groove-v rib case is the highest among the group (TPF ~1.8-2.5). When compared with some innovative rib designs found in open literature, it performs better or at the same level for the range of Reynolds numbers considered.

CHAPTER 6: ENTRANCE GEOMETRY RESULTS

6.1 Experimental heat transfer study under stationary condition

All of the studies concerning the heat transfer in internal cooling channel geometries examine simplified canonical entrance geometries such as a contraction, 90-degree entrance, or straight entrance. In actual turbine engines, the entry geometry can include other shapes such as a S-shape entry, 90 degree entry, or twisted entry. Some of the actual entrance geometries found in actual gas turbine blades are shown in Figure 6.1.

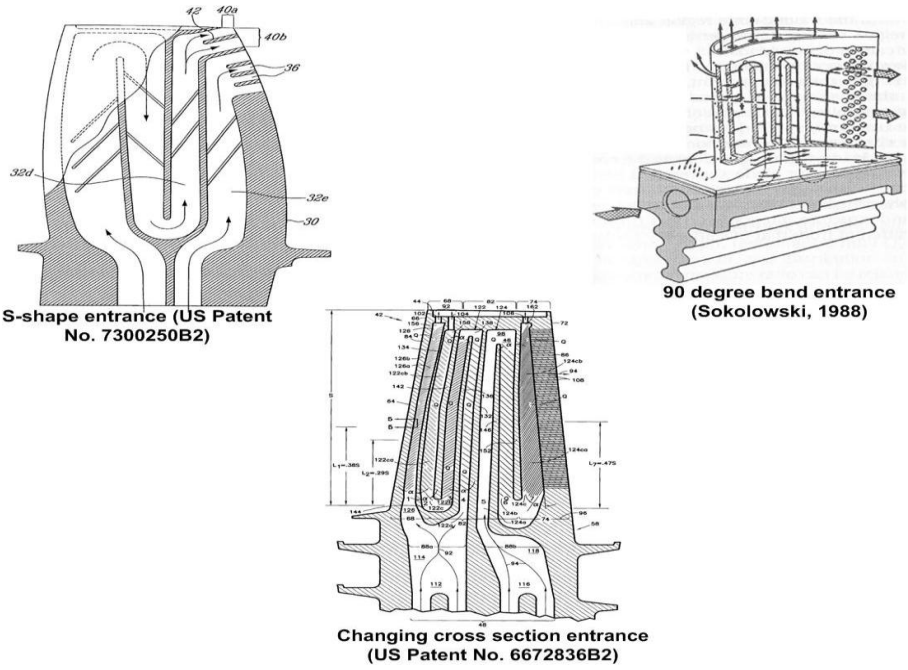

Figure 6.1: Some of the entrance geometries used in real turbine blades

The effect of such realistic entry geometries has not been studied before. Further, earlier studies provide single-point local data or regionally-averaged heat transfer coefficient values. Detailed heat transfer coefficient measurements showing the spanwise variation of heat transfer coefficient due to relevant entrance geometries has not been presented before and is of interest to the engine designer. The current work presents three different entrance geometries that are of

relevance to gas turbine engines: an S-shaped entrance, a 90-degree bend entrance, and a twisted entrance with the aspect ratio changing from a 4:1 rectangle at inlet entry to 1:4 before the test section. Detailed heat transfer coefficient values are obtained with transient liquid crystal technique in a stationary frame at four set of Reynolds number (15000<Re<55000). Tests were done with the entrance geometries for both smooth and angled ribbed channel. Heat transfer values obtained with the three entrance geometries are compared with a fully developed straight entrance (baseline) to understand the effect of the entrance geometry on the heat transfer enhancement.

6.1.1 Geometries used during the test: The test section is a two pass rectangular channel with an aspect ratio of 1:4. The width W of the test section is 0.49 in. (12.446 mm) and the height H of the test section is 1.96 in. (49.784 mm). The divider wall thickness is kept at 0.118 in. (2.997 mm). The entrance section is 4 in. (101.6 mm) and the test section is 8 in. (203.2 mm) long in the streamwise direction. The walls of the entrance section and the test section are made out of a 0.75 in. (19.05 mm) thick clear polycarbonate sheet.

Three entrance geometries are used for the experiments. These geometries are relevant to specific turbine cooling configurations found in practice. The schematics of the entrance geometries are shown in Figure 6.2. In all cases, the main coolant passage is downstream of the entry geometry. Figure 6.2(a) shows an S-shaped entrance where the exit of the entrance is offset from the entry. The offset of the S-shape is 4 times the width of the channel. Figure 6.2(b) is a 90 degree bend entrance where the flow takes two 90 degree turns before entering the test section. Figure 6.2(c) shows the schematic of the twisted entry where the flow enters a 4:1 AR channel at the base of the entry and exits to a 1:4 AR channel leading up to the coolant passage. In our test apparatus, the entrance geometries are removable from the test section and are attached with the

test section by a flange. For comparison, a fully developed straight entrance of 13 hydraulic diameters in length is also tested, and is used as the baseline.

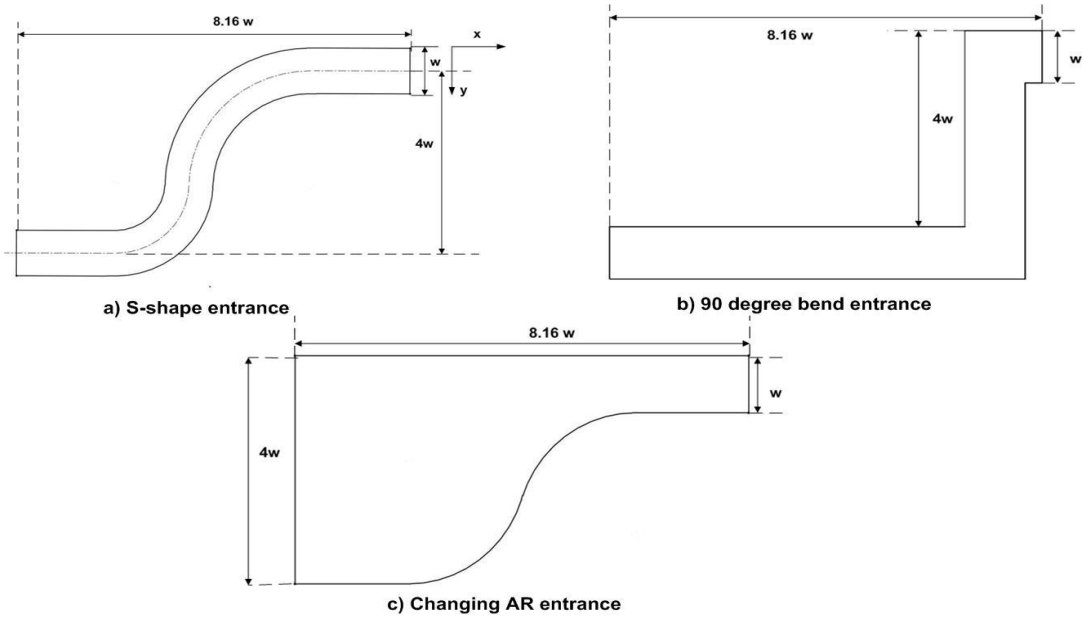

Figure 6.2: Schematics of the entrance geometries used

For the rib-roughened test section, polycarbonate ribs are attached to the test section surface using double sided tape. The schematic of the rib arrangement is shown in Fig. 6.3. The ribs are square in cross section and are inclined to the flow at an angle β of 45°. The rib height to channel hydraulic diameter ratio (e/D_h) is 0.1 and the rib pitch to rib height ratio (P/e) is 10. The ribs are attached in inline arrangement for both the walls.

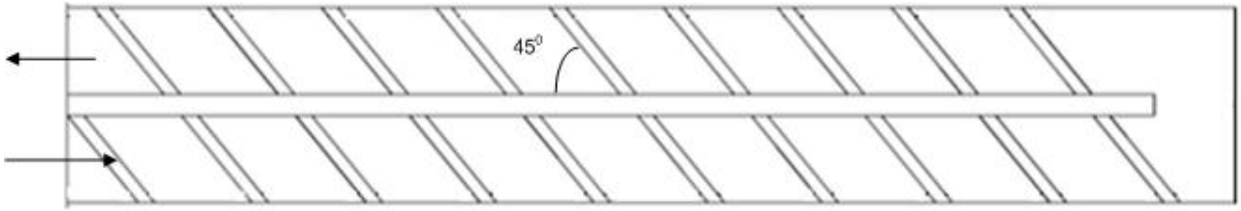

Figure 6.3: Schematic of the ribbed test section

6.1.2 Results: Heat transfer coefficient maps are obtained for the entrance geometries and the test section at four different Reynolds number (Re) of 15000, 25000, 40000, and 55000. Nusselt number is obtained from the heat transfer coefficient and normalized with the Nusselt number (Nu_0) for a simple smooth channel given by the Dittus-Boelter correlation (Dittus and Boelter, 1930).

$$Nu_0 = 0.023.Re^{0.8}Pr^{0.4} \qquad (6.1)$$

The Nu/Nu_0 contour maps are presented for both the entrance geometries and the smooth and ribbed test sections. Line plots showing the Nu/Nu_0 variation in the (spanwise) y-direction at different streamwise locations are shown to characterize the quantitative development of the Nusselt number profiles due to the entrance geometry effects. Streamwise averaged and total averaged Nu/Nu_0 plots inside the test section are plotted to see the overall effect of the entrance geometries on the heat transfer from the test section wall.

6.1.2.1 Detailed Nu/Nu_0 distribution: Figure 6.4 (a)-(c) represent the detailed Nu ratio distribution for the three entrance geometries at Re = 15000 and Re = 40000 with the smooth test section. The Nusselt number ratio profile for the other Reynolds numbers are not shown here, but are similar with the Nu ratio decreasing with increasing Re value. The high heat transfer enhancement at the entrance is because of the transition from a circular pipe to rectangular diverging cross section. For the s-shape channel, the flow is close to the inner wall (higher y/Dh) at the exit of the second bend toward which the flow migrates (See Fig. 6.5a). The high velocity air sticks to the inner portion of the second bend of the s-shaped channel contributing to higher values of heat transfer enhancement in this region (Fig. 6.4a). Dean (1928), Miller (1978) explained the formation of secondary flow in a curved duct. The core flow is initially deflected

to the outer bend because of centrifugal and pressure force and the fluid approaching the outside of the bend experiences an adverse pressure gradient. This results in the formation of two counter rotating vortical structures at the end of the first bend. The secondary flow takes the core fluid from the outer side to the inner side of the bend. Taylor et al. (1982), Ng et al. (2006) further extended this to the s-shape bend and concluded that in the second bend of the s-shape there still exist two vortical structures like the first bend. In an s-shape bend the flow migrates towards outside of the first bend and exits near the inside wall of the second bend. Due to the higher velocity of air close to the inner bend of the s-shape, the heat transfer enhancement in the test section close to the inner wall of the bend is higher compared to the side close to the outer bend.

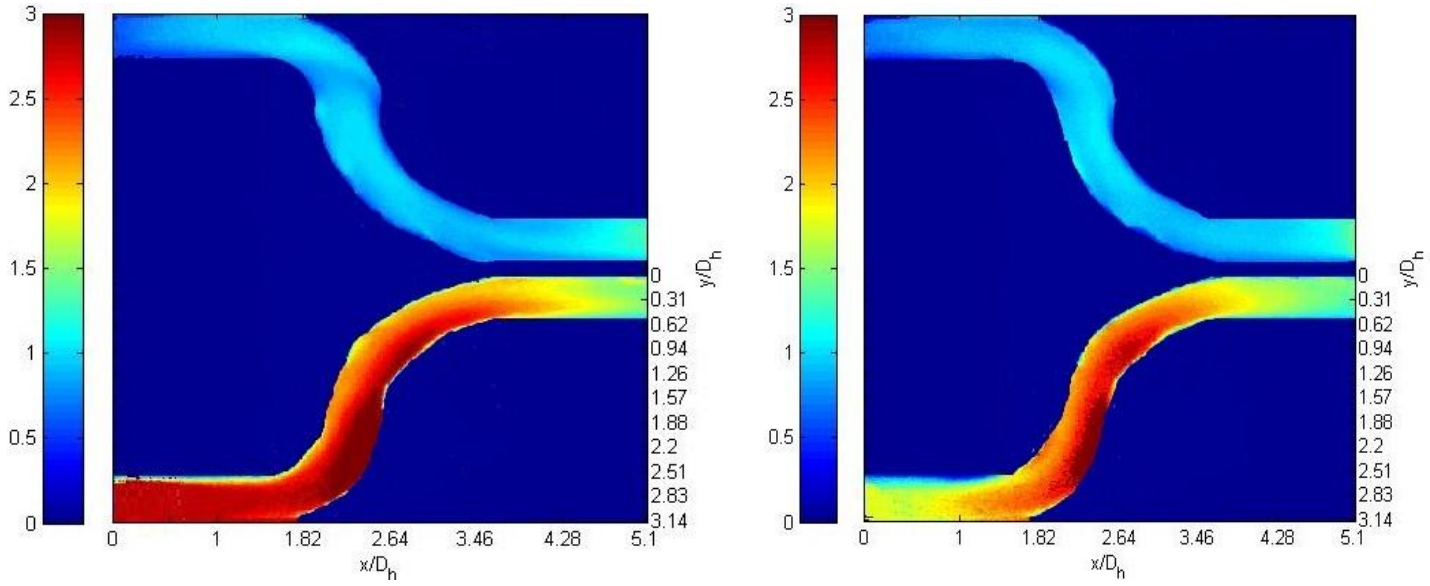

a) Re =15000 b) Re =40000

a) Nu/Nu_0 contour map for the s-shape entrance

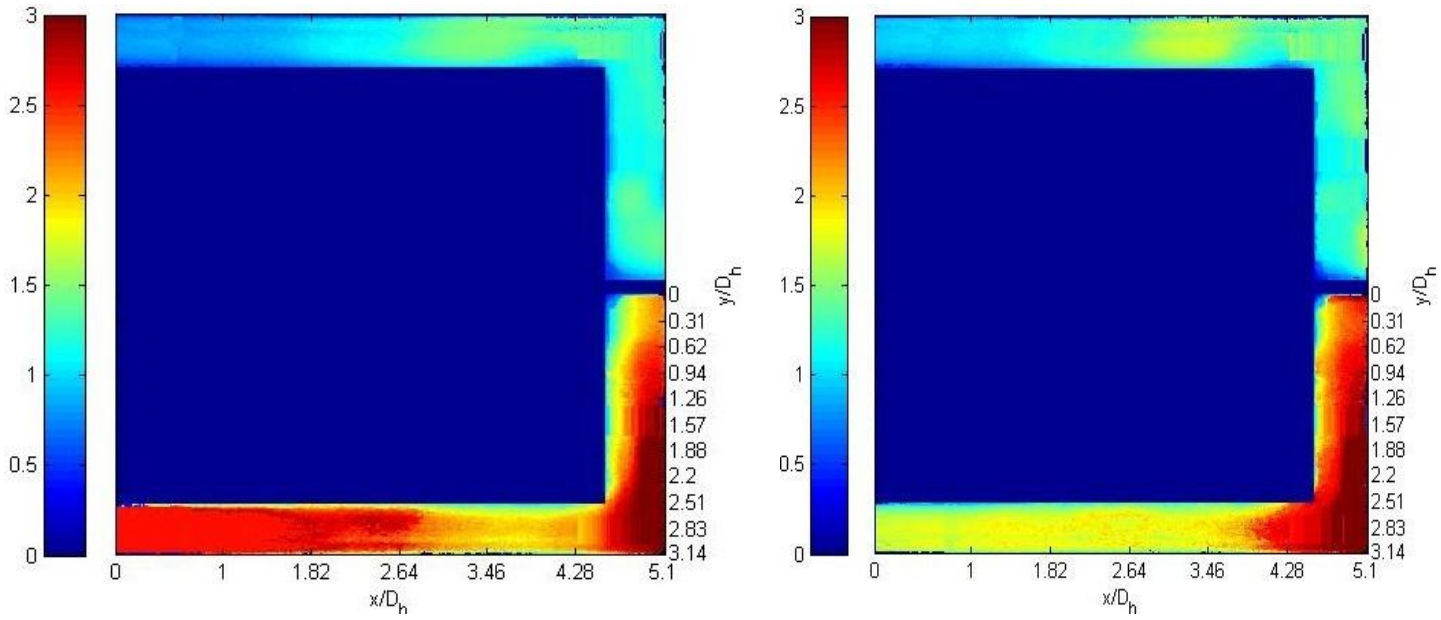

a) Re =15000 b) Re =40000

b) Nu/Nu_0 contour map for the 90 degree bend entrance

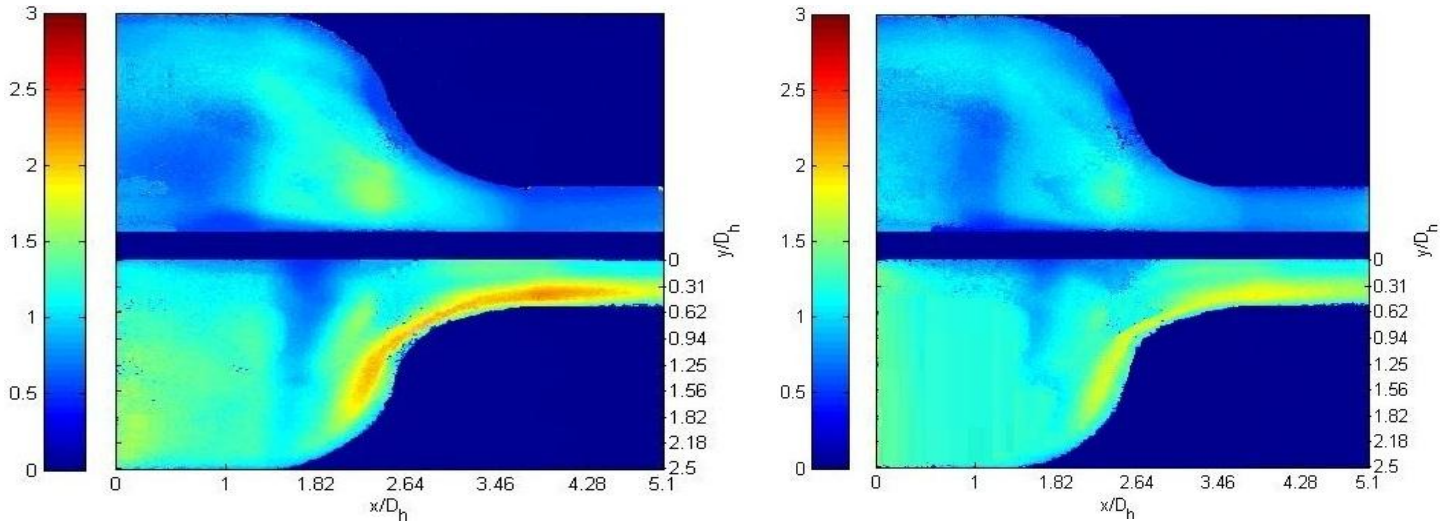

a) Re=15000 b) Re =40000

c) Nu/Nu_0 contour map for the changing AR entrance

Figure 6.4: Nu/Nu_0 contour for the entrance geometries

In the 90 degree bend entrance geometry, the flow takes two 90 degree turns before entering the test section. This results in high heat transfer at the flow turn region. Initial high Nu/Nu_0 values are due to the diverging circular to rectangular cross-section upstream of the geometry. Heat

transfer coefficient gradually starts to reduce as the flow progresses through until it hits the first 90° bend. The flow is unable to take such a sharp bend and hits on the outside of the wall to produce impingement effects resulting in high heat transfer coefficient values. As the flow progresses further, it approaches the second 90 degree bend. Here also a high heat transfer coefficient zone is observed at the impingement region downstream of the turn. Due to the second impingement effect, higher heat transfer enhancement in the entrance region is observed close to the divider wall of the two pass test section.

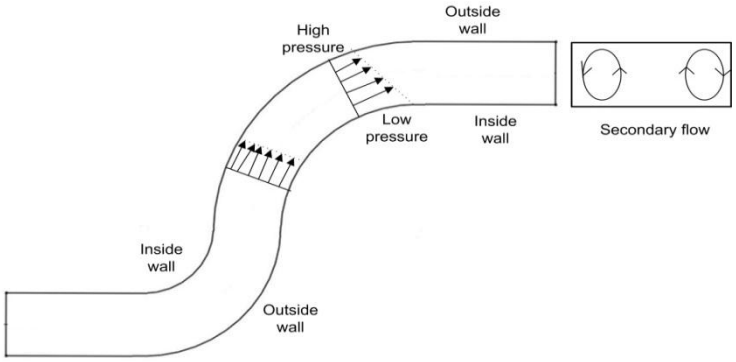

a) S- shape channel

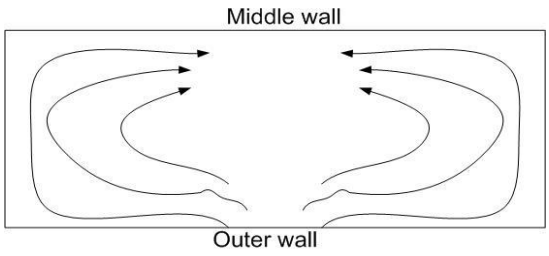

b) Cross section secondary flow pattern after the change in cross section

Figure 6.5: Cartoon of the flow patterns in (a) S-shaped and (b) twisted-changing AR channel

For the twisted entry with changing ARs, the change in cross section produces a complex flow path which increases heat transfer enhancement greatly due to the secondary flows. In this changing AR entrance case, the flow is fully developed before in enters the changing cross section entrance geometry. A long 4:1 AR developing test section is used before the changing cross section entrance geometry. The schematic of the anticipated flow pattern is shown in Figure 5b. As the flow approaches the test section, the cross section reduces in the streamwise direction which results in the convergence of streamlines. But the cross section increases in a direction perpendicular to the plane of the paper which results in secondary flows. The flow

convergence and secondary flows causes high heat transfer enhancement before the entrance to the test section. The heat transfer pattern is non-uniform just like the s-shape case as Nu/Nu_0 values is higher in the higher y/D_h side.

Figure 6.6 shows the heat transfer enhancement contour map for the smooth test section at Re = 15000 with the three entrance geometries. As noted earlier, the test sections are located immediately downstream and contiguous to the entrance geometries. Attention should be focused near the entry regions of the test section since this is where the mal-distribution of the upstream flow has the greatest impact. The contour plot for the smooth test section with s-shape entrance also show that the heat transfer enhancement is low closer to the middle wall and higher towards the inner bend of the s-shape. As the flow progresses through the test section the entrance effect seems to die down, but still persists all the way to the 180° bend. From the entrance to the 180° the length of the test section is only 9.5 times the hydraulic diameter and the flow does not get to fully developed condition within this length. Downstream of the U-turn in the test section, the usual patterns of high heat transfer near the outer regions of the bend (associated with impingement) and low heat transfer past the inner corner (associated with separation) are observed. From the heat transfer enhancement contour map of the test section with the 90 degree bend entrance, the high heat transfer enhancement zone due to impingement is clearly visible close to the divider wall of the test section. There seems to be a recirculation zone close to the inner wall of the 1st pass which contributes to low heat transfer enhancement. Entrance effects die down downstream of the test section inlet but it is still present in some form up to the 180° bend. For the test section with the twisted, changing-AR entrance, a more uniform distribution of heat transfer enhancement is observed compared to the s-shape entrance or the 90 degree bend entrance at the start of the test section. After a length of about 2 times the hydraulic diameter, the

flow shifts a little bit away from the middle wall. This effect is present till the end of the 1st pass and the flow does not reach fully developed condition in the 1st pass. For all the entrance geometries, the effect of entrance geometry is not present after the turn.

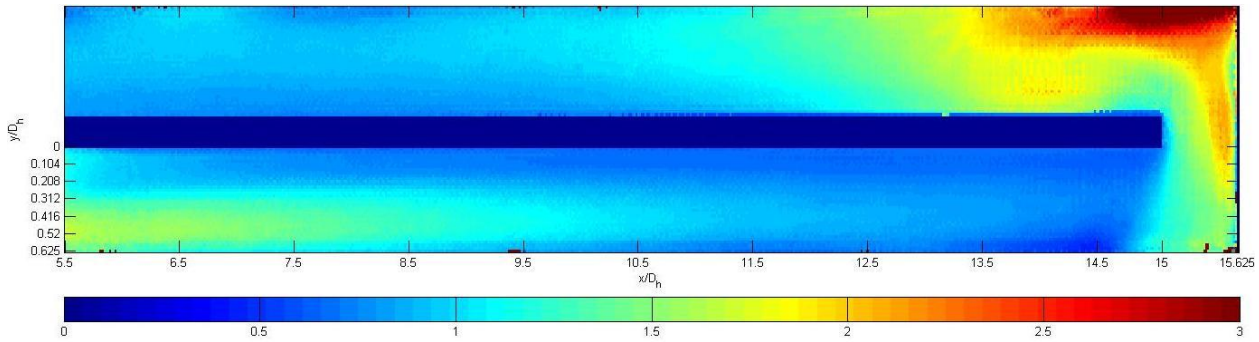

a) Nu enhancement contour map for the s-shape entrance

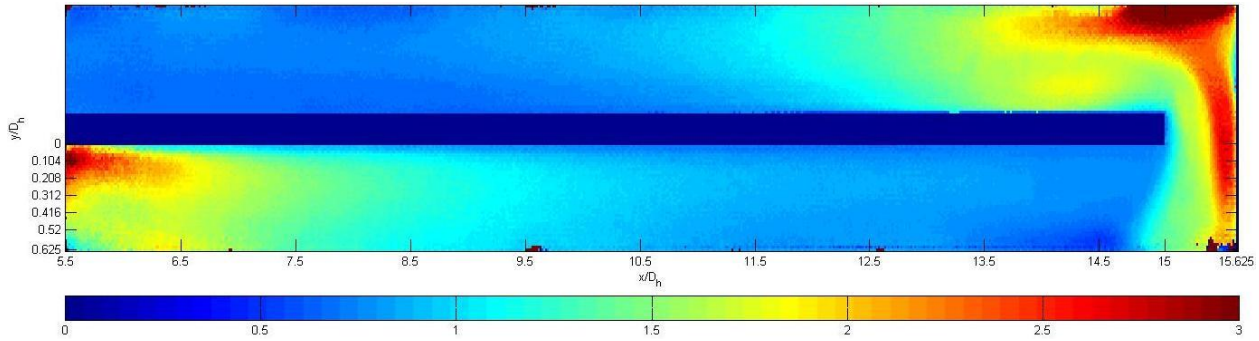

b) Nu enhancement contour map for the 90 degree bend entrance

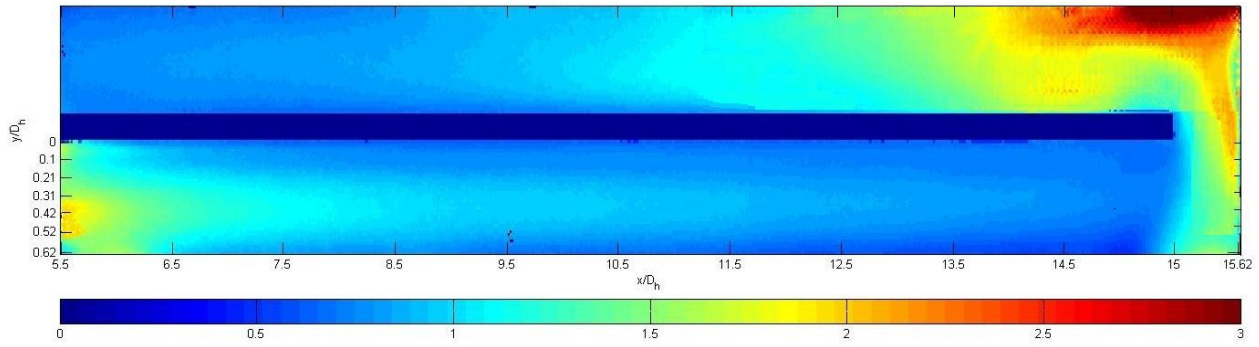

c) Nu enhancement contour map for the changing AR entrance

Figure 6.6: Nu enhancement contour map for the smooth test section with different entrance geometries

Turning attention to the ribbed geometries, we will focus attention primarily in the region downstream of the entrance section. Figure 6.7 shows the heat transfer enhancement contour map for the ribbed test section at Re = 15000 with the three entrance geometries. Of specific interest is to see if the entry effect in the ribbed channel is similar to the smooth channel.

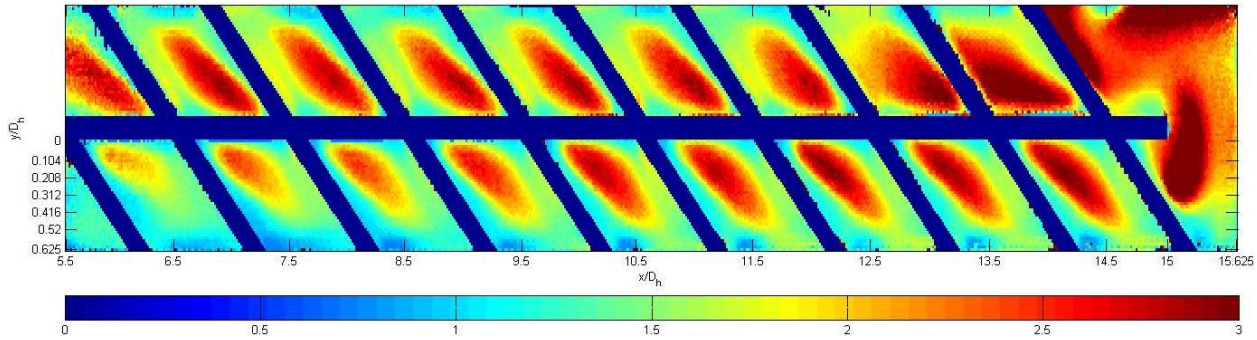

a) Nu enhancement contour map for the s-shape entrance

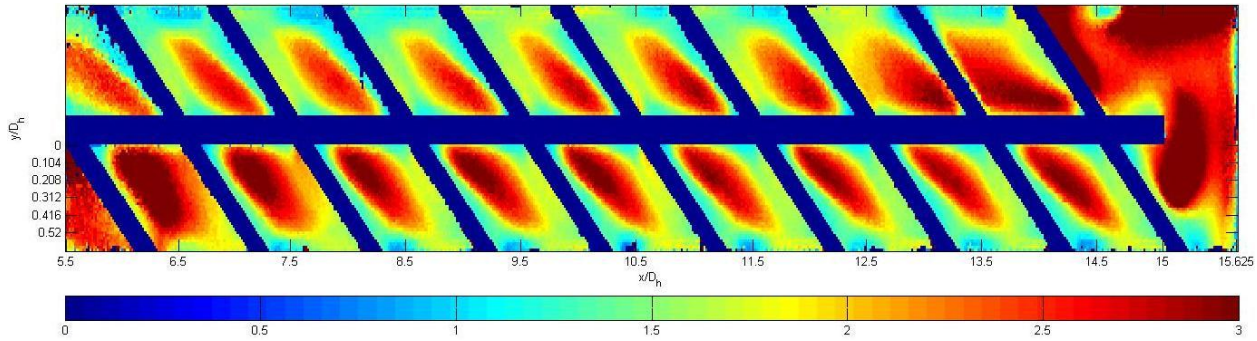

b) Nu enhancement contour map for the 90 degree bend entrance

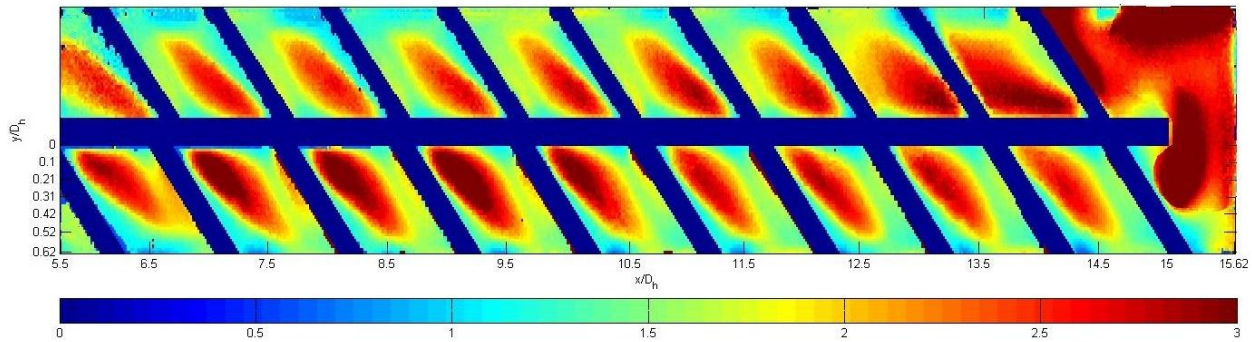

c) Nu enhancement contour map for the changing AR entrance

Figure 6.7: Nu enhancement contour map for the ribbed test section with different entrance geometries

It can be seen from Fig. 6.7(a) that the s-shape entrance reduces the heat transfer enhancement in the entrance of a ribbed test section. The schematic of the flow patterns due to interaction of the entrance geometry induced flow and rib induced secondary flow is shown in Figure 6.8.

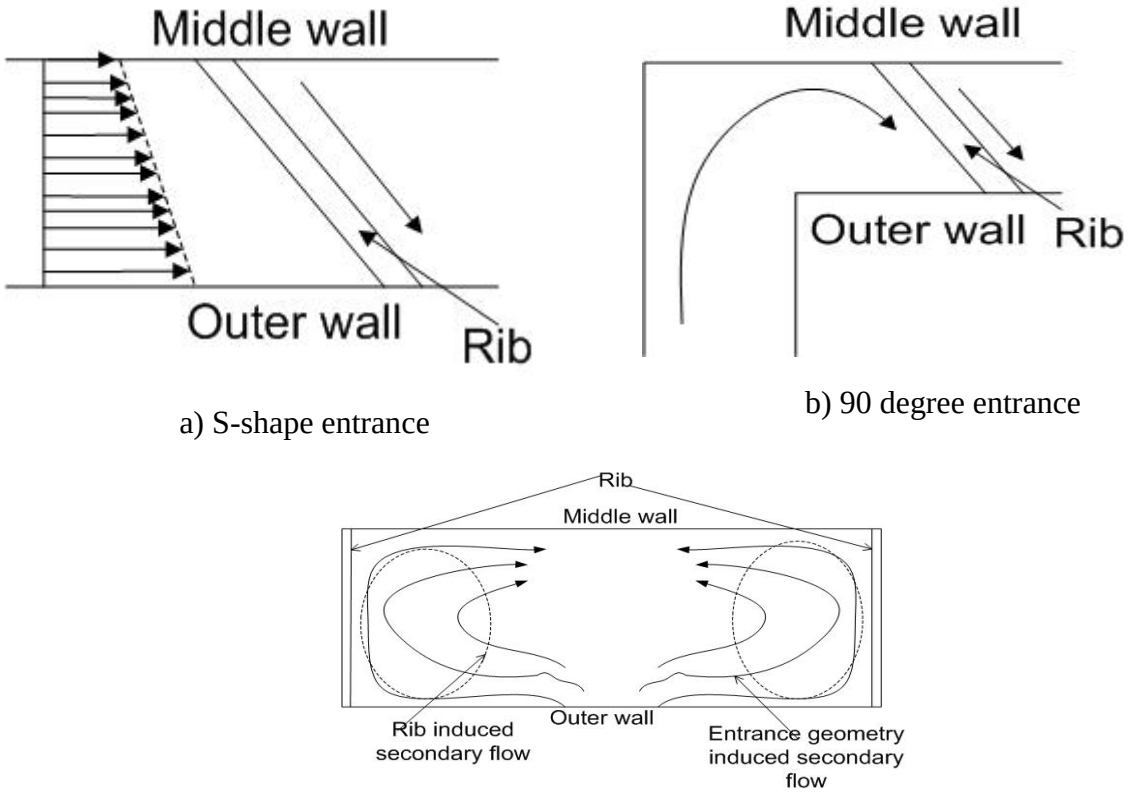

a) S-shape entrance

b) 90 degree entrance

c) Changing AR entrance

Figure 6.8: Schematic of flow pattern in the entrance of ribbed test section

For the s-shape entrance, the higher velocity fluid sticks to the outer wall of the 1st pass. The rib induced secondary flow is directed from the middle wall to the outer wall close to the sidewall (liquid crystal painted surface) and from the outer wall to the middle wall close to the core of the test section. So, two cells of a moving counter rotating vortex are produced which enhances the heat transfer more closer to the middle wall than along the outer wall. The presence of the S-shape entrance alters this flow field since more high velocity air is available close to the outer

wall of the test section compared to the middle wall. The interaction of the S-shape induced flow pattern and rib induced secondary flow therefore reduces the heat transfer enhancement at the entrance of the test section and thus the heat transfer is more uniform in the y direction.

For the 90 degree bend entry and changing-AR entry, more heat transfer enhancement is obtained at the entrance of the ribbed test section compared to the other regions of the 1st pass. In case of the 90 degree bend entrance, the flow takes a sharp 90 degree turn and impinges on the middle wall side of the test section. The secondary flow due to the ribs is also directed from the middle wall to the outer wall. So for the 90 degree bend entrance case, most of the flow is close to the middle wall which gets convected due to the rib induced secondary flow, resulting in higher heat transfer enhancements close to the middle wall. For the changing-AR entrance geometry, the secondary flow due to the change in cross section is in clockwise direction before entering the ribbed test section. The rib induced secondary flow is in the counter clockwise direction. The interaction of the secondary flows going in opposite directions increases turbulence and enhances the heat transfer coefficient at the entrance of the ribbed test section.

6.1.2.2 Nu ratio line plots: Figure 6.9 shows the Nu ratio line plots at different streamwise locations for Re =25000. From the smooth test section Nu ratio plots (Figs. 6.9 (a), (c) and (e)), it can be seen that the 90 degree entrance produces highest localized Nu ratio close to the middle wall due to impingement effect where the impingement zone Nu ratio is about 100% higher than the Nu ratio close to the outer wall. Nu ratio values are also high at the entrance with the changing-AR entrance but the profile is more uniform. The effect of high velocity air sticking to the outer wall side is prominent from the Nu ratio profile inside the test section with s-shape entrance.

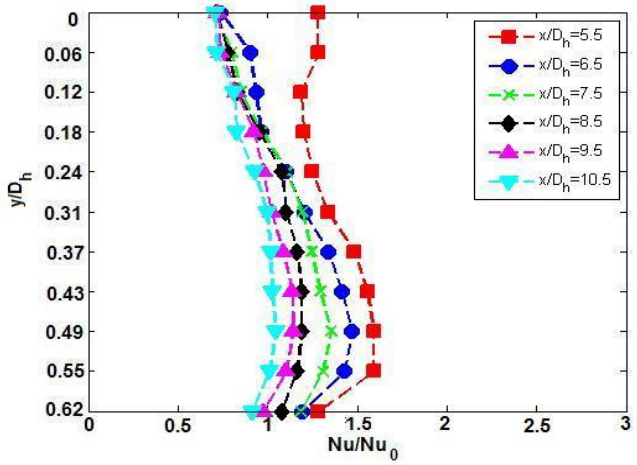

a) S- shape entrance smooth test section

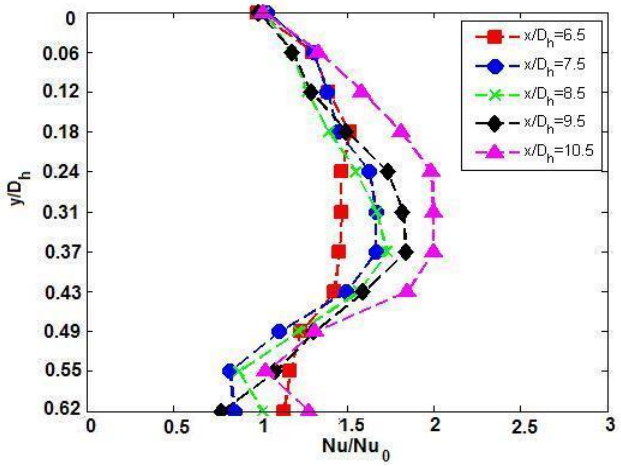

b) S- shape entrance ribbed test section

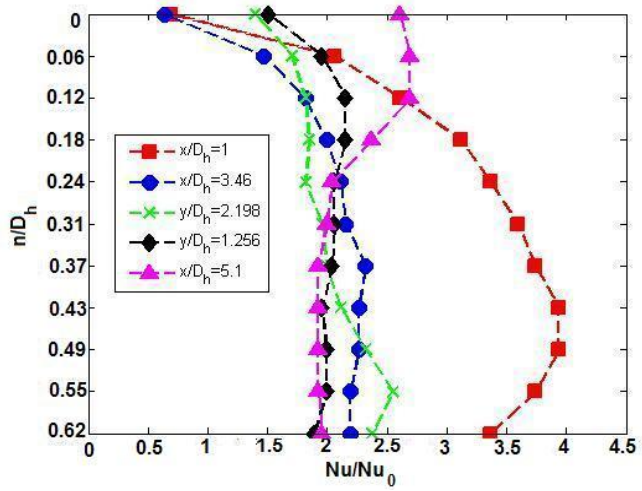

c) 90 degree entrance smooth test section

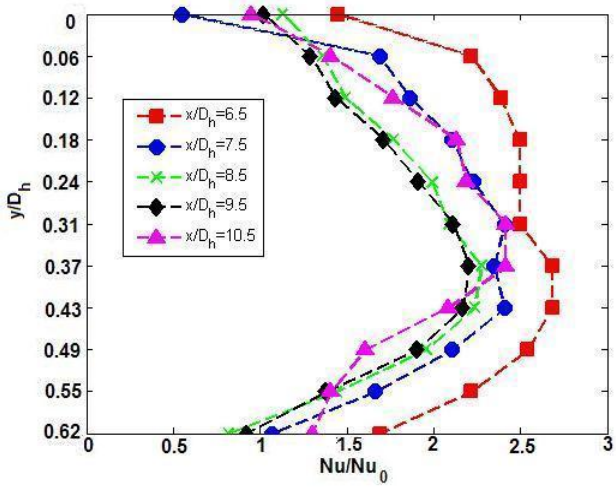

d) 90 degree entrance ribbed test section

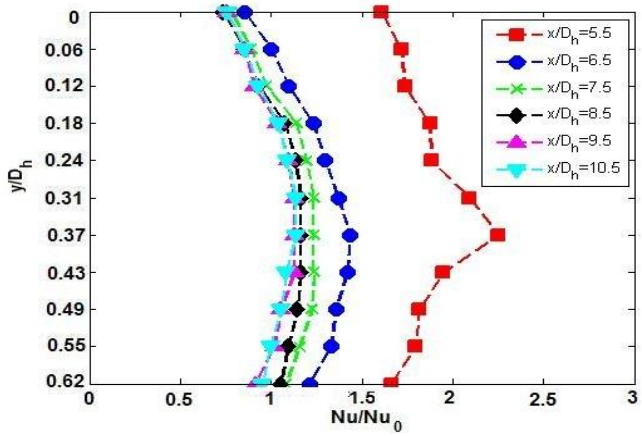

e) Changing AR entrance smooth test section

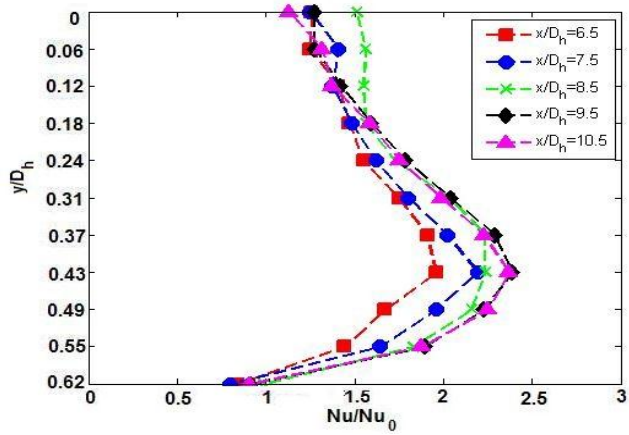

f) Changing AR entrance ribbed test section

Figure 6.9: Nu ratio line plot at different streamwise locations (Re =25000)

For the ribbed test section (Figs. 6.9 (b), (d) and (f)), it can be seen that the Nu ratio values are low for the first few hydraulic diameters with the S-shape entrance but increases afterwards. The 90 degree bend entrance and changing AR entrance shows high Nu ratio values at the entrance of the test section and Nu ratio reduces as the flow progresses further in the test section.

6.1.2.3 Averaged data: Heat transfer enhancement values are averaged to compare the performances of all the entrance geometries tested. Figure 6.10 shows the averaged Nu ratio plot for all the entrance geometries at Re = 55000. Here $x/D_h = 0$ means the inlet of the test section, not the inlet of the entrance geometry. Nu ratio values are averaged over one hydraulic diameter length. The average values are compared with a fully developed entrance geometry. It can be seen that all the entrance geometries produces significant heat transfer enhancement in the first pass of the channel compared to the fully developed case. The heat transfer enhancement values begin to decrease as the flow progresses further inside the first pass. Close to the end of the 1st pass (x/D_h =9.6), the heat transfer enhancement value increases slightly due to the presence of the turn. But heat transfer enhancement values for none of the geometries reach fully developed value. The 90 degree bend entrance and the changing AR entrance performs better than the s-shape entrance.

The S-shape entrance geometry performs worst with the ribbed test section. Throughout the 1st pass, averaged Nu ratio values are lower compared to the other entrance geometries. The changing AR entrance geometry performs similar to the fully developed entrance, thought the averaged Nu/Nu_0 values are slightly lower than the fully developed case. The 90 degree entrance increases Nu ratio values at the entrance of the test section initially and then the Nu ratio reaches an asymptotic value as the flow progresses further in the ribbed test section.

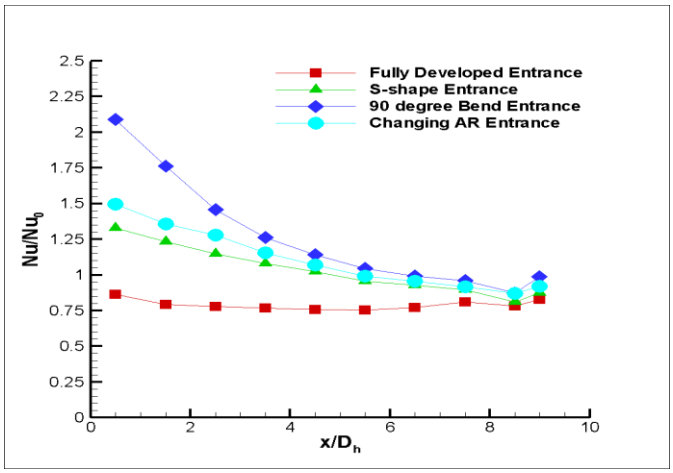

a) Smooth test section

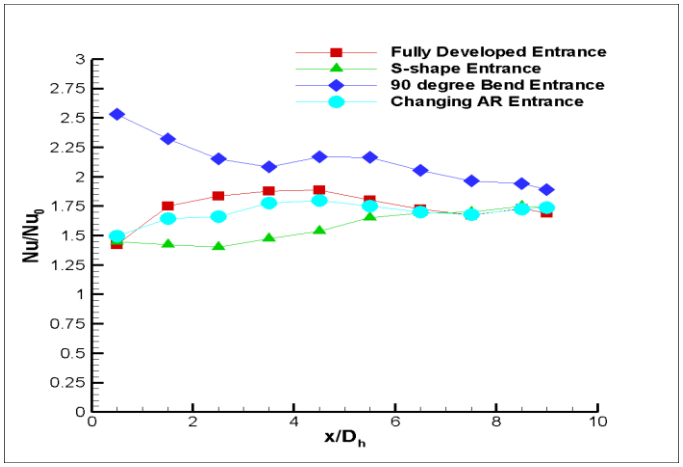

b) Ribbed test section

Figure 6.10: Averaged Nu/Nu_0 in the 1st Pass (Re=25000)

Figure 6.11 shows the overall averaged Nu/Nu_0 values for the two pass test section with different entrance geometries. The 90 degree bend entrance produces the highest heat transfer enhancement both for smooth and ribbed test section. A change in entrance geometry from the fully developed entrance to 90 degree bend entrance for a smooth test section increases the averaged heat transfer enhancement values by about 11%. For the ribbed case, the S-shape entrance reduces overall Nu ratio compared to fully developed entrance by about 7%, but the 90 degree bend entrance increases it by 8% compared to fully developed entrance. Compared to the

fully developed entrance, introduction of the changing AR entrance also has got detrimental effect on the overall heat transfer values.

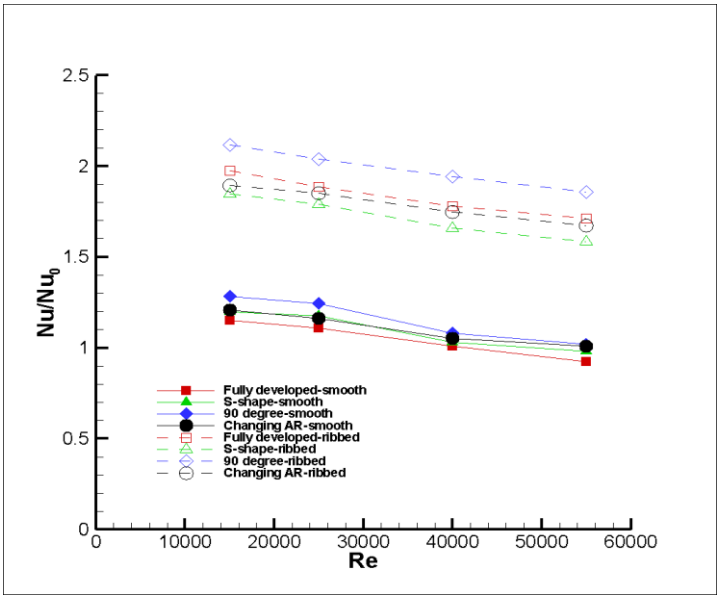

Figure 6.11: Comparison of overall Nu ratio of the 2 pass channel with different entrance geometries

6.1.3 Conclusions: Three entrance geometries of a gas turbine blade internal cooling channel are tested in stationary frame. Detailed and averaged heat transfer enhancement data are presented for a smooth and ribbed test section. The conclusions from the study are:

1) Effect of entrance geometry is prominent with a smooth test section. The S-shape entrance makes the high velocity air flow away from the divider wall of a two pass channel and enhances the regional heat transfer. Instead of a fully developed velocity profile at inlet of the test section, the velocity and heat transfer profile is skewed towards the outer wall. Flow impingement in the bend region just after a 90 degree bend increases heat transfer values at the entrance of test section. A small recirculation zone is formed after the impingement zone which results in low localized heat transfer enhancement

values. Complex change in entry cross section creates secondary flows that results in increase of heat transfer coefficient at the entrance of the smooth test section.

2) Effect of entrance geometry is less prominent with a ribbed test section. The velocity profile at the inlet of the ribbed test section with S-shape entrance affects the rib generated secondary flows and reduces heat transfer enhancement at the entrance of the test section. Impingement at the entrance of the ribbed test section enhances heat transfer with 90 degree bend entrance. The generated secondary flow after impingement assists the rib generated secondary flow. For the changing-AR entrance, the rib generated secondary flow and entrance generated secondary flow are in opposite direction. Their interaction reduces the overall Nu ratio values compared to a fully developed case.
3) Heat transfer enhancement for a smooth channel with the entrance geometries is always higher than the fully developed entrance throughout the 1^{st} pass. At the entrance, the averaged heat transfer values for a smooth test section can be more than 2 times higher than the fully developed entrance values. For the ribbed test section, the effect of entrance geometry is present for first few hydraulic diameters only.
4) Overall averaged heat transfer enhancement values for a smooth test section are lowest for a fully developed entrance and highest for a 90 degree bend entrance (about 11% higher than fully developed entrance). All the entrance geometries provide more heat transfer enhancement than the fully developed entrance. For a ribbed test section, the overall averaged heat transfer values with S-shape entrance is about 7% lower than the corresponding fully developed entrance. Here also the 90 degree bend entrance provides the highest heat transfer enhancement (about 8% higher than fully developed entrance).

6.2 Numerical study under rotating condition

6.2.1 Grid generation and computational setup: The numerical data is presented for a single pass only. Tetrahedral unstructured meshes were generated using ANSYS ICEM CFD. The grid topology for the S-shape entrance geometry is shown in Figure 6.12.

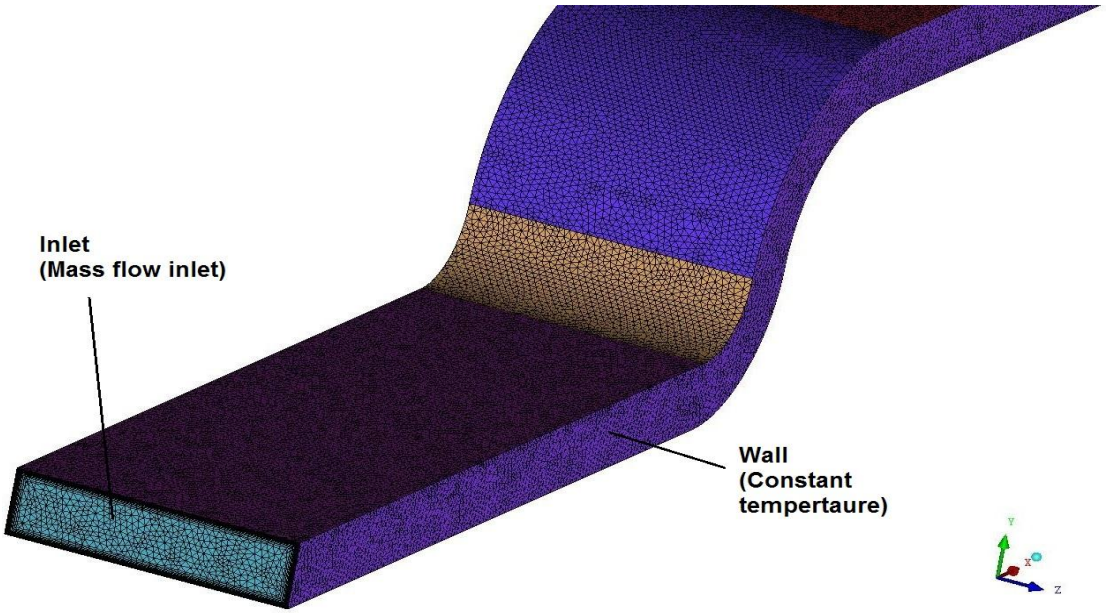

Figure 6.12: Tetrahedral mesh with prism layers (s-shape entrance geometry)

The main flow volume was meshed using tetrahedral meshes and the near wall was meshed using prism layers. RANS equations were solved using a low-Re realizable k-ε model. To maintain the requirement of the turbulence model, a y+ value of 0.5 was chosen for the first grid point near the wall, and the near-wall region was represented by 20 prism layers that are generated close to the wall. A total number of about 4 million cells were used for the simulations. Previous studies by researchers have shown that the RANS formulation gives reasonable agreement with the experimental data (Schüler et al. 2011, Chen et al. 2011, Schüler et al. 2011a) and it takes much less computational time than RSM or LES. In this study, the low-

Re realizable k-ε model (Wilcox, 2006) with enhanced wall treatment was used in the commercial finite volume solver FLUENT (Fluent Inc., 2006) as a compromise between computational time and accuracy. Air was used as the working fluid. A steady state pressure based solver was used in FLUENT for the solution and pressure-velocity coupling was handled by the SIMPLE (Acharya et al., 2007) algorithm. To achieve fully developed boundary condition at the inlet of the entrance geometry and downstream test section, a long straight length is used upstream of the entrance geometry. Constant wall temperature of T_w=353 K was chosen for all the channel walls. The outflow boundary condition is used at the exit. The Reynolds number based on the hydraulic diameter of the channel was 15000. For convergence criteria, the residuals are chosen as 10^{-6} for the continuity, the momentum and the turbulence equations and 10^{-9} for the energy equation. The average heat transfer coefficient on wall was also used as an additional convergence criterion. Rotation is introduced by moving the reference frame at constant speed and relative velocity formulation is used for the pressure based solver. Moving wall boundary conditions are specified for all the walls with zero rotational speed relative to the adjacent cell zone.

6.2.1.1 Data reduction: The wall heat flux and the local bulk air temperature were obtained from the numerical solution, and the heat transfer coefficient was then obtained by

$$h = {q_w}/{(T_w - T_{bulk})} \qquad (6.2)$$

where q_w is the wall heat flux, T_w is the constant wall temperature and T_{bulk} is the mainstream air temperature. The Nusselt number is obtained from the heat transfer coefficient as

$$Nu = {hD_h}/{k} \qquad (6.3)$$

where k is the thermal conductivity of air.

To present the results, the Nusselt number was normalized using the Dittus Boelter correlation (1930)

$$Nu_0 = 0.023.Re^{0.8}Pr^{0.4} \qquad (6.1)$$

6.2.1.2 Rotational parameters: For every entrance geometry two Rotation numbers are studied. Rotation number is defined as

$$Ro = \frac{\omega D_h}{V} \qquad (6.4)$$

where ω is the rotational speed and V is the mainstream air velocity.

For each Rotation numbers four Density ratios are studied. Density ratio is defined as

$$DR = \frac{\rho_b - \rho_w}{\rho_b} = \frac{T_w - T_b}{T_w} \qquad (6.5)$$

Reynolds number is kept fixed at Re =15000 for all the cases. Table 6.1 shows all the parameters studied. For all the cases, the wall was kept at a fixed temperature of T_w =353 K. The inlet bulk temperature was varied from 213 K to 317 K to achieve different Density ratios.

Table 6.1: Range of parameters studied

Entrance geometry	Re	Ro	DR
S-shape	15000	0.1	0.1, 0.2, 0.3, 0.4
		0.2	0.1, 0.2, 0.3, 0.4
90 degree bend	15000	0.1	0.1, 0.2, 0.3, 0.4
		0.2	0.1, 0.2, 0.3, 0.4
Changing AR	15000	0.1	0.1, 0.2, 0.3, 0.4
		0.2	0.1, 0.2, 0.3, 0.4

6.2.2 Results: In order to validate the numerical scheme, predicted results are compared with heat transfer experimental data under rotation by Liou et al. (2001). The comparison between the regionally averaged Nu/Nu_0 values is shown in Figure 6.13.

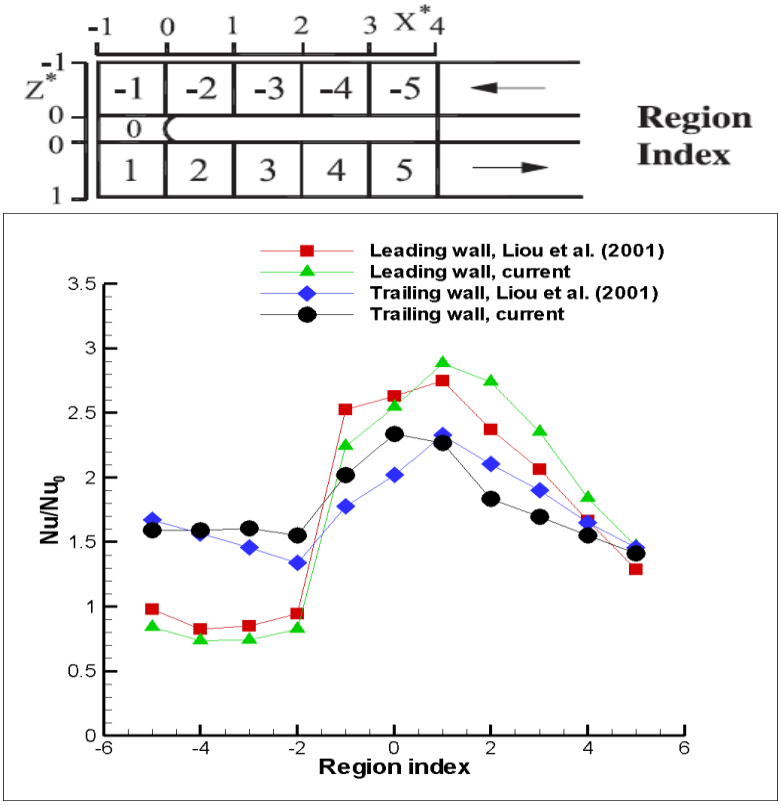

Figure 6.13: Regional averaged Nu/Nu_0 comparison with experimental data (Liou et al., 2001)

In most of the regions, the agreement between numerical and experimental data is within 10%. The maximum deviation from the experimental data is about 15%. The disagreement is maximum in the bend region.

Detailed Nu/Nu_0 contour plots, streamwise plane and cross plane velocity contour plots and streamlines are plotted for each geometry at two extremes of rotation, i.e. Ro =0.1, DR =0.1 and Ro =0.2, DR =0.4. Rotation effects at intermediate values are shown in area averaged Nu/Nu_0 plots.

6.2.2.1 S-shape results: Heat transfer contour maps are shown for the two cases (Ro =0.1, DR=0.1 and Ro=0.2, DR=0.4) showing the two extremes of rotational parameters. Figure 6.14 shows the Nu/Nu_0 contour plot for Ro =0.1, DR=0.1 case.

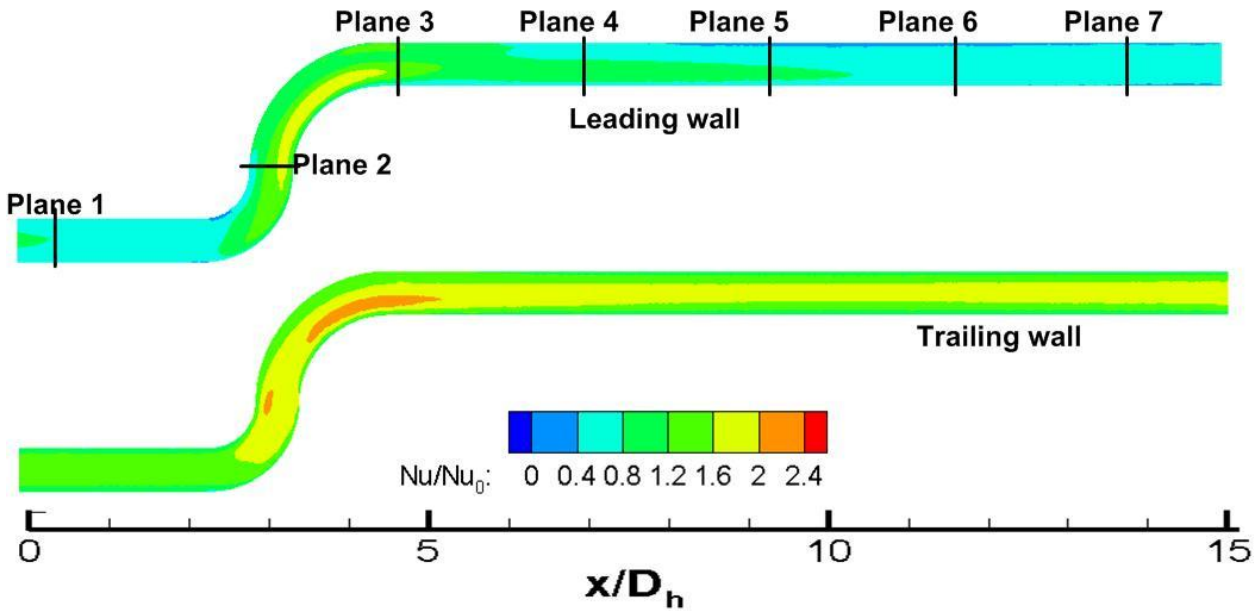

Figure 6.14: Nu contour map for the s-shape entrance (Ro =0.1, DR=0.1)

It can be seen that the trailing wall side has in general 60-70% higher heat transfer values compared to the leading wall side. Heat transfer close to the inner bend is higher than the outer bend for both the leading and trailing wall though the value of Nu/Nu_0 is different. The asymmetrical heat transfer distribution is more prominent for the leading wall side and the entrance effect is present up to about 5 hydraulic diameters downstream of the entrance geometry. Highest Nu/Nu_0 value is seen close to the inner bend of the trailing wall side (Nu/Nu_0 ~2).

Figure 6.15 shows streamwise velocity contours at two planes close to the leading and trailing wall respectively (distance of z/D_h =0.25 from wall). Here the streamwise velocity is normalized by the mean streamwise velocity. As expected, flow acceleration is seen close to the trailing wall

side and the streamwise velocity is lower close to the leading wall side, leading to lower Nu/Nu_0 values in the leading wall.

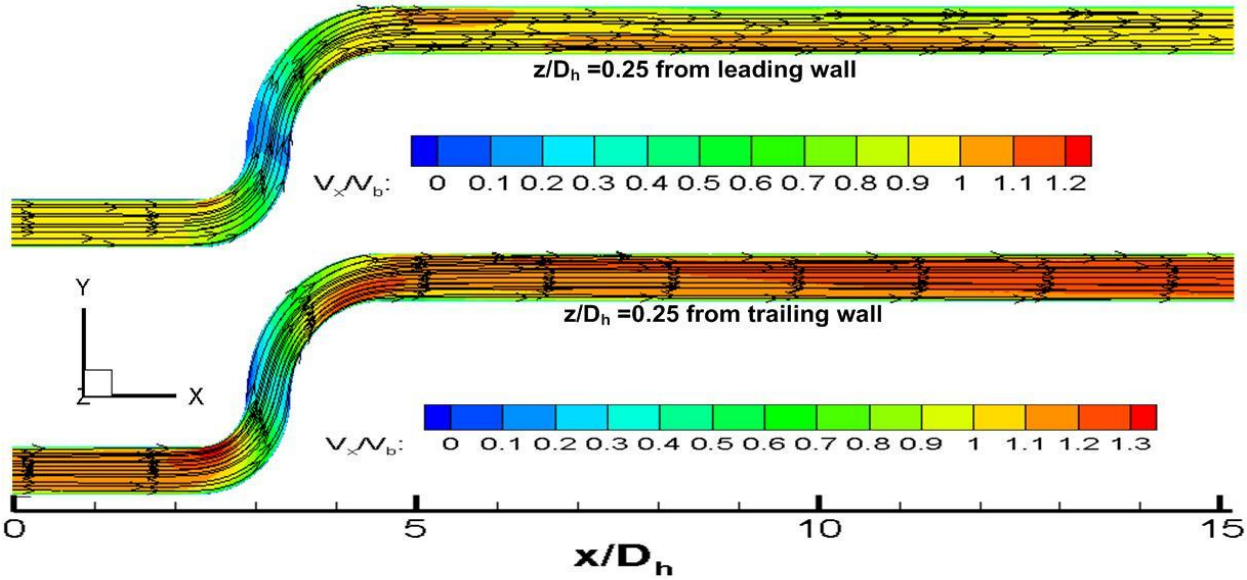

Figure 6.15: Streamwise velocity contour at two different streamwise planes for the s-shape entrance (Ro =0.1, DR =0.1)

Figure 6.16 shows the secondary flow profiles at different planes perpendicular to the mainstream velocity. The planes are shown in Fig. 6.14. The scales of the contour plots 4-7 are the same and a single legend is used for them.

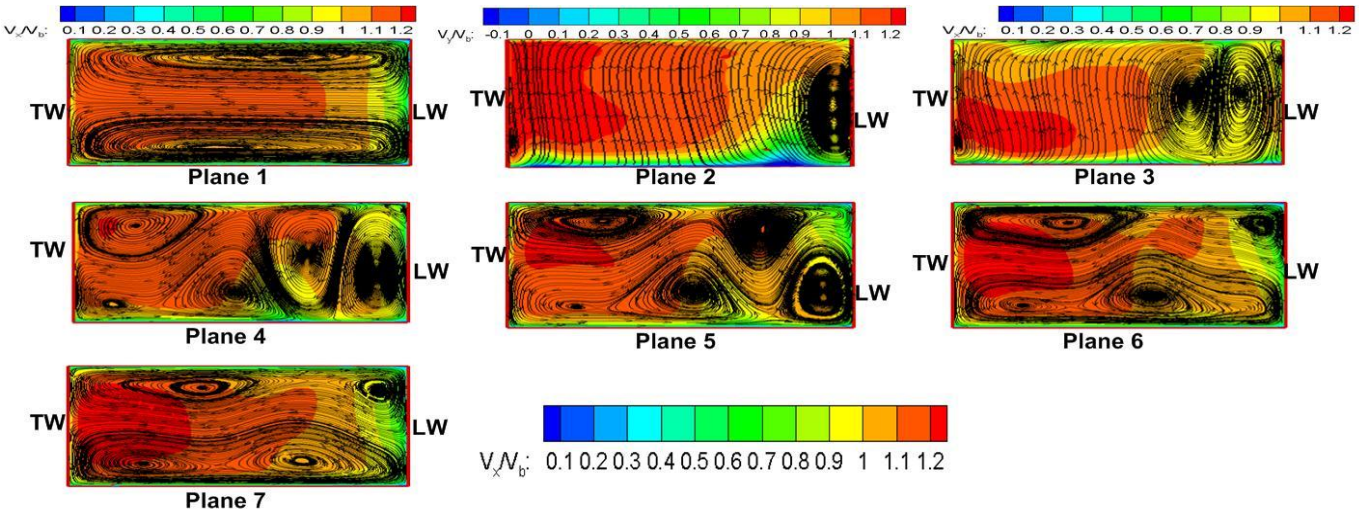

Figure 6.16: Streamline pattern at different cross planes for the s-shape entrance (Ro =0.1, DR =0.1)

For planes 1 and 3-7, the upper side represents the outer bend side (higher y) and the lower side represents the inner bend side of the test section. For plane 2, the upper side means higher x value. Without the rotation force, the cross velocity is in y direction. The original cross stream pattern is preserved close to the leading wall side up to about plane 4. Rotation effect breaks up this pattern and as the flow progresses further in the streamwise direction, the streamline pattern is dominated by the rotation force, which is evident by the fact that core fluid is driven from the leading wall to trailing wall side (z direction). As expected, higher velocity is seen close to the trailing wall side and lower velocity close to the leading wall side due to the combination of Coriolis and centrifugal buoyancy force.

Heat transfer enhancement contour map at the highest rotational parameter (Ro =0.2, DR =0.4) of the current study is shown in Figure 6.17.

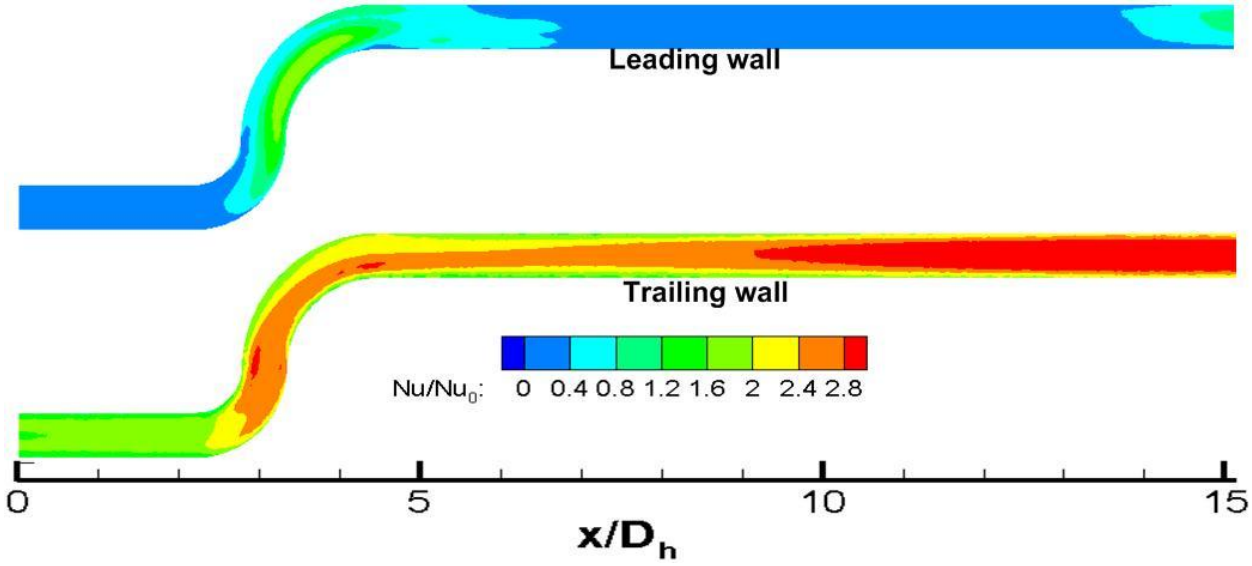

Figure 6.17: Nu contour map for the s-shape entrance (Ro =0.2, DR=0.4)

As the rotational speed is increased, more core fluid is pushed towards the trailing wall side due to increase in Coriolis force. The centrifugal buoyancy force tries to push the cooler, heavier fluid away from the rotation axis. Due to Coriolis force, the cooler fluid is already inclined towards the trailing wall. So the buoyancy force augments the Coriolis force and increases the coolant velocity further close to the trailing wall. The centrifugal buoyancy force is increased by the combinational increase of Ro and DR. As the buoyancy force is increased, reverse flow starts to happen close to the leading wall side, which results in increased turbulence close to the leading wall. This is evident by the higher Nu/Nu_0 values towards the end for the leading wall side (Fig. 6.17). The onset of reverse flow increases the local heat transfer values close to the leading wall to about 100% compared to the without reverse flow case. The effect of entrance geometry is present only for about 2 hydraulic diameters downstream of the entrance geometry. Trailing wall side Nu/Nu_0 values as high as 3 are seen as the flow progresses in the streamwise direction.

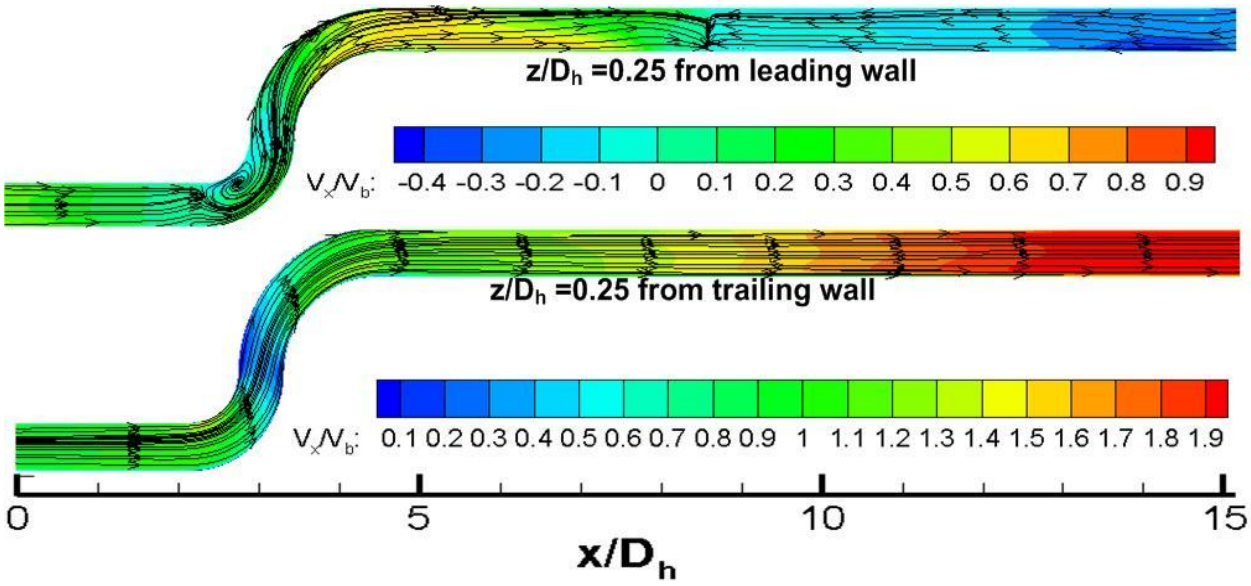

Figure 6.18: Streamwise velocity contour at two different streamwise planes for the s-shape entrance (Ro =0.2, DR =0.4)

Figure 6.18 shows the streamwise velocity contour at two streamwise planes close to the leading and trailing wall respectively. The reverse flow is clearly evident from the plot close to the leading wall. Reverse flow starts to happen close to the leading wall, after about 3 hydraulic diameter distance downstream of the entrance geometry. Reverse flow is also seen upstream of the s-shape entrance geometry but it disappears as the flow encounters the entrance geometry. The local streamwise velocity close to the trailing wall side is up to 35% higher compared to the Ro =0.1, DR =0.1 case.

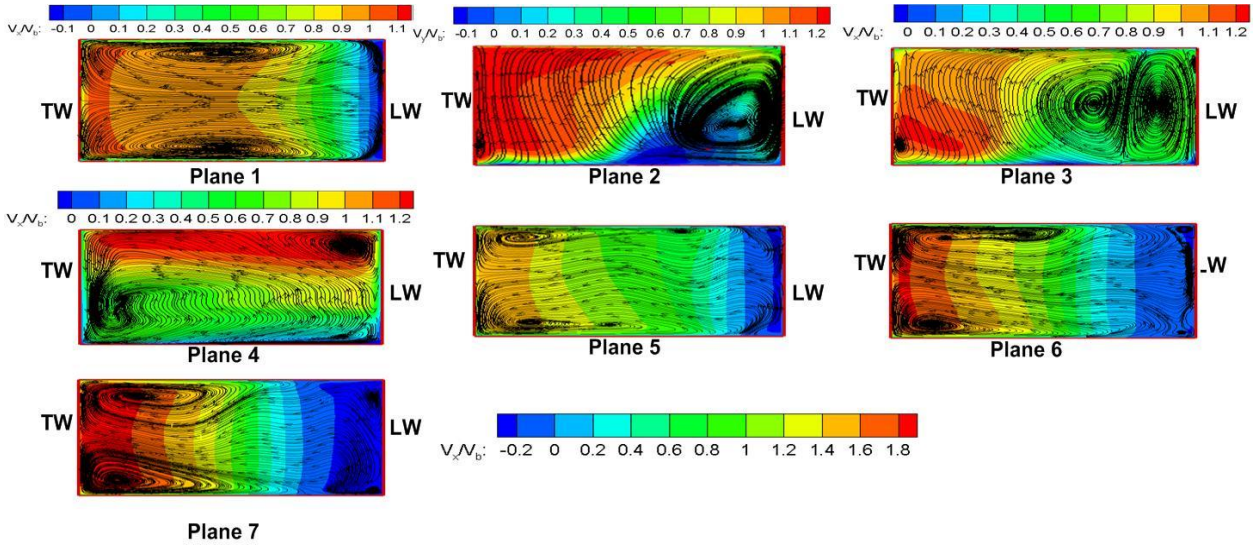

Figure 6.19: Streamline pattern at different cross planes for the s-shape entrance(Ro =0.2, DR =0.4)

Figure 6.19 shows the streamline pattern at different planes perpendicular to the mainstream flow. Reverse flow is seen close to the leading wall at plane 1 and the vortical structure due to the entrance geometry is preserved for plane 3 but as the flow progresses further in the streamwise direction, the entrance effect dies down rapidly and the rotation effect becomes dominant. Close to the trailing wall, the streamwise velocity is about 1.8 V_b and is about 50% higher compared to the Ro =0.1, DR =0.1 case. Reverse flow is seen from plane 5 and the reverse velocity goes on increasing as the flow progresses further.

6.2.2.2 90 degree bend results: Figure 6.20 shows the Nu/Nu_0 contour plot for Ro =0.1, DR=0.1 case with the 90 degree bend entrance geometry.

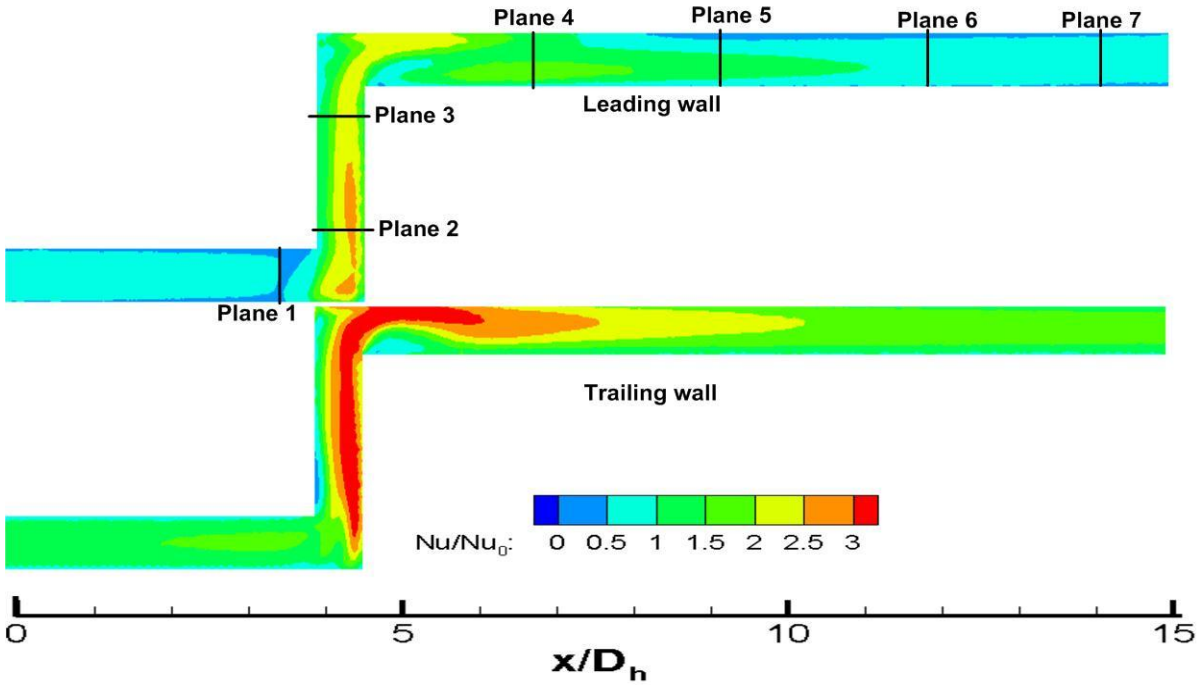

Figure 6.20: Nu contour map for the 90 degree bend entrance (Ro =0.1, DR=0.1)

As the flow encounters the sharp 90 degree bend, it cannot take such a sharp turn and impinges on the outer wall of the first bend. This impingement effect is present for both the leading and trailing walls. There is also a second impingement zone at the second 90 degree bend. The impingement zone pattern and the flow development pattern downstream is almost the same for both walls but the trailing wall Nu/Nu_0 values are higher than leading wall side due to the rotation effect. Impingement zone Nu/Nu_0 values as high as 3.5 are seen on the trailing wall side. A separation zone is present at the inner side of the 2nd 90 degree bend. This separation zone Nu/Nu_0 values are of the order of 1 and are the same for both the leading and trailing walls. Spanwise non-uniformity of heat transfer values are seen up to about 5 hydraulic diameters downstream of the entrance geometry.

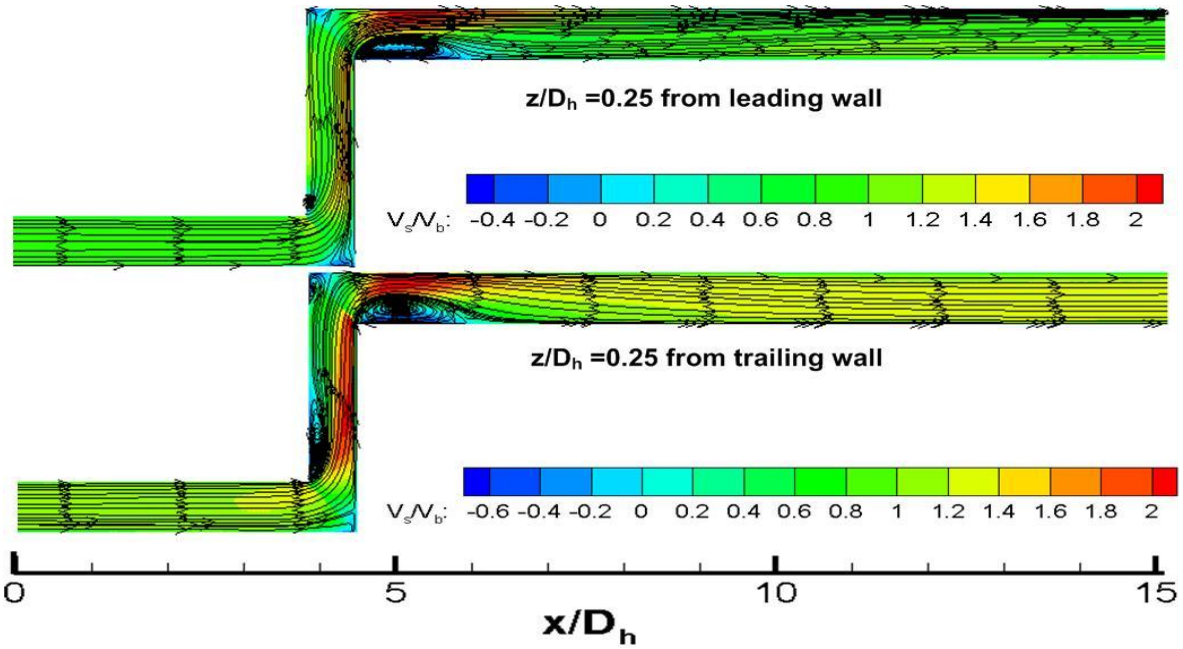

Figure 6.21: Streamwise velocity contour at two different streamwise planes for the 90 degree bend entrance (Ro =0.1, DR =0.1)

Figure 6.21 shows the streamwise velocity contour at two streamwise planes close to the leading and trailing wall. The velocity contour pattern looks the same for both the planes but the streamwise velocity in general is about 30-40 % higher close to the trailing wall side, compared to the leading wall side. The separation zone at the corner of the 1st 90 degree bend is more prominent for the trailing wall side as it occupies almost half of the flow width but this is almost absent for the leading wall side. The separation zone at the 2nd 90 degree bend corner is prominent for both the leading and trailing wall side and occupies about half the flow width. The impingement zone velocity is about 2 times the average mainstream velocity and this value is same for both leading and trailing wall side.

Secondary flow pattern at different cross planes (as shown in Fig. 6.20) is demonstrated in Figure 6.22. The scales of the contour plots for planes 5-7 are the same and a single legend is shown for them. For planes 1 and 4-7, the upper side represents the outer bend side (higher y)

and the lower side represents the inner bend side of the test section. For plane 2-3, the upper side means higher x value.

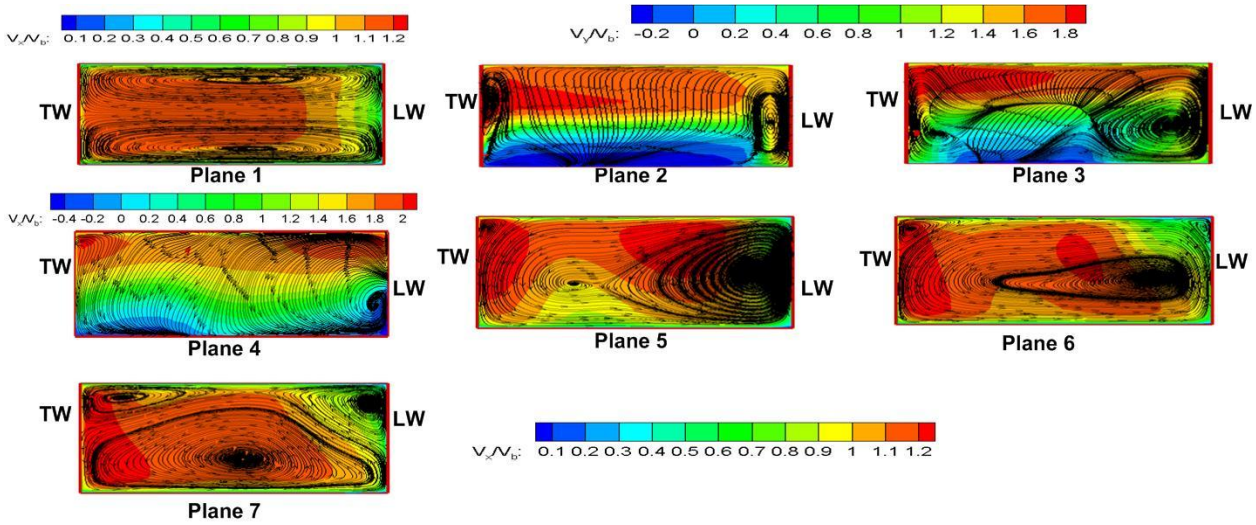

Figure 6.22: Streamline pattern at different cross planes for the 90 degree bend entrance(Ro =0.1, DR =0.1)

The separation zone at the corner of the 1st bend is evident at plane 2 plot. It is seen that flow separation is not there close to the leading wall. Plane 4 represents the plane after about 2 D_h downstream of the 2nd bend but it still shows the effect of separation. The effect of rotation is almost absent here and bend effect is dominant, as is evident by the y direction secondary flow velocity. From plane 5 onwards, the effect of rotation is more dominant as the core flow is taken from the leading to trailing wall side due to rotation. The trailing wall side velocity is about 80-100% higher compared to the leading wall side velocity.

Heat transfer enhancement contour map at the highest rotational parameters (Ro =0.2, DR =0.4) of the current study is shown in Fig. 6.23. The increase in rotational effect is clearly evident on the heat transfer plot. Flow reversal occurs for the leading wall side upstream of the 1st bend though this effect is not prominent downstream of the second bend. Heat transfer values at the 1st impingement zone are about the same for both the walls but the impingement zone spans a

wider distance for the leading wall side. The impingement zone Nu/Nu_0 values at the 2nd bend are about 40-50% higher for the trailing wall side compared to the leading wall side. The trailing wall side Nu/Nu_0 values are about 25-30% higher for this case compared to the Ro =0.1, DR =0.1 case.

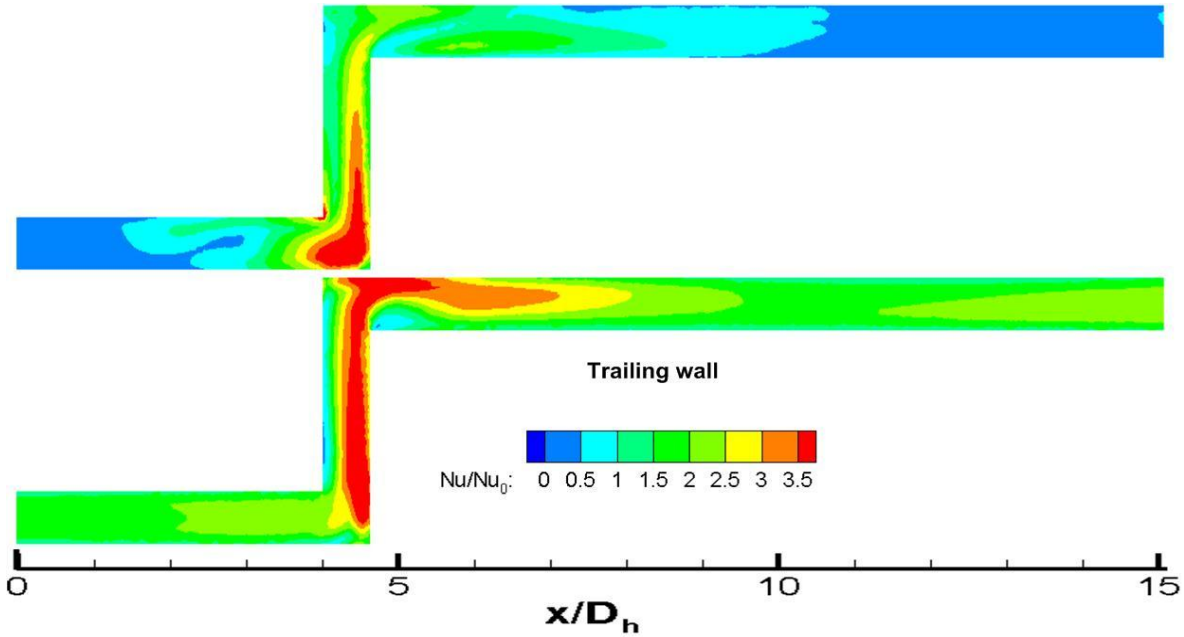

Figure 6.23: Nu contour map for the 90 degree bend entrance (Ro =0.2, DR=0.4)

Flow streamlines are shown at two planes close to the leading and trailing wall in Fig. 6.24. A strong reverse flow is seen downstream of the 1st bend close to the leading wall side. The flow pattern between the 1st and 2nd bend is similar to the Ro =0.1, DR =0.1 case with the rotation effect becoming more prominent (as evident by the higher trailing wall side and lower leading wall side streamwise velocity). The size of the separation bubble is about 50% smaller close to the leading wall side but the trailing wall side separation bubble size is almost the same. The flow reversal close to the leading wall starts to happen after about 8 D_h downstream of the bend. The increased turbulence effect due to flow reversal is not prominent and as a result the leading wall side Nu/Nu_0 values do not increase due to flow reversal.

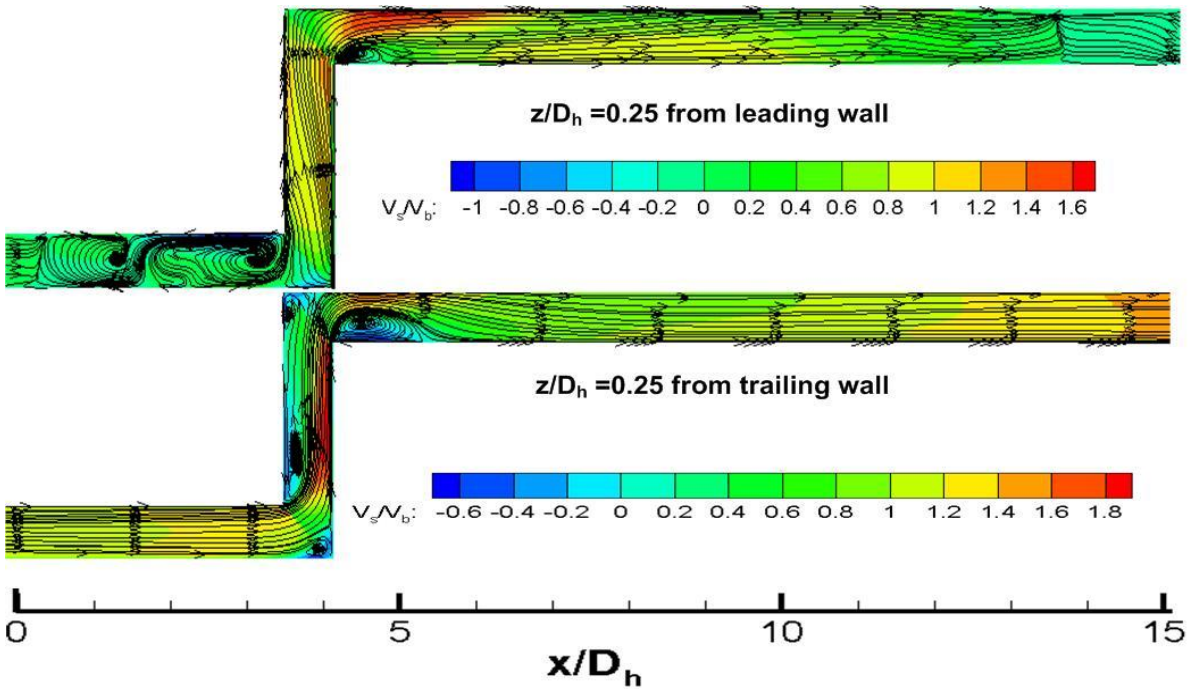

Figure 6.24: Streamwise velocity contour at two different streamwise planes for the 90 degree bend entrance(Ro =0.2, DR =0.4)

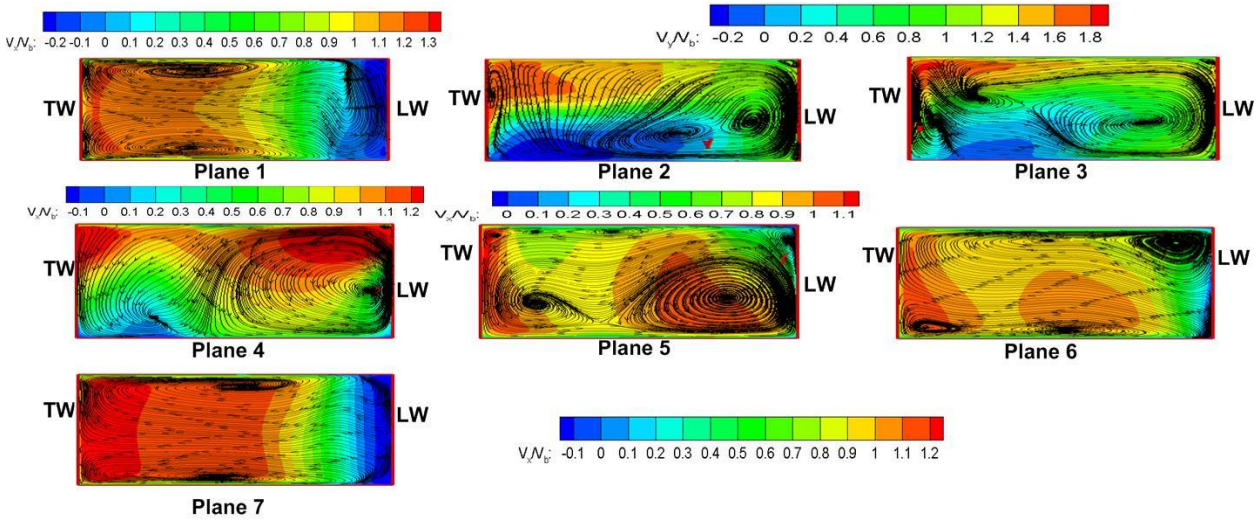

Figure 6.25: Streamline pattern at different cross planes for the 90 degree bend entrance (Ro =0.2, DR =0.4)

Figure 6.25 shows the secondary flow streamline pattern at different cross-sectional planes. Flow reversal is seen at plane 1, leading wall side. The effect of the bend is still preserved for planes 2-3 but the rotation distorts the vortices and tries to align them in z direction. One interesting thing

to note is that, at plane 4 is that the impingement zone velocity downstream of the second turn is higher for the leading wall side than the trailing wall side. Plane 6 shows signs of flow reversal close to the leading wall side which is more prominent for the plane 7. The streamwise velocity close to the trailing wall is about 40% lower and the reverse flow velocity close to the leading wall is also lower compared to the s-shape case.

6.2.2.3 Changing AR entrance results: Figure 6.26 shows the Nu/Nu_0 contour plot for Ro =0.1, DR=0.1 case with the changing AR entrance geometry.

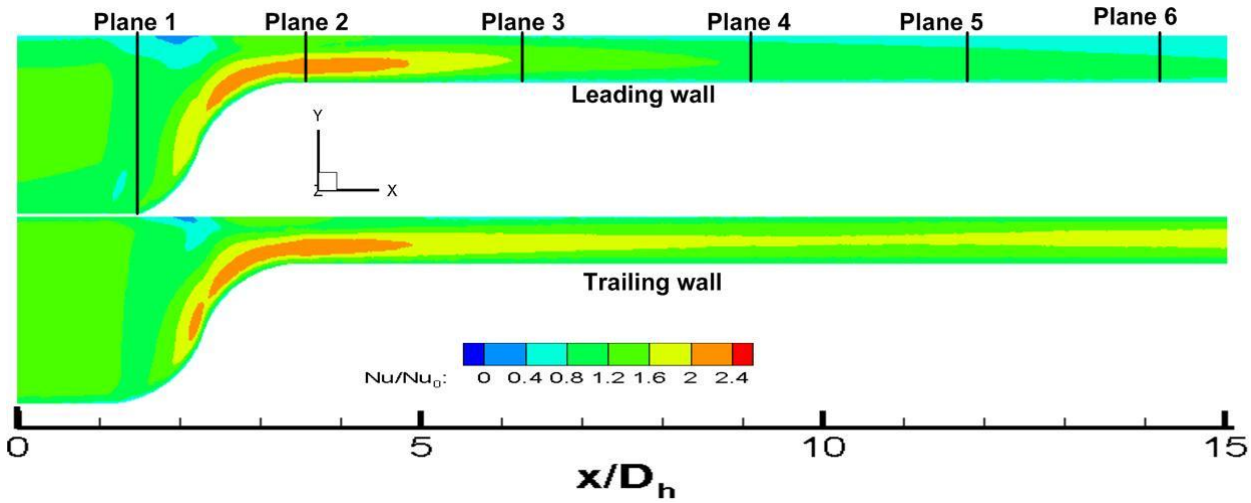

Figure 6.26: Nu contour map for the changing AR entrance (Ro =0.1, DR=0.1)

For the changing AR entrance geometry, the cross section of the channel is a 4:1 AR channel up to about x/D_h =1.27. The cross section of the geometry changes from 4:1 to 1:4 within a distance of x/D_h =2.55 and downstream of the entrance geometry a 1:4 AR channel is present. The difference in Nu/Nu_0 values from the leading wall and trailing wall is only about 20% in the 4:1 AR portion. Flow convergence in the y direction is dominant which overcomes the rotational effect and the Nu contour pattern is similar for the leading and trailing wall side up to about 4 D_h downstream of the entrance geometry. The Nu/Nu_0 distribution is similar to the s-shape entrance,

where the Nu/Nu_0 values in the bottom side can be about 50% higher compared to the top side. Rotation effect starts to dominate as the flow progresses further in the 1:4 AR test section, which is evident by the increasing difference in trailing wall and leading wall Nu/Nu_0 values.

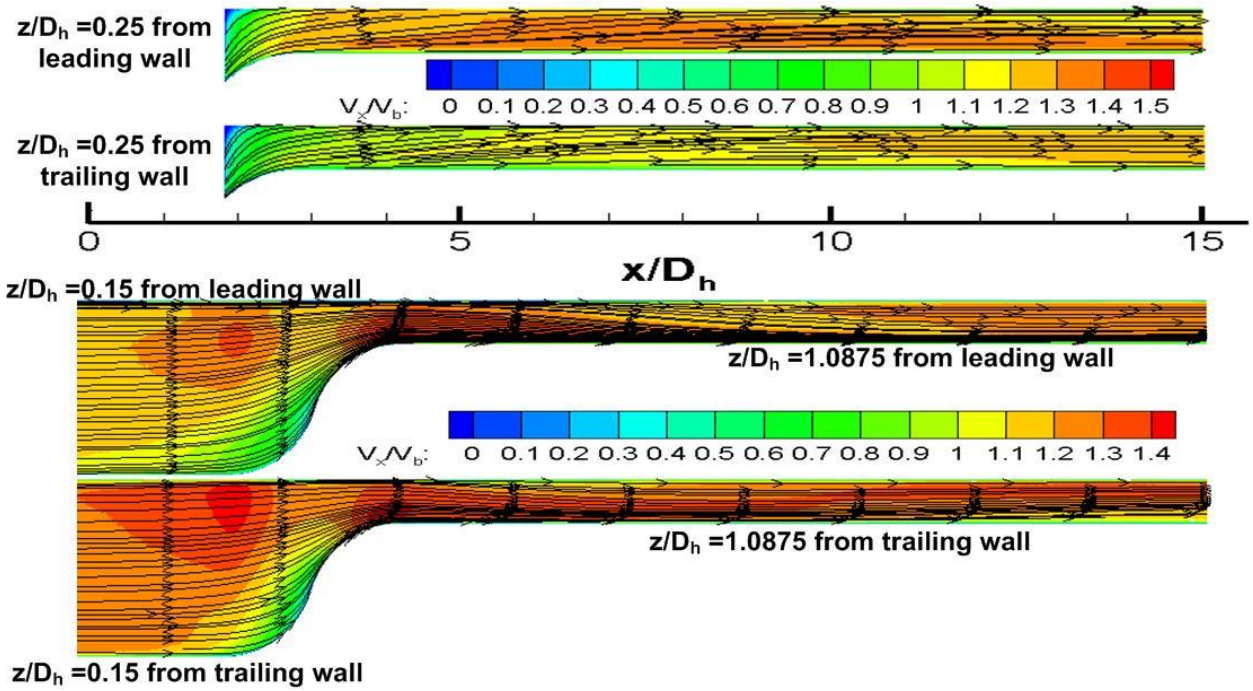

Figure 6.27: Streamwise velocity contour at four different streamwise planes for the changing AR entrance (Ro =0.1, DR =0.1)

Figure 6.27 shows the streamwise velocity contour at four different planes close to the leading and trailing walls. The top two figures represent two planes close to the walls in the 1:4 AR portion and the bottom two figures represent two planes close to the walls in the 4:1 AR portion. Streamwise velocity is of the same range for both the leading and trailing wall side in all the regions. There is no flow separation anywhere in the flow field and the flow convergence due to change in cross section in y direction leads to increase in streamwise velocity right after the entrance.

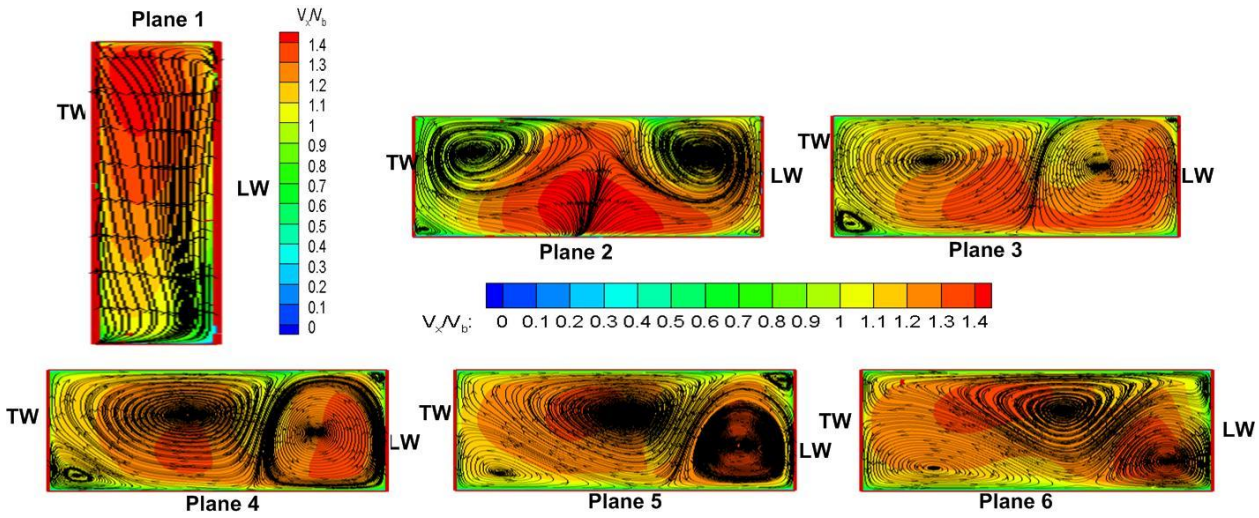

Figure 6.28: Streamline pattern at different cross planes for the changing AR entrance(Ro =0.1, DR =0.1)

Secondary flow pattern at different cross planes (as shown in Fig. 6.26) is demonstrated in Fig. 6.28. The scales of the contour plots for planes 2-6 are the same and a single legend is shown for them. The flow profile is almost symmetrical for plane 2 and gets asymmetrical as the flow progresses downstream. After the change in cross section, the increase in streamwise velocity on the bottom side is evident at plane 2. The core flow is driven from the bottom side to the top side and forms vortices as there is an increase in cross section in z direction as well. The flow pattern due to the entrance geometry is preserved up to about plane 5 and after that the rotation effect distorts the flow pattern but even at plane 6, the effect of rotation is not fully realized. It is to be noted that planes 3-6 are at the same streamwise locations as of the planes 4-7 in the s-shape and 90 degree bend case. For the same rotational parameters, the effect of the entrance geometry is most preserved for the changing AR case.

Figure 6.29 shows the Nu contour map for the Ro =0.2, DR =0.4 case. Heat transfer coefficient values upstream of the changing cross section are slightly higher for the trailing wall than the leading wall. Same level of Nu/Nu_0 values are seen in the region where cross section change

takes place. There is no flow separation close to the leading wall and the trailing wall Nu/Nu_0 values can be more than 2 times the leading wall Nu/Nu_0 values.

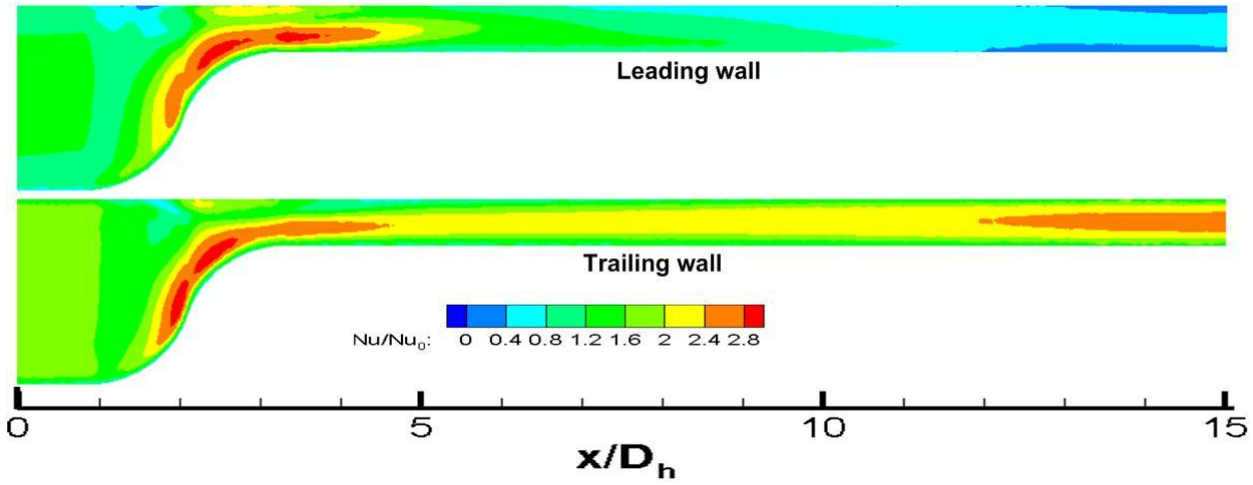

Figure 6.29: Nu contour map for the changing AR entrance (Ro =0.2, DR=0.4)

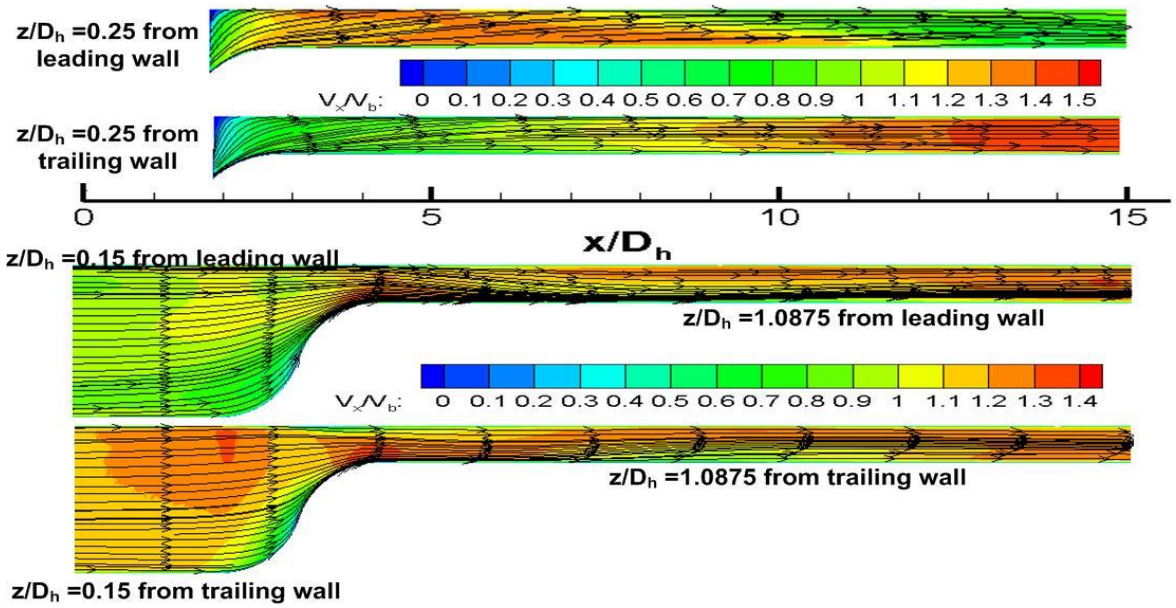

Figure 6.30: Streamwise velocity contour at four different streamwise planes for the changing AR entrance(Ro =0.2, DR =0.4)

Figure 6.30 shows the streamwise velocity contour at four different planes close to the leading and trailing wall. It is evident that there is no flow reversal at the extreme rotational parameters like the s-shape or 90 degree bend entrance geometry. Rotation effect slowly starts to take effect

as the flow progresses in the streamwise direction and the streamwise velocity close to the trailing wall can be about 100% higher compared to the leading wall side.

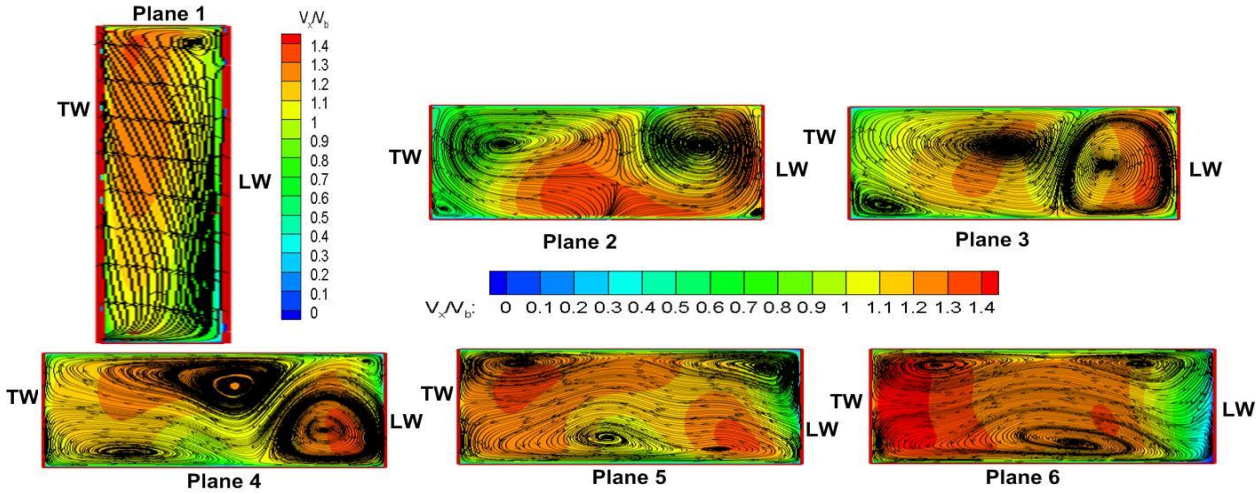

Figure 6.31: Streamline pattern at different cross planes for the changing AR entrance(Ro =0.2, DR =0.4)

Secondary flow pattern at different cross planes are shown in Fig. 6.31. The secondary flow pattern due to the entrance geometry starts breaking up earlier than the Ro =0.1, DR =0.1 case. The flow pattern at plane 2 is due to the change in cross section but it becomes asymmetrical due to the rotational effect. The effect of rotation is fully realized at plane 6 where the trailing wall side velocity is about 2 times compared to the leading wall side velocity.

6.2.2.4 Averaged results: Zonal averaged Nu/Nu_0 values are plotted at two different Ro and four density ratios. Figure 6.32 shows the zonal averaged Nu/Nu_0 values for the s-shape entrance geometry. For the left hand side plot, Ro is kept constant at Ro =0.1 and the DR is varied from 0.1 to 0.4. For the right hand side plot, Ro is kept constant at Ro =0.2 and the DR is varied from 0.1 to 0.4. For the Ro =0.1 case, the difference in Nu/Nu_0 values between the leading and trailing wall is least in the entrance zones (zones 2-4), where the difference is about 30% for the lowest DR and about 60% for the highest DR. As the flow progresses further in the test section, the

difference goes on increasing and the trailing wall Nu/Nu_0 values can be as high as 3-9 times than the leading wall values. For the Ro =0.2 case, the difference in leading wall and trailing wall heat transfer values are about 50-80% in the entrance zones and goes on increasing as the flow progresses forward. Increase in DR has a huge impact on the trailing wall heat transfer values as the values increase by about 60% from the lowest to highest DR. The leading wall side Nu/Nu_0 values reduce significantly until the onset of reverse flow. The reverse flow related increase in Nu/Nu_0 values does not happen for DR =0.1,0.2 and starts to happen after the DR is increased further.

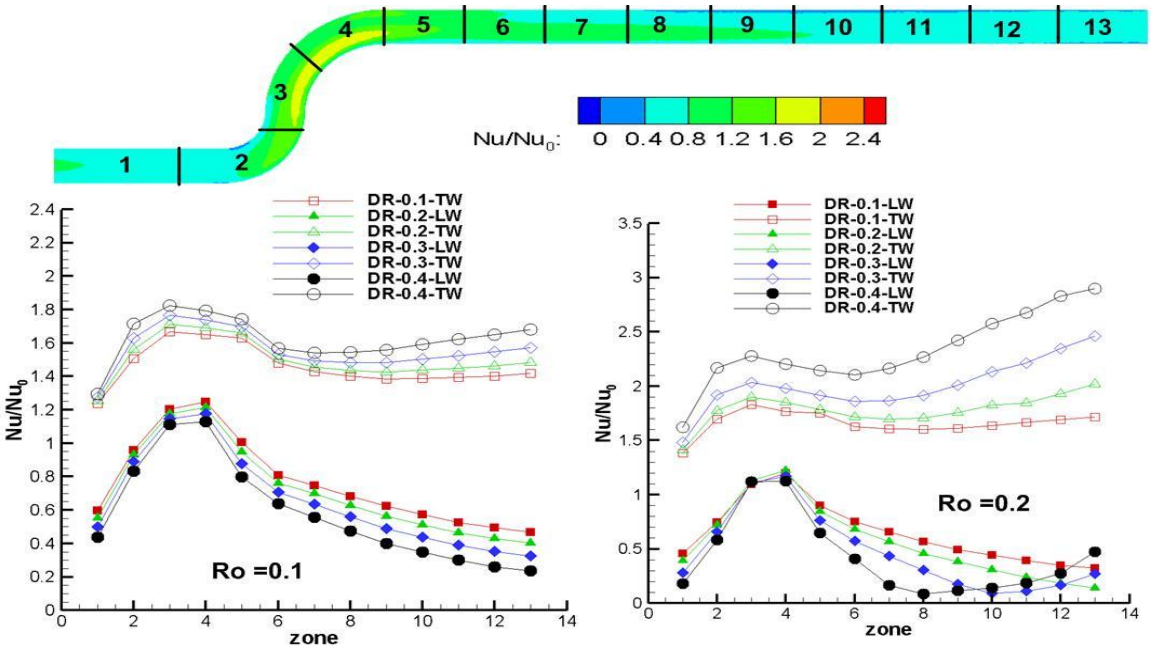

Figure 6.32: Zonal averaged Nu/Nu_0 values for the s-shape entrance

Figure 6.33 shows the zonal averaged Nu/Nu_0 values for the 90 degree bend entrance geometry. For Ro =0.1, the leading wall and trailing wall values are almost the same in the 1st impingement zone (zones 4-5). The trailing wall Nu/Nu_0 values can be about 1.4 and the leading wall values can go as low as 0.5. It is to be noted that the Nu/Nu_0 values goes on decreasing for both the leading and trailing wall in the downstream direction. For Ro =0.2, the 1st impingement zone

Nu/Nu_0 values for the leading wall side even exceeds the trailing wall side values. Heat transfer values for the trailing wall side initially decreases in the downstream direction but as the DR is increased beyond 0.3, it starts to increase from zone 12. The increase in Nu/Nu_0 values due to reverse flow close to the leading wall is only seen for the DR =0.4 case at zone 14. It is to be noted that the DR effect at a fixed Ro is not as significant as the s-shape case. The trailing wall Nu/Nu_0 values varies by only 10-15% from the lowest to highest DR.

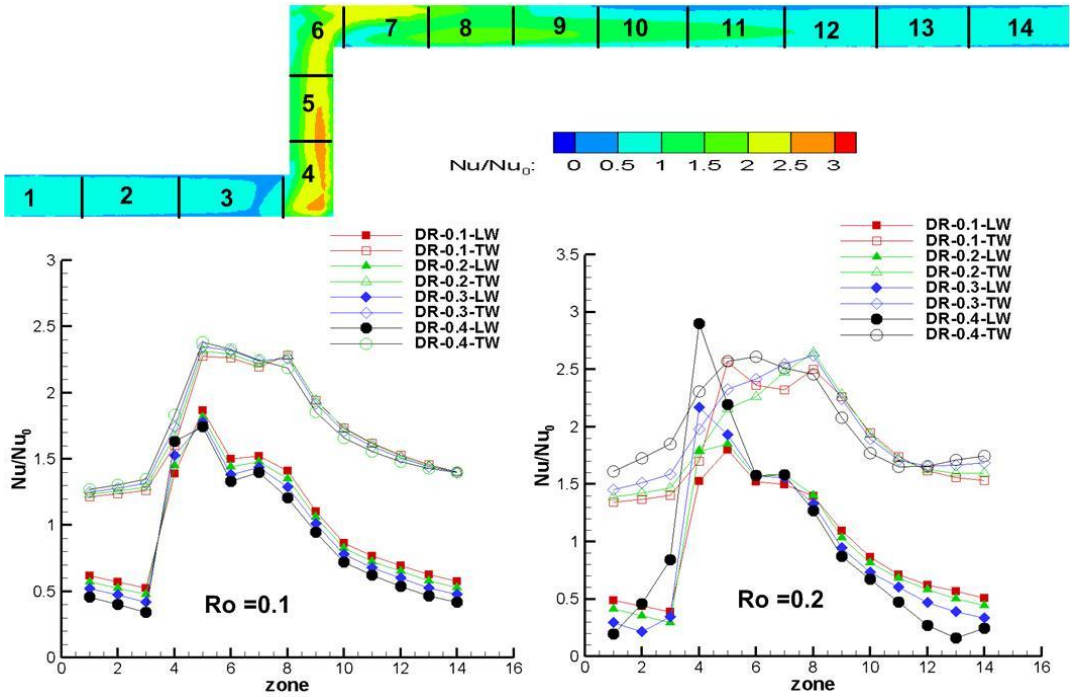

Figure 6.33: Zonal averaged Nu/Nu_0 values for the 90 degree bend entrance

Figure 6.34 shows the zonal averaged Nu/Nu_0 values for the changing AR entrance geometry. For the zones with change in cross section and right after that (zones 2-4), the leading wall and trailing wall Nu/Nu_0 values are almost the same. The deviation between leading wall and trailing wall Nu/Nu_0 values starts to take place from zone 6. The trailing wall Nu/Nu_0 values goes on increasing in the downstream direction and can reach as high as 1.5 for Ro =0.1, DR =0.4. For this case the trailing wall value is about 2.5 times higher than the leading wall value. For Ro

=0.2, the leading wall Nu/Nu_0 values at zones 3-4 are even higher than the trailing wall values. With the changing AR entrance geometry, flow reversal is totally absent and the Nu/Nu_0 values on the leading wall go on decreasing with increasing DR.

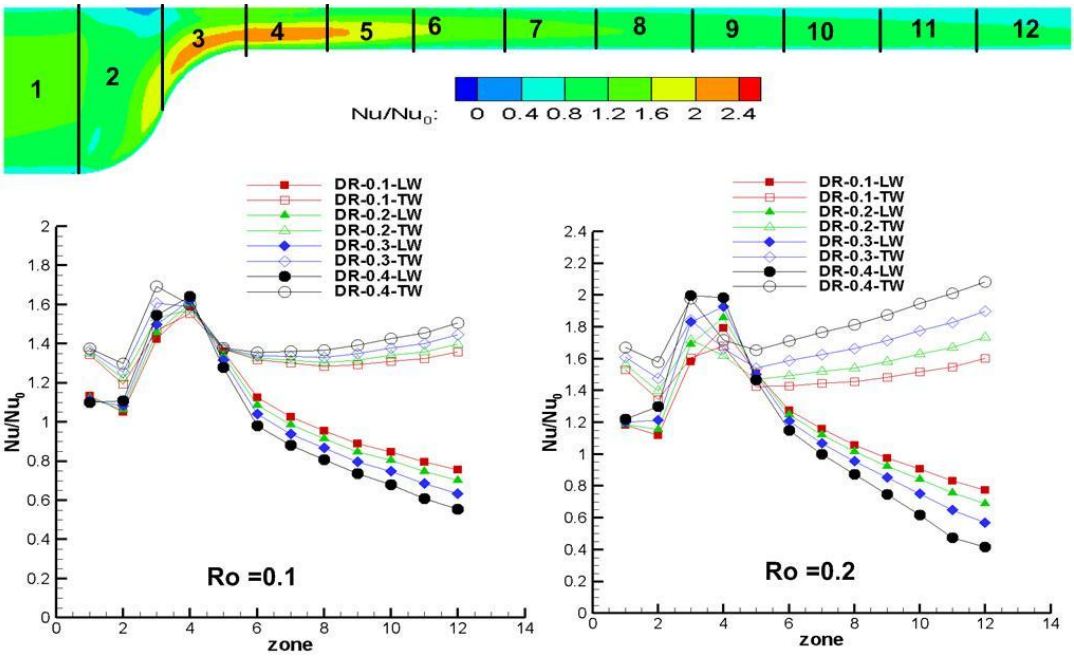

Figure 6.34: Zonal averaged Nu/Nu_0 values for the changing AR entrance

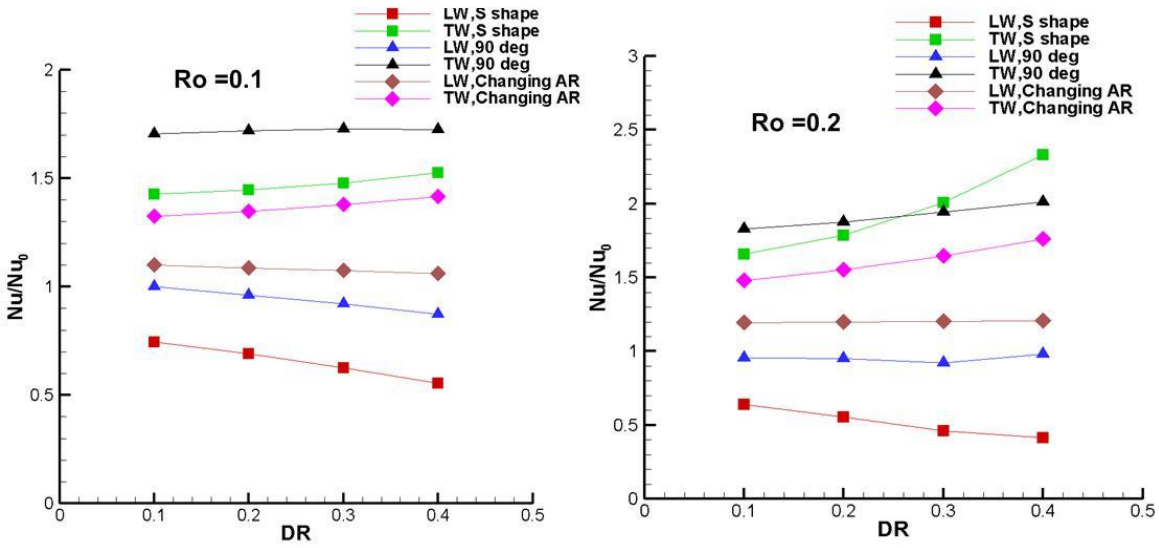

Figure 6.35: Overall averaged Nu/Nu_0 values for all the geometries

Figure 6.35 shows the overall heat transfer data comparison for different entrance geometries. For Ro =0.1, the 90 degree bend entrance trailing wall shows Nu/Nu_0 values about 1.6 and the leading wall shows Nu/Nu_0 values about 0.9-1. The s-shape entrance trailing wall shows Nu/Nu_0 values about 1.4-1.5 and the leading wall shows Nu/Nu_0 values about 0.6-0.8. The changing AR entrance leading wall and trailing wall values are about 1-1.1 and 1.3-1.4. For Ro =0.2, the s-shape entrance trailing wall Nu/Nu_0 values exceeds even the 90 degree bend trailing wall. The trailing wall side value can reach as high as 2.3. The average Nu/Nu_0 values go on reducing with increasing DR and can reach as low as 0.4. The 90 degree leading wall side Nu/Nu_0 value increases at DR =0.4 compared to DR =0.3 case.

6.2.3 Conclusions: A numerical study is done on a 1:4 AR channel with three different entrance geometries at Ro =0.1-0.2 and DR =0.1-0.4. Detailed and averaged heat transfer values are presented and detailed flow profile at different streamwise and cross stream planes are presented. The following conclusions are obtained from the study

1) The s-shape entrance pushes the fluid towards the inner bend and as a result higher values of heat transfer are seen close to the inner bend. This effect is seen for both the leading wall and trailing wall. Flow pattern due to the entrance geometry starts breaking up and as the flow progresses further in the streamwise direction, the streamline pattern is dominated by the rotation force, which is evident by the fact that core fluid is driven from the leading wall to trailing wall side. As the rotational parameters are increased, reversed flow starts to happen close to the leading wall. This reversed flow increases local turbulence and increases the local heat transfer values close to the leading wall to about 100% compared to the without reverse flow case.

2) The 90 degree bend entrance has two significant impingement zones which increases the local heat transfer values. The impingement zone Nu/Nu_0 values are about the same for both leading and trailing wall. A separation exists at the corner of the 1st bend for the trailing wall side but this is absent for the leading wall side. The separation at the corner of the 2nd bend is present for both leading and trailing wall and varies in size with change in rotational parameters. Reverse flow is seen about $8D_h$ downstream of the entrance geometry for Ro =0.2, DR =0.4 case but the increase in heat transfer values at the leading wall due to reverse flow is weaker compared to the s-shape entrance case.
3) A change in cross section from a 4:1 AR channel to a 1:4 AR channel takes place for the changing AR entrance case. There is flow convergence in y direction and flow divergence in z direction. A combined effect of this two makes the heat transfer pattern the same like the S-shape case. At the changing cross section portions, the leading wall and trailing wall side heat transfer values are about the same. The effect of entrance geometry is preserved furthest for this entrance case. There is no reverse flow close to the leading wall for the range of parameters studied.

CHAPTER 7: CONCLUSIONS AND FUTURE WORK

7.1 Conclusions

This research was conducted with a goal to explore new innovative geometries in gas turbine internal cooling channel. Few major modifications in design are suggested and their performance is documented. The major conclusions of this study are summarized below:

1) Use of lattice structure in internal cooling channels is explored. Lattice structures, inserted between the leading and trailing wall of the blade can increase the structural strength of a blade significantly. Lattice structures produce multiple flow turnings and flow impingement which greatly increases the heat transfer from the gas turbine blade.

2) Two converging lattice structures are studied which can be used in the trailing edge region of the blade. Both the lattice structures performed well in terms of heat transfer when compared with a pin-fin configuration, commonly used in gas turbine trailing edge region. The lesser the number of sub-channel for a lattice structure, the better is the heat transfer performance. The pressure drop produced is also higher for a larger number of channel lattice.

3) The two inlet sub-channel lattice structure provided comparable or higher thermal performance factor compared to a standard pin-fin configuration.

4) A constant cross section lattice, suitable for endwall cooling application is also studied. The thermal performance factor produced by this structure is in the same range as a conventional rib-turbulator design.

5) In a multipass internal cooling passage, the 180° bend produces the largest pressure drop. Several modifications of the bend geometry are studied numerically to find a geometry which produces a significant reduction in pressure drop and enhancement in Nu/Nu_0 values in the bend region. The modifications are compared with a baseline U-bend to showcase their effectiveness.

6) A turning vane configuration is used which reduced the pressure drop significantly but reduced the bend region heat transfer values as well. An asymmetrical bulb added to the divider wall and couple of symmetrical bulbs is studied. The asymmetrical bulb reduced the pressure drop due to the removal of separation bubble at the 2^{nd} pass divider wall, but did not enhance heat transfer much. Some of the symmetrical bulbs proved to be beneficial as it increased the bend region heat transfer and also produced a significant reduction in pressure drop.

7) A bow shaped area contraction is used in the bend region to accelerate the flow which increased the local heat transfer in the bend region. The pressure drop produced depends on the amount of area contraction. Couple of rows of dimples is used in conjunction with the symmetrical bulb and bow which increased the local Nu/Nu_0 values without increasing the pressure drop much. The optimum design came out to be the one with dimple, symmetrical bulb and bow which increased the thermal performance factor by 41% compared to the baseline case.

8) A symmetrical bulb and a bulb-bow combination is downselected from the numerical study for an experimental evaluation at different Reynolds number. Based on Reynolds number, the thermal performance factor of the bow-bulb combination showed about 17-

33% enhancement compared to the baseline case with the higher enhancement at higher Reynolds number.

9) The symmetrical bulb and the bulb-bow combination case is further tested numerically with rotation and it is seen that the degree of performance enhancement is not as high as the stationary case. The bow-bulb combination case showed a performance enhancement of 24% compared to the baseline case.

10) The idea of using groove as turbulence promoter to enhance the surface heat transfer from the blade is explored. Some 45° angled parallel and V grooves are studied and 45° ribs are also introduced in combination with the grooved geometries to enhance heat transfer more. The idea is to produce some secondary flow along the angled grooves. The interaction of the secondary flow coming out of the groove and streamwise flow increases the local turbulence and enhances heat transfer significantly.

11) A separation zone exists at the upstream side of the groove where low values of Nu/Nu_0 are seen. This separation zone grows in size along the groove from the nose to the leg of the groove. The intra-groove Nu/Nu_0 values reduces in the streamwise direction until the next groove is reached. Same level of heat transfer enhancement is seen in the zones just downstream of the grooves and inside the grooves for different pitches of grooves but the intra-groove Nu/Nu_0 values are generally lower for the higher pitched groove cases.

12) The introduction of the angled ribs in conjunction with the angled grooves produces very high levels of heat transfer enhancements. The interaction of rib produced flow reattachment, groove produced upwash flow and mainstream flow increases the Nu/Nu_0 values to as high as 8. Averaged heat transfer value is highest for the V groove-v rib case

and the angled groove-angled rib case comes second. Thermal performance wise, the V groove-v rib case performs the best with TPF in the range of 1.8-2.5. When compared with some innovative rib designs it performs better or at the same level at a particular Reynolds number.

13) The effect of different entrance geometries on the heat transfer performance of an internal cooling channel is investigated. The entrance geometries studied included a s-shape entrance, a 90 degree bend entrance and a changing AR entrance. Experiments are done in stationary condition to characterize the effect of the entrance geometries on smooth and ribbed test section. It is seen that the effect of entrance geometry is more prominent with the smooth test section. Significant spanwise non-uniformity is seen in the test section downstream of the entrance geometries.

14) The S-shape entrance makes the high velocity air flow away from the divider wall of a two pass channel and enhances the regional heat transfer. Instead of a fully developed velocity profile at inlet of the test section, the velocity and heat transfer profile is skewed towards the inner bend. Flow impingement in the bend region just after a 90 degree bend increases heat transfer values at the entrance of test section. A small recirculation zone is formed after the impingement zone which results in low localized heat transfer enhancement values. Complex change in entry cross section creates secondary flows that result in increase of heat transfer coefficient at the entrance of the smooth test section.

15) The interaction of the bend generated flow and rotation generated flow is studied numerically. It is seen that the presence of entrance geometries delays the separation and reversed flow closed to the leading wall of the blade. For the range of rotation parameters

studied (Ro =0.1-0.2, DR=0.1-0.4), the changing AR case did not show any reversed flow close to the leading wall. The s-shape case had the least influence on rotation as the degree of flow reversal is much higher for this case. The 90 degree bend case also produced flow reversals close to the leading wall but the reversed velocity is less than the s-shape case.

7.2 Future work

All of the experiments done in this study were done in a stationary frame. It would be interesting to see the effect of rotation on the new turbulence enhancement devices like the lattice or the groove-rib combination. The interaction of the secondary flows generated due to these turbulence promoters and rotation induced flow can significantly alter the heat transfer coefficient distribution compared to a stationary case.

The bend geometry modifications are done for a smooth channel only. Actual gas turbine blades are always mounted with some turbulence promoters. So, the bend geometry modifications suggested in the current study can be tested with some ribs to gauge their usability in actual gas turbine blade applications.

The entrance geometries used in the current study are connected with a 1:4 AR channel which is typically used closed to the leading edge of the blade. There may be a need to see the effect of these entrance geometries at different aspect ratios to understand the behavior at different locations of the blade.

REFERENCES

Acharya, S., Zhou, F., Lagrone, J., Mahmood, G., and Bunker, R. S., (2005), "Latticework (Vortex) Cooling Experiments: Rotating Channel Experiments," Trans ASME, Journal of Turbomachinery, vol. 127, pp. 471-478

Acharya, S., Baliga, B., Karki, K., Murthy, J., Prakash, C., and Vanka, S. P., (2007), "Pressure-Based Finite Volume Methods in Computational Fluid Dynamics," Trans ASME, Journal of Heat Transfer, vol. 129, pp. 407-424

Advanced Materials for Gas Turbine Engines – High Pressure Turbine http://www.azom.com/details.asp?articleid=90

Al-Hadhrami, L., and Han, J.C., (2003), "Effect of Rotation on Heat Transfer in Two-Pass Square channels with Five Different Orientations of 45° angled rib Turbulators," International Journal of Heat and Mass Transfer, vol. 46, pp. 653-669

Al-Qahtani, M. S., Jang, Y. J., Chen, H. C., and Han, J. C, (2002), "Prediction of Flow and Heat Transfer in Rotating Two-Pass Rectangular Channels With 45-deg Rib Turbulators," Trans ASME, Journal of Turbomachinery, vol. 124, pp. 242-250

Astarita, T., and Cardone, G., (2003), "Convective Heat Transfer In a Square Channel With Angled Ribs on Two Opposite Walls," Experiments in Fluids, vol. 34, pp. 625-634

Azad, G.S., Uddin, M.J., Han, J.C., Moon, H.K., and Glezer, B., (2002), "Heat Transfer in a Two-Pass Rectangular Rotating Channel With 45-deg Angled Rib Turbulators," Trans. ASME, Journal of Turbomachinery, vol. 124, pp. 251-259

Bilen, K., Cetin, M., Gul, H., and Balta, T., (2009), "The Investigation of Groove Geometry Effect on Heat Transfer for Internally Grooved Ducts," Applied Thermal Engineering, vol. 29, pp. 753-761

Bons, J.P., and Kerrebrock, J.L., (1999), "Complementary Velocity and Heat Transfer Measurements in a Rotating Cooling Passage with Smooth Walls," Trans. ASME, Journal of Turbomachinery, vol. 121, pp. 651-662

Bunker, R.S., and Metzger, D.E., (1990), "Local Heat Transfer in Internally Cooled Turbine Airfoil Leading Edge Regions, Par I: Impingement Cooling Without Film Extraction," Trans ASME, Journal of Turbomachinery, vol. 112, pp. 451-458

Bunker, R.S., and Osgood, S.J., (2003), "The Effect of Turbulator Lean on Heat Transfer and Friction in a Square Channel," ASME Paper No. GT2003-38137

Bunker, R.S., (2004), "Latticework (Vortex) Cooling Effectiveness Part 1: Stationary Channel Experiments," ASME Paper No. GT-2004-54157

Burgess, N.K., and Ligrani, P.M., (2005), "Effect of Dimple Depth on Channel Nusselt Numbers and Friction Factors," Trans ASME, Journal of Heat Transfer, vol. 127, pp. 839-847

Burggraf, F., (1970), "Experimental Heat Transfer and Pressure Drop With Two-Dimensional Turbulence Promoter Applied to Two Opposite Walls of a Square Duct," in *Augmentation of Convective Heat and Mass Transfer*, edited by A. E. Bergles and R. L. Webb, ASME, New York, pp. 70–79

Chang, S.W., Liou, T.M., Chiang, K.F., and Hong, G.F., (2008), "Heat Transfer and Pressure Drop in Rectangular Channel with Compound Roughness of V-Shaped Ribs and Deepened Scales," International Journal of Heat and Mass Transfer, vol. 51, pp. 457–468

Chang, S.W., and Cai, Z.X., (2010), "Heat transfer and pressure drop in two-pass rib-roughened square channels with bleed from sharp bend," International Journal of Heat and Fluid Flow, vol. 31, pp.19-31

Cheah, S. C., Iacovides, H., Jackson, D. C., Ji, H., and Launder, B. E., (1996), "LDA Investigation of the Flow Development through Rotating U-Ducts," Trans. ASME, Journal of Turbomachinery, vol. 118, pp. 590-596

Chen, H. C., Jang, Y. J., and Han, J. C., (1999), "Computation of Flow and Heat Transfer in Rotating Two-Pass Square Channels by a Reynolds Stress Model," ASME Paper 99-GT-174.

Chen, W., Ren, J., and Jiang, H., (2011), "Effect of Turning Vane Configurations on Heat Transfer and Pressure Drop in a Ribbed Internal Cooling System," Trans. ASME, Journal of Turbomachinery, vol. 133, pp. 041012-1 – 041012-11

Chyu, M. K., Hsing, Y. C., Shih, T. I. P. and Natarajan, V., (1999)," Heat transfer contributions of Pins and Endwall in Pin-Fin Arrays: Effects of Thermal Boundary Condition Modeling," Trans ASME, Journal of Turbomachinery, vol. 121, pp. 257-263.

Chyu, M. K., Oluyede, E. O., and Moon, H. K., (2007) "Heat Transfer on Convective Surfaces with Pin Fins Mounted in Inclined Angles," ASME Paper No. GT-2007-28138

Dean, W.R., (1928), "Fluid Motion in a Curved Channel," *Proceedings of the Royal Society of London. Series A, Containing Papers of a Mathematical and Physical Character*, vol. 121, pp.402-420

Dutta, S., Han, J.C., and Zhang, Y., (1995), "Influence of Rotation on Heat Transfer from a Two-Pass Channel with Periodically Placed Turbulence and Secondary Flow Promoters," International Journal of Rotating Machinery, vol. 1, pp. 129-144

Dutta, S., Andrews, M.J, and Han, J.C, (1996), "Prediction of turbulent heat transfer in rotating smooth square ducts," International Journal of Heat and Mass Transfer, vol. 39, pp. 2505-2514

Dutta, S., Andrews, M.J, and Han, J.C, (1996a), "Prediction of turbulent flow and heat transfer in rotating square and rectangular smooth channels," ASME Paper No. 96-GT-234

Dutta, S. and Han, J.C., (1996b), "Local Heat Transfer in Rotating Smooth and Ribbed Two-Pass Square Channels with Three Channel Orientations," Trans ASME, Journal of Heat Transfer, vol. 118, pp. 578-584

Dittus, F. W., and Boelter, L. M. K., (1930), *Publications on Engineering*, 2, University of California at Berkeley, Berkeley, CA, p. 443

Ekkad, S.V., and Han, J.C., (1995), "Local Heat Transfer Distributions Near a Sharp 180° Turn of a Two-Pass Square Channel with a Transient Liquid Crystal Image Technique," Journal of Flow Visualization and Image Processing, vol. 2, pp. 285-297

Ekkad, S., and Han, J. C., (1997), "Detailed Heat Transfer Distributions in Two Pass Square Channels with Rib Turbulators," International Journal of Heat and Mass Transfer, vol. 40, pp. 2525–2537

Eiamsa-ard, S., Promvonge, P., (2008), "Numerical Study on Heat Transfer of Turbulent Channel Flow over Periodic Grooves," International Communications in Heat and Mass Transfer, vol. 35, pp. 844-852

Eiamsa-ard, S., Promvonge, P., (2009),"Thermal Characteristics of Turbulent Rib-Grooved Channel Flows," International Communications in Heat and Mass Transfer, vol. 36, pp. 705-711

Fann, S., Yang, W.J., Zhang, N., (1994), "Local Heat Transfer in a Rotating Serpentine Passage with Rib-Roughened Surfaces," International Journal of Heat and Mass Transfer, vol. 37, pp 217-228

Fluent Inc., (2006), FLUENT 6.3 User's Guide

Fu, W. L., Wright, L. M., and Han, J. C., (2005), "Buoyancy Effects on Heat Transfer in Five Different Aspect-Ratio Rectangular Channels With Smooth Walls and 45-Degree Ribbed Walls," ASME Paper No. GT 2005-68493

Gee, D.L., and Webb, R.L., (1980), "Forced Convection Heat Transfer in Helically Rib-Roughened Tubes," International Journal of Heat and Mass Transfer, vol. 23, pp. 1127-1136

Gillespie, D., Ireland, P. T., and Dailey, G. M., (2000), "Detailed Flow and HeatTransfer Coefficient Measurements in a Model of an Internal Cooling Geometry Employing Orthogonal Intersecting Channels," ASME Paper No. 2000-GT-653

Goreloff, V., Goychengerg, M., and Malkoff, V., (1990), "The Investigation of Heat Transfer in Cooled Blades of Gas Turbines," 26th Joint Propulsion Conference. AIAA Paper No. 90-2144

Griffith, T. S., Al-Hadhrami, L., and Han, J. C., (2002), "Heat Transfer in Rotating Rectangular Cooling Channels (AR=4) with Angled Ribs," Trans ASME, Journal of Heat Transfer, vol. 124, pp. 617-625.

"Handbook of Thermochromic Liquid Crystal Technology", Hallcrest Inc

Han, J.C., Glicksman, L.R., and Rohsenow, W.M., (1978), "An Investigation of Heat Transfer and Friction for Rib-Roughened Surface," International Journal of Heat and Mass Transfer, vol. 21, pp. 1143-1159

Han, J. C., (1984), "Heat Transfer and Friction in Channels with Two Opposite Rib-Roughened Walls," Trans ASME, Journal of Heat Transfer, vol. 106, pp. 774-784

Han, J.C. and Park, J. S., (1988), "Developing Heat transfer in Rectangular Channels with Rib Turbulators," International Journal of Heat and Mass Transfer, vol. 31, pp. 183-195

Han, J.C., Ou, S., Park, J.S., and Lei, C.K., (1989), "Augmented Heat Transfer in Rectangular Channels of Narrow Aspect Ratios with Rib Turbulators," International Journal of Heat and Mass Transfer, vol. 32, pp. 1619-1630

Han, J.C., Zhang, Y.M., and Lee, C.P.,(1991), "Augmented Heat Transfer in Square Channels With Parallel, Crossed, and V-Shaped Angled Ribs," Trans. ASME, Journal of Turbomachinery, vol. 113, pp 590-596

Han, J.C., and Zhang, Y.M., (1992), "High Performance Heat Transfer Ducts With Parallel Broken and V-Shaped Broken Ribs," International Journal of Heat and Mass Transfer, vol. 35, No. 2, pp 513-523

Han, J. C. And Zhang, Y. M., (1992a), "Effect of Uneven Wall Temperature on local Heat Transfer in a Rotating Square Channel with Smooth Walls and Radial Outward Flow," Trans ASME, Journal of Heat Transfer, vol. 114, pp. 850-858

Han, J.C., Huang, J.J., and Lee, C.P., (1993), "Augmented Heat Transfer in Square Channels with Wedge-Shaped and Delta-Shaped Turbulence Promoters," Journal of Enhanced Heat Transfer, vol.1, No. 1, pp. 37-52

Han, J.C., Zhang, Y.M., and Kalkuehler, K., (1993a), "Uneven Wall Temperature Effect on Local Heat Transfer in a Rotating Two-Pass Square Channel with Smooth Walls," Trans ASME, Journal of Heat Transfer, vol. 115, pp. 912-920

Han, J.C., Zhang, Y.M., and Lee, C.P., (1994), "Influence of Surface Heating Condition on Local Heat Transfer in a Rotating Square Channel With Smooth Walls and Radial Outward Flow," Trans ASME, Journal of Heat Transfer, vol. 116, pp. 149-158

Han, J. C., Dutta, S., and Ekkad, S., (2000), "Gas Turbine Heat Transfer and Cooling Technology", Taylor and Francis, New York.

Hirota, M., Fujita, H., Syuhada, A., Araki, S., Yoshida, T., and Tanaka, T., (1999), "Heat/Mass Transfer Characteristics in Two-Pass Smooth Channels with a Sharp 180-Deg Turn," International Journal of Heat and Mass Transfer, vol. 42, pp. 3757-3770

Hsieh, S.S, and Liu, W.J., (1996) , "Uneven Wall Heat Flux Effect on Local Heat Transfer in Rotating Two-Pass Channels With Two Opposite Ribbed Walls," Trans ASME, Journal of Heat Transfer, vol. 118, pp. 864-876

Hsieh, S.S. Wang, Y.S, and Chiang, M.H., (1997), "Local Heat Transfer and Velocity Measurements in a Rotating Two-Pass Square Channel with Uneven Wall Temperatures," Trans ASME, Journal of Heat Transfer, vol. 119, pp. 843-848

Huh, M., Liu, Y.H., and Han, J.C., (2009), "Effect of Rib Height on Heat Transfer in a Two Pass Rectangular Channel (AR=1:4) with a Sharp Entrance at High Rotation Numbers," International Journal of Heat and Mass Transfer, vol. 52, pp. 4635-4649

Huh, M., Liu, Y.H., and Han, J.C., (2009a), "High Rotation Number Effects on Heat Transfer in a Rectangular (AR=2:1) Two Pass Channel," ASME Paper No. GT2009-59421

Hwang, J. J., Lai, D. Y. and Tsia, Y.P. , (1999), "Heat Transfer and Pressure drop in Pin Fin Trapezoidal Ducts," Trans ASME, Journal of Turbomachinery, vol. 121, pp.264-271

Hwang, G.J., Tzeng, S.C., Mao, C.P., and Soong, C.Y., (2001), "Heat Transfer in a Radially Rotating Four-Pass Serpentine Channel With Staggered Half-V Rib Turbulators," Trans ASME, Journal of Heat Transfer, vol. 123, pp. 39-49

Hwang, S.D., and Cho, H.H., (2006), "Heat Transfer Enhancement of Internal Passage Using Dimple/Protrusion," 13th International Heat Transfer Conference, Sydney, Australia

Iacovides, H., Jackson, D.C., Ji, H., Kelemenis, G., Launder, B.E., and Nikas, K., (1998), "LDA Study of the Flow Development Through an Orthogonally Rotating U-Bend of Strong Curvature and Rib-Roughened Walls," Trans. ASME, Journal of Turbomachinery, vol. 120, pp. 386-391

Iacovides, H., (1998a), "Computation of Flow and Heat Transfer through Rotating Ribbed Passage," International Journal of Heat and Fluid Flow, vol. 19, pp. 393-400

Johnson, B. V., Wagner, J. H., Steuber, G. D., and Yeh, F. C., (1994), "Heat Transfer in Rotating Serpentine Passages With Trips Skewed to the Flow," Trans ASME, Journal of Turbomachinery, vol. 116, pp 113-123

Johnson, B.V., Wagner, J.H., Steuber, G.D., and Yeh, F.C., (1994a), "Heat Transfer in Rotating Serpentine Passage with Selected Model Orientations for Smooth or Skewed Trip Walls," Trans. ASME, Journal of Turbomachinery, vol. 116, pp. 738-744

Kays, W. M., and Crawford, M. E., (1993), *Convective Heat and Mass Transfer*, 3rd Ed., McGraw–Hill, New York.

Kiml, R., Mochizuki, S., Murata, A., (2001), "Effects of Rib Arrangements on Heat Transfer and Flow Behavior in a Rectangular Rib-Roughened Passage: Application to Cooling of Gas Turbine Blade Trailing Edge," Journal of Heat Transfer, vol. 123, pp. 675-681

Kline, S. J., and McClintock, F. A., (1953), "Describing Uncertainties in Single-Sample Experiments," Mech. Eng.Am. Soc. Mech. Eng., vol. 75, pp. 3-8

Kobayashi, M., Maekawa, H., Takano, T., and Kobayashi, M., (1994), "Experimental Study of Turbulent Heat Transfer in a Two-Dimensional Curved Channel: Time-Mean Temperature and Multiple Temperature/Velocity Correlations in the Entrance Section," JSME International Journal, Series B: Fluids and Thermal Engineering, vol. 37, pp. 545–553

Kumaran, T.K., Han, J.C., and Lau, S.C., (1991), "Augmented Heat Transfer in a Pin Fin Channel with Short or Long Ejection Holes," International Journal of Heat and Mass Transfer, vol. 42, pp. 2617-2628

Lau, S.C., Han, J.C., and Kim, Y.S., (1989), "Turbulent Heat Transfer and Friction in Pin Fin Channels With Lateral Flow Ejection," Trans. ASME, Journal of Heat Transfer, vol. 111, pp. 51-58

Lau, S.C., Cervantes, J., and Han, J.C., (2008), "Internal Cooling Near Trailing Edge of a Gas Turbine Airfoil With Cooling Airflow Through Blockages With Holes," Trans. ASME, Journal of Turbomachinery, vol. 130, pp. 031004-1 – 031004-9

Ligrani, P.M., and Hedlund, C.R., (1998), "Transition to Turbulent Flow in Curved and Straight Channels with Heat Transfer at High Dean Numbers," International Journal of Heat and Mass Transfer, vol. 41, pp. 1739-1748

Ligrani, P.M., Harrison, J.L., Mahmood, G.I., and Hill, M.L., (2001), "Flow Structure Due to Dimple Depressions on a Channel Surface," Physics of Fluids, vol. 13, pp. 3442-3451

Ligrani, P.M., Oliveira, M.M., and Blaskovich, T., (2003), "Comparison of Heat Transfer Augmentation Techniques," AIAA Journal, vol. 41, pp. 337-362

Ligrani, P.M., and Hedlund, C.R., (2004), "Experimental Surface Heat Transfer and Flow Structure in a Curved Channel with Laminar, Transitional, and Turbulent Flows," Trans. ASME, Journal of Turbomachinery, vol. 126, pp. 414-423

Liou, T.M., and Hwang, J.J., (1992), "Developing Heat Transfer and Friction in a Ribbed Rectangular Duct with Flow Separation at Inlet," Trans ASME, Journal of Heat Transfer, Vol. 114, pp. 565-573

Liou, T.M., and Chen, C.C., (1999), "LDV Study of Developing Flows through a Smooth Duct with a 180 deg Straight-Corner Turn," Trans. ASME, Journal of Turbomachinery, vol. 121, pp. 167-174

Liou, T.M., Tzeng, Y.Y., and Chen, C.C., (1999a), "Fluid Flow in a 180 deg Sharp Turning Duct with Different Divider Thicknesses," Trans ASME, Journal of Turbomachinery, vol. 121, pp. 569-576

Liou, T.M., Chen, C.C., Tsai, T.W., (2000), "Heat Transfer and Fluid Flow in a Square Duct with 12 Different Shaped Vortex Generators," Trans. ASME, Journal of Turbomachinery, vol. 122, pp. 327-335

Liou, T.M., Chen, C.C., Tzeng, Y.Y., and Tsai, T.W., (2000a), "Non-intrusive Measurements of Near-Wall Fluid Flow and Surface Heat Transfer in a Serpentine Passage," International Journal of Heat and Mass Transfer, vol. 43, pp. 3233-3244

Liou, T.M., Chen, C.C., and Chen, M.Y., (2001), "TLCT and LDV Measurements of Heat Transfer and Fluid Flow in a Rotating Sharp Turning Duct," International Journal of Heat and Mass Transfer, vol. 44, pp. 1777-1787

Liou, T.M., Chen, M.Y., and Tsai, M.H., (2002), "Fluid Flow and Heat Transfer in a Rotating Two-Pass Square Duct with In-Line 90-deg Ribs," Trans ASME, Journal of Turbomachinery, vol. 124, pp. 260-268

Liou, T.M., Chen, M.Y., Wang, Y.M., (2003), "Heat Transfer, Fluid Flow, and Pressure Measurements Inside a Rotating Two-Pass Duct with Detached 90-Deg Ribs," Trans ASME, Journal of Turbomachinery, vol. 125, pp. 565-574

Liou, T.M., and Dai, G.Y., (2004), "Pressure and Flow Characteristics in a Rotating Two-Pass Square Duct with 45-Deg Angled Ribs," Trans ASME, Journal of Turbomachinery, vol. 126, pp. 212-219

Liou, T.M., Hwang, Y.S., and Li, Y.C., (2006), "Flowfield and Pressure Measurements in a Rotating Two-Pass Duct with Staggered Rounded Ribs Skewed 45 Degrees to the Flow," Trans. ASME, Journal of Turbomachinery, vol. 128, pp. 340-348

Liou, T.M., Chang, S.W., Hung, J.H., Chiou, S.F., (2007), "High Rotation Number Heat Transfer of a 45° Rib-Roughened Rectangular Duct with Two Channel Orientations," International Jouranl of Heat and Mass Transfer, vol. 50, pp. 4063-4078

Liu, Y.H., Huh, M., and Han, J.C., (2008), "Heat Transfer in a Two-Pass Rectangular Channel (AR=1:4) Under High Rotation Numbers," Trans ASME, Journal of Heat Transfer, vol. 130, pp. 081701-1 – 081701-9

Lorenz, S., Mukomilow, D., and Leiner, W., (1995), "Distribution of the Heat Transfer Coefficient in a Channel with Periodic Transverse Grooves," Experimental Thermal and Fluid Science, vol. 11, pp. 234-242

Luo, J., and Razinsky, E.H., (2009), "Analysis of Turbulent Flow in 180 deg Turning Ducts with and without Guide Vanes," Trans ASME, Journal of Turbomachinery, vol. 131, pp. 021011-1 – 021011-10

Mahmood, G.I., Hill, M.L., Nelson, D.L., Ligrani, P.M., Moon, H.K., and Glezer, B., (2001), "Local Heat Transfer and Flow Structure on and Above a Dimpled Surface in a Channel," Trans ASME, Journal of Turbomachinery, vol. 123, pp. 115-123

McMillin, R.D., and Lau, S.C., (1994), "Effect of Trailing Edge Ejection on Local Heat(Mass) Transfer in Pin Fin Cooling Channels in Turbine Blades," Trans. ASME, Journal of Turbomachinery, vol. 116, pp. 159-168

Metzger, D. E., Plevich, C. W., and Fan, C. S., (1984), "Pressure Loss Through Sharp 180° Turns in Smooth Rectangular Channels," Trans ASME, Journal of Engineering for Gas Turbine and Power, vol. 106, pp. 677–681

Metzger, D.E., Fan, C. S. and Haley, S.W., (1984a), "Effects of Pin shape and Orientation on Heat Transfer and Pressure Loss in Pin Fin Arrays," Trans ASME, Journal of Heat Transfer, - vol.106, pp. 252-257

Metzger, D. E., and Plevich, C. W, (1990), "Effects of Turn Region Treatments on Pressure Loss through Sharp 180° Bends," Proceedings of Third International Symposium on Transport Phenomena and Dynamics of Rotating Machinery (ISROMAC-3) 301–312

Metzger, D. E., Bunker, R. S. and Bosch, G., (1991), "Transient Liquid Crystal Measurement of Local Heat Transfer on a Rotating Disk with Jet Impingement," Trans ASME, Journal of Turbomachinery, vol. 113, pp. 52-59

Miller, D.S., (1978), "Internal Flow systems," BHRA Fluid Engineering System, UK, pp 43

Mochizuki, S, Takamura, J, Yamawaki, S and Yang, W.J., (1994), "Heat Transfer in Serpentine Passages with Rotation," Trans ASME, Journal of Turbomachinery, vol. 116, pp. 133-140

Murata Lab, http://www.mmlab.mech.tuat.ac.jp/mmlab/fig/fig_01.jpg

Nagoga, G. P., (1996), "Effective Methods of Cooling of Blades of High Temperature Gas Turbines," Moscow Aerospace Institute, Moscow, Russian, pp.100

Nakayama, H., Hirota, M., Fujita, H., Yamada, T., and Koide, Y., (2006), "Fluid Flow and Heat Transfer in Two-Pass Smooth Rectangular Channels with Different Turn Clearances," Trans ASME, Journal of Turbomachinery, vol. 128, pp. 772-785

Namgoong, H., Son, C., and Ireland, P., (2008), "U-bend shaped turbine blade cooling passage optimization," 12th AIAA/ISSMO Multidisciplinary Analysis and Optimization Conference, Victoria, Canada

Ng, Y.T., Luo, S.C., Lim, T.T., and Ho, Q.W., (2006), "On Swirl Development in a Square Cross-sectioned, S-shaped duct," Experiments in Fluids, vol. 41, pp. 975-989

Park, J.S., Han, J.C., Huang, Y., and Ou, S., (1992), "Heat Transfer Performance Comparisons of Five Different Rectangular Channels with Parallel Angled Ribs," International Journal of Heat and Mass Transfer, vol. 35, pp 2891-2903

Park, C.W., and Lau, S.C., (1998), "Effect of Channel Orientation of Local Heat (Mass) Transfer Distributions in a Rotating Two-Pass Square Channel with Smooth Walls," Trans ASME, Journal of Heat Transfer, vol. 120, pp. 624-632

Parsons, J.A., Han, J.C., and Zhang, Y.M.,(1994), "Wall Heating Effect on Local Heat Transfer in a Rotating Two-Pass Square Channel With 90° Rib Turbulators," International Journal of Heat and Mass Transfer, vol. 37, pp 1411-1420

Prakash, C. and Zerkle, R., (1992), "Prediction of Turbulent Flow and Heat Transfer in a Radially Rotating Square Duct," Trans. ASME, Journal of Turbomachinery, vol. 114, pp. 835-846

Prakash, C., Zerkle, R., (1995), "Prediction of Turbulent Flow and Heat Transfer in a Ribbed Rectangular Duct With and Without Rotation," Trans. ASME, Journal of Turbomachinery, vol. 117, pp. 255-264

Rao, D. V. R., Babu, C. S., and Prabhu, S. V., (2004), "Effect of Turn Region Treatments on the Pressure Loss Distribution in a Smooth Square Channel With a Sharp 180° Bend," International Journal of Rotating Machinery ,vol. 10, pp. 459–468

Saha, A.K. and Acharya, S., (2005), "Flow and Heat Transfer in an Internally Ribbed Duct with Rotation: An Assessment of Large Eddy Simulations and Unsteady Reynolds-Averaged Navier-Stokes Simulations," Trans ASME, Journal of Turbomachinery, vol. 127, pp 306-320

Saha, A.K., and Acharya, S., (2007), "Turbulent Heat Transfer in Ribbed Coolant Passages of Different Aspect Ratios: Parametric Effects," Trans ASME, Journal of Heat Transfer, vol. 129, pp. 449-463

Saha, K, Acharya, S., and Nakamata, C., (2008), "Heat Transfer and Pressure Drop in a Converging Lattice Structure for Airfoil Trailing Edge Cooling," ASME Paper No. IMECE-2008-68152

Saha, K., and Acharya, S., (2011), "Effect of Entrance Geometry on Heat Transfer in a Narrow (AR=1:4) Rectangular Two Pass Channel with Smooth and Ribbed Walls," ASME Paper No. GT2011-46076

Samad, A., Lee, K.D., and Kim, K.Y., (2008), "Multi-objective Optimization of a Dimpled Channel for Heat Transfer Augmentation," Heat and Mass Transfer, vol. 45, pp. 207-217

Schüler, M., Zehnder, F., Weigand, B., Wolfersdorf, J.V., and Neumann, S.O., (2011), "The Effect of Turning Vanes on Pressure Loss and Heat Transfer of a Ribbed Rectangular Two-Pass Internal Cooling Channel," Trans ASME, Journal of Turbomachinery, vol. 133, pp. 021017-1 – 021017-10

Schüler, M., Zehnder, F., Weigand, B., Wolfersdorf, J.V., and Neumann, S.O., (2011a), "The Effect of Side Wall Mass Extraction on Pressure Loss and Heat Transfer of a Ribbed Rectangular Two-Pass Internal Cooling Channel," Trans ASME, Journal of Turbomachinery, vol.133, pp.021002-1 – 021002-11

Schabacker, J., Bolcs, A., and Johnson, B.V., (1998), "PIV Investigation of the Flow Characteristics in an Internal Coolant Passage with Two Ducts Connected by a Sharp 180° Bend," ASME Paper No. GT1998-544

Son, S. Y., Kihm, K. D., and Han, J. C., (2002), "PIV Flow Measurements for Heat Transfer Characterization in Two Pass Square Channels with Smooth and 90° Ribbed Walls," International Journal of Heat and Mass Transfer, vol. 45, pp. 4809–4822

Taslim, M. E., Rahman, A. and Spring, S. D., (1991), "An Experimental Investigation of Heat Transfer Coefficients in a Spanwise Rotating Channel with Two Opposite Rib-Roughed Walls," Trans ASME, Journal of Turbomachinery, vol.113, pp. 75-82

Taslim, M.E., Li, T., Kercher, D.M., (1996), "Experimental Heat Transfer and Friction in Channels Roughened With Angled, V-Shaped, and Discrete Ribs on Two Opposite Walls," Trans. ASME, Journal of Turbomachinery, vol. 118, pp. 20-28

Taslim, M.E., and Wardsworth, C.M., (1997), "An Experimental Investigation of the Rib Surface-Averaged Heat Transfer Coefficient in a Rib-Roughened Square Passage," Trans. ASME, Journal of Turbomachinery, vol. 119, pp. 381-389

Taslim, M.E., and Lengkong, A., (1998), "45 deg Staggered Rib Heat Transfer Coefficient Measurements in a Square Channel," Trans. ASME, Journal of Turbomachinery, vol. 120, pp. 571-580

Taylor, A.M.K.P, Whitelaw, J.H., and Yianneskis, M., (1982), "Developing flow in S-shaped ducts 1: Square Cross Section Duct," NASA Contractor Report 3550

Vedula, R.J., and Metzger, D.E., (1991) ,"A Method for the Simultaneous Determination of Local Effectiveness and Heat Transfer Distributions in Three-Temperature Convection Situations," ASME Paper No. 91-GT-345

Viskanta, R., (1993), "Heat Transfer to Impinging Isothermal Gas and Flame Jets," Experimental Thermal and Fluid Science, vol. 6, pp. 111-134

Vogel, G., and Weigand, B., (2001), "A New Evaluation Method for Transient Liquid Crystal Experiments," National Heat Transfer Conf., NHTC2001-20250, California

Wagner, J. H., Johnson, B. V. and Kopper, F. C, (1991), "Heat transfer in Rotating Serpentine Passage with Smooth Walls," Trans ASME, Journal of Turbomachinery, vol. 113, pp. 321-330

Wagner, J. H., Johnson, B. V., Graziani, R. A., and Yeh, F. C., (1992), "Heat Transfer in Rotating Serpentine Passages With Trips Normal to the Flow," Trans. ASME, Journal of Turbomachinery, vol. 114, pp. 847-857

Wang, T.S., and Chyu, M.K., (1994), "Heat Convection in a 180 deg Turning Duct with Different Turn Configurations," Journal of Thermophysics and Heat Transfer, vol. 8, No.3, pp. 595-601

Wang, L., Sunden, B., (2007), "Experimental Investigation of Local Heat Transfer in a Square Duct with Various-shaped Ribs," Heat Mass Transfer, vol. 43, pp. 759-766

Webb, R.L., (1981), "Performance Evaluation Criteria for Use of Enhanced Heat Transfer Surfaces in Heat Exchanger Design," International Journal of Heat and Mass Transfer, vol. 24, pp. 715-726

Wilcox, D.C., (2006), "Turbulence Modeling for CFD," 3rd Edition, DCW Industries, Incorporated

Won, S.Y., Zhang, Q., and Ligrani, P.M., (2005), "Comparisons of Flow Structure Above Dimpled Surfaces with Different Dimple Depths in a Channel," Physics of Fluids, vol. 17, pp. 045105-1 – 045105-9

Wright, L.M., Fu, W.L., Han, J.C., (2004), "Thermal Performance of Angled, V-Shaped, and W-Shaped Rib Turbulators in Rotating Rectangular Cooling Channels (AR=4:1)," Trans. ASME, Journal of Turbomachinery, vol. 126, pp 604-614

Wright, L. M., Fu, W. L., and Han, J. C., (2005), "Influence of Entrance Geometry on Heat Transfer in Rotating Rectangular Cooling Channels (AR=4:1) with Angled Ribs," Trans ASME, Journal of Heat Transfer, vol. 127, pp. 378-387

Zhang, Y. M., Gu, W.Z., and Han, J. C., (1994), "Heat Transfer and Friction in Rectangular Channels With Ribbed or Ribbed-Grooved Walls," Trans ASME, Journal of Heat Transfer, vol. 116, pp. 58-65

Zhang, Y. M., Han, J. C., Parsons, J. A., and Lee, C. P., (1995), "Surface Heating Effect on Local Heat Transfer in a Rotating Two-pass Square Channel with 60 deg Angled Rib Turbulators," Trans. ASME, Journal of Turbomachinery, vol. 117, pp. 272-280

Zhou, F., Lagrone, J., and Acharya, S., (2007), "Internal Cooling in 4:1 AR Passages at High Rotation Numbers," Trans ASME, Journal of Heat Transfer, vol. 129, pp 1666-1675

Zhou, F., and Acharya, S., (2008), "Heat Transfer at High Rotation Numbers in a Two-Pass 4:1Aspect Ratio Rectangular Channel With 45 deg Skewed Ribs," Trans. ASME, Journal of Turbomachinery, vol. 130, pp. 021019-1 - 021019-12

VITA

Krishnendu Saha was born in Kolkata, India, on 22nd June, 1985. He is the younger son of Mr. Dilip Kumar Saha and Mrs. Sarama Saha. He received his B.E in Mechanical Engineering degree from Jadavpur University, Kolkata, India, in 2006. He then joined the Ph.D. program in Mechanical Engineering at Louisiana State University under the supervision of Dr. Sumanta Acharya. He is a student member of the American Society of Mechanical Engineers (ASME). He is a Ph.D. candidate in Mechanical Engineering at the commencement of Fall 2012.